Investigation into the Synthesis of Polymeric Core and Shell Nanoparticles for the Controlled Release of Small Hydrophobic Payloads

by

Braden Kristopher Hahn

A dissertation submitted to the Graduate Faculty of
Auburn University
in partial fulfillment of the
requirements for the Degree of
Doctor of Philosophy

Auburn, Alabama
May 6, 2023

Keywords: Drug Delivery, Polymers, Nanoparticles, Controlled Release

Approved by

Allan E. David, Chair, Associate Professor of Chemical Engineering
Bryan Beckingham, Professor of Chemical Engineering
Selen Cremaschi, Professor of Chemical Engineering
Robert Arnold, Professor of Harrison School of Pharmacy

Abstract

Effective and safe delivery of drugs into the body, where it will provide the maximum benefit to the patient, is the ultimate treatment goal. Factors such as the drug's bioavailability and pharmacokinetics can lessen efficacy and decrease the safety of these drugs, increasing the cost and potential adverse effects. This is a particular problem for small, hydrophobic drugs, which make up the majority of existing drugs and newly discovered drug candidates. This drug delivery problem is exacerbated for many chemotherapeutics, which have extremely narrow concentration windows where they are safe and effective. This makes delivering these drugs without systemic side effects very challenging. A number of methods and systems have been developed to address this drug delivery limitation, such as controlled release of these drugs from polymeric nanoparticles. These particles are inherently safe, being made of biodegradable, biocompatible, FDA-approved polymers whose release kinetics are well understood and customizable. In addition, more complex designs, such as the core and shell nanoparticle, have allowed greater flexibility and customizability of release without sacrificing size or material. However, clinical translation of these particles has been limited thus far, with some of the main reasons being the lack of control over key performance-defining properties such as size and size distribution.

This research explores synthesis conditions, output parameters, and performance of polymeric nanoparticle formation methods. Our goal is to understand synthesis conditions and parameters which will allow us to predict and control the formation of polymeric nanoparticles made of common and safe polymers: poly (D,L) lactic-co-glycolic acid (PLGA) and poly (L) lactic acid (PLLA). To achieve this goal, we analyzed and modeled a common laboratory method for producing PLGA nanoparticle cores. Machine learning and component trend analysis were used

to develop a practical, scalable model for best control over particle size and size distribution, before characterizing the effect on release of model, small drugs. We then investigated different methods for coating these cores with a PLLA shell for improved controlled release kinetics and flexibility, attempting to find synthesis parameters which maximize formation efficiency and allow for control of both the core and shell dimensions. Finally, we analyzed the performance of these particles in different formulations of chitosan hydrogel wound dressings. We believe this research sets an important foundation for polymer nanoparticle synthesis and small, hydrophobic drug release by expanding knowledge on the features and performance of these systems and illuminating favorable procedures and methods that optimize their controlled release. This includes the main findings: a practical, scalable power law for dimension control of PLGA nanoparticles, important insights into a modified emulsion method for core/shell nanoparticle production and how it could be further improved for higher formation efficiency, as well as a proof of concept for a hydrogel-PLGA nanoparticle system which showed highly variable release with controlling swelling and structure.

Acknowledgments

The list of people to thank is endless, because we never journey alone.

I first want to give enormous thanks to my adviser, Dr. Allan E. David, for mentoring, guiding, and supporting me in my time at Auburn. His kindness, insight, and guidance has allowed me to grow and excel in this new role in my life. I count myself blessed for having him as adviser and a mentor for my academic journey.

I would like to thank my committee members Dr. Robert Arnold, Dr. Bryan Beckingham, and Dr. Selen Cremaschi for their time, support, and comments for both my preliminary defense and my final dissertation defense. I would also like to thank Dr. Ed Davis for graciously agreeing to act as my university reader for my dissertation.

Many thanks to Dr. Michael Miller, Dr. Ramsis Farag, Dr. Vitaly Vodyanoy, Dr. Virginia Davis, David Crumbley, Tripp Hinkle, Armin Seyedesfahani, Daniel Meadows for their assistance and access to their equipment and knowledge in my experiments.

Thank you to all staff and members of the CCTS at UAB, who supported and provided me with a diverse and interesting network during my time with the TL1 fellowship program.

I would like to thank former and current members of the David Lab research group as guides on how to be a researcher, collaborator, and friend: Dr. Xin Fan, Dr. Tareq Anani, Dr. Barry Yeh, Dr. Alexander Kelly, Dr. Alan Hanley, Dr. Prachi Sangle, Dr. Richard Cullum, Dr. Marjan Azadi, Dr. Nayer Sultana, Shiva Rahmati, Pegah Tayeb, Sehar Ahmed, and Dr. Sadia Sikder. I also want to thank many of the undergraduate researchers who inspired me with their dedication: Janset Aksoy, Ashley Fountain, Jonathan Hall, Javier Nishikawa, Caleb Puckett, Al Stumm, and

TA Sluis. Of course, I would like to acknowledge every member of the Chemical Engineering Department especially, Dr. Mario Eden, Elaine Manning, and Georgetta Dennis for their help and support through the years.

I would like to extend my enormous thanks to all my friends I have gained while pursuing this degree. All their support and fellowship, and especially their friendship, was needed, and I will always cherish the movie nights, tailgates, get-togethers, and hangouts together.

I feel confident in saying that I would not have been able to complete this program without the love and support of my parents, Kris and Alicia. Their love, guidance, and support mean more than I can fully put into words. They were always there for a call or to come and support in person, and I am eternally grateful. I also want to sincerely thank my father-in-law Danny Rivera and his wife Erica Rivera, for supporting and loving unconditionally my wife and I, and for providing a close, safe space. I am of course grateful for the love and support of the rest of my family: my twin sister Hannah and her husband John, my brother-in-law Chris, grandmothers Patricia, Judy, and Karla, as well as my numerous aunts and uncles who have loved and supported me.

Thank you to my fluffy boy, Nano, whose snores, snuggles, and playtimes helped me as I worked and lived.

Finally, I cannot begin to express my love and thanks for my wife, Francheska. She is my rock, the one I always looked to and went to when times were difficult. She is my person, simply and completely, without whom I wouldn’t be the man I am today. I am confident saying that I would not be here without her, and I thank her for agreeing to take on this journey with me.

War Eagle

Table of Contents

List of Tables

List of Figures

List of Abbreviations

BET	Brunauer-Emmet-Teller Theory
BJH	Barrett-Joyner-Halenda
CD	Crosslink Density
C/S	Core/Shell
CEDA	Coaxial electrohydrodynamic Atomization
Chit	Chitosan
CSB	Chitosan-Schiff Base
CSHG	Chitosan hydrogel
DB	Degree of Burst
DCM	Dichloromethane
DDS	Drug Delivery System
DFT	Density Functional Theory
DLS	Dynamic Light Scattering
DOX	Doxorubicin
ESEM	Emulsion Solvent Evaporation Method
FDA	Food & Drug Administration
GA	Glycolic acid (glycolide)
GoF	Goodness of Fit
GMM	Gaussian Mixture Model
GTA	Glutaraldehyde
HD	Hydrodynamic diameter
LA	Lactic acid (lactide)
MAE	Mean Absolute Error
MEC	Minimum effective concentration
MTC	Minimum toxic concentration
MW	Molecular weight
NP	Nanoparticle
PDI	Polydispersity Index
PEG	Polyethylene glycol
PK	Pharmacokinetics
PLGA	Poly-lactic-co-glycolic acid
PLLA	Poly (L) lactic acid
PTX	Paclitaxel
PVA	Polyvinyl alcohol
RF	Random Forest
RMSE	Root Mean Square Error
RPM	Revolutions per minute
SEM	Scanning Electron Microscopy
SSA	Specific Surface Area
TEW	Therapeutic Effective Window
US	United States (of America)

Chapter 1: Introduction

1.1 Drug Delivery

Drug development and discovery in modern medicine continues to advance the treatment capabilities and survival prognoses of numerous diseases and conditions. Despite these advances, the safe and effective delivery of those drugs to the patient remains a complex and challenging task. Proper delivery of the desired drug dose relies on numerous factors, dependent on patient condition, genetics, and administration route. This chapter will introduce key concepts and challenges with drug delivery, before outlining the motivation, targeted application, and description of the experimental work laid out in the following chapters.

1.1.1 Bioavailability and Pharmacokinetics

The first important factor when considering drug delivery is the route of administration and how it affects the drug's bioavailability and pharmacokinetics. A drug's bioavailability is the amount of active drug available to the body for its intended purpose[1]. Oral routes such as pills, liquids, or tablets are the most common but often lead to the lowest bioavailability due to the extreme environments of the gastrointestinal tract and the metabolic barriers necessary for adsorption into the system.[2] Membranal administration via intranasal, rectal, inhalation, or sublingual routes requires transfer across a barrier such as membrane or tissue for systemic distribution, but bypasses metabolic pathways leading to overall higher bioavailability.[3] Intravenous administration or injection results in 100% bioavailability by bypassing any transfer barrier.[3,4] Post-administration, many factors independent of route affect the true bioavailability over time, such as lipid solubility, molecular size and charge, patient blood flow, and pharmacologic effect.. These factors represent the pharmacokinetics (PK) of the drug, defined by the processing by, interaction with, and pharmacologic effect to the body.[5] One important interaction is protein adsorption, where drugs may non-specifically bind to plasma proteins such as albumin. This binding can be reversible or even act as a sustained release reservoir. However, this binding often eliminates free drug available to the body and leads to lower plasma concentration and increased drug elimination.[6] Ideally, drug-protein interaction should be considered before dosing, and often drugs should be protected from this phenomenon. Drug elimination occurs via several systems, including the renal and biliary systems, via sweating, saliva, or hair deposition. Drugs can also be inactivated via metabolization, although some drugs are activated post-administration by interacting with certain enzymes.[7] Taken together, the bioavailability from the administration route and the specific pharmacokinetics of the drug once in circulation determine the effective drug concentration in the plasma and ultimately how effectively a drug can be delivered.

1.1.2 Therapeutic Effective Window

The effective dose of an administered drug is often measured by the plasma drug concentration, as it is often easier to measure than the drug concentration at the desired site[8]. Every drug has a concentration range for its highest effectiveness and lowest toxicity called the therapeutic effective window (TEW). Two concentrations demarcate this range: the minimum effective concentration (MEC), below which there is no therapeutic effect, and the minimum toxic concentration (MTC), above which systemic toxic interactions dominate, causing harmful side effects.[9–11] Deviation of drug concentrations outside the TEW results in suboptimal drug performance.[12] A therapeutic effective window is displayed in Figure 1.1.1, as is the effect of different injection administration methods on the drug plasma concentration relative to the TEW. The administration route and the pharmacokinetics ultimately determine whether the drug plasma concentration remains within the TEW or how severe and long lasting the side effects will be, and so are critical when considering drug delivery.

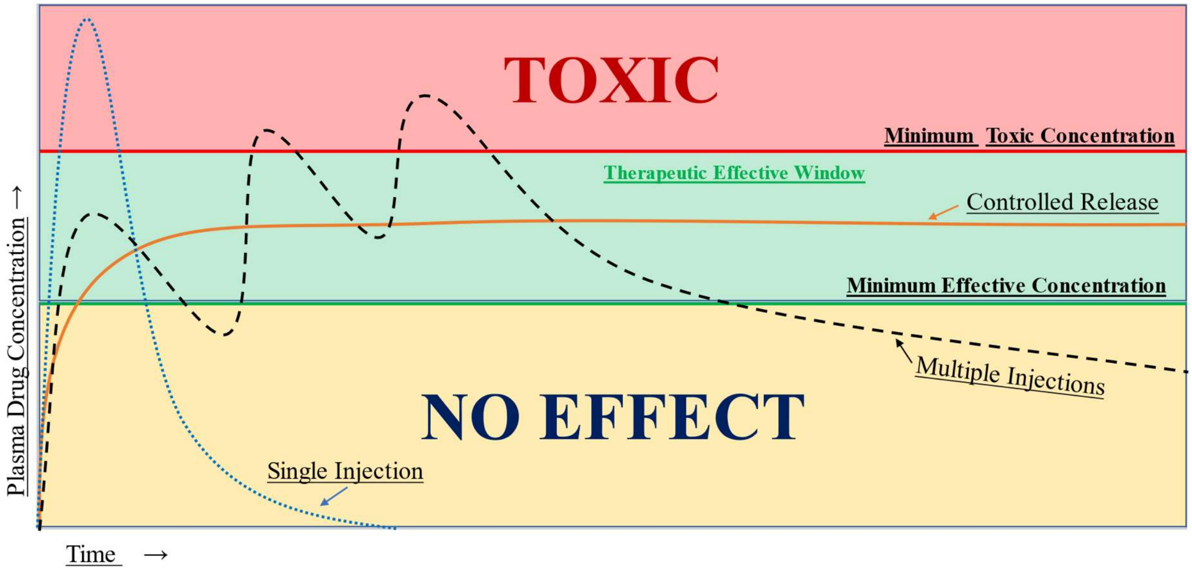

Figure 1.1.1: Drug Plasma Concentration vs. Injection Methods, Adapted from Lee et al[9]

1.1.3 Single & Multiple Injections

For highest bioavailability, intravenous injections are the typical administration method. The specific injection frequency greatly affects plasma drug concentration relative to the TEW. Figure 1.1.1 shows this effect for a single intravenous injection (dotted blue line) and a multiple injection regimen (dashed black line). A single injection rapidly raises the concentration above the toxic level, causing side effects before quickly being cleared and eliminated from the body by various metabolizing and elimination methods[9]. Delivering multiple injections of smaller doses based on the patient's PK maintains the concentration within the TEW for a longer time. However, timing the injections and calculating appropriate dose patient-by-patient for sufficient bioavailability is extremely challenging. These parameters will almost certainly change from patient to patient and even in the same patient over time depending on their pharmacokinetic factors such as weight, age, hydration etc.[11] Perfect maintenance of concentration within the TEW therefore is practically impossible for most drugs.

1.1.4 Controlled Release

Properly maintaining a therapeutic effective dose is elusive. Several drug delivery systems were developed for controlled drug release over a tunable period of time, as shown in Figure 1.1.2[13]. Many act as depots or reservoirs, such as patches, films, wound dressings, and intrauterine devices, by slowly releasing a small amount of drug from a large, stored amount while remaining embedded in a stationary location, ensuring that enough drug will be bioavailable and therefore effective. Other systems are mobile, smaller, and designed to overcome drug solubility or offer specific site targeting, such as nanoparticles, conjugates, and cell targeting systems. All these systems can ideally be tuned so that their release matches the elimination and metabolization rate from the drug's pharmacokinetics, called controlled release. Represented by the orange solid line in Figure 1.1.1, the level quickly reaches therapeutic levels and holds until the drug is finally exhausted. Not only does this release type improve the drug's efficacy, but the ability to control the release timing and rate also has other advantages, such as co-delivery of various payloads. Patients are also more likely to comply with this multiple dose single injection type. Due to this, controlled release drug delivery systems are highly sought-after to improve the delivery of more toxic and less bioavailable drugs.

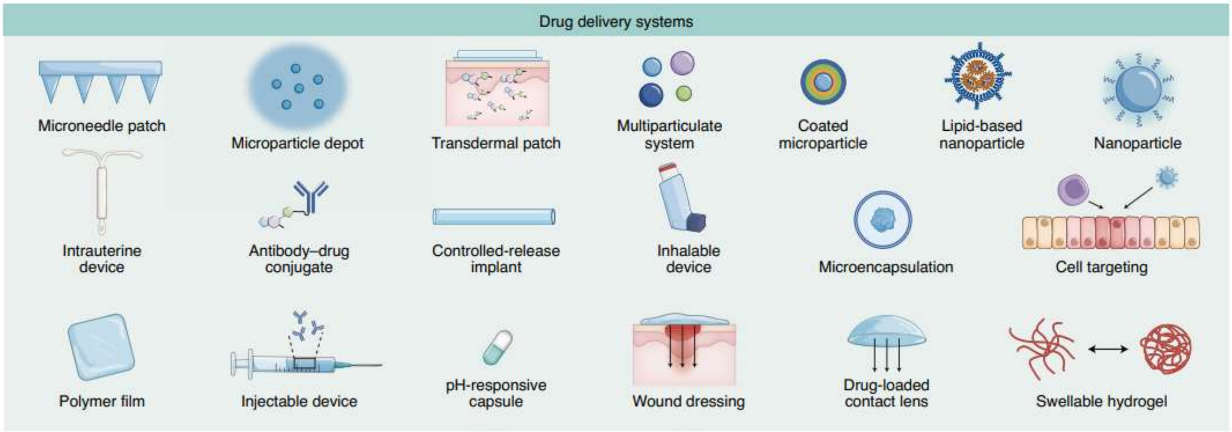

Figure 1.1.2: Drug Delivery Systems Displaying Multiple Strategies for Drug Payload Protection and Release[13]

1.2 Challenges and Motivation for Work

1.2.1 Drug Hydrophobicity and Molecular Weight

Drugs which are ideal candidates for controlled release drug delivery systems (DDS) are those whose bioavailability is low regardless of administration route. This poor bioavailability is most commonly due to the lipid solubility characteristics of the drugs, i.e., hydrophobicity. The more hydrophobic a drug is the more easily it aggregates upon entering circulation, leading to inactivity, rapid clearance, or embolisms[14,15]. The dosage of these drugs must be increased to ensure any therapeutic effect, often exceeding the MTC and causing severe side effects[16]. This inefficiency is prevalent in drug discovery and development, as most drugs are hydrophobic and classified as small molecule (< 100 atoms)[17]. Figure 1.2.1, from Harashima et al[17], shows the prevalence of small and hydrophobic drugs from FDA new drug reports from 2015 to 2019[18]. While hydrophobic drugs are detrimental to bioavailability, small molecule drugs are generally preferrable, characterized by predictable pharmacokinetics, simple manufacturing, and higher stability than larger drugs like biomolecules[19]. However, they are also non-targeted, leading to systemic toxic effects, especially for small molecule drugs used to treat highly complex diseases such as cancer.

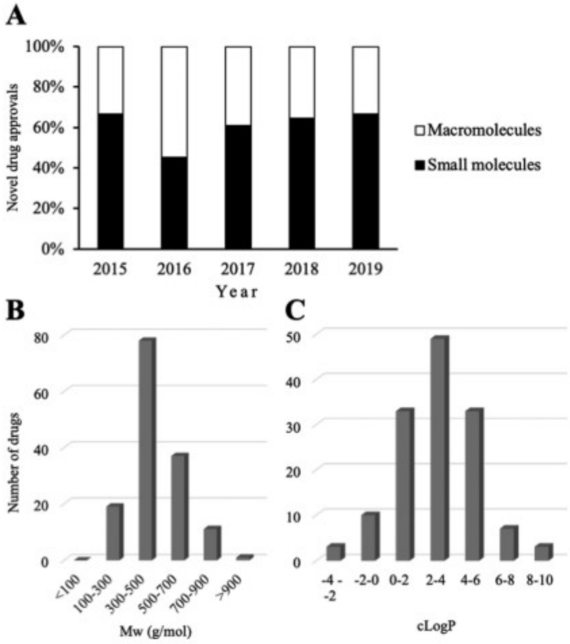

Figure 1.2.1: Recent Drug Approval Statistics A) Small Molecules vs. Macromolecules 2015-2019 and Distribution of MW (B) and hydrophobicity (C) of new drug approvals[17]

1.2.2 Cancer & Chemotherapeutics

Cancer is one of the deadliest diseases today, resulting in roughly 10 million deaths worldwide and 19 million new cases in 2020[20]. In the US alone, there will be a projected 2 million new cases and over 600,000 deaths attributed to cancer in 2023[21]. The complexity and deadliness of cancer lies in its ability to avoid destruction due to its heterogeneity and drug resistance[22,23]. Different antitumor drugs were developed to overcome this resistance, with roughly 89 small molecule drugs being approved today for chemotherapy worldwide[24]. Chemotherapy, a first line co-treatment with surgery and/or radiation for most cancers, looks to avoid cancer's challenges by delivering a cocktail of drugs at once. As previously discussed, most drugs are small molecule and hydrophobic, and typically intravenously administered, exceeding their narrow TEW and causing severe side effects which can themselves be fatal. For example, Doxorubicin (DOX) is a common chemotherapeutic used for treating various cancers, including childhood lymphoblastic leukemia[25], breast cancer[26], ovarian[27], and lung cancers[28,29]. DOX has an extremely small therapeutic effective window of roughly 30 mg/m^2 to around 45 mg/m^2 for cumulative dose according to several studies[30,31] and its most severe side effect is cardiotoxicity which can lead to heart failure[28,32]. Therefore, the correct dosing of DOX and other similar small hydrophobic chemotherapeutics is critical but often very challenging. Instead of using injections, nanoparticle (NP) drug delivery systems have emerged as prime candidates for improving the delivery of these chemotherapeutics. They have shown a wide range and good customization of controlled release, with the ability to efficiently encapsulate and protect small and hydrophobic molecules from protein adsorption or clearance.[33] Their surface can also be targeted improving the efficacy and uptake of encapsulated chemotherapeutics by localizing the drug effects[14]. In fact, the first FDA-approved nanoparticle drug delivery was Doxil, which was a surface-modified liposomal DDS for the improved delivery of DOX[31,34]. Despite this, some challenges remain, such as optimized drug loading, control over properties such as size, surface morphology, distribution, variable controlled release, and difficulties in scale-up manufacturing, necessary for clinical translation.

1.3 Summary of Chapters

The following chapters will detail the experimental results and analysis of this research which seeks to address some of the challenges remaining for nanoparticle drug delivery systems: size control, varied controlled release, and initial investigation for scale-up manufacturing.

Chapter 2 provides background on controlled release terminology, including release profiles and kinetic models and techniques used to characterize nanoparticles, as well as the materials and development of two types of nanoparticle drug delivery systems relevant to this work: polymeric core nanoparticles and core and shell polymeric nanoparticles.

Chapter 3 details the investigation and subsequent modeling of the synthesis method common to produce the polymeric nanoparticle cores for both size control and scale-up, as well as the experiments for characterizing their release and preservation of size during storage.

Chapter 4 describes the investigations and optimization experiments for two methods developed to produce core and shell polymeric nanoparticles, focusing on synthesis parameters' effect on formation efficiency, particle dimensions, and release kinetics.

Chapter 5 focuses on a further application of the knowledge and optimization thus far, with the initial experimentation of impregnation of polymeric nanoparticles into chitosan hydrogels for complex wound treatment and drug delivery.

Chapter 6 summarizes and concludes the work presented for small molecule, hydrophobic drug delivery, and presents future directions for further knowledge and development.

Chapter 2: Background

2.1 Release Behavior and Kinetics

Here we discuss four release profile types for nanoparticle drug delivery systems. The desired profile varies with application and situation; ideally the exact release rate and dosage could be tailored on a patient-by-patient basis. This section will introduce each type of release profile so we can better understand what controlled release means and the models typically used to quantify their kinetics.

2.1.1 Burst vs. Sustained Release

The most common type of release is the burst release, characterized by the quick release of most of the encapsulated payload in a short time. Burst release is generally undesirable for most applications due to the inability to control the release so drug concentration remains in the therapeutic effective window. With a burst release, the majority of drug is immediately released very early post-administration before full circulation and distribution. This results in extremely high local drug concentration. All the drug released at this site is quickly degraded and removed from circulation, shortening the drug's half-life and increasing the number of doses needed and thus the cost of the treatment.[35] Figure 2.1.1 from Brazel and Huang (2001)[35] shows an example of a burst release profile compared to a zero-order controlled release.

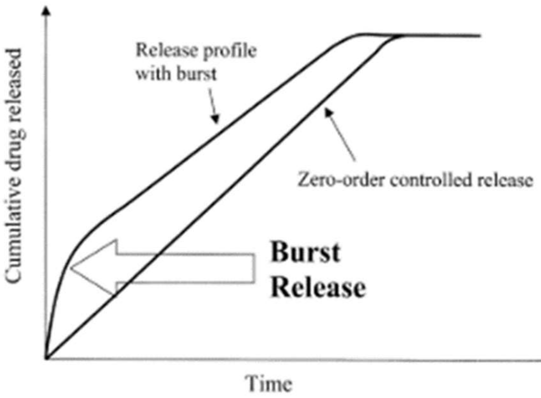

Figure 2.1.1: Burst Release Compared to Zero Order Controlled Release[35]

The exact amount of time that qualifies for a burst release is not well defined. However, Brazel and Huang[36] have defined a Degree of Burst (DB) as the ratio of instantaneous release at a given time to the rate the system reaches at steady, generally after a long time.

$$DB = \frac{\left(\frac{dM_i}{dt}\right)_t}{\left(\frac{dM_i}{dt}\right)_{SS}} \quad (1)$$

Where M_i is the mass released at time *t.* A DB of 1 means no burst release, and a steady sustained release. A DB less than 1 indicates a lag effect while a DB greater than 1 indicates a burst effect.

A burst release can be a desirable profile for certain applications. For example, for complex and extensive wounds an immediate delivery of pain medication and antibiotics to the target site is necessary for successful treatment. Drugs that have minimal toxic effects and need to be delivered quickly are good candidates for burst release, and these would not necessarily benefit from polymeric nanoparticles for drug delivery. Other nanoparticle systems however such as liposomes can shield drugs from clearance while also providing a burst release.

Sustained release is the highly sought-after release profile for nanoparticle-based drug delivery. It is the release of encapsulated payload at a constant rate over longer periods, usually greater than a few hours. Sustained and controlled release are often interchangeable in literature, but controlled release will be variable sustained release in this dissertation.

Ideally, sustained release rate would be a linear trend with the slope representing the rate. Current research in producing a sustained release almost always shows a small burst release followed by a long-sustained release[37,38]. This small burst is due to drug molecules trapped on or near the surface being released almost immediately upon application. An example of this is seen in Figure 2.1.2 from Yao et al.[39], where red dye loaded into polymeric microspheres has an initial burst release followed by a week of sustained release.

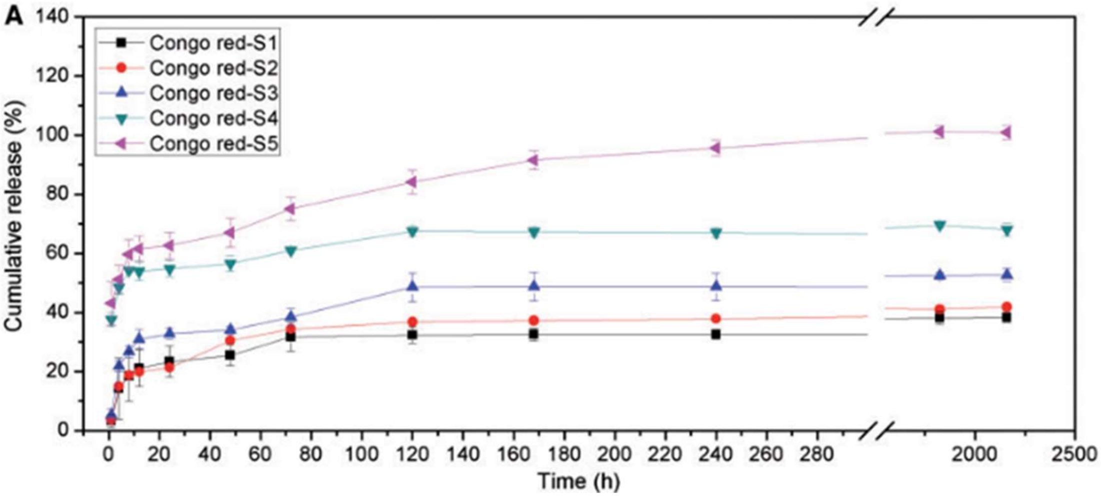

Figure 2.1.2: Example of Sustained Release of Congo Red Dye from PLGA Microspheres[39]

2.1.2 Delayed Burst and Delayed Sustained

Burst and sustained release profiles can be modified by adding a delay time until the release begins. This delay time is outlined by the red brackets in Figure 2.1.3[40] , with examples of delayed burst (yellow star) and delayed sustained (green star) release profiles.

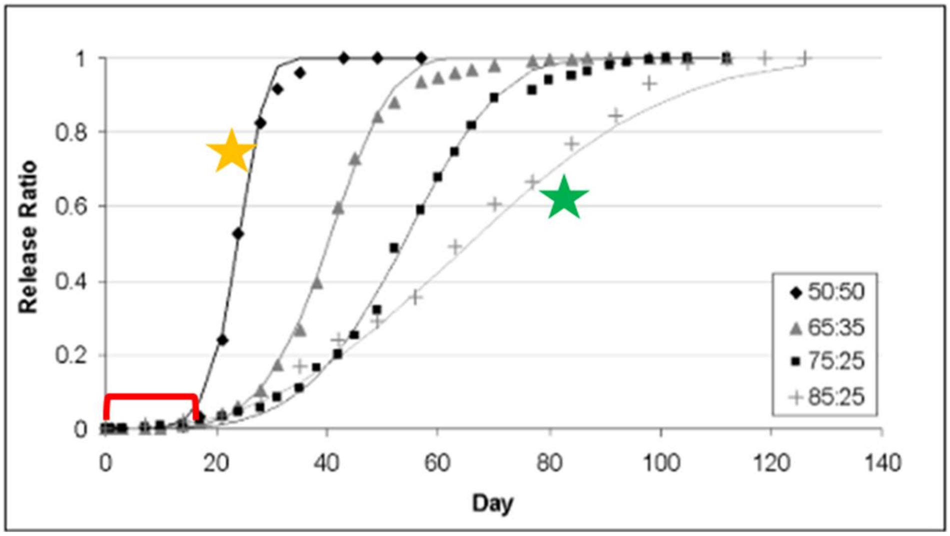

Figure 2.1.3: Example of Delayed Burst (yellow) and Delayed Sustained Release (green) from PLGA Microparticles[40]

There are a few applications where adding a delay time to nanoparticle release is desirable. A delay in release would allow targeted nanoparticles to reach the desired site before release, eliminating side effects and improving the drugs' bioavailability. Additionally, injecting particles with different delay times would provide sustained drug concentrations over long periods, potentially reducing the number of injections necessary for vaccines or chemotherapies and increasing the long-term dosages. The ability to vary this delay and the overall rate is ideal controlled release.

2.1.3 Release Kinetic Models

There are several models used to model release kinetics of drug delivery systems. These models usually correspond to a dominating release mechanism, with different kinetic constants derived from fitting these models. The most common models typically used in drug delivery release quantification are the following.

Korsmeyer-Peppas

Korsmeyer-Peppas[41–44] release is the simplest drug release, described by the following equation:

$$\frac{M_t}{M_\infty} = kt^n \qquad (2)$$

M_t is the drug release mass at time t, M_∞ is the total mass released, and $\frac{M_t}{M_\infty}$ is the fraction of drug over time t, k is the release rate constant and n is the release exponent. This equation is only valid for the first 60% of release and one dimensional release[44]. Once found, n can be used to determine the drug transport mechanism. Table 2.1.1 shows the interpretation of release mechanism based on the values of n. For swellable polymer systems, n shows the contribution of release of polymeric relaxation and Fickian diffusion.[43]

Table 2.1.1: Interpretation of Release Exponent n for Korsmeyer-Peppas Model[41]

Release Exponent (n)	**Drug Transport Mechanism**
0.5	Fickian diffusion
0.45 < n =0.89	Non-Fickian transport (chain relaxation and diffusion roughly equal)
0.89	Case II (Swelling Driven) Transport
>0.89	Super case II transport (diffusion and chain relaxation/swelling relaxation)

Peppas-Sahlin

The Peppas-Sahlin equation is a modification of the Korsmeyer-Peppas[42–44] equation. It considers contributions from polymeric relaxation and the diffusion contribution on total drug release by using two separate terms. The drug release fraction $\frac{M_t}{M_\infty}$ over time *t* can be determined by:

$$\frac{M_t}{M_\infty} = k_1 t^m + k_2 t^{2m} \qquad (3)$$

Where k_1 is the Fickian diffusion rate constant, k_2 is the polymer relaxation rate constant, and m is the diffusional exponent. The substitution method provides the solution to this equation.[43] The fraction of mass released at two time points is used to simultaneously solve for both rate constants. Once these rate constants are found, we find the diffusion exponent. Comparing the rate constants can determine the contributions of individual mechanisms.

Hopfenberg

The Hopfenberg model describes drug release from surface eroding polymers:

$$\frac{M_t}{M_\infty} = 1 - \left(1 - \frac{k_0 t}{C_L a}\right)^n \qquad (4)$$

k_0 is the zero-order rate constant, C_L is the initial loaded drug concentration, a is the system's half thickness (radius for spheres), and *n* is the geometric exponent. Depending on the geometry, *n* is 1 for a slab, 2 for a cylinder, and 3 for a sphere.[41,42,44] It is assumed for this model that the release is not influenced by changing diffusion rates and instead is dominated by surface erosion, with any secondary surface erosion (from within pores) being neglible.[45]

Higuchi

The Korsmeyer-Peppas can be simplified to the Higuchi model:

$$Q = k_H t^{0.5} \qquad (5)$$

Where k_H is the Higuchi dissolution constant.[41,42,44] This equation can be plotted as the total percentage of mass release over time.

Weibull

The Weibull model was developed as a robust fit for most drug release profiles. The model advantage is that it takes a lag time into account for the release profile.

$$M = M_0 \left[1 - e^{\frac{-(t-T)^b}{a}} \right] \qquad (6)$$

Where M is the amount of drug dissolved at time t, M_0 is the total amount of drug released, T is the lag time of the dissolution process. The parameters a and b describe the time and shape dependence of the curve, respectively.[41,44] This equation can be linearized, where b is the slope of the line and a is estimated from value at t=1. This model is empiric, and so cannot characterize the dissolution mechanism of the drug in matrices.[44] However, it has the advantage of including a lag parameter which is useful for modeling delayed burst and delayed sustained releases. This model is very effective in modeling complicated release from composite polymer matrices of different layers, as shown in Hadjitheodorou et al.[46] where they used Monte Carlo simulations to relate the exponential coefficient b and time parameter a to physical properties of the particle itself. They do not consider the degradation mechanism of release in their model, instead just modeling the release due to Fickian diffusion. Further work continues modifying this model to better relate to physical components.[47]

2.2 Nanoparticles for Drug Delivery

This section will discuss the methods used to characterize polymeric nanoparticles' size and size distribution. It will then discuss the development, evolution, and remaining challenges of the single core polymeric nanoparticles and core and shell polymeric nanoparticles. Finally, applications that use these types of nanoparticles in bulk systems are discussed for background on Chapter 5.

2.2.1 Characterization Methods

Nanoparticles' size and size distribution is measured using Dynamic Light Scattering (DLS) method (Malvern Zetasizer ZS ,Malvern, UK). DLS measures the velocity of nanoparticles moving through a fluid via Brownian motion. A 633 nm laser scatters through the sample, creating an interference pattern. As the nanoparticles move, the interference pattern changes and correlated against an autocorrelation function determined via settings in the program. From this correlation function the translational diffusion coefficient D_t is calculated. The Stokes-Einstein equation then calculates the hydrodynamic radius R_H of the measured nanoparticle, where k_B is the Boltzmann constant, T is temperature, η is absolute viscosity.[48]

$$D_t = \frac{k_B T}{6\pi\eta R_H} \qquad (7)$$

By collecting numerous measurements of different particles, a size distribution is found and the intensity average (Z-avg) of that distribution is reported with the size distribution width, also called the polydispersity index (PDI). Hydrodynamic radius (or diameter, HD) is not the true hard diameter of the nanoparticle; it is the hypothetical size of hard sphere which moves at the same velocity. Realistically the nanoparticle is often surrounded by a corona of proteins or ions from the surrounding fluid, and thus the true size is slightly smaller than what is reported by the DLS.[48–51]

Direct visualization of the nanoparticles is accomplished using Scanning Electron Microscopy (SEM). Briefly, SEM uses magnetic lenses to focus a beam of electrons onto a sample coated with a layer of conductive metal atoms. The electron beam quickly scans across the sample and the electrons interact with the sample, releasing and scattering other electrons and X-rays.[49,52] These scattered electrons are collected by sensors and producing an image.

2.2.2 Polymeric Nanoparticles

Perhaps the largest area of research into controlled release is nanoparticles made from biodegradable polymers. As briefly discussed in Chapter 1, this type of system has shown great promise in achieving precise customizable controlled release rate, tunable to application needs. They can encapsulate small and large molecule drugs, although there is some concern with large biomolecules retaining therapeutic activity post-encapsulation. Various polymers have cleared FDA approval for drug delivery applications including polyethylene glycol (PEG), poly lactic acid, polycaprolactone, poly glycolic acid, poly N-vinylpyrrolidone[15]. But while many clinical trials are underway in different phases, very few polymeric nanoparticle drug delivery systems are currently available for clinical use. From Abdellatif et al.[53], there are currently 58 approved nanoparticle formulations, with roughly 20 of those being polymeric formulations. Figure 2.2.1 shows the approved types distribution. This clinical translation bottleneck is due to two issues: lack of scalable manufacturing[54] and batch heterogeneity[55].

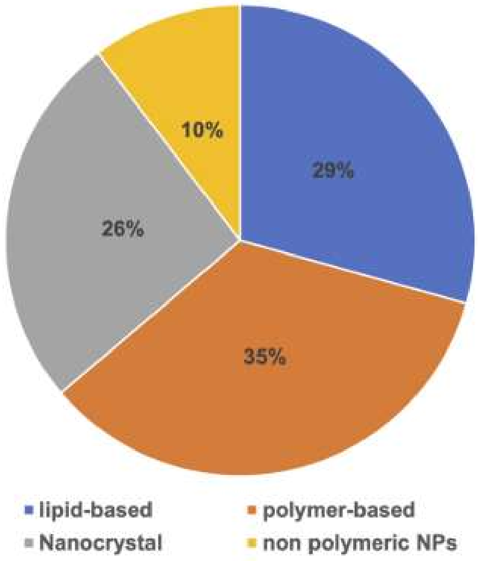

Figure 2.2.1: FDA-Approved Nanoparticle Formulations, 2021[53]

The scalability issue derives from the two diametric manufacturing methods, categorized as top-down or bottom-up techniques. (Figure 2.2.2, from Operti et al..[54]) Top-down methods begin with pre-synthesized bulk polymer, using various solvent methods to form the chains into particles. These methods include emulsion evaporation, diffusion, nanoprecipitation, salting out and dialysis, and are lab-scale batch processes. While they can offer good control over different properties, they are not easily scalable due to the equipment and mechanisms involved which become inefficient or ineffective at larger volumes. Bottom-up methods synthesize the polymer chains as required from their monomeric units, and while they offer fine control over polymer chain length and are more easily scalable there is less control over batch particle properties such as size, shape, and PDI.[54]

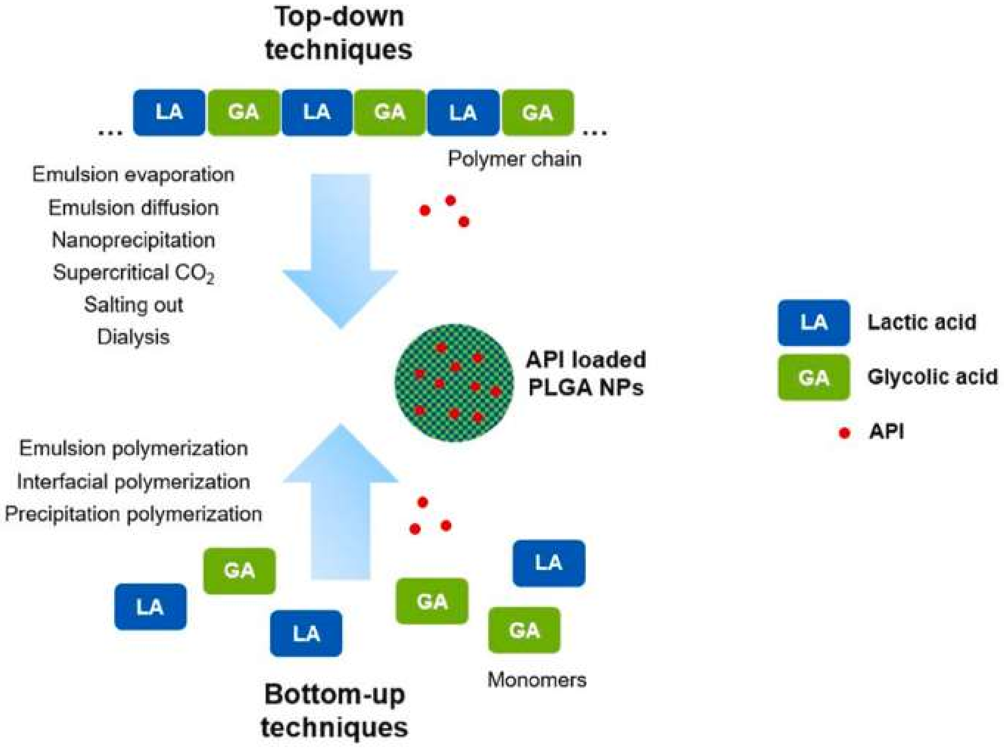

Figure 2.2.2: Top-down and Bottom-up Polymeric Nanoparticle Synthesis Techniques for Polymeric Nanoparticles, From Operti et al.[54]

Heterogeneity batch-to-batch has been shown to greatly affect final properties and lead to greatly increased cost of downstream processes. For instance, for size-dependent properties such as diffusion, degradation, release, cellular uptake, and cellular binding and uptake, even a small deviation in radii can have an order of magnitude propagation of change of all these properties.

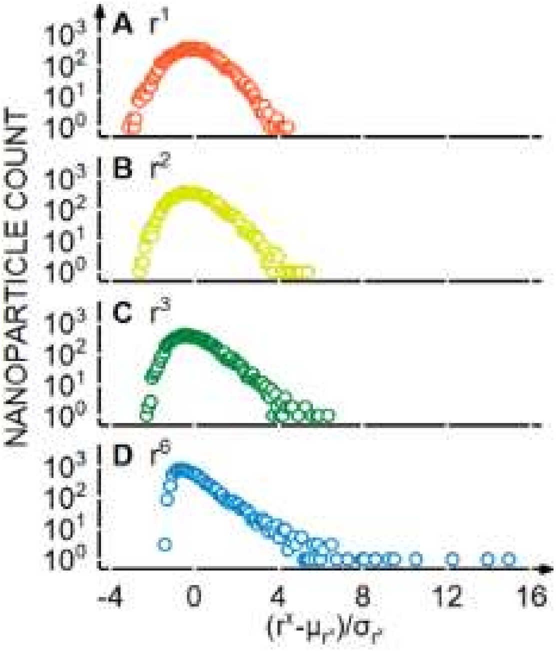

Figure 2.2.3: Feature Deviation Propagation for Properties based on power of radii (r), from Stavis et al.[55]

2.2.3 Nanoparticle Properties and Effect on Release

Several nanoparticle properties influence release kinetics. These can be grouped in three categories, seen in Figure 2.2.4. Physical characteristics include the size (and the size distribution when more than one particle), shape, particle stiffness, and any electromagnetic properties. The chemical characteristics make up the polymer material properties themselves, including the chain length (molecular weight), hydrophobicity, polymer chain degradation mechanism, and any responsiveness the polymer may have to external stimuli such as pH, light, heat, or triggering molecules. Finally, the surface properties include the particles' porosity, morphology, surface charge, and any targeting moieties used for active targeting applications[56]. The following sections will examine each category and its properties' effect, especially on particles' release kinetics.

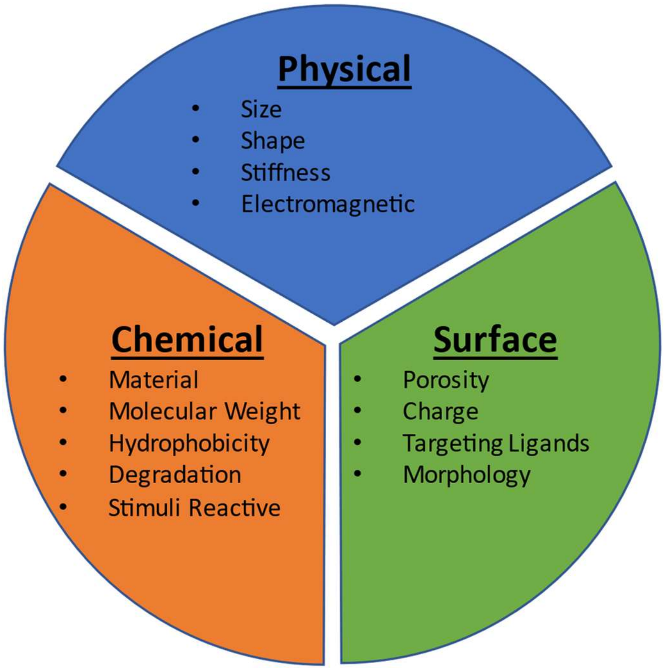

Figure 2.2.4: Nanoparticle Properties which affect Release and Pharmacokinetics

Physical Properties: Size and PDI

The size of particle, and the distribution of the sizes of all the particles, quantified by the PDI, has shown to be critical to the biodistribution and nanoparticles' release. Biodistribution studies of polymeric nanoparticles 200 nm and greater demonstrate preferential accumulation in the liver and the spleen upon intravenous injection[57,58]. Below 10 nm the particles are quickly cleared out of the body by the kidneys. Therefore, without considering release effects, there is an optimum range for nanoparticles of 10nm to 200nm for *in vivo* circulation.[59] When targeting different diseases, size also affects targeting effectiveness. For example, many cancer tumors often encourage leaky vasculature in their microenvironment, causing circulating fluid accumulation at the tumor site. This “pooling” effect improves circulating tumor site accumulation for average nanoparticle diameters of 150-200 nm, a passive targeting phenomenon called the Enhanced Permeability and Retention (EPR) effect.[33,60] Polymeric nanoparticles’ ability to encapsulate drugs also depends on the polymer-drug compatibility and the size of each. The larger the particle, the more drug can be encapsulated, or the more efficient it can encapsulate large biomolecules or drugs.[61] The particle size’s effect on release is also glaring. For eroding polymers, a larger size in turn results in a greater surface area exposed to the aqueous environment, but the volume change outweighs the surface area change due to the difference in power of the radii when calculating each. This is clear when considering the Hopfenberg model; that as the particle’s radius increases (a) the term beneath the exponent will cause the percent release to change at a slower rate. Therefore, with similar properties larger polymeric nanoparticles will degrade and so release at a slower rate than smaller particles with similar erosion kinetics. An example of this can be seen in Dawes et al.[62], with release of two PLGA microparticle sizes, the larger (20 μm) has a more sustained release than the smaller (1 μm) particles.

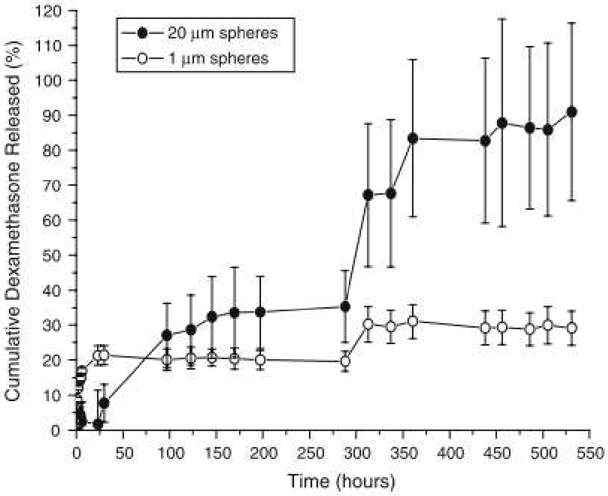

Figure 2.2.5: From Dawes et al.[62]*, Size Effect on Release from PLGA Microspheres, 20 μm and 1 μm*

For polymers for whom diffusion release dominates, the size effect is similar. The larger the radius increases the diffusion barrier which increases the mass transfer resistance. Thus, the release rate for most of the drug will be slower as the radii increases, although if the drug is nearer to the surface, a larger radius will result in a larger initial burst release. The size effect then translates directly to the size distribution effect, where particles of different radii will give different release rates, and the deviation increases as radii increases. For instance, following the Hopfenberg model again, a 10% radius increase will result in a smaller release deviation at smaller radii than it will at larger radii. This has a compounding effect if the PDI is polydisperse, causing the overall release kinetics to be inconsistent and unpredictable.

Chemical Properties and Degradation Mechanisms

The chemical properties effects how the polymer chains themselves interact with their surroundings and themselves during the release process. Certain polymers, such as PLLA, are semi-crystalline, and release is typically slower than amorphous polymer such as PLGA. The solubility and hydrophobicity of the polymer, especially in relation to the drug payload, affects the release mechanism as well. If the polymer and drug are incompatible, the drug can still be loaded, however there will be cost to loading efficiency. The loading procedure contains the drug within an interior fluid region surrounded by the polymer. This results in a burst release, with the drug releasing once the interior fluid is exposed to the surroundings. If the polymer and the drug are compatible (both hydrophobic or hydrophilic), drug loading is easier, with the drug dispersed throughout the matrix. The dispersed drug release can occur by four mechanisms, as seen in Figure 2.2.6[63]. If the polymer matrix is porous, the drug can diffuse out as the aqueous surrounding penetrates the pores (Figure 2.2.6A). If the polymer is nonporous, the drug can diffuse through the polymer itself (Figure 2.2.6B). Release via osmotic pumping can occur for materials with a large pore network. Water can be taken into the particle and cause an osmotic gradient, driving release out of the particle (Figure 2.2.6C). The final mechanism is erosion (Figure 2.2.6D). Erosion is mostly specific to polymeric systems and occurs when the polymer chains react to the surroundings and break down into small units, causing the drugs to be released. Realistically, true release is often a mixture of two or three mechanisms. In addition, each of these can be affected by a wide range of other chemical and surface factors, such as interactions between components, temperature, pH, molecular weight, size, and porosity.[63]

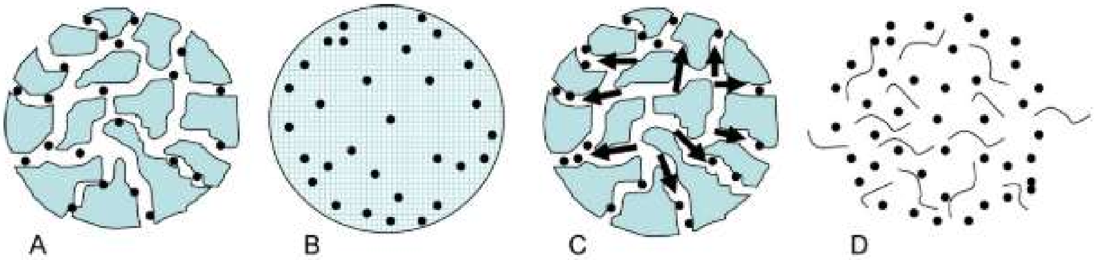

Figure 2.2.6: Mechanisms of Release from Polymeric Nanoparticles[63] (A) Pore Diffusion (B) Bulk Diffusion (C) Osmotic Pumping and (D) Polymer Erosion

Surface Properties

Along with size, morphology and charge also greatly affect performance. Different morphologies and aspect ratios can increase or decrease clearance rates, drug loading capacity, and uptake by changing how the particle physically interacts with the cells in the body. Ideally, the charge would be cationic or close to neutral.[59] If the particle's charge is too negative, this can interact with proteins in the blood or be cleared out very quickly. A slightly positive charge allows the particle to attract to the negatively charged cellular membranes and avoid opsonization and rapid clearance. Most bare particles aggregate easily, are rapidly cleared, are negatively charged, or do not fully protect the drug payloads. Surface modifications can address all these limitations. PEGylation is a common way to add "stealth" to reduce clearance, protein adsorption, and improve particle half-life. Targeting moieties can also be attached to the ends of these linkers to improve site accumulation. Other polymers can be added within the structure to increase its stability *in vivo* or add a response to different stimuli. The number of manipulatable variables allows polymeric nanoparticles to be highly customizable.

PLGA

One of the most common materials for polymeric nanoparticles is poly (D,L) lactic-co-glycolic acid (PLGA)[23] due to its favorable degradation and safety properties, biocompatibility, and biodegradability. Due to these properties, it's one of the few polymers FDA-approved for drug delivery applications[40]. A copolymer of the monomers lactic acid (LA) and glycolic acid (GA) (Figure 2.2.7), different ratios of the two monomers can be used to make different forms of PLGA. Common formulations range from 50:50 to 85:15 LA:GA, and each ratio has different release kinetics, as shown in Makadia et al in Figure 2.1.3[40]. In general, the more glycolic acid, the faster the release because adding more glycolic acid decreases the crystallinity and introduces more radical acidic groups thus increasing the polymer backbone's hydrolyzation. PLGA is hydrophobic and has a glass transition temperature around 44°C, meaning it is hard and glassy at room temperature. For drug delivery, bare PLGA nanoparticles have some limitations.[59] As mentioned, the polymer is hydrophobic, meaning it does not disperse easily into biological environments without modification. Aggregation in aqueous environments can be a problem, affecting the size and size distribution. Many current synthesis techniques produce a polydisperse sample of nanoparticles, decreasing the reliability.

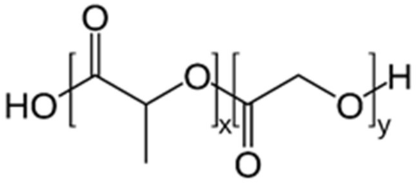

Figure 2.2.7: Poly(D,L) lactic-co-glycolic Acid (PLGA) Structure

PLLA

Poly (L) lactic acid (PLLA) is a chiral isomer of poly lactic acid, made of one of the monomeric units of PLGA. Figure 2.2.8 shows its structure. Due to its structural regularity, it is semi-crystalline and has a glass transition temperature at 53-60°C and a melting temperature at 160°C.[23] This makes it very durable and strong, and thus highly investigated for long-term release for biomedical applications. In most applications PLLA or racemic mixtures form implants or microparticles.[64] Like PLGA, it is also hydrophobic, biodegradable, and biocompatible, and FDA-approved for drug delivery. Because of the semi-crystalline nature, PLLA nanoparticles' release is much slower than that of PLGA. With no glycolic acid groups to autocatalyze the hydrolysis, the release mechanism is more diffusion driven, with a very slow erosion component.

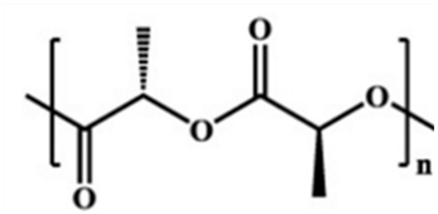

Figure 2.2.8: Poly (L) lactic Acid Structure

2.2.4 Core and Shell Polymeric Nanoparticles

While polymeric nanoparticles have shown great promise in achieving controlled release for long periods, as discussed, the size, formulation, or morphology needs to be changed to manipulate the release rate effectively. These modifications in turn negatively change the nanoparticle's *in vivo* behavior, charge, or exceed the size for efficient targeting. Certain modifications introduce complex triggering molecules on the surface which further complicates the already challenging scale-up and clinical translation. Importantly, there is significant difficulty preventing the initial burst release seen in many release studies due to the drug adsorbed on or near the surface.[65] This burst effect could raise drug concentration above toxic concentrations so different ways to eliminate additional surface modification have been investigated. One favorable method because of its simplicity and versatility is coating a drug-loaded nanoparticle with another polymer, forming a polymer shell. This polymer shell is often made of a slower degrading polymer than the core material adding a time delay and eliminating the burst release. There is an added advantage of core and shell systems: it introduces another region of the DDS so that multiple drugs can be loaded within different components of the particle for simultaneous controlled release. This is especially beneficial for combinational therapy, when two drugs can have a greater cumulative effect when released together at a site than when delivered alone. This is often the case for chemotherapy treatment regimens, where "cocktails" of drugs are administered together for a synergistic effect[66]. Core and shell polymeric nanoparticles provide an easy way to deliver both and tune each release to maximize their therapeutic effect.

Current Synthesis Methods

The most common synthesis technique for core and shell polymeric nanoparticles is via coaxial electrohydrodynamic atomization (CEDA), also called coaxial electrospray. Figure 2.2.9 shows the general process. The core fluid contains the dissolved core polymer and the drug, while the outer liquid contains a different immiscible liquid that contains the shell polymer. The two liquids are injected or pumped through a dual cone nozzle, where the inner fluid exits into outer fluid flow before both exit. The nozzle is electrified with a high voltage to create a potential which accelerates the liquids. Immediately after exiting the nozzle, the dual flow passes through a high voltage ring and forms what is called a Taylor cone. A Taylor cone forms by the electrical force and forces the fluid into a jet resulting in the core and shell droplets spray. These core and shell droplets fall into a collection vessel, sometimes containing a stabilizing fluid, until the polymer solvents evaporate, leaving the dry core/shell particles. The particles' size and morphology are altered by changing factors such as the two flowrates, viscosities, and voltage.

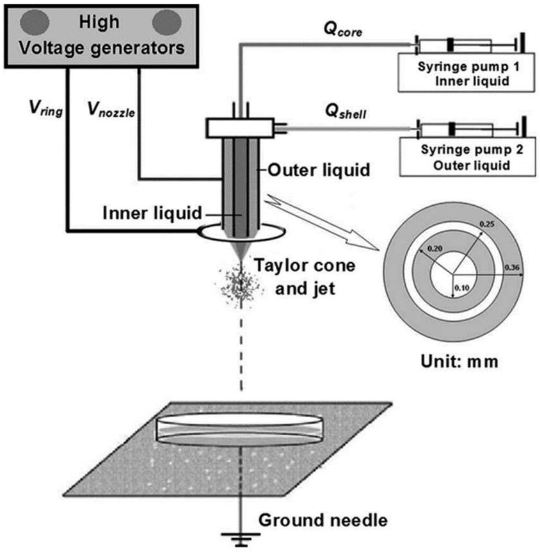

Figure 2.2.9: Coaxial Electrospray Equipment Setup[65]

Another more recent technique that has become popular is microfluidics. The general process involves the flow of two immiscible fluids in which the core fluid droplets pass through a channel containing the shell fluid. This channel then diverts so a third immiscible fluid surrounds the core and shell droplet and carries it to a collection tube, allowing the core and shell solvents to evaporate, leaving the dry polymeric particle. While both techniques have shown excellent ability to form core and shell nanoparticles with high loading efficiencies, there are some limitations. The equipment is costly and the optimization of all parameters to achieve the desired size, dispersity, and morphology can be difficult. CEDA has a high throughput and good scale-up potential. However, currently the minimum achievable size is several hundred nanometers and the polydispersity is very high, too large for drug delivery.[67] Microfluidics can produce nanoparticles at a very consistent size distribution; however high throughput and scalability is a challenge that will need to be improved.[68] For laboratory scales, another less popular technique has been experimented with for core and shell microparticles: the emulsion-solvent evaporation (ESE) method.

Previous Formulations

Numerous material combinations for core and shell nanoparticles have been tested. Most all involve PLGA as one of the components due to its desirable biocompatibility and release. The release mechanism of this system follows that of the pure polymeric particles explained previously. The shell adds resistance to diffusion and depending on the thickness prevents premature core erosion and thus release. This diffusion barrier can result in extremely long controlled releases. However, the shell must be uniform and nonporous for predictable degradation. Cardoso et al[69] investigated the synthesis and release kinetics of PLGA/PLLA core/shell particles for controlled release of DOX. Using the solubility difference of PLLA and PLGA in dichloromethane (DCM), they created an oil-oil-water emulsion via sonication, changing the particle size (and thus the theoretical shell thickness) by changing the mass ratio of PLLA to PLGA. The scaled-up microparticle confirmed the core/shell structure with DOX distributed throughout primarily the core. (Figure 2.2.10). The average diameter of the particles confusingly remained roughly constant with additional mass PLLA per mass PLGA, with a 2:1 ratio resulting in a size range of 450-610 nm but a ratio of 4:1 resulting in a range of 430-480 nm, before rising to 510-730 nm for 6:1. The expectation would be that for uniform shell formation, size would increase with mass ratio, dependent on the number of nanoparticles and volume change. The researchers did see a decreasing release rate with increasing mass ratio as one would expect (Figure 2.2.11), which is highly desired for customizable controlled and sustained release. This work confirms that core/shell PLGA/PLLA particles could be formed from a simple emulsion technique; a technique that is well studied for polymeric core nanoparticles. However, the size distribution and lack of control over core and shell dimensions leads to concerns for the clinical translation and batch heterogeneity.

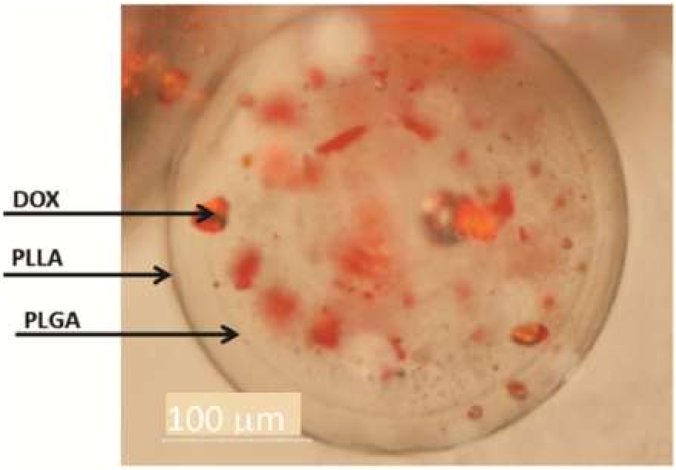

Figure 2.2.10: Doxorubicin-loaded in a PLGA/PLLA core/shell Microparticle[69]

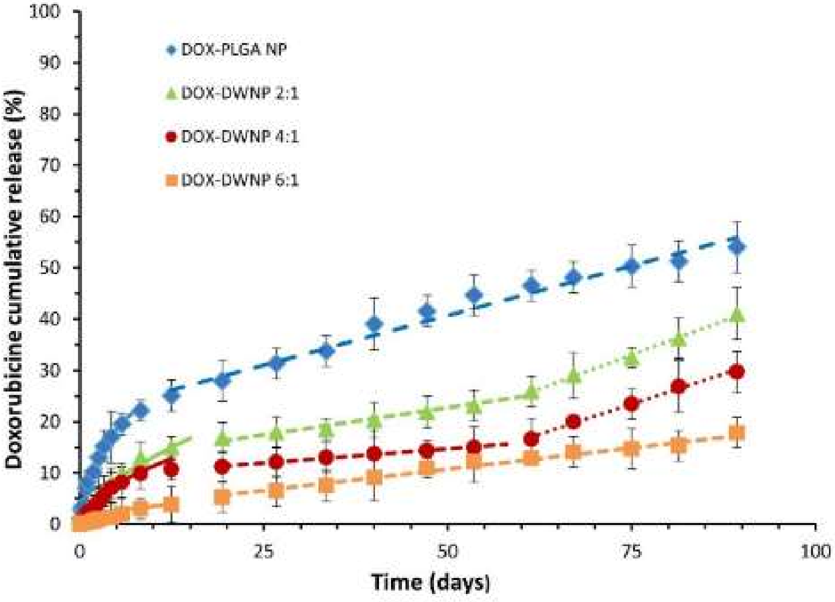

Figure 2.2.11: Release From PLGA/PLLA core/shell Nanoparticles (Sizes >400 nm)[69]

When both materials are polymeric, the ordering and distribution of the polymer layers can result in a time delay and burst effect elimination. Figure 2.2.12 shows the release of aspirin from microparticles with PLLA as the core and PLGA as the shell from Xiao et al[70]. The PLGA shell caused there to be a long period of no release of the hydrophobic model drug, followed by a sustained release for nearly 700 hours. In this case, the PLLA/PLGA nanoparticles were formed via the ESE method, taking advantage of dissimilar solubility in certain organic solvents.[70,71] Such a time delay was not seen with the previous example likely due to the PLLA shell not being homogenous or equally distributed to all nanoparticles, and so some initial release could be seen.

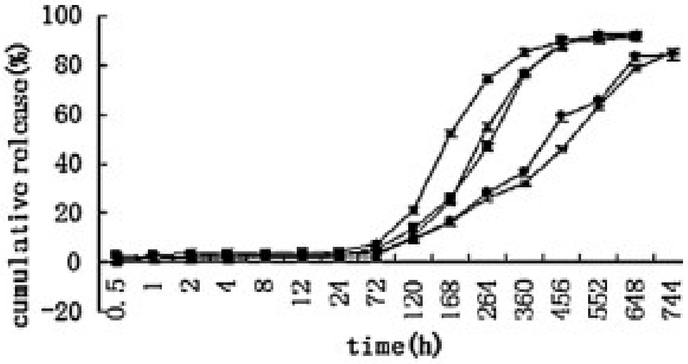

Figure 2.2.12: Release of Aspirin from PLLA/PLGA Core/Shell Microparticles from Xiao et al.[70]

Figure 2.2.13 shows a SEM image of these microparticles from Xiao et al.[70]., clearly showing the differentiation of the two polymer regions whose composition was confirmed via other methods. This experiment again proves that particles of two very similar polymers can be formed with uniform and distinct regions using a very straightforward method.

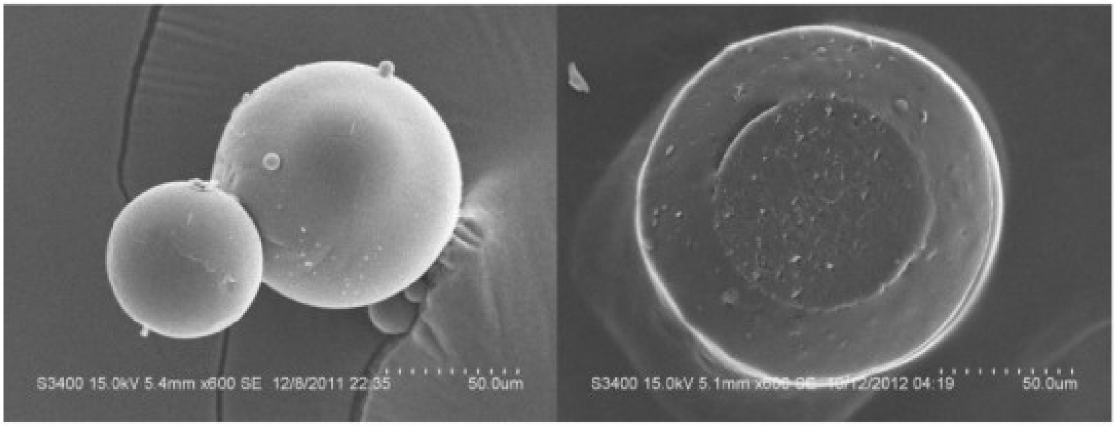

Figure 2.2.13: SEM: PLLA/PLGA Core/Shell Microparticle formed via Modified ESE from Xiao et al[70]

Along these same lines and contrary to what was seen in the first example, if the shell thickness is controllable the release rate can also be controlled. Figure 2.2.14 shows how the release rate decreased significantly by increasing the shell thickness, in this case by several hundred nanometers of PLGA on a core of PLGA.[72] These particles were synthesized using CEDA. Another example is Xia et al[73], where PLGA/PLA core/shell microparticles were fabricated using CEDA. As the mass ratio of PLA to PLGA increase (from sample B1 to B3 in Figure 2.2.15), the shell thickness increases, and the release rate decreases with respect to each other. From Figure 2.2.15, all release rates of core/shell nanoparticles (B1-B3) are slower than the release from the core alone (O). These studies all demonstrate that core and shell polymeric particles with shell thicknesses of controlled makeup and thickness can achieve controlled release over long periods. This allows the nanoparticles drug release rate to be varied to maintain drug concentration within the therapeutic effective window. The question remains whether this dimension control is achievable at sizes more relevant to circulating drug delivery (200 nm), which has yet to be proven experimentally.

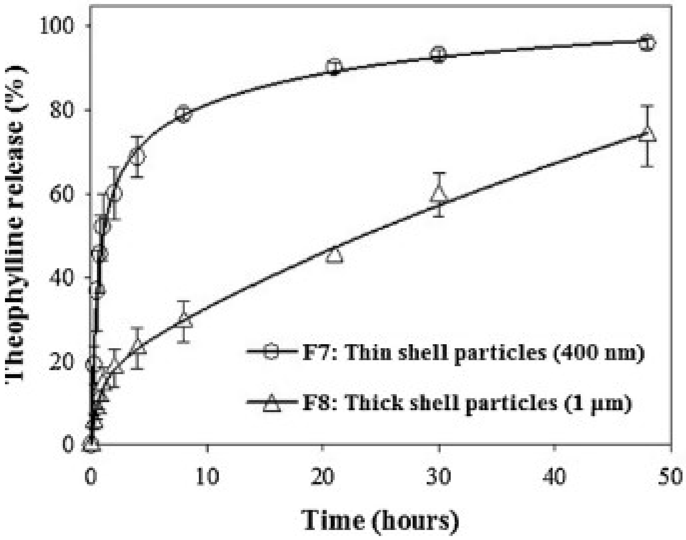

Figure 2.2.14: Drug Release with Thin and Thick Shell Thickness of PLGA/PLGA Core/Shell Particles from Yeh et al.[72]

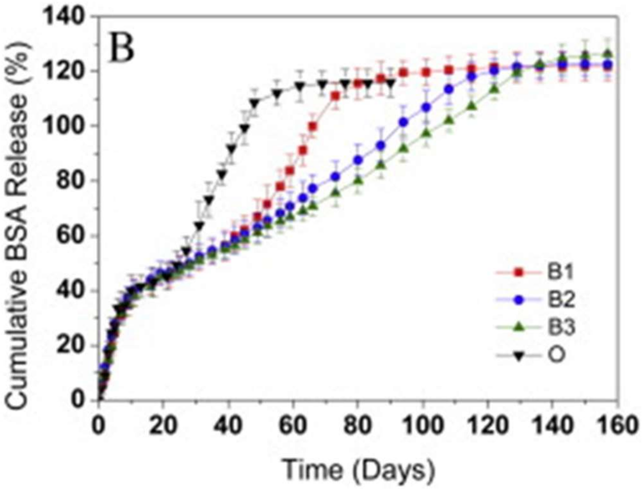

Figure 2.2.15: Cumulative % Release from PLGA/PDLLA Microspheres from Xia et al[73] *showing slowing release with increasing shell to core mass ratio.*

When multiple drugs are loaded into individual components, each component's release depends on the polymer they are encapsulated in and their distance from the surface. An example is seen in Figure 2.2.16 also from Yeh et al[72]. These particles are large (1 micron) and consist of a PLGA core and shell of PLGA with a higher molecular weight produced via CEDHA. Both the hydrophilic drug Theophylline and the hydrophobic drug Budesonide are encapsulated within the core and begin releasing simultaneously at different rates. The faster release rate for the hydrophilic drug (Theo.) is expected due to it being encapsulated in a semi aqueous region of the core, while the release of the hydrophobic drug (Bud.) displays an initial fast release from adsorbed drug followed by a slow sustained release rate as it is released from the polymer matrix of the core. These drugs can be loaded in different regions of the particle and show region dependent release as well.[72]

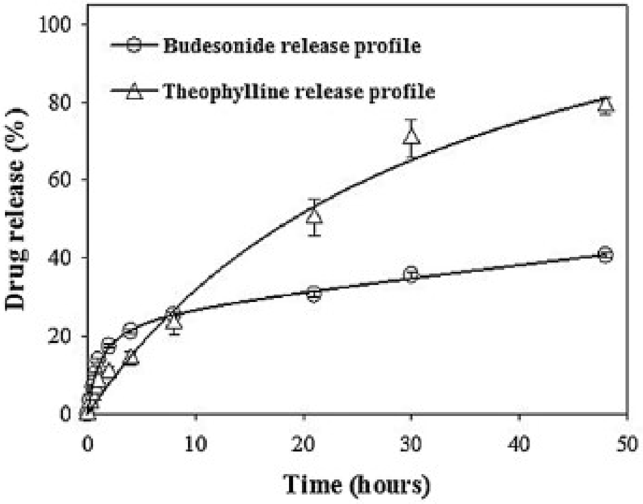

Figure 2.2.16: Hydrophobic and Hydrophilic Simultaneous Release from PLGA/PLGA Core/Shell NPs (Yeh et al.[72])

2.3 Hydrogel Systems for Controlled Release

Depending on the application, nanoparticles may be an inappropriate system for controlled drug delivery. For instance, applications that require a larger surface area than what nanoparticles could reasonably cover, such as large surface wounds or topical ocular applications. Additionally, hydrogel microparticles encapsulate larger biomolecules or hydrophilic agents better than many nanoparticle systems, release at near constant rates[74], and often are more stable in harsh environments such as the gastrointestinal tract. For these cases, a hydrated material capable of complete coverage and sustained doses would be more effective. These materials are hydrogels made of interconnected or crosslinked hydrophilic polymer networks which perform with high water content[75]. There are many types of hydrogels, both natural and synthetic. Synthetic polymer hydrogels have emerged as the dominant type due to their structural consistency and stability. However, recently hydrogel blends of both naturally derived and synthetic monomers have been developed to lower cost but increase swelling, mechanical, and release behavior. Forming and loading hydrogels for controlled drug delivery is very simple, with the main steps being polymer dissolution, crosslinking, purification, drying, drug loading, and processing, as seen in Figure 2.3.1.

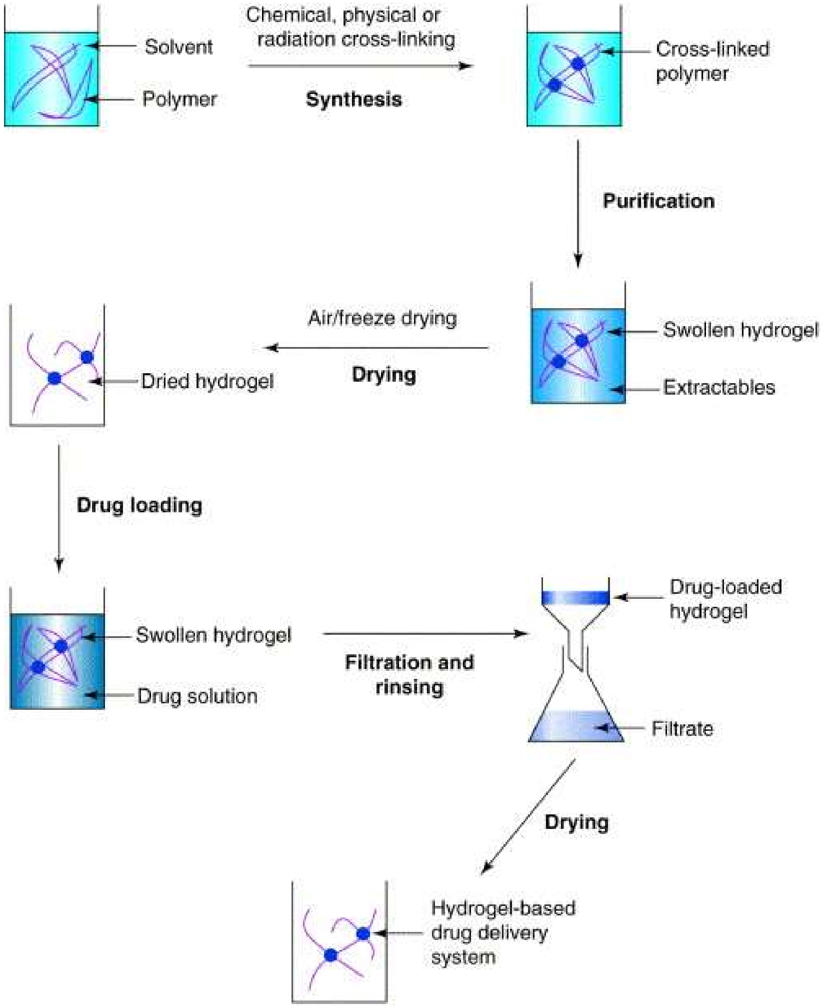

Figure 2.3.1: Preparation Technique of Drug-loaded Hydrogel, from Gupta et al.[74]

Crosslinking is a simple process that uses chemical reactions to covalently bond the polymer chain network together, increasing mechanical and swelling stability. There are different types of crosslinking, such as small molecules (glutaraldehyde), polymer-polymer (hyaluronic acid), or stimuli-responsive (acrylate, HRP)[76]. Crosslinking of any type can improve hydrogels' mechanical strength and stability and change their performance. Hydrogel performance is generally quantified using various techniques, as seen in Table 2.3.1.

Table 2.3.1: Hydrogel Characterization Parameters and Measurement Techniques

Parameter(s)	Measurement Techniques	Reference
Crosslinking	Mechanical Testing, Polymer solubility, Colorimetry	77,78
Network Pore Size and Surface Area	BET, Electron Microscope, Porosimetry, Equilibrium Swelling	79
Degree of Swelling/% Mass Change	Mass/volume change over time, water content	80
Drug Distribution/Diffusion	UV-Vis Fluorescent Microscopy, SEM, N-MR Controlled Release Experiments, Permeability	80

The hydrogel release mechanism differs from other previously mentioned polymers and depends on the payload type. While erosion and diffusion through the polymer are release components, the primary driving factor is polymer swelling due to water intake.[81,82] For small molecule free drugs, there is a burst release from the surface-adsorbed drug as water or other medium penetrates the initially glassy matrix of the dry polymer. Depending on the crosslink density and the pore network volume, the medium will penetrate the polymer network at a rate dictated by non-Fickian diffusion. The penetration will cause the polymer chains to relax and separate, allowing for free drug diffusion out of the matrix in hours or days.[74] Depending on the chain polymer or medium, simultaneous degradation and relaxation could occur. High loading efficiency and a low chance of drug deactivation characterize this release type, and it typically lasts from hours to days[76]. The drug release mechanism slightly alters for slightly larger payloads such as peptides or micro/nanoparticles. Due to the surface charge or characteristics of the payloads, localized gelation can occur surrounding them, slowing their release to days or weeks. Incorporating polymeric nanoparticles (such as PLGA) into hydrogels can improve the loading of hydrophobic payloads, however it can lead to drug inactivation.

2.3.1 Chitosan Hydrogels

Chitosan is a polysaccharide commonly used in nanoparticle and hydrogel drug delivery systems. It is an aminated cyclic compound similar in structure to glucose (Figure 2.3.2), hydrophilic if dissolved in low pH, and mucoadhesive, which increases its ability to target mucosal membranes and circulate *in vivo*.[81] It is biodegradable, antibacterial, hemostatic, and can easily encapsulate large molecules such as DNA, making it highly promising for biomedical applications.[83] This includes sutures, wound dressing, cancer therapy, gene therapy, ocular and oral delivery, and as a coating on other nanomaterials.[23,81]

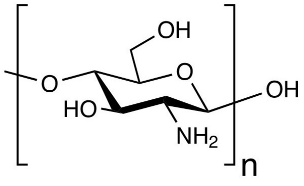

Figure 2.3.2: Chitosan Structure

Chitosan hydrogels have long been studied for controllable sustained drug delivery.[84] For instance, chitosan and gelatin crosslinked together in a co-network were used to deliver the drugs lidocaine[85] and dopamine[86] for treating local pain and Parkinson's disease, respectively. Chitosan hydrogels have been a particular interest for the controlled delivery of chemotherapeutics. From Chang et al.[87], an injectable self-healing chitosan hydrogel coating was loaded with 5-fluorouracil and showed pH-sensitive controllable release at tumor sites. Zhang et al.[88] loaded

DOX within a temperature and pH-sensitive chitosan/hyaluronic acid for an injectable drug delivery system. Their system demonstrated faster release at more acidic conditions, with controllable release as hyaluronic acid content increased (Figure 2.3.3)[88]. Several more examples of chitosan hydrogel drug delivery systems can be found in Peers et al.[84]

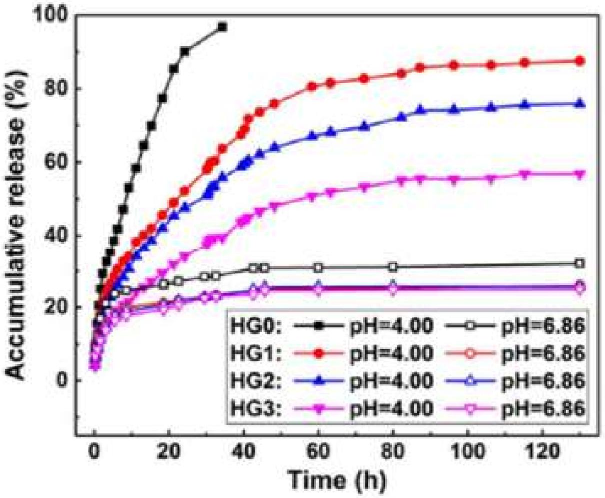

Figure 2.3.3: Chitosan/Hyaluronic Acid Hydrogel Release of Doxorubicin (DOX) for pH responsive Chitosan, from Zhang et al[88]

While chitosan clearly has shown great promise for improving the biocompatibility and drug delivery of drug delivery systems, there are limitations. Precise release control can be difficult, as an initial burst often occurs for bare chitosan, or manufacturing variations lead to heterogeneous performance. Chitosan is deemed safe by the US FDA but unapproved for drug delivery applications, only approved for wound dressing and dietary applications. Another limitation is that chitosan is poorly soluble in neutral to high pH and must be dissolved in acidic fluid before forming particles or bandages, but this means any chitosan-based hydrogels tend to prematurely break down when taken orally[82]. As with many nanoparticles, the scale-up and feasibility of chitosan coatings for nanoparticles must be addressed.[89] Finally, while chitosan hydrogels excel at loading and releasing hydrophilic drugs, it is challenging to load hydrophobic or cationic drugs, making it inappropriate for most small molecule drug markets.[84]

2.3.2 Nanoparticles-Hydrogel Co-Delivery Systems

To overcome the poor loading of small molecule hydrophobic drugs, many have investigated the incorporation of polymeric particles within the hydrogel polymer chain network. This incorporation allows for better hydrophobic loading, but since the hydrogel can encapsulate free hydrophilic drugs, multiple co-delivery of drugs is possible. An example of this system was developed by Osswald et al.[90] for ocular drug delivery. This study suspended PLGA microparticles loaded with a model drug ovalbumin throughout a poly(N-isopropyl acrylamide) hydrogel network. The PLGA particles' porosity and LA:GA ratio was varied with a subsequent varied release rate, with a faster release with higher porosity morphology and 50:50 ratios (see left and center plots of Figure 2.3.4 from Osswald et al.) When embedded within the hydrogel, the microparticles showed less burst release, and there was more sustained release for over 180 days (right plot Figure 2.3.4). The hydrogel network was hypothesized to both slow the particle degradation and drug diffusion from particles impregnated within them, improving the sustained release of polymeric nanoparticles and allowing for simultaneous hydrophilic release.

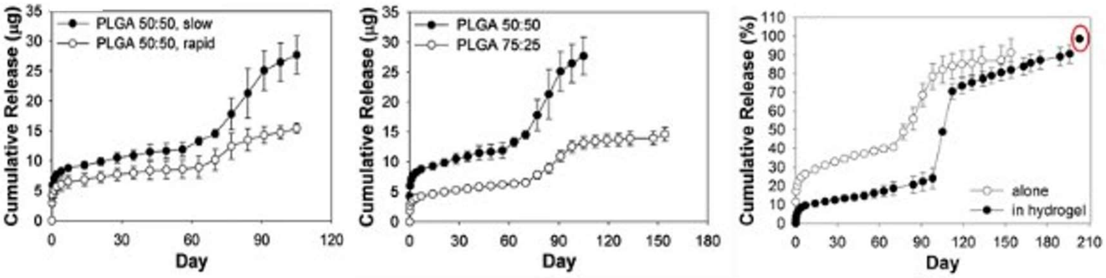

Figure 2.3.4: PLGA Microparticle Release with different Evaporation rate (left), LA:GA ratio (center), and within Hydrogel (right)

Chapter 3: Modeling and Optimization of Synthesis Conditions for Control of PLGA Polymeric Nanoparticles

3.1 Introduction

Polymeric nanoparticles are able to improve the bioavailability and pharmacokinetics of small hydrophobic drugs, such as chemotherapeutics, by releasing them in a controlled and sustained rate. The clinical translation of polymeric nanoparticles has been limited, whether core-and-shell or single core. This lab-to-clinic bottleneck is partially due to a lack of manufacturing scalability and reproducible control of properties such as size and polydispersity. Well-understood, predictable, and precise control of the polymeric cores is necessary before the shell formation can be optimized and controlled. The work presented in this chapter will describe the analysis of a common synthesis method for producing PLGA nanoparticles to determine significant parameters controlling the size and PDI and the characterization of the release behavior based on these properties. Knowledge gained from the lab scale modeling will then be used to evaluate potential scale-up methodology.

3.1.1 Previous Work

Several studies have evaluated process parameter's effect on the average size and PDI of particles produced by the emulsion solvent evaporation method. Hernández-Giottonini et al.[91] evaluated the impact of PLGA concentration, polyvinyl alcohol (PVA) concentration, organic solvent (volume) fraction, sonication amplitude, and the mixing speed used during the evaporation step. Their findings indicated that PLGA concentration within 5–15 mg/mL (0.5–1.5% w/v) did not significantly change the nanoparticle size or PDI. This result contradicted other published findings by Song et al.[61] that reported a positive correlation between size and PLGA concentration; it was suggested that variation in properties of PLGA used could be a contributing factor to this discrepancy. A positive correlation was also observed in a study reported by Halayqa et al.[92], who saw an increase in average nanoparticle diameter as PLGA concentration increased from 0.8% to 1.3% or 1.6% for two formulations. One of the most striking examples of different studies showing conflicting effects on size and PDI can be seen when comparing Hernández-Giottonini[91] et al., Iqbal et al.[93], Song et al.[61], and Zambaux et al.[94] studies on PVA concentration versus polymeric nanoparticle size and PDI using the ESE method. Figure 3.1.1 shows the comparison of all four, with some showing an increasing trend for size (top left), while others show different variations of decreasing trends within similar PVA concentration ranges.

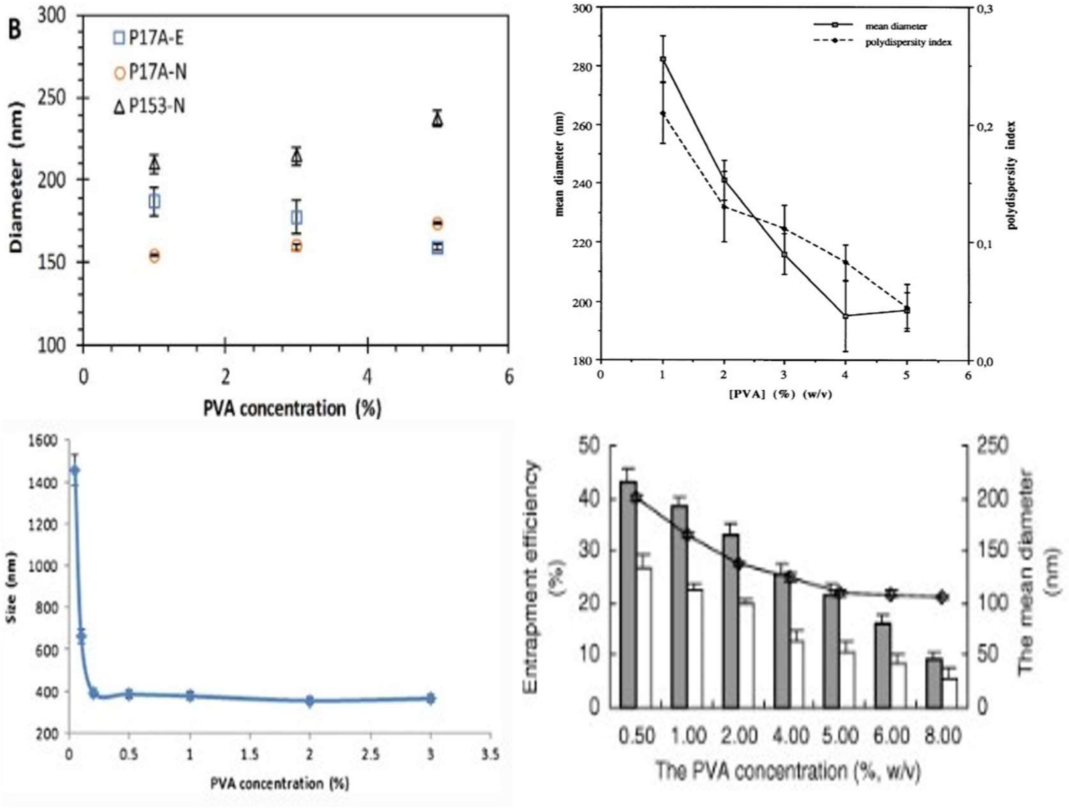

Figure 3.1.1: Example of conflicting Size/PDI Effect of PVA Concentration from comparing (top left) Hernández-Giottonini[91] et al., (top right) Iqbal et al.[93], (bottom left) Song et al.[61], and (bottom right) Zambaux et al.[94]

This effect, where the concentrations of both PLGA and PVA components have contrasting effects on final nanoparticle size, was hypothesized to occur because it varies the interfacial surface tension and the bulk phase viscosity of the emulsion droplets, which changes the droplet coalescing stability[95]. As expected, particle size increased with larger organic-phase volume fractions since total surface energy is a function of surface area. It should also be noted that PDI increased significantly as the organic volume fraction was increased to 0.500. Hernández-Giottonini[91] et al. also observed that increasing the mixing speed yielded smaller particles, with no change to PDI, and increased sonication energy during emulsion formation also decreased size. Haque et al.[96] developed multiple variations on the emulsion solvent evaporation method by changing the surfactant and the emulsification method. They varied the emulsion technique between homogenization and sonication for different sizes, with sonication preferred for smaller sizes. They reported that at set amplitudes and times, they could achieve good reproducibility for sizes from 400 nm to 50 nm using one of the schemes. The PDI for most schemes was above 0.100, and they did not produce a model for achieving other sizes at lower PDI. However, they were able to change the surface zeta potential by changing the surfactants from PF68 (negative) to PVA (neutral) to chitosan (positive) but did not wash the particle, which deviated from the majority of synthesis schemes. An excellent summary of other attempts to control PLGA nanoparticle size is provided by Rao et al.[97]. The results of these studies, as mentioned, often conflict with each other or look at entirely different parameters, which are often difficult to scale or replicate with the information given. What is missing is a rigorous, consistent assessment of the synthesis parameters, their effect, and their potential use for controlling particle size and polydispersity, ideally at different scales and laboratory conditions.

3.2 Materials and Methods

3.2.1 Materials

Poly (D, L) lactic-co-glycolic acid (PLGA 50:50) (MW: 45kDa) and Polyvinyl alcohol (PVA) (MW: 50kDa) were purchased from Sigma Aldrich (St. Louis, MO). Dichloromethane (DCM, ≥99.5%, Macron Fine Chemicals TM) was purchased from VWR. MISONIX QSonica Q700 Sonicator with microtip (MISONIX, NY) was used during the emulsion formation. Deionized (DI) water was obtained using a PURELAB Flex2 water purifier. All hydrodynamic size and PDI measurements were made by DLS with a Malvern Zetasizer Nano ZS (Malvern, UK). Beckman Coulter Microfuge 16 Centrifuge was used for all washing and separating. A Zeiss EVO50 Scanning Electron Microscope was used for all SEM images.

3.2.2 SEM Sample Preparation

For SEM analysis, particle samples were redispersed in deionized (DI) water via sonication, after which 25 µL pipetted onto an aluminum stub prepped with a small square of double-sided carbon tape. The droplet dried overnight, before being gold sputter-coated and observed with SEM under 15 kV.

3.2.3 Emulsion Solvent Evaporation Method

Single Emulsion Method

The primary method for producing PLGA nanoparticles is via the emulsion-solvent evaporation (ESE) method. This well-established method is highly popular for uniform polymeric nanoparticle production because it is simple to adjust parameters and can achieve high encapsulation efficiencies.[98] The method uses the immiscibility of an organic solvent and aqueous bulk phase to form an oil-in-water (o/w) emulsion by adding energy into the system via ultrasonication. The chosen polymer (PLGA) is first dissolved in the organic solvent (dichloromethane (DCM)). This polymer solution is added to an aqueous phase containing a surfactant (polyvinyl alcohol (PVA)). These two phases are then sonicated to produce an emulsion where contained polymer-organic phase droplets are stabilized by surfactant throughout the aqueous phase. This emulsion is then added to more PVA to ensure emulsion stabilization and left to stir for several hours, allowing the organic solvent in the droplets to evaporate and the NPs to dry. These nanoparticles are collected and washed via centrifugation. Before they are placed in the -80°C freezer, a small sample (50 μL) is measured in the DLS to determine the size and PDI. The remaining nanoparticles are frozen overnight in the -80°C cryo-freezer and then lyophilized to remove the liquid so that they can be weighed and further characterized. This process is seen in Figure 3.2.1.

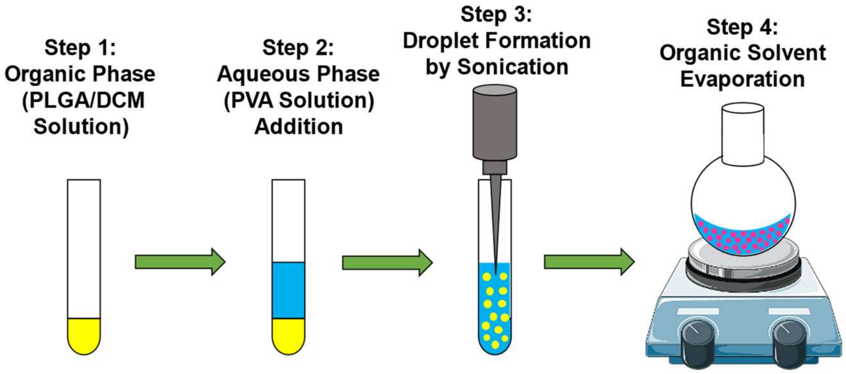

Figure 3.2.1: Single Emulsion Solvent Evaporation Method

This process slightly varies for hydrophobic and hydrophilic polymers. If the polymer is hydrophilic, such as chitosan, the emulsion formed will be a water-in-oil (w/o) emulsion. The general steps remain the same, with switching roles between the organic phase and aqueous phase.

Drugs or dyes can be encapsulated within these nanoparticles quite easily. If the drug and polymer are both hydrophobic or hydrophilic, the drug is added to the same phase as the polymer and becomes equally dispersed throughout the nanoparticle. If, however, the drug is insoluble with the polymer being used, the process is slightly changed, using a double emulsion method.

Double Emulsion Method

To encapsulate a hydrophilic drug in a hydrophobic polymer (or vice versa), we use a double emulsion solvent evaporation (DESE) method[99]. The hydrophilic drug is dissolved in an aqueous phase. This phase is combined with the organic/polymer phase and emulsified via sonication to form a w/o emulsion. This first emulsion is added to the bulk aqueous-surfactant phase and sonicated again to form a final water$_1$-oil-water$_2$ ($w_1/o/w_2$) double emulsion. The rest of the process is the same as the ESE method.

3.2.4 Features and Parameters

For modeling, certain parameters were kept as potential control features. Many are interdependently calculated, but each is recorded and designated with unique names to examine the potential parameter effect. Table 3.2.1 describes the parameters, tested ranges and units for the system analysis. Concentrations were calculated as mass by volume percents for both PLGA in DCM and the PVA aqueous phase. For example, 5 mg PLGA dissolved in 500 μL of DCM is 0.01 mg/μL or 1% w/v. The total PVA volume (V_t^{PVA}) is the sum of three steps utilizing PVA: 1) used to create the emulsion (V_E^{PVA} , “emulsion” PVA), 2) stirred as the bulk aqueous phase to which emulsion is added (V_f^{PVA}, “flask” PVA); and 3) in a wash step of the emulsion tube (V_w^{PVA},“wash” PVA). The emulsion PVA volume (V_E^{PVA}) added directly to the DCM phase volume (V_E^{DCM}) giving the total emulsion volume (V_t^{Emuls}). The total emulsion volume is divided into the total sonication energy (E, J) to get the specific energy (E_v, J/mL) for a given run. The volumes and concentration of the PVA in each step can be changed independently, but the typical volume distributions were 43% "flask", 43% "emulsion", and 14% wash. The total moles of PVA (N_t^{PVA}) and PLGA (N^{PLGA}) and the ratio of the moles ($R_N. R_N^E$) were calculated from the average molecular weight of the polymers. Some controllable parameters such as stirring and washing conditions were kept constant. The emulsion was stirred at 500 RPM under atmospheric conditions for at least 3 hours. The solidified particle suspension was centrifuged at 14,800 rpm or greater for 30 minutes. Sonication amplitude and time were not designated as separate control parameters, instead the total energy was used. This will be discussed in later sections.

Table 3.2.1: Parameters, Variables, Ranges, and Units for PLGA Nanoparticle Synthesis Modeling via ESEM

Parameter	Variable	Range	Units
Controllable Parameters			
PLGA concentration	C_{PLGA}	1-10	% w/v
Oil Phase (DCM) volume	V_E^{DCM}	0.500	mL
PVA concentration	C_{PVA}	1-10	% w/v
Aqueous phase (PVA) total volume	V_t^{PVA}	0.5-10	mL
Flask PVA Volume	V_f^{PVA}	0.4-8.0	mL
Emulsion PVA Volume	V_E^{PVA}	0.5-10	mL
Wash PVA Volume	V_W^{PVA}	0.0-3.0	mL
Evaporation temperature	-	22	°C
Sonication amplitude	-	10-100	%
Sonication time	-	5-1500	s
Evaporation stirring speed	-	500	RPM
Sonication Energy	E	15-15000	Joules
Calculated Parameters			
PLGA Moles	N^{PLGA}	0.25-11 x10^{-7}	Moles
Total PVA Moles	N_t^{PVA}	0.5-21 x10^{-6}	Moles
Flask PVA Moles	N_f^{PVA}	0.25-10 x10^{-6}	Moles
Emulsion PVA Moles	N_E^{PVA}	0.1-8 x10^{-6}	Moles

Wash PVA Moles	N_W^{PVA}	0.0-4.2 x10^{-7}	Moles
Total Emulsion Volume	V_t^{Emuls}	1.0-10.5	mL
Total PVA/PLGA molar ratio	R_N	1.4-198	Moles PVA/moles PLGA
Emulsion PVA/PLGA molar ratio	R_N^E	0.4-88.1	Moles PVA/moles PLGA
Specific Energy	E_v	10-6400	J/mL

3.2.5 Machine Learning Methodology, Models, and Performance Parameters

Several computational models were utilized to evaluate the process parameters' effects on the average hydrodynamic size and PDI of synthesized nanoparticles. This machine learning was done in collaboration with Dr. Cremaschi's group by Dr. Samira Mohammadi, who led the coding and implementation of the machine learning models data training, testing, and editing. These models include a power-law model and six different machine learning techniques – Random Forests (RFs), Gaussian process (GP), Artificial neural networks (ANNs), Extreme learning machines (ELMs), Support vector machines (SVMs), and Multi-adaptive regression splines (MARS). Three performance parameters are used to quantify the most precise and accurate model: R^2, RMSE, and MAE. R^2 determines the goodness of fit, with values closer to 1 representing a good agreement between regression model predictions and actual measurements. Root Mean Square Error (RMSE) gives the mean value over the squared errors in the predictions, while the Mean Absolute Error (MAE) gives the average absolute error values of the predictions. For both, lower values are preferred. The equations for RMSE and MAE are given below.

$$RMSE = \sqrt{\frac{1}{n}\sum_{j=1}^{n}\left(y_j - \hat{y}_j\right)^2} \qquad MAE = \frac{1}{n}\sum_{j=1}^{n}\left|y_j - \hat{y}_j\right| \qquad (8)\ and\ (9)$$

For primary analysis of feature importance, optimization, and prediction modeling, the initial experimental data were divided into training (118 points) and testing sets (20 points). Data points in the testing set were selected randomly from the 20 equal width bins across the range of sizes obtained experimentally. Monte-Carlo cross-validation with 30 replications and 20/80 split was implemented for tuning model parameters during training. After the initial round of machine learning and analysis, more data was collected for further investigate and attempt to optimize for both size and PDI control. We also incorporated a small, hydrophobic dye as a model payload in some runs to investigate whether the loading of such payloads influences the size and PDI predictions. Including the cohort used in the initial round of analysis, the second set of experimental data consisted of 420 points. For the subsequent machine learning, which was not as extensive as with the initial (118 points) data set, 30-fold cross validation was performed on an 20/80 split for test/train, and the same performance parameters of R^2, RMSE and MAE were used.

3.3 Modeling Results and Discussion

3.3.1 SEM Morphology

Scanning electron microscopy (SEM) was used on early runs to verify morphology and DLS size measurements. Different samples of various average hydrodynamic diameters were selected for visual analysis. Figure 3.3.1 shows an example of one image. The nanoparticles showed smooth morphology and highly spherical shape. The images also show that the average hydrodynamic diameter measured via the DLS is near the hard-sphere diameter of the nanoparticles. The images also showed the monodispersity of the nanoparticle samples being produced, confirming the PDI measurements from the DLS analysis. Thus, the DLS measurement was used for all subsequent data collection.

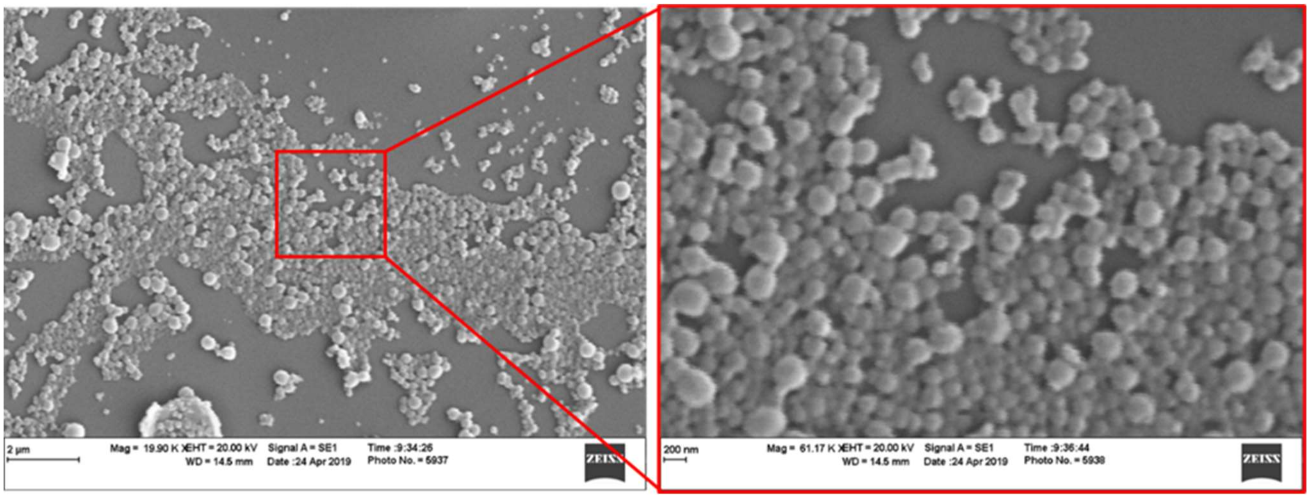

Figure 3.3.1: SEM Images of PLGA Nanoparticles showing smooth and uniform size and morphology.

3.3.2 Energy Input vs. Sonication Amplitude and Time

As mentioned, sonication amplitude and time were not considered as separate features. In others' studies, these two features were considered as separate factors for controlling the size of polymeric nanoparticles.[91,92] Observing that these factors together determine the total sonication energy input, we initially investigated whether amplitude and time could be combined into one parameter, total energy (in Joules). Furthermore, we hypothesized that the specific energy density (J/mL) of the emulsion was the main contributing parameter determining droplet size. Therefore, we accounted for this by dividing the total energy by the total emulsion volume (mL). This simplified approach was validated by running several paired experimental runs, seen in Table 3.3.1. Using different emulsion volumes (asterisks in Table 3.3.1), the measured mean diameter of the particles was found to be highly similar, while the PDIs were also similar and considered monodisperse. A standard t-test between populations was done, with p-value for the size being 0.994 and the PDI being 0.525, meaning we fail to reject the null hypothesis that the two populations are the same. This is also evident just from visual approximation. Based on these initial investigations, we removed the sonication time and amplitude setting as separate parameters and instead considered specific energy, with units of Joules/mL.

Table 3.3.1: Amplitude/Time Energy Paired Experimental Run Conditions vs. Size and PDI of NPs

Run Names	Total Emulsion Volume (mL)	Specific Energy Used (J/mL)	Amplitudes Used	Average Sonication Time (s)	Final Measured Mean Diameter (nm)	Final Measured PDI
S20 / S26	1.387 / 2.906	56.95 / 53.2	30 / 50	46.5 / 37.5	244.4 / 245.0	0.042 / 0.054
S27 / S32*	2.473 / 2.380	64.7 / 65.5	50 / 20	36 / 156	262.3 / 252.6	0.062 / 0.109
S42 / S61*	3.243 / 3.629	75.55 / 75.65	50 / 60	50 / 34	287.6 / 288.5	0.168 / 0.062
S43 / S58*	3.243 / 2.301	100.22 / 100.37	50 / 40	67 / 84	232.1 / 233.0	0.042 / 0.025
S66 / S67	2.609 / 2.609	120.4 / 121.7	30 / 60	121.5 / 45	237.4 / 242.0	0.022 / 0.056
S98/Rep2-6*	4.594 / 2.413	1200 / 1201	80 / 40	492 / 267	150.4 / 151.3	0.012 / 0.040
CL4/CL6	3.500 / 3.500	950 / 950	50 / 60	655 / 548	168.2 / 170.1	0.145 / 0.144
cAB12/cAB56	3.500 / 3.500	135 / 135	70 / 30	81 / 236	203.9 / 192.4	0.116 / 0.120
F9/F13	3.000 / 3.000	300 / 300	50 / 60	256 / 168	182.7 / 193.6	0.030 / 0.150
D45/S95	3.000 / 3.000	400 / 400	60 / 80	219 / 181	173.6 / 173.5	0.035 / 0.011
S158/F11*	1.843 / 3.000	600 / 600	75 / 50	188 / 424	170.4 / 174.1	0.027 / 0.098

The total energy reported by the sonicator is the energy required by the instrument to achieve a desired amplitude at the tip, which may be an overestimation of actual delivered energy.

3.3.3 Dye Payload Effect on Size and PDI

For a larger data set, an additional 300 points were collected, for a total of 410 points. There was a focus on capturing data throughout our input parameter ranges that were defined earlier (Table 3.2.1). Additionally, we also included a small hydrophobic fluorescent green dye, Coumarin 6, at different concentrations to investigate whether the use of such dyes, which is commonly done in laboratory applications, would affect size or PDI. For dye effect investigation, 100 of the additional 300 points were dyed runs. The left plot on Figure 3.3.2 below shows that little difference is seen with dyed vs non-dyed runs for size. However, for the same runs the fluorescent dye had a distinct effect on PDI, with a much larger deviation from the non-dyed runs and increase towards the more polydisperse. A potential explanation for this asymmetric effect is described by Geißler et al.[100] Their work discusses that while low fluorescent dye concentrations is shown to have little effect on DLS measurement of size and PDI, at higher concentrations incident light absorption can lead to decreased correlation coefficients and thus a noticeable effect. It is thus hypothesized that in this case, the dye concentrations of “Mod” and “ModHi”, corresponding to 0.01 mg dye/mg PLGA and > 0.01 mg dye/mg PLGA respectively, is sufficiently high enough to explain this PDI effect. Therefore, so that a more accurate and meaningful model can be trained or fitted to this new data set, for all PDI models that are discussed in subsequent sections, only non-dyed runs were used. For size models, all data points were used due to no effect being seen.

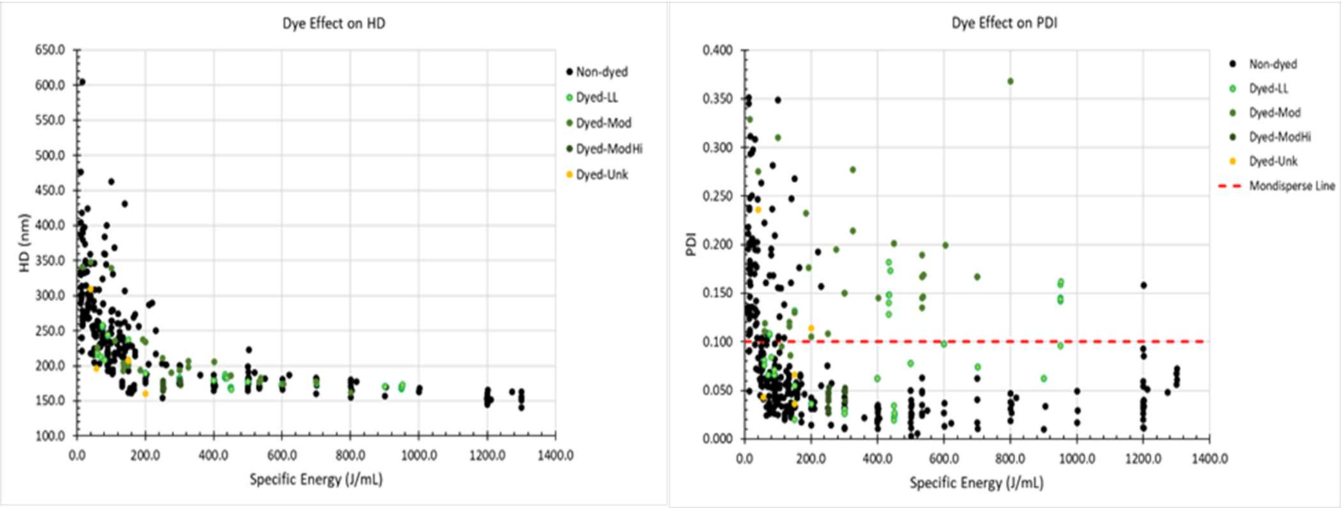

Figure 3.3.2: Effect of Dye on Average Hydrodynamic Diameter (nm) (left) and PDI (right), with red dashed line representing threshold on monodispersity (0.1). Specific Energy (x-axis) is scaled to 1400 J/mL to better show dyed run distributions

3.3.4 Synthesis Effects on Size

Modeling for size control was done in two stages, as previously mentioned. The initial data set had fewer points (118), none of which were dyed, and rigorously fit to machine learning models and a power law model to evaluate potential control parameters and prediction power. This was done to better understand which features were better for control and if there were further features which needed to be explored at different ranges. Once this initial training and feature importance was done, a second (full) data set was gathered. This second data set consisted of 300 additional points, with 100 of those dyed, for a total of 410. These further points were gathered at a wider range of parameters, such as the molar ratios, and introduced more variability for the regression model fitting.

Model Fits and Performance - Size

The six machine learning models and the power law model were trained to predict the size of the nanoparticles with the initial data set. The comparison of the trained machine learning and power law models' performances based on RMSE and MAE is given in Table 3.3.2. From the initial hypothesis and screening runs, the specific energy feature (E_v) showed the highest impact on the size. Thus, only this feature was used to fit the power law model. We consider the power law as the baseline model for comparison to all machine learning models, as it represents the simplest, best linear regression model and thus any machine learning model must exceed its performance to be considered. The power fit from this initial data set is shown below, with the performance seen in Table 3.3.2.

$$Diameter = 1309.3\, E_v^{-0.575} + 149.15 \qquad (10)$$

Interestingly, this power law suggests that the minimum size that can be achieved via sonication of a PVA/DCM system using specific energy (E_v) as the only controlling feature would be 149.15 nm. However, this “minimum” size is specific to the process parameter ranges that were tested and does not take into account changes in the centrifugation collection process, which was tested but could affect size. Additionally, changing solvents or surfactants/co-surfactants would change the emulsion thermodynamics and could lead to smaller achievable sizes. For example, it is reported that using a partially water-miscible solvent such as ethyl acetate could result in much smaller achievable diameters.[96]

Of the machine learning models, Random Forest (RF) was the best performing for predicting size on the initial training and test sets with the lowest RMSE and MAE values. The other techniques, generally, overfit the data, yielding lower errors for the training set but higher for the test set. This Random Forest model was used to evaluate feature importance regarding the size, which will be discussed in the next section.

Table 3.3.2: Performance of Machine Learning Models for Initial Data Set for NP Size

Model	RMSE-train	MAE-train	RMSE-test	MAE-test
Power-law	33.41	24.27	37.74	27.06
GP	34.30	23.39	38.17	27.64
ANN	21.85	12.71	32.32	24.45
ELM	28.18	19.34	34.49	24.49
MARS	20.17	12.18	30.78	19.28
SVR	27.72	18.51	34.88	24.08
RF	26.62	21.06	22.19	17.51

Using the expanded dataset, we retrained the same model types, with the same 30-fold Monte Carlo cross-validation and 20/80 test/train split. Once again, Random Forest performed the best, and so we will just display these results for further discussion. In Table 3.3.3, you can see that when compared to the performance of the first Random Forest model, the RMSE and MAE increased for both the train (26.62 to 43.34, 21.06 to 26.99) and the test (22.19 to 35.64, 17.51 to 23.03). The new Random Forest model also performed worse than the first power law model for the training data but performed slightly better on the test data. As this was the best performing machine learning model, the additional data runs introduced enough variability that the machine learning algorithms may not result in the most accurate predictions.

Table 3.3.3: Performance Parameters for Random Forest for Size Control, on Full Data Set

Random Forest Performance - Size - 2nd Data Set		
	Train	**Test**
R^2	0.57	0.71
RMSE	43.34	35.64
MAE	26.99	23.03

Neither Random Forest on the initial data set nor on the full data set performed better than the power law fit on the full data set. From Table 3.3.4, the R^2 was not calculated for the initial machine learning models, but the RMSE is lower (24.4 vs 26.62 for RF1) and the MAE is comparable. The power law model also only uses specific energy as the input and is much simpler and more practical to use. Thus, it is clearly the preferred model of the ones tested for the most accurate size control, using the gathered experimental data.

Table 3.3.4: Power Law Regression Fit Size Constants and Performance: Full Data Set

Power Law Regression Fits	
$\boldsymbol{a * E_V^b + c}$	**Diameter (nm)**
a	403.2
b	-0.2265
c	78.42
R^2	0.864
RMSE	24.4
MAE	29.5

Feature Importance - Size

In the RF model, each feature (i.e., input) can have a different weighted impact on predicting the output. A useful feature of RF and other machine learning modeling technique is an embedded function that quantifies these impacts via a metric called relative importance.[101] Table 3.3.5 shows the top seven most important features from this relative importance test of the initial data set.

Table 3.3.5: Feature Importance from RF Model (Initial Data Set) Predicting Size

Size	
Feature	**Importance**
$\boldsymbol{E_v}$	0.897
$\boldsymbol{R_N}$	0.041
$\boldsymbol{N_e^{PVA}}$	0.021
$\boldsymbol{N^{PLGA}}$	0.020
$\boldsymbol{N_t^{PVA}}$	0.013
$\boldsymbol{N_f^{PVA}}$	0.004
$\boldsymbol{N_w^{PVA}}$	0.003

Specific energy (E_v) was specified as the most important feature contributing around 90% (importance of 0.897 in Table 3.3.5) for size prediction. The molar ratio (R_N) of the PVA to PLGA was the second most important feature. The importance of the specific energy (E_v) and molar ratio (R_N) features is expected and significant when considering the thermodynamic base of emulsion formation. The work, W, needed to reduce the size of the droplets can be represented simply by below, where γ is the droplet interfacial tension, ΔA is the total surface area change which is a function of the number of droplets and their average size.

$$W = \gamma \Delta A \qquad \Delta A = n_{droplets,i}(4\pi r_i^2) - n_{droplets,f}\left(4\pi r_f^2\right) \qquad (11) \text{ and } (12)$$

The sonicator tip, via the specific energy (E_v), applies direct work on the droplet. This increases the number of droplets and decreases the average radius. The work W is not fully captured by specific energy because there is some emulsion temperature change and the sonicator tip itself. Instead, it is the energy used by the sonicator equipment to maintain desired tip vibrational amplitude, and a portion of it will be lost to temperature change as stated as well as translation to tip kinetic energy.

The molar ratio affects the interfacial tension of the emulsion, because as it increases the available PVA molecules available to coat the surface of each droplet also increases, which in turn decreases the free surface tension of each droplet. However, this also suggests that there is limit to the effect this ratio will have, as once each droplet surface is fully coated, any additional PVA molecule will not change free surface tension. Combined, the significance of both features means they can be used to control size (and PDI) in other systems as well.

3.3.5 Synthesis Effect on PDI

For PDI, there were the same two states of data collection, model fitting, and analysis as for size. The initial data set had fewer points (118), none of which were dyed, and rigorously fit to machine learning models and a power law model to evaluate potential control parameters and prediction power.

Model Fits and Performance – PDI

Table 3.3.6 list the performance of models trained to predict PDI, with the last row being the performance of the power law linear fit of the initial data set. Random Forest again was the best performing model, with the lowest RMSE and MAE for the training data, and reasonably low RMSE and MAE for test, meaning that it did overfit the initial training data.

Table 3.3.6: Performance of Machine Learning Models for Initial Data Set for PDI

Model	**RMSE-train**	**MAE-train**	**RMSE-test**	**MAE-test**
GP	0.038	0.026	0.041	0.033
ANN	0.033	0.021	0.056	0.043
ELM	0.041	0.029	0.056	0.043
MARS	0.036	0.023	0.051	0.036
SVR	0.041	0.025	0.047	0.033
RF	0.017	0.013	0.042	0.030
Power	0.035	0.028	0.041	0.032

The same machine learning was performed on the non-dyed data set for polydispersity (PDI), with the performance results of the best model, again the Random Forest. Again, the performance of the newly trained model with the expanded data set was worse for both training and test data, with RMSE rising from 0.017 to 0.05724 and MAE from 0.013 to 0.039783 for training set and 0.042 to 0.04978 and 0.03 to 0.032644 for test set. In contrast, the power law fit slightly improved from the initial data set to the full data set. The R2 (not shown) increased, meaning the goodness of fit increased. RMSE decreased from 0.035 to 0.031 and MAE increased slightly from 0.028 to 0.0369.

Table 3.3.7: Power Law Regression Fit PDI Constants and Performance: Full Data Set

Power Law Regression Fits	
$a * E_V^b + c$	**PDI**
a	1.271
b	-0.861
c	0.03216
R^2	0.814
RMSE	0.0311
MAE	0.0369

Based on the performance parameters, the PDI models for more varied full data set had decent accuracy and error for PDI control, but the models for PDI were more accurate and gave better predictions with using just specific energy as inputs. Technically, PDI control is not the goal, rather it is preferable to just ensure that the PDI is minimized. Thus, further analysis was done with other input features to optimize the size control and minimize PDI.

Feature Importance – PDI

Using the Random Forest model on the initial data set, the relative importance of the synthesis parameters on the PDI was determined. Table 3.3.8 shows the ranked importance of the top seven features. Once again, specific energy showed the greatest importance, accounting for around 74% (0.744) of the total importance. Total molar ratio (R_N) was again the second most important feature, and the importance increased compared to its importance on size, tripling from 4% to 13%. Again, the moles of PLGA and PVA (total and in each step) had minimal but ranked effect. However, with less predictable control seen for PDI than for size, more analysis into how exactly the molar ratios can be used to minimize PDI is needed.

Table 3.3.8: Feature Importance from RF Model (Initial Data Set) Predicting PDI

PDI	
Feature	**Importance**
$\boldsymbol{E_v}$	0.744
$\boldsymbol{R_N}$	0.130
$\boldsymbol{N^{PLGA}}$	0.070
$\boldsymbol{N_e^{PVA}}$	0.025
$\boldsymbol{N_t^{PVA}}$	0.014
$\boldsymbol{N_f^{PVA}}$	0.009
$\boldsymbol{N_w^{PVA}}$	0.008

Molar Ratio Trend Analysis and Performance Optimization

A simple model with one scalable input factor would be more desirable, especially one that provides precise control of both size and PDI. We saw with the feature importance analysis that other factors influence both outputs. These features were determined to be the molar quantities of PVA and PLGA for size and PDI. To maintain the practicality of both power law fits and improve them, we desired to find scalable process parameters which could be optimized to provide higher prediction accuracy for size and minimize PDI. For this, we chose to analyze the effect of the total molar ratio (the total moles of PVA used divided by the moles of PLGA used) and the emulsion molar ratio (PVA moles used in the emulsion step divided by PLGA moles).

They are both scalable and can be held constant while still changing the other factors, such as PLGA moles or PVA emulsion moles, which were determined to have some importance on size and PDI. For this analysis, the data (all data for size, non-dyed for PDI) was grouped in bins of molar ratios that contained roughly equal number of points, and the molar ratios were log-scaled to distribute more evenly. For the quantification of effect on accuracy, a best fit power law model with specific energy was found for the data in each bin, and the adjusted R^2 was then plotted vs. the natural logarithm of the right edge of each bin. Each bin contained a comparable range of specific energies, and so the molar ratios (total or emulsion) which have the best fit and thus best prediction can be analyzed. To quantify whether there exists a bin range with higher monodispersity, we used the same bins for both total and emulsion molar ratios and calculated the percentage of the points in each bin that lie below the monodispersity threshold (≤ 0.1). These percentages were then plotted against the natural logs of the bin edges as was done with the Goodness of Fit analysis.

Figure 3.3.3 shows the Adj R^2 for both size (green) and PDI (red) for the various total molar ratio bin ranges. The prediction accuracy of the size data is poor for very low total molar ratios, but quickly improves as it increases into the second bin, with goodness of fit (GoF) about 0.9. There is a decrease in GoF as total molar ratio increases from third bin to fourth, but this is likely due to the unequal number of points in this one bin, which was a result of the sorting. Beyond this one bin, the fit remains above 0.90 for all bins up to ln $(\boldsymbol{R_N})$ of 4.5, before it decreases to 0.7. PDI GoF varies more widely with total molar ratio. It is highest in the fifth bin, but no general trend can be reliably determined for PDI.

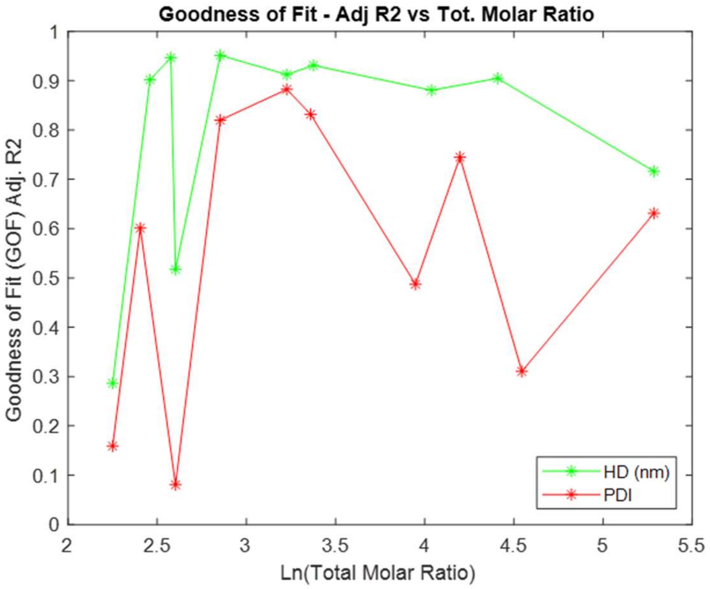

Figure 3.3.3: Goodness of Fit (Adj. R2) vs Total Molar Ratio of Size (green) and PDI (red)

Figure 3.3.4 shows the percent monodispersity across the total molar ratio bins. The lower ranges of total molar ratio (bins 1-3) fluctuates in the number of runs which are monodisperse, but at Ln($\boldsymbol{R_N}$) or greater, a high percentage of every run is monodisperse. The points within the sixth and seventh bins, particularly, are the highest percentage.

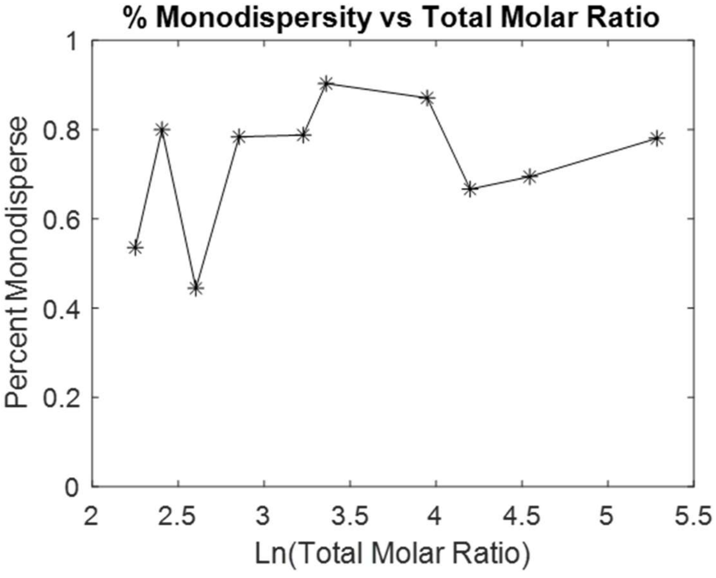

Figure 3.3.4: Percent Monodispersity within each bin for Total Molar Ratio

Figure 3.3.5 shows the GoF for size and PDI with respect to the log of the emulsion PVA molar ratio ($\ln R_N^E$). Size control was good after the lower emulsion molar ratios, but PDI showed high variability, with the best control in bins 4-6.

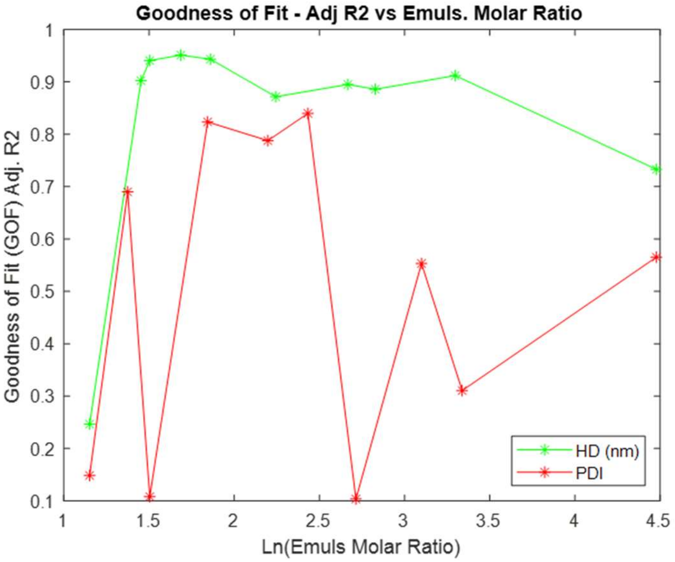

Figure 3.3.5: Goodness of Fit (Adj. R2) vs Emulsion Molar Ratio of Size (nm) and PDI

However, when looking at the percent monodispersity (Figure 3.3.6), a similar trend as for total molar ratio is evident. PDI percent fluctuates from bin 1-3 but remains fairly high and constant as emulsion molar ratio increases, with highest percentage in bin 6.

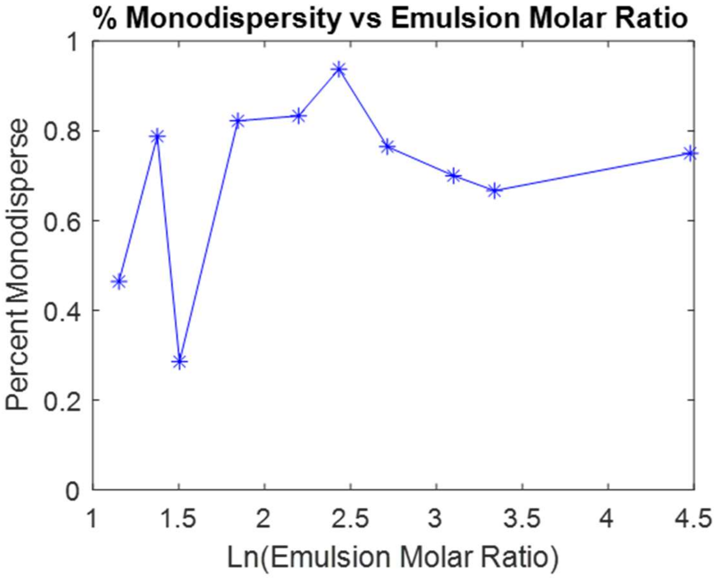

Figure 3.3.6: Percent Monodispersity within each bin of Emulsion Molar Ratio

Based on this analysis, the greatest precision for controlling size and highest probability of monodisperse nanoparticles occurs at total molar ratios is within bin 5-6. This corresponds to total molar ratios of 13.5 to 28. For the emulsion molar ratios, bin 6 also showed the greatest GoF for size control combined with the highest percentage monodispersity, corresponding to emulsion molar ratios of 6.4 to 11.4.

We tested the accuracy of the power law model to ten points with which the total and emulsion molar ratios were kept within these newly found bin range values. The synthesis conditions for these points were specifically set so that different PVA concentrations and volumes were used. Roughly equal specific energies were also chosen for each set, concentrated in the lower specific energy to test the fit at the most dynamic region of the predicted trend line. In addition, for every pair between sets that have the same specific energy, different amplitudes and times were used to demonstrate the flexibility for desired power setting to achieve a necessary energy input. These settings can be seen in Table 3.3.9, as well as the measure average diameters and PDI and the predicted diameter and PDI from the power law for the desired specific energy.

Table 3.3.9: Specific Energy, Amplitudes, and Sonication Times for Molar Ratio Power Law Test Points

Run Names	**Total Emuls Vol (mL)**	**Specific Energy (J/mL)**	**Amp %**	**Sonication Time (s)**	**Obs HD (nm)**	**Obs PDI**	**Predicted HD (nm) and PDI**
PowerTest1/6	2.700 / 3.500	16 / 18	20 / 50	25 / 12	305 / 287	0.216 / 0.213	291 0.149
PowerTest2/7		30 / 30	30 / 50	41 / 26	244 / 241	0.075/0.102	265 0.100
PowerTest3/8		50 / 53	30 / 50	76 / 46	221 / 219	0.074/0.074	244 0.076
PowerTest4/9		251 / 250	50 / 70	208 / 144	188 / 184	0.045/0.057	194 0.043
PowerTest5/10		450 / 450	70 / 80	213 / 168	179 / 178	0.059/0.042	179 0.039

The resulting measurements were very close to the predictions from the updated power law model fit. At both the lower specific energy points (largest sizes) and the higher specific energy points (smallest sizes), the difference was the smallest, meaning that the updated power law model was better at predicting both parameters at these ranges. It seemed to overpredict size and the intermediate specific energies test, and slightly underestimate the PDI for the lowest specific energy (see Figure 3.3.7).

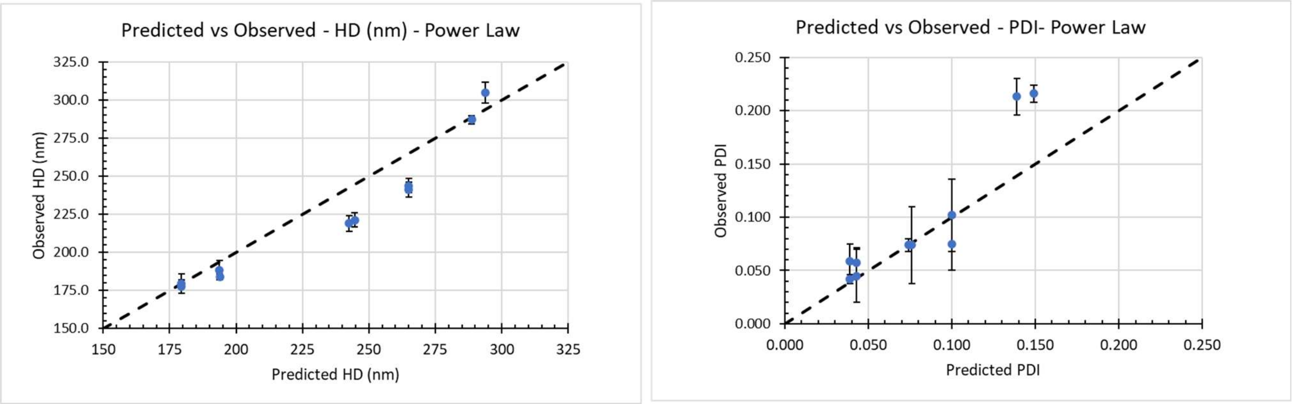

Figure 3.3.7: Predicted vs. Observed Values for Size (nm) (left) – Polydispersity Index (right) for Molar Ratio Test

We calculated the new goodness of fit, RMSE, MAE, and the number of points which can be considered monodisperse with the size control power law model determined in Section 4.5.2. The results can be seen in Table 3.3.10**.** For both size and PDI, all performance parameters improved from the training data (Table 3.3.4 and Table 3.3.7). This demonstrates that the proposed optimum ranges for total and emulsion molar ratios improved the predictability of nanoparticle size within the specific energy ranges tested, with achievable sizes from 300 nm to 170 nm. It also demonstrated that PDI control could be achieved, with the majority of points being monodisperse (≤ 0.100) and all points being less than 0.250, which is often considered acceptable for many applications.

Table 3.3.10: Performance of Molar Ratio Test Points to Power Law Model Fit

Updated Power Law Model Fit Test Data Performance		
	Size (nm)	**PDI**
R^2	0.9251	0.852
RMSE	15.4	0.033
MAE	12.2	0.021
% Monodisperse	70%	

3.4 Particle Release Kinetics Fits and Analysis

Developing a model which uses scalable and variable parameters for size control is the first step in achieving controlled release from polymeric nanoparticles. We also much characterize their release behavior and mechanism before forming shells around them. The following sections summarize this characterization of the release kinetics of the PLGA nanoparticles as well as PLLA nanoparticles so that baseline kinetics can be established for the shell material and compared to those of core/shell nanoparticles in the next chapter.

3.4.1 Dye Standard and Quantification Method

A dye standard was developed for each solvent condition since different mixtures of solvents are used for release and loading analysis for each dye. The general protocol is that eleven different concentrations of a dye in desired solvent was made using serial concentrations, along with a blank. This dye was added to a black 96-well plate and the SpectraMax fluorescent wavelength optimization determines the excitation and emission wavelengths for future readings for those specific conditions. At least 6 wells of each standard concentration are read at the optimum wavelengths. If the trend is linear, then this range is fitted to a linear trend where the y-intercept is 0 for future loading and release studies. Table 3.4.1 shows a table of linear fits of standards.

Coumarin-6 (C6): hydrophobic dye, 350.436 Da

5(6)-Carboxyfluorescein (CF): hydrophilic dye, 376.32 Da

Table 3.4.1: Fluorescent Standards

Standard	λ_{exc}	λ_{emiss}	m	Blank
CF + 1%PVA + 1M NaOH	465	515	7.7112E-12	22600819.5
C6 50:50 1X PBS/EtOH	475	515	2.3800E-09	43118.5
C6 Undissolved + 1X PBS	460	640	5.8600E-09	1981.625
C6 33% EtOH	475	515	1.2684E-10	38548.125

For all release studies, the same general protocol is used. A known mass of lyophilized nanoparticles are dispersed in 1mL of 1X PBS (pH 7.4). Equal masses (roughly 1mg) are separated into individual microfuge tubes for all the replications, and all are diluted back to 1 mL. All release tubes are sonicated briefly and placed in a Rotoflex inside a 37°C incubator and set to rotate. At a given time point, every tube is removed from the incubator and immediately centrifuged at 14,800 RPM for 30 minutes. The supernatants are quickly transferred to fresh microfuge tubes, being careful not to disturb the pellet. One milliliter of fresh 1X PBS is added to the pellet microfuge tubes and all are sonicated to fully disperse the pellet before they are returned to the incubator rotation. For coumarin 6, 0.5 mL of ethanol is added to each supernatant microfuge tubes and the tubes are vortexed and left covered overnight to fully dissolve dye. Two 100 μL samples of each supernatant are then read in the SpectraMax and calibrated using the relevant standard to determine the total mass released at that time point.

3.4.2 Model Fit Analysis for Release Mechanism

Eight PLGA nanoparticle formulations and nine pure PLLA nanoparticle formulations were loaded with hydrophobic Coumarin-6 (C6) dye as a model for small molecule hydrophobic chemotherapeutics. The first four PLGA nanoparticle runs (with PDI > 0.10) had 0.0097 mg of C6 per 1 mg of PLGA (0.97% loading capacity), with a loading efficiency on average of 97% ± 1.2%. The other four PLGA nanoparticles runs (PDI < 0.1) had on average 0.0047 mg C6 dye per 1 mg of PLGA (0.47% loading capacity), with an average loading efficiency of 94% ± 2.4%; the reason less dye was used was due to decrease the PDI to measure more consistent release. The pure PLLA nanoparticle formulations all had similar loading to the monodisperse PLGA, with 0.0049 mg C6 dye per 1 mg of PLLA, with a loading efficiency of 98%. The loading efficiency was measured by mass balance, with known mass of dye put in and subtracting the total massed release of the known mass of PLGA in the release sample (each around 1 mg) The release kinetic models previously discussed were fit to each nanoparticle run. Each model assumes different release mechanisms dominate, so the best model's goodness of fit and kinetic constants elucidate what effect, if any, the nanoparticle polymer, size, and PDI have.

Table 3.4.2 shows the model fits for one PLGA run, representing all runs. The goodness of fit is best for the diffusion-driven models, Korsmeyer-Peppas and Peppas-Sahlin, followed closely by the Hopfenberg model, the Higuchi, and the Weibull. This result would suggest that the release from PLGA nanoparticles is diffusion-driven from initial inspection. Looking at Table 2.1.1, the Korsmeyer-Peppas exponent fits the non-Fickian diffusion, with contributions from chain relaxation and diffusion equally. The Peppas-Sahlin fit separates these terms into two different rate contributions, with k1 being the diffusional contribution which was larger for the PLGA release. However, these fits are only valid for the first 60% release, and when looking at the fit of the plot (Figure 3.4.1), another mechanism is more appropriate. The Hopfenberg model is a better overall fit for the entire release profile, while the diffusion driven models tended to underestimate the release at later times. This suggests that the dominant release mechanism is surface erosion, not diffusion, especially at later times. For the entire release, diffusion likely contributes some early, supported by the close fit of the diffusion driven models early on, before the polymer chains hydrolyze and accelerates. This agrees with literature, where PLGA with higher GA content hydrolyzes more quickly than one with more LA[40], but takes more time to get speed up from initial hydration. It is to be noted that the Weibull particularly had both high goodness of fit and good overall graphical fit for the release time (not shown). It was not used for mechanism analysis, as it is purely experimental and does not correlate to any physical properties of the system.

Table 3.4.2: PLGA NP Release Kinetic Model Fits

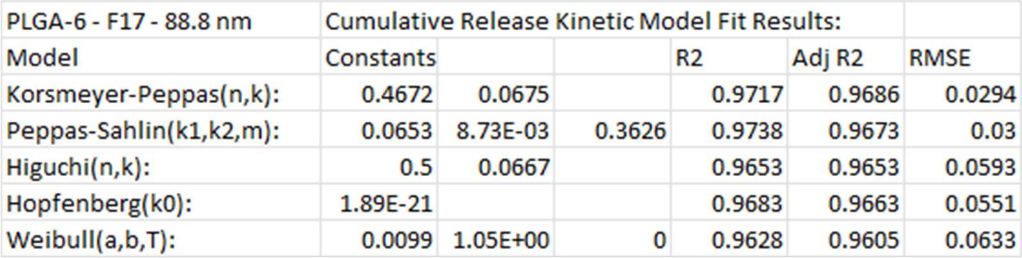

PLGA-6 - F17 - 88.8 nm	Cumulative Release Kinetic Model Fit Results:					
Model	Constants			R2	Adj R2	RMSE
Korsmeyer-Peppas(n,k):	0.4672	0.0675		0.9717	0.9686	0.0294
Peppas-Sahlin(k1,k2,m):	0.0653	8.73E-03	0.3626	0.9738	0.9673	0.03
Higuchi(n,k):	0.5	0.0667		0.9653	0.9653	0.0593
Hopfenberg(k0):	1.89E-21			0.9683	0.9663	0.0551
Weibull(a,b,T):	0.0099	1.05E+00	0	0.9628	0.9605	0.0633

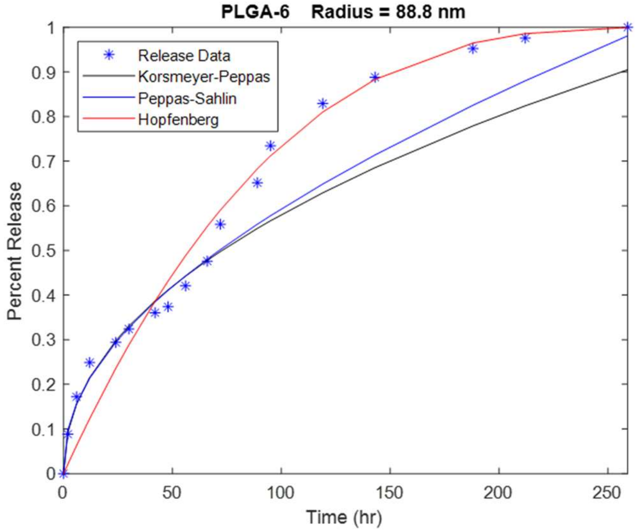

Figure 3.4.1: PLGA NP Fit Plots – Hopfenberg, Korsmeyer-Peppas, Peppas-Sahlin

The pure PLLA nanoparticles fit to the models displayed a different dominant release mechanism than the PLGA nanoparticles. Korsmeyer-Peppas and Peppas-Sahlin were again the best GoF and lowest RMSE (one example seen in Table 3.4.3). The Hopfenberg model was the worst fit, and looking at the plots (Figure 3.4.2), did not fit the overall release time as was the case for the PLGA nanoparticles. The n exponent from the Korsmeyer-Peppas fit was just over 0.45, meaning the diffusion match with that of non-Fickian diffusion, but with a slower rate that PLGA nanoparticles (0.034 versus 0.068). The rate constants for the Peppas-Sahlin also were lower for PLLA than PLGA, with k1 higher than k2 by an order of magnitude. This first rate constant corresponds to the contribution of diffusion over polymer chain relaxation, and so a larger rate suggests that the release from PLLA is dominated by non-Fickian (n>0.45) diffusion.

Table 3.4.3: PLLA NP Release Kinetic Model Fits

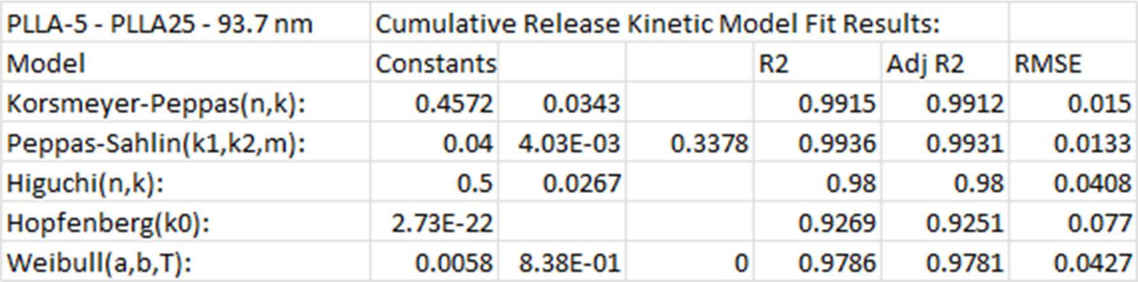

PLLA-5 - PLLA25 - 93.7 nm	Cumulative Release Kinetic Model Fit Results:					
Model	Constants			R2	Adj R2	RMSE
Korsmeyer-Peppas(n,k):	0.4572	0.0343		0.9915	0.9912	0.015
Peppas-Sahlin(k1,k2,m):	0.04	4.03E-03	0.3378	0.9936	0.9931	0.0133
Higuchi(n,k):	0.5	0.0267		0.98	0.98	0.0408
Hopfenberg(k0):	2.73E-22			0.9269	0.9251	0.077
Weibull(a,b,T):	0.0058	8.38E-01	0	0.9786	0.9781	0.0427

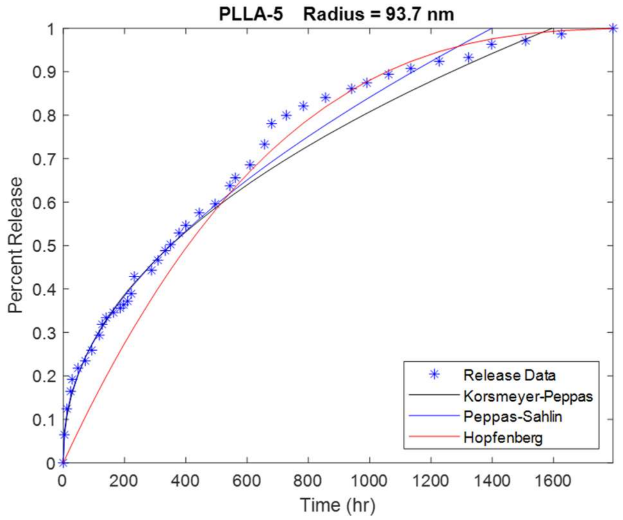

Figure 3.4.2: PLLA NP Fit Plots – Hopfenberg, Korsmeyer-Peppas, Peppas-Sahlin

3.5 Investigation into Model Adaptation for Scale-Up

The main barriers to the clinical translation of polymeric nanoparticles are the lack of control and scale-up manufacturing. By modeling the ESE method at the lab scale, we determined a relationship between size and the scalable parameter, specific energy, achieving a good level of control. However, this batch process must be translated into a continuous flow process for realistic scalability. Others, such as Schiller et al.[102], have successfully translated the ESE method to a larger (2.5 g/batch) scale using contact-free transducers and energy input as the controlling parameter of size. However, they do not use an actual continuous process; instead, it is a semi-batch process. We have done initial theoretical modeling for translating the batch size power law relationship found in our earlier modeling work to a continuous flow process. To retain the same size control, it must deliver the same specific energy into a volume by controlling the amplitude power setting and the volumetric flow rate. We have chosen to model this based on existing equipment made for this purpose, the QSonica High Volume Continuous Flocell with 1-inch probe (see Figure 3.5.1).

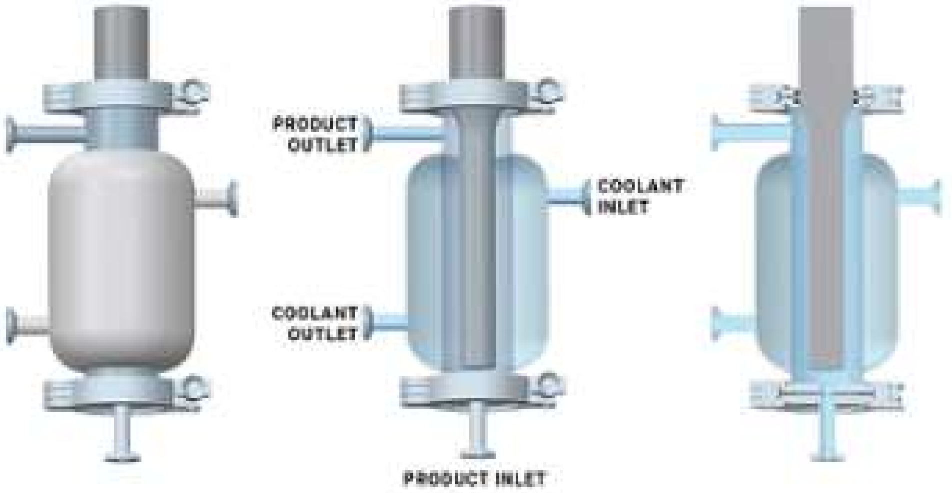

Figure 3.5.1: QSonica High Volume Continuous Flocell Equipment Setup

The added benefit of this system is the cooling jacket. High amplitudes can raise emulsion fluid temperatures in seconds, reaching the boiling point of the organic solvents and destroying the emulsion. A jacketed sonication chamber can eliminate this complication.

To convert the batch specific energy to a continuous energy input per working volume, we used the known specifications of the probe tip sonicator and the Flocell probe and vessel. The 1/16th inch probe microtip as well as the 1” Flocell probe vibrates at a known frequency (20 kHz) and a known amplitude, a linear function of the power setting and the maximum amplitude. For example, at the 80% amplitude setting, the tip amplitude is 80% of the maximum specification, which we call the vibrational distance. During one cycle, the tip travels that distance four times (forward and back one direction, then forward and back the other). Therefore, the total vibrational distance in one cycle is the vibrational distance times four. Figure 3.5.2 shows a simple diagram of this vibration.

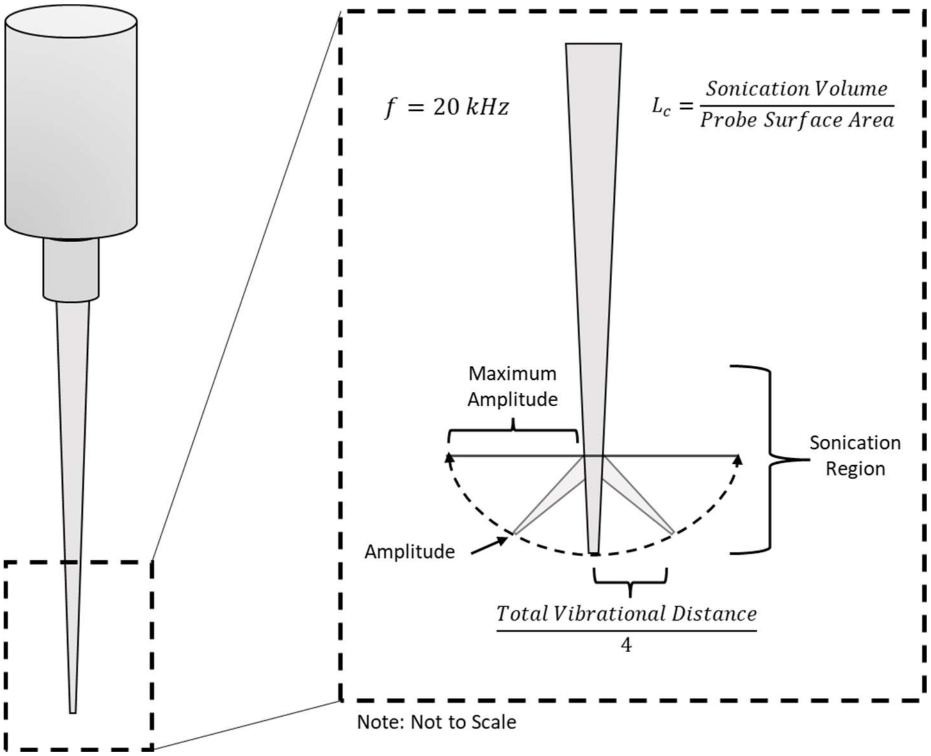

Figure 3.5.2: Batch Probe Tip Sonicator Vibration Amplitude Diagram

Multiplying this vibrational distance by frequency results in the vibrational rate, in cm/s, which is a function of the amplitude power setting. For each PLGA data point, we found the vibrational rate and multiplied by the total sonication time to determine the total vibrational distance during the batch sonication. This total vibrational distance is applied to a certain fluid volume over a known length down the probe tip. Therefore, the probe's characteristic length is the sonication volume divided by the probe surface area available for sonication, in units of cm. This is similar to the characteristic length of a cylinder, which we are approximating. We then multiplied by the probe's characteristic length to account for different probe tip surface areas and working volumes. In simple terms, we are finding the translational distance of the probe tip necessary to achieve a specific energy. This translation is the mechanism by which the specific energy is delivered and occurs down the length of the entire probe. A larger probe tip, with more surface area, can vibrate less but remain in contact with the emulsion for longer, resulting in the same energy delivered per volume. O'Sullivan et al.[103] saw this in their work in food-grade emulsion batch-to-continuous scaling, where they used different geometries of in-flow sonicators to achieve more efficient sonication at lower amplitudes. We calculated the characteristic lengths and vibrational rates of the batch probe tip and the continuous flow tip. We used them to convert the total vibrational distance to the continuous flow probe tip. We can then find the required volumetric flow rate and amplitude power setting to achieve a desired specific energy, which we have found is what mainly determines the final nanoparticle size. The PDI can be minimized by adjusting the fluid conditions, but O'Sullivan et al.[103] saw that evenly-distributed sonication is more easily achieved with larger surface area probes. Figure 3.5.3 shows the generated calibration chart for achieving specific nanoparticle diameters. Smaller desired diameters require much larger specific energies so the volumetric flow rate remains low for all amplitudes to allow for complete sonication tip translation. Larger sizes require smaller specific energies, so the volumetric flowrate can be quite fast at larger amplitudes.

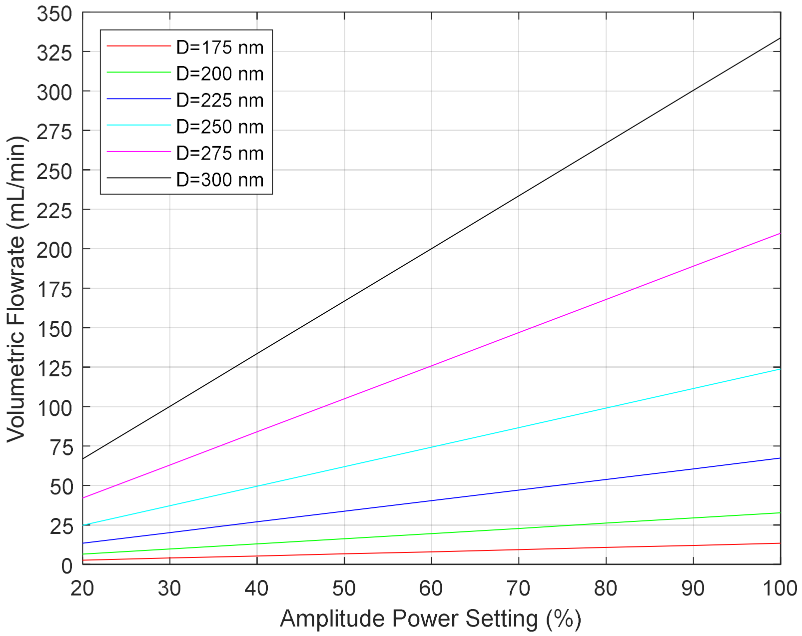

Figure 3.5.3: Continuous ESE Sonication Method Calibration Chart

Using the PLGA data as a basis, there was an average of 2.5 mg per mL of emulsion volume. If the same concentration was used for this system, theoretically this process could produce roughly 62 mg of 200 nm particles per min if operated at 100% amplitude, which is roughly 90 g/day if run continuously for this setup. This drastically improves the scalability of this process, and this polymer concentration could be increased. These calculations are preliminary and entirely theoretical, and more experiments are needed to test and calibrate the accuracy of these predictions. The evaporation process setup is another hurdle, as in the batch system this takes at least 30 minutes to an hour per batch. This could be avoided by combining this method with a nanoprecipitation step, which would replace the time-consuming evaporation and lead to flash drying. Potentially, this could be done with microfluidics to maintain the continuous process setup.

3.6 Cryoprotectant for Size Retention

No matter the scale, the nanoparticle size and PDI must be retained post-synthesis to retain the desired release behavior. For long-term storage nanoparticles are often lyophilized (freeze-dried) until shipment or further modification. Freeze-drying, though, can damage the particles and accelerate degradation. The PLGA nanoparticle degradation occurs due to mechanical stress from water crystals upon freezing before lyophilization.[104] Sugar solutions such as trehalose, glucose, fructose, and sorbitol have been used as cryoprotectants to prevent aggregation and reduce the stress from ice crystals.[105] Cryoprotectant concentrations typically range from 1% to 10% (w/v), but less cryoprotectant is preferable to not introduce extra mass. For this study, three different concentrations (0.5%, 1.5%, 3.0% w/v) of glucose and trehalose were investigated and compared to control particles with deionized water. Glucose is a reducing sugar while trehalose is non-reducing, with each chosen for comparison. Once synthesized and washed, nanoparticles are sized via DLS, with the remainder centrifuged again for at least 30 minutes at 14,800 RPM and then resuspended in 1 mL of their corresponding cryoprotectant solution before being frozen at -80°C overnight. The particles with cryoprotectants are then lyophilized and stored in different temperatures to study the storage stability.

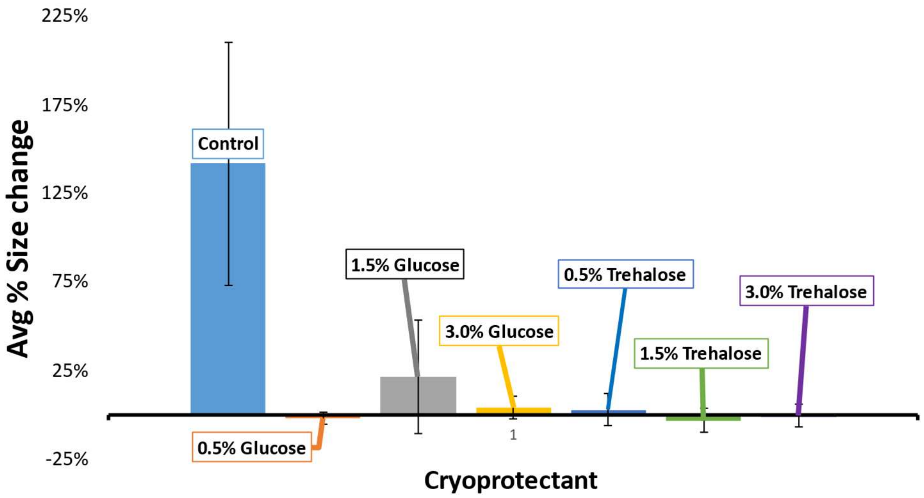

Figure 3.6.1: Average Percent Change of Size vs Cryoprotectant Concentration – Room Temperature

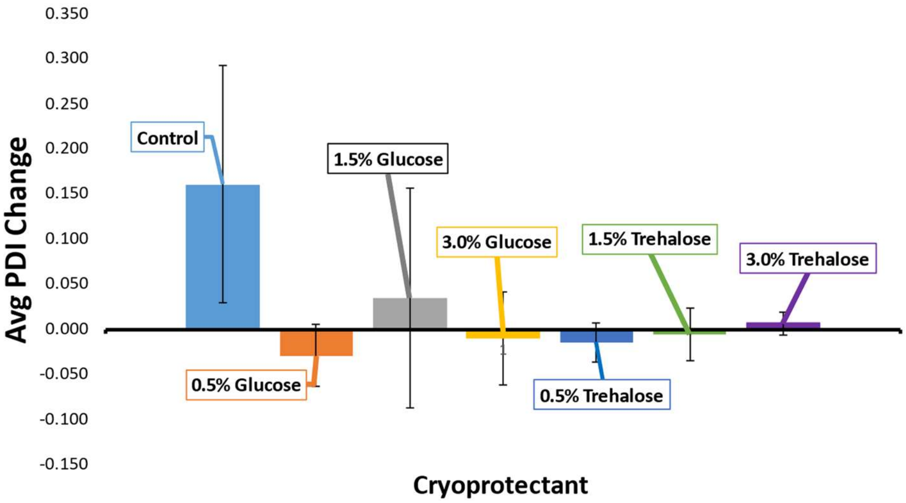

Figure 3.6.2: Average PDI Change vs Cryoprotectant Concentration – Room Temperature

For this discussion, only the results for room temperature storage are displayed as at this temperature the nanoparticles were the least stable, and all results carry over to lower temperatures (Figure 3.6.1 and Figure 3.6.2). The experiment showed that for the tested time (12 weeks), the average percent change of size with no cryoprotectant was +24.8% for storage at -80°C and increased with increasing storage temperature, with +55.5% increase for -4°C and

+142% for room temperature storage. PDI did not change at -80°C for the control but also increased as storage temperature increased. This result is due to the higher humidity at higher temperatures, accelerating polymer hydrolyzation and thus particle degradation, and emphasizes the importance of cryoprotectants. Between glucose and trehalose, trehalose showed improved storage stability over glucose, which had more variability between samples for both size and PDI change at all temperatures. All three concentrations of trehalose showed excellent size and PDI retention over the tested time at each temperature. More variation occurred with 0.5% trehalose, so 1.5% trehalose was chosen as the cryoprotectant concentration. SEM visualization was done on the degraded and cryopreserved particles as well. Figure 3.6.3 shows the control particles' fused morphology and degraded structure, while Figure 3.6.4 shows the retained smooth spherical morphology and size distribution of the trehalose-preserved nanoparticles. This further demonstrates the need for cryoprotectant for storage of these particles, whether in the lab or commercial use.

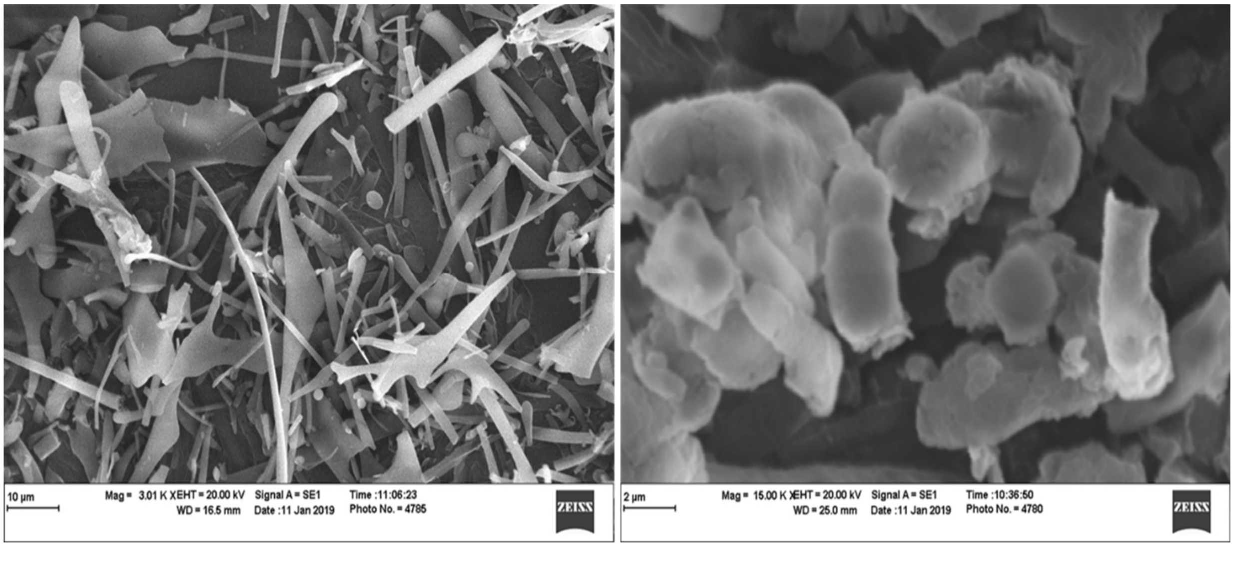

Figure 3.6.3: PLGA Nanoparticles with Degraded and Aggregated Structure from Storage at -80°C with no Cryoprotectant

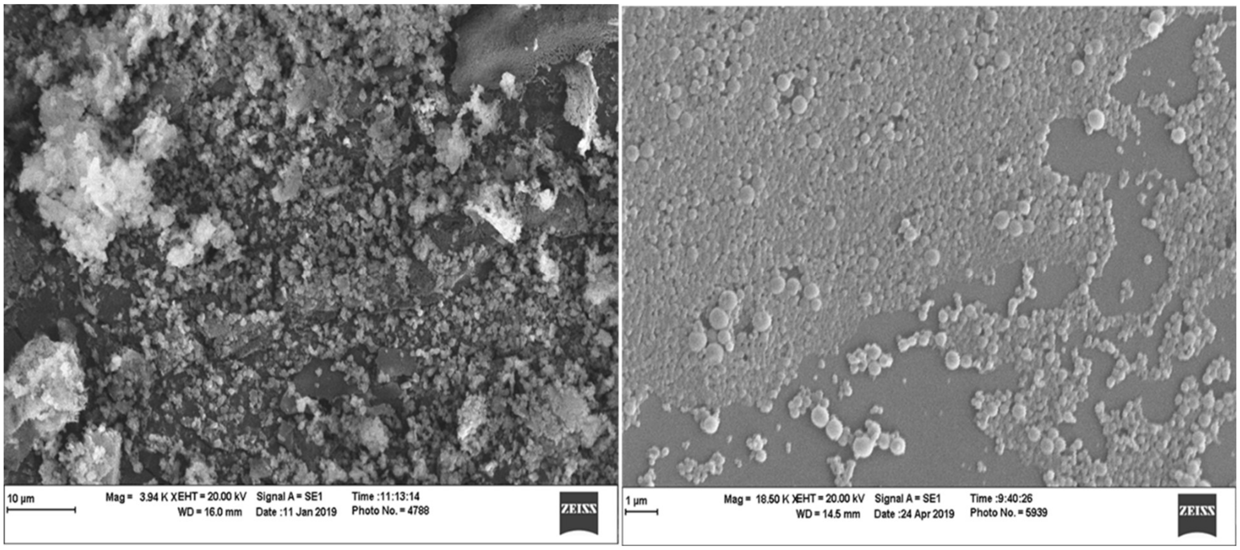

Figure 3.6.4: Intact and Spherical PLGA Nanoparticles Showing Trehalose Cryoprotectant Effect

3.7 Conclusion

Before investigating how core and shell polymeric nanoparticles can be formed efficiently, we required better understanding and control of the cores' properties. The size and PDI of PLGA nanoparticles affect their release and *in vivo* performance, and so are what we chose to focus on controlling. We used machine learning and trend analysis with the most common PLGA NP formation methods to find features which could control size and minimize PDI. We found that a scalable feature, specific energy, is the dominant factor for controlling size, and determined other process parameters could be tuned so that the size distribution was minimized. We characterized the nanoparticles' release and dominant release mechanisms, before doing initial calculations on how the model and knowledge we gained about the batch process could be applied to a continuous formation process. Finally, we determined the cryoprotectant conditions necessary to maintain the size and PDI we achieved in long-term storage, facilitating use for later core and shell formation experiments.

Chapter 4: Investigation into Core and Shell Synthesis Methods, Efficiency and Controlled Release

4.1 Introduction

Single polymeric core nanoparticles have many advantages for controlled drug delivery. Properties such as polymer makeup, size, and surface characteristics are tunable for high loading efficiency and varied controlled release of a wide range of payloads. Specifically, small hydrophobic drugs are easily loaded within biocompatible and biodegradable polymers such as PLGA and PLLA due to their compatible solubility. This encapsulation significantly improves their bioavailability and residence time within the TEW. We have shown in the previous chapter that we can use scalable synthesis features to reasonably control the size and PDI of PLGA nanoparticles, which can then effectively tune the release rate. However, this tuning has its limitations. There often is an optimum nanoparticle size range based on the application. Circulating nanoparticles' diameters meant to target solid tumors, for instance, should remain between 150 to 200 nm to utilize the EPR effect and reduce their *in vivo* clearance.[33,60] Single polymer nanoparticles' size can only be tuned within this range to vary the release rate, limiting their variable range. Additionally, PLGA nanoparticle cores often still have a period of burst release from near-surface drugs, causing off-target systemic effects[69]. One solution is introducing stimuli-responsive surface ligands that shield the negatively charged particle's surface.[53] These molecules limit any initial burst release but introduce materials unapproved by the U.S. FDA, require more extensive safety and efficacy testing for clinical translation, and suffer the same scalability challenges as polymeric nanoparticles.[106] Instead, coating the polymeric cores with another degradable polymer can shield the interior encapsulated drug and overcome these challenges. Suppose the polymer shell coating degrades relatively slowly. In that case, the necessary shell thickness to slow the overall release rate is reduced, allowing for greater variation within the optimum total size range. This advantage is the motivation for using core and shell (C/S) polymeric nanoparticles.

We investigated several polymers with preliminary release experiments (not shown) for the ideal core and shell formulation. PLGA seemed the obvious choice for the core. We have already demonstrated reasonable size control with good monodispersity, and the baseline release kinetics are well understood. When determining an appropriate shell polymer, we investigated several materials, including chitosan, polycaprolactone, and poly (L) lactic acid (PLLA). Due to electrostatic interactions and hydrophilicity, chitosan demonstrated favorable adhesion to the PLGA cores. However, the release kinetics are generally too fast for sustained release at the nanoscale, and the hydrophilic nature led to unpredictable swelling in early tests. Polycaprolactone (PCL) is FDA-approved and biocompatible but degrades extremely slowly and has high mechanical strength, which makes it ideal for implants or depots but makes it difficult to combine with PLGA. Poly (L) lactic acid (PLLA), a semi-crystalline conformation of PLA, demonstrated the right balance between sustained release kinetics, compatible mechanical strength, and solubility for the shell polymer. Therefore, PLLA was chosen as the shell material.

Previous Work

Core and shell polymeric particles are synthesized in various ways, including consecutive emulsions, dispersions, or multi-step free radical polymerization.[107] Free-radical polymerization can be highly efficient but time-consuming, difficult to scale, and costly. Emulsion and dispersion-based methods can be simple and cost-effective, but lack control over particle properties such as size and PDI and are also difficult to scale. Other researchers have investigated PLGA/PLLA core/shell particles, and they are typically formed using a top-down method such as electrospraying (CEDA) or the emulsion methods. The emulsion methods, such as the method used by Lee et al.[108], look to take advantage of the immiscibility of PLGA and PLLA when dissolved at high enough concentrations in DCM. Using an ultrasonicator, they formed an oil-oil-water emulsion. These PLGA/PLLA core/shell microspheres achieved a delayed controlled release profile, as seen in Figure 4.1.1. However, these particles were too large (> 10 μm) for cancer targeting, and they could not control the sizes of both the cores and the shells.

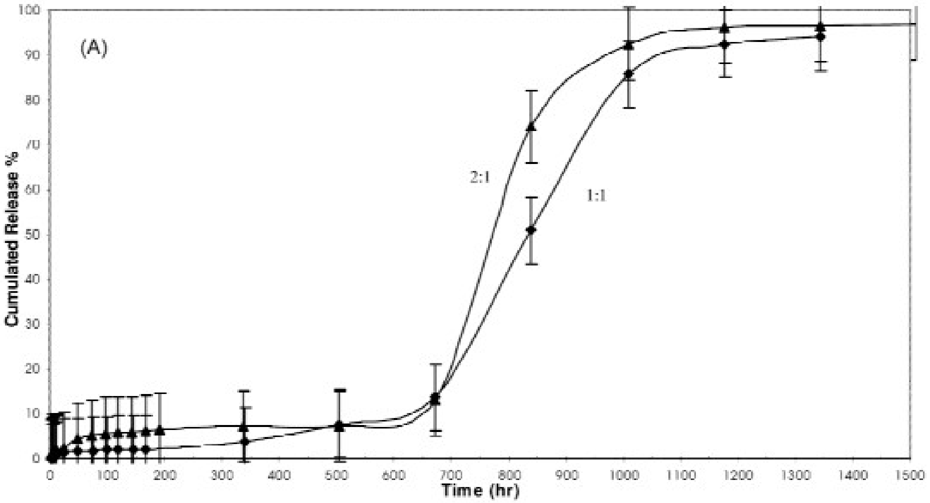

Figure 4.1.1: Delayed Release from PLGA/PLLA Core/Shell Microspheres, from Lee et al.[108]

Although simple and translatable from the ESE method, the core/shell emulsion method has been limited in its success in producing true nanoscale, monodisperse PLGA/PLLA core/shell nanoparticles whose dimensions are well controlled. Another method, developed in the early 2000s, has grown in prominence for its potential to produce polymeric nanoparticles with complex morphologies and monodisperse size distributions: nanoprecipitation. This technique uses a combination of solvents and non-solvents to quickly change polymer solubility within different solution phases, essentially flash-solidifying droplets as they form. This technique is commonly used to produce nanoparticle cores. For example, Bilati et al.[109] used a combination of solvents, and non-solvents and stirring to produce sub-400 nm monodisperse PLGA and PLA nanoparticles with high entrapment of hydrophilic payloads. Chiesa et al.[110] incorporated microfluidic platforms with nanoprecipitation and optimized the system to produce PLGA nanoparticles ranging from 100-900 nm with high loading of hydrophilic payloads. This process substantially improved the core size control and scalability of the process, but the PDI was often too high (>0.2) to be considered monodisperse. However, it represents the great potential and flexibility nanoprecipitation methods have for producing complex polymeric nanoparticle structures. Recently, Yan et al.[111] highlighted several efforts of combining different polymers, co-polymers, solvents, and non-solvents to form highly complex morphologies, such as stacked lamellae, two-faced, swirl-mixed, and core and shell nanoparticles (see Figure 4.1.2). These methods generally use the ratios between phases, the volumetric flow rate, or Reynolds number for microfluidic methods, to adjust the total core/shell nanoparticle size. They can achieve uniform nanoparticles from 50-300 nm by finding the phase compositions where the "Ouzo effect" occurs. The "Ouzo effect" is a phenomenon where stable solid particles form spontaneously from droplets with no surfactant present[112]. Liu et al.[113] developed a consecutive coaxial microfluidic system that was impressively versatile in its ability to form high uniform core and shell nanoparticles of a wide range of polymer combinations at a high production rate (700 g/day) by remaining in the "Ouzo effect" regime. It was able to achieve high loading of small hydrophobic chemotherapeutics such as docetaxel and paclitaxel (PTX) with reproducible total diameters of 200 nm and below, within the optimum size range of cancer targeting. However, there are several drawbacks to this method. It is often difficult to determine exact synthesis conditions (flow rate, Reynolds number, volumetric ratio) for the "Ouzo effect" as it changes for each system composition[112]. Importantly, independently controlling the core and shell dimensions has been limited, and work on this is in its infancy. Individual control of the size of the cores and shells would provide stronger rational design and improved performance, especially for multimodal controlled release. Additionally, many of the microfluidic systems are custom and difficult to scale-up effectively.

Figure 4.1.2: Possible Complex Polymeric Nanoparticle Morphology via Nanoprecipitation

There is high potential for the core and shell nanoparticle system because of the improved controlled release of small hydrophobic drugs and optimum size range. Two different synthesis methods, the emulsion method and the nanoprecipitation method, have distinct advantages and disadvantages associated with them. This chapter outlines our investigations in adapting the emulsion method Lee et al.[108] and other groups used due to the similarity with the PLGA core method we modeled previously. Early experiments were performed with an adapted solvent/non-solvent precipitation method to form PLGA/PLLA core/shell nanoparticles, but this data is preliminary and thus will not be discussed in this document. We seek to combine our knowledge gained from the PLGA core synthesis modeling and analysis to produce PLGA/PLLA core/shell nanoparticles with high efficiency and precise and controllable core and shell dimensions, something that has been limited thus far in other promising studies. The control of these dimensions and the efficiency will attempt to use scalable parameters, as was done for the PLGA core synthesis in Chapter 3, to facilitate process scale-up if the processes are capable of optimization.

4.2 Materials and Synthesis Method

4.2.1 Materials and Equipment

Poly (L) lactic acid (PLLA) (MW: 90 kDa) was purchased from Polysciences Inc. (Warrington, PA). Polyvinyl alcohol (PVA) (MW: 50 kDa) were purchased from Sigma Aldrich (St. Louis, MO). Dichloromethane (DCM, ≥99.5%, Macron Fine Chemicals TM) was purchased from VWR. MISONIX QSonica Q700 Sonicator with microtip (MISONIX, NY) was used during the emulsion formation. Deionized (DI) water was obtained using a PURELAB Flex2 water purifier. Coumarin-6 (MW: 350.4 Da) and Rhodamine B (MW: 479.02 Da) were purchased from Acros Chemicals and Sigma Aldrich, respectively.

4.2.2 Modified Emulsion Evaporation Method

Our method modifies the ESE method to attempt to use similar hydrophobicity of pre-formed PLGA cores and dissolved shell polymer to form core and shell nanoparticles. The process can be seen in Figure 4.2.1, and is similar to methods used by Xiao et al.[70] and Lee et al.[108]. PLGA nanoparticles of known size and PDI are resuspended in PVA via sonication. The PLGA nanoparticles PDI should ideally be monodisperse for equal distribution of the shell phase around each core. The PLLA shell material is dissolved in the organic solvent (DCM) and these two phases are combined and sonicated. This sonication has a dual purpose: simultaneously reducing the PLLA droplet diameter and forcing the pre-formed PLGA cores into the droplets. This will ideally form a s/o/w emulsion. After allowing the organic solvent to evaporate, the particles are collected, washed, measured, lyophilized, and weighed. With the PLGA synthesis modeling as a basis, the same features were recorded for trend analysis, primary component analysis, and feature importance ranking using machine learning (Table 4.2.1). Some additional features, specific to the core and shell methods, were also recorded.

Additional features are necessary to capture how the PLLA/DCM droplets are forming around the cores. For the modeling, we will use the input features and the measured outputs to estimate the efficiency of core/shell nanoparticle formation. This efficiency is dependent on the original core sizes and the number of cores available in the system. As we have determined, the core diameter is a function of the specific energy used. This is also true for the PLLA/DCM droplet which we want to form a shell around the core. We hypothesize that a similar power law relationship should exist for the PLLA droplets, so that similar specific energies will result in similar average diameters. Therefore, we should expect that using a specific energy much greater than the specific energy used for the core will lower the core/shell formation efficiency. We test this hypothesis in a later section, but to account for the relationship, we record the core specific energy and the ratio between both specific energies.

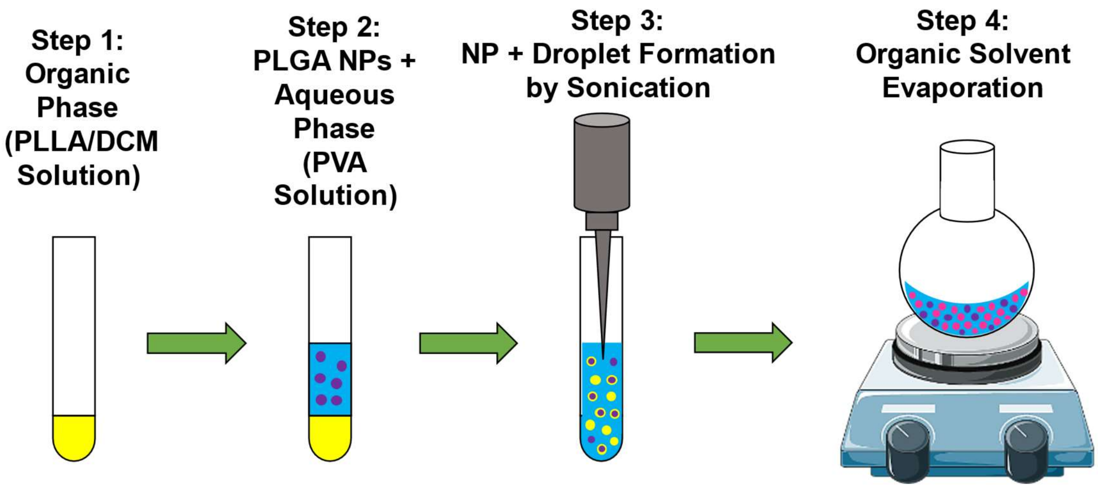

Figure 4.2.1: Modified Core/Shell Emulsion Evaporation Method

Table 4.2.1: Input Parameters, Variables, and Ranges for Core and Shell Formation Modeling and Optimization

Parameter	Variable	Range	Units
Core and Shell Specific Input Parameters			
Specific Energy – Core	E_v^{core}	20-650	J/mL
Average Core Diameter	Z_{PLGA}	160-380	nm
PLGA mass added	m_{PLGA}	0.55-5.5	mg
PLLA mass added	m_{PLLA}	0.6-33.0	mg
Multiple (mass PLLA/mass PLGA)	M	0.25-10.5	dimensionless
Specific Energy Ratio	E_R	0.08-3.8	dimensionless
Controllable Parameters			
PLLA concentration	C_{PLLA}	0.5-7.5	% w/v
Oil Phase (DCM) volume	V_E^{DCM}	0.026-2.0	mL
PVA concentration	C_{PVA}	1-6	% w/v
Aqueous phase (PVA) total volume	V_t^{PVA}	2.2-8.2	mL
Flask PVA Volume	V_f^{PVA}	1.00-4.00	mL
Emulsion PVA Volume	V_E^{PVA}	0.75-3.0	mL
Wash PVA Volume	V_W^{PVA}	0.0-1.6	mL
Sonication amplitude	-	20-85	%
Sonication time	-	13-360	s
Sonication Energy	E	25-2000	Joules

Calculated Parameters			
PLLA Moles	N^{PLLA}	0.6-37 x10^{-7}	Moles
Total PVA Moles	N_t^{PVA}	0.45-4.5 x10^{-6}	Moles
Flask PVA Moles	N_f^{PVA}	0.2-1.8 x10^{-6}	Moles
Emulsion PVA Moles	N_E^{PVA}	0.15-2.7 x10^{-6}	Moles
Wash PVA Moles	N_W^{PVA}	0.0-4.4 x10^{-7}	Moles
Total Emulsion Volume	V_t^{Emuls}	1.0-5.0	mL
Total PVA/PLLA molar ratio	R_N	4.0-333	Moles PVA/moles PLGA
Emulsion PVA/PLLA molar ratio	R_N^E	1.6-131	Moles PVA/moles PLGA
Specific Energy	E_v	19-600	J/mL

4.3 Formation Efficiency Modeling Methodology

The primary method we will analyze is emulsion-based due to the process similarity with the PLGA core synthesis. We hypothesize will allow us to translate the size and PDI control. We gathered 101 points for the emulsion-based method, with parameters and variables within the ranges defined in Table 4.2.1.

4.3.1 Particle Population Theory and General Equations

Ideally, upon mixing and sonication, both polymers' entire mass would produce core and shell nanoparticles of uniform core and shell dimensions (left side, Figure 4.3.1). When others have studied this method, a 100% formation efficiency has been assumed[69]. In our experience, based on these results, this is an inaccurate assumption. Inefficiencies with both the PLGA and PLLA distribution could occur. Not all the PLGA cores could gather shells, and not all PLLA could go on to form shells, instead forming solid cores all on their own. This creates a mix of three particle types: pure PLGA nanoparticles, pure PLLA nanoparticles, and core/shell nanoparticles (right side, Figure 4.3.1).

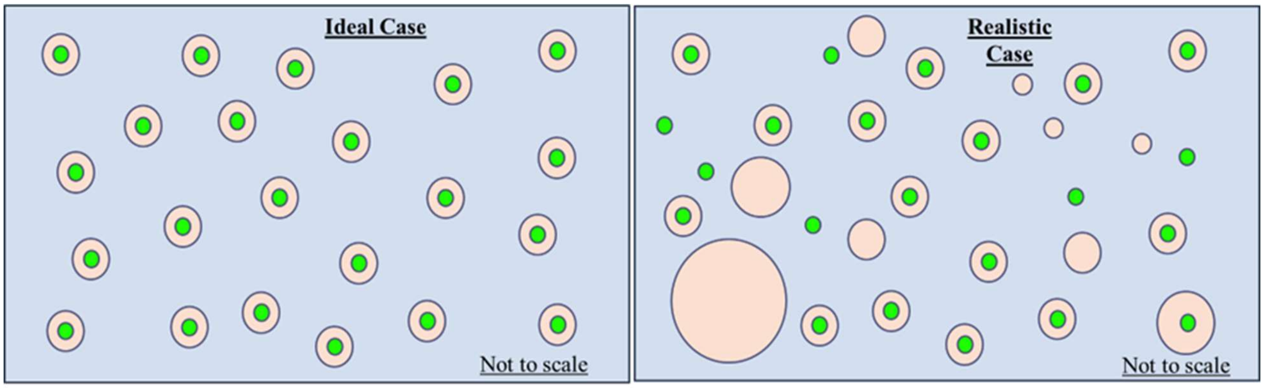

Figure 4.3.1: Ideal Core and Shell Formation vs Realistic Formation Case – Modified ESEM

Optimizing this system toward the ideal case requires defining the efficiency parameters and the methodology for estimating those parameters. We also want to ultimately control the core and shell dimensions by controlling a scalable synthesis parameter with high or ideal efficiency. A typical scalable parameter used in core/shell emulsion and nanoprecipitation methods is the ratio (molar or mass) between the shell polymers and the cores. We define this term as the multiple M, or the PLLA mass divided by the PLGA mass.

$$M = \frac{m_{PLLA}}{m_{PLGA}} \qquad (13)$$

Our goal is to solve for and maximize the efficiency, quantified by how many of the total particles remaining post-synthesis are our desired core/shell. Therefore, knowing the shell thickness and the number of core/shell nanoparticles would be beneficial. Unfortunately, we cannot solve directly for the shell thickness, nor can we measure the core/shell diameter. We also do not know how many of each type of particle is being made. However, we can measure the average diameter of the mixture of three particles post-synthesis using DLS, and we also know (or can reasonable estimate) the size and PDI of the pure PLGA and pure PLLA particles remaining. Thus we want to use the known information (mixture, pure PLGA, pure PLLA sizes and PDIs) to solve for how many particles of each type we are left with and the size and PDI of any core/shell particles being produced. The number fraction of core/shell particles to the total number of particles is the quantification of the core and shell formation efficiency. The general equation for this is a weighted average of the average diameters (Z_i) of each different population of nanoparticles: (1) pure PLGA nanoparticles (2) pure PLLA nanoparticles (3) Core/Shell (PLGA/PLLA) nanoparticles.

$$Z_{mix} = f_{PLGA}Z_{PLGA} + f_{PLLA}Z_{PLLA} + f_{C/S}Z_{C/S} \qquad (14)$$

Where f_{PLGA}, f_{PLLA}, and $f_{C/S}$ are the number fractions of each particle type, adding up to 1.

$$f_{PLGA} + f_{PLLA} + f_{C/S} = 1 \qquad (15)$$

We can assume the particle distribution is normally distributed around the Z-average mean reported by the DLS. This assumption is valid based on typical DLS results, showing single normal peaks for the data runs. We can then use a sum of a mixture of normally distributed random variables to relate this mixed diameter to the individual particle diameters. Since we are assuming a normal distribution for each particle population, we can also introduce the size distribution (PDI) as a separate equation dependent on the weighted average of the sum of the variances for each particle population. The variance can be found by using the relationship between PDI and average diameter to find the standard deviation (sigma), and then squaring the sigma.

$$\sigma_i = Z_i\sqrt{PDI} \qquad (16)$$

$$\sigma_{mix}^2 = f_{PLGA}\sigma_{PLGA}^2 + f_{PLLA}\sigma_{PLLA}^2 + f_{C/S}\sigma_{C/S}^2 \qquad (17)$$

General Equations Test with Particle Mixing

We tested the accuracy of these mixture equations with PLGA/PLLA nanoparticle mixture studies, using two populations of particles with known properties instead of three for simplicity.

PLGA particles of known size and PDI were mixed in known ratios with one of three samples of PLLA nanoparticles with known sizes and PDIs. The combined Z-average (Z_{mix}) was measured and compared to the model prediction. Figure 4.3.2 shows the model size predictions versus what was measured. There was good agreement for two samples, using PLLA NPs that were 216 nm and 201 nm and monodisperse (PDI < 0.08). When the larger PLLA NPs were used (PLLA 1, 268 nm, 0.076), there was a greater deviation from the predicted mixture diameter. This is explained by the variance, which is a function of the PDI and the average diameter. This group's (PLLA1) variance was the highest (5471), nearly double the variances of the other two (2654 and 3859). This affected the variance prediction as well, as seen in Figure 4.3.3. Therefore, using monodisperse particles and synthesis conditions (specific energy and molar ratios) that minimize each particle's PDI will decrease the variance and lead to better predictions especially at larger mean sizes.

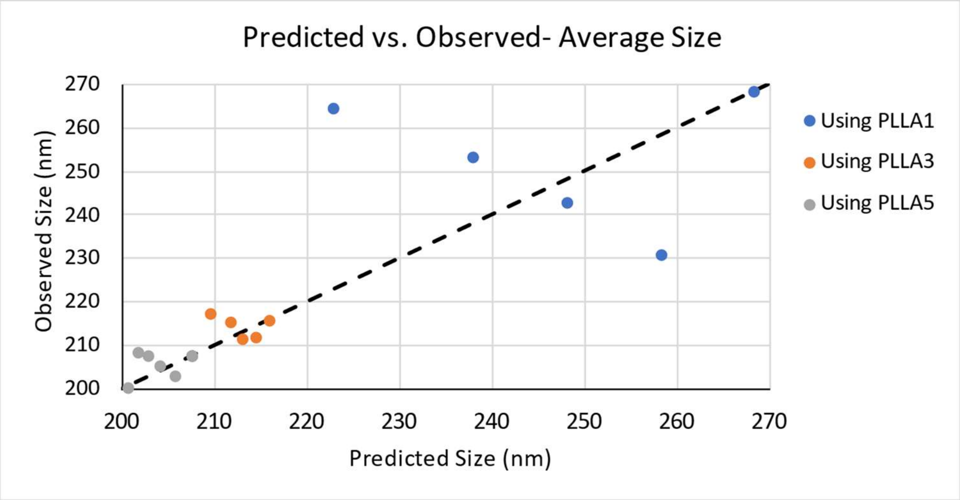

Figure 4.3.2: Predicted Diameter vs Observed Diameter for Mixture Study

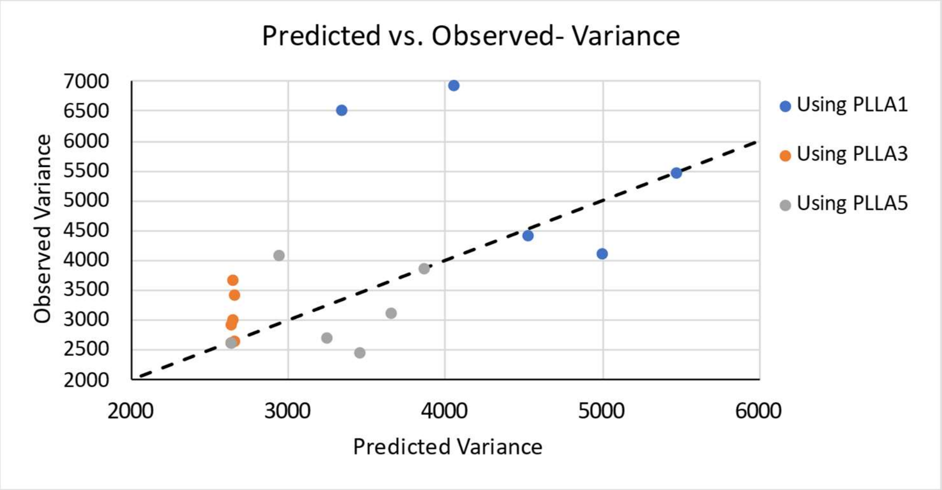

Figure 4.3.3: Predicted Variance vs. Observed Variance for Mixture Study

PLLA Nanoparticle Size and PDI Prediction

We know the sizes of the cores (Z_{PLGA}) from measuring them prior to core/shell formation, but we need to estimate the size and PDI of the pure PLLA nanoparticles (Z_{PLLA}). We performed a power law model fit on 36 runs of pure PLLA nanoparticles to estimate Z_{PLLA}, using the specific energy as the input as was done in Chapter 3 for the PLGA core synthesis. The best fit can be seen below, with R^2 and Adj. R^2 of 0.8904 and 0.8826, with RMSE of 7.0339.

$$Z_{PLLA} = 1724(E_v^{-0.8676}) + 173.7 \qquad (18)$$

With the specific energy known, we want also to estimate the pure PLLA nanoparticles PDI and use it to calculate the sigma and variance of the particle distribution. These parameters can be combined with the known mu's and variances of PLGA nanoparticle cores put into the system and compared to the final mixture mu and variance to estimate the core/shell diameter and number fractions of each type of particle (Eqns 14 and 17). To predict the PLLA variance, we fit a power law to the PDI as we did with the PLGA cores, with the best fit shown below.

$$PDI_{PLLA} = 551(E_v^{-2.431}) + 0.05902 \qquad (19)$$

The RMSE is 0.0352, which is reasonable. However, the R^2 and Adj. R^2 did not show a high GoF (0.1655,0.1059), likely due to the presence of dye affecting the PDI, the number of points run, and the spread of PDIs seen over the specific energies tested. Therefore, use of the PDI model will likely introduce some error for calculating the variance for the solution method.

Model Assumptions

Two assumptions were necessary to solve this system of equations for core/shell dimensions and efficiency:

1) The densities of both polymers are constant and can be estimated using known literature values.
2) The shell thickness around the core/shell nanoparticles distributes so that the size distribution is a normal distribution.

The densities must be known to estimate the masses and volumes of the nanoparticles and were estimated as the bulk polymer density. Calculating individual shell thicknesses for all possible scenarios would introduce more unknown variables. The shell thickness distribution should follow the observed normal size distribution curves of the PLGA nanoparticles and the mixture of nanoparticles when measured via DLS.

4.3.2 Core and Shell Mixture Solution Method

Distribution Curve Gaussian Mixture Model Method

The complexity of solving for the actual solution is high because, as a system, it is underdefined, with 4 independent unknowns and two general equations. For both general equations listed above (Equation 14 and 17), we must solve for at least two number fractions and the core/shell diameter and variance. There are many possible solutions for number fractions and diameters/variances which the weighted sum would give the same mixture diameter and variance. We want to solve for the size distribution curve (mu and sigma) of the most probable core/shell particle being formed for each data point (the black dashed line in Figure 4.3.4 as an example). In the figure below, the amplitudes of each peak are controlled by the weights given to each particle population, corresponding to the number fractions of each particle population, which we also need to solve for.

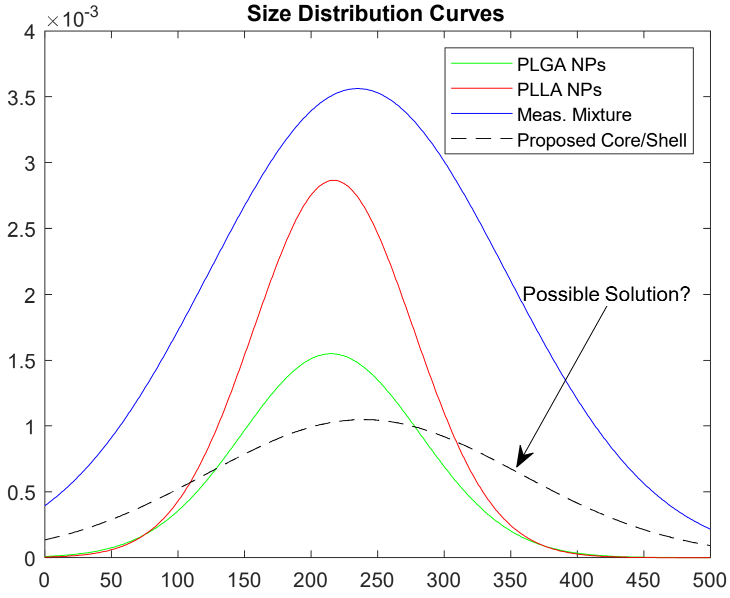

Figure 4.3.4: Mixture of Size Distribution Curves Showing Possible Core/Shell Solution for Mixture

To do this, we use a distribution fitting algorithm that will find the most probable solution called the Gaussian Mixture Model (GMM). GMM is often used in engineering and research to analyze highly complex clusters of data , such as patient charts[114], soil samples[115], and air particulates[116] , to reveal hidden subgroups. The general form for a GMM is below.

$$GMM\ PDF = \sum_{m=1}^{n} N f_m(x; \mu_m \sigma_m) \qquad (20)$$

Where the GMM probability density function is assumed to be a normal distribution (N) made up of a number (m) of other normal distributions defined by the weights (f_m), mean (μ_m), and covariance (σ_m). The size distribution data in this system is univariate, consisting of size distribution in one dimension and defined by the mu and the variance, which is calculated from the PDI equation (Eqn. 16). The algorithm uses the expanded form of the Gaussian density function to calculate the solutions[117]. The differentiated linearized form of this equation allows us to solve for the Maximum Likelihood Estimate or our most probable solution. In essence, the GMM determines how the probability that independent random observation falls into one of several distributions, leading to clusters of points centered around different means at different variances.[118] It then finds the most probable clustering by maximizing the total probability across all the points. We will use this method in a slightly different way, by generating three distribution curves from the individual particle dimensions and fractions (PLGA, PLLA, C/S) and comparing them to a regression GMM that is solely based on the mixture measurement. These represent solving both sides of Equations 14 and 17 twice, once using only the number fractions and individual particle dimensions and once using only the mixture measurements. The final solutions will be the convergence of these two solutions, if there is convergence.

Our first step is to use our known mixture measurements to generate an unbiased most probable solution. We start by generating 2000 random points that are normally distributed around the mixture mu and variance which we measured post-synthesis (Z_{mix} and σ_{mix}). We then specify a GMM to find three "subcurves" which when added together will give the initial mixture curve. This results in a solution of three most probable weights (number fractions, f_i) and mean sizes and variances, which we call GMMix. We hope that the means and variances of two of these curves correspond to the known values that pure PLGA and pure PLLA should have based on the specific energy used, but these are not inputs and so they may not.

We want to see if the three curves found by GMMix correspond to our other known values for pure PLGA and PLLA. If they converge, then this will allow us to know the most probable particle numbers as well as the core/shell dimensions. But since we only know the PLGA and PLLA dimensions, we need to generate all possible solutions for the core/shell dimensions, based on the constraint that the number fractions must sum to one and the weighted sums must be the mixture diameter and variance. Therefore, we use a new GMM to generate all possible core/shell diameters and variances for each data point based on these constraints, as can be seen in Figure 4.3.5. We do this via the brute force method: using the sum of weighted sizes and variances equations above we input the known PLGA and PLLA sizes and variances together with all combinations of f_i that add up to one (4873 combinations for hundredths precision) and solve for the required core/shell diameter at those fractions and core and PLLA dimensions. Some of these core/shell "solutions" are unrealistic; the solution to the general equations could solve for a negative core/shell diameter or one smaller than the smallest core size. We filter these solutions out to reduce iterations in later steps. Before filtering, however, these 4873 possible solutions make up a matrix we call GM1. We can reasonably assume that the actual solution to what is actually occurring in our system post-synthesis, is one of these 4873 solutions. To narrow down these to one, most probable solution, we compare each to the three curves that are generated by GMMix. The heights (weights), mu's, and variances of these three curves should closely match one of our possible solutions for us to feel confident in determining the actual solution. We quantify this by calculating the solution which gives the minimum sum of differences, which is calculated after sorting the GMMix solutions and the GM1 solutions each from smallest to largest, and subtracting each of the 9 total values (mu's, variance's, and fractions for three particle types) from each other. This gives us 9 differences, and we add these up and find which solution has the lowest overall difference, closest to zero. This gives the most likely solution. We will then use these predictions to compare input parameters and analyze whether we can optimize the system for maximum core/shell formation and predict the shell thickness.

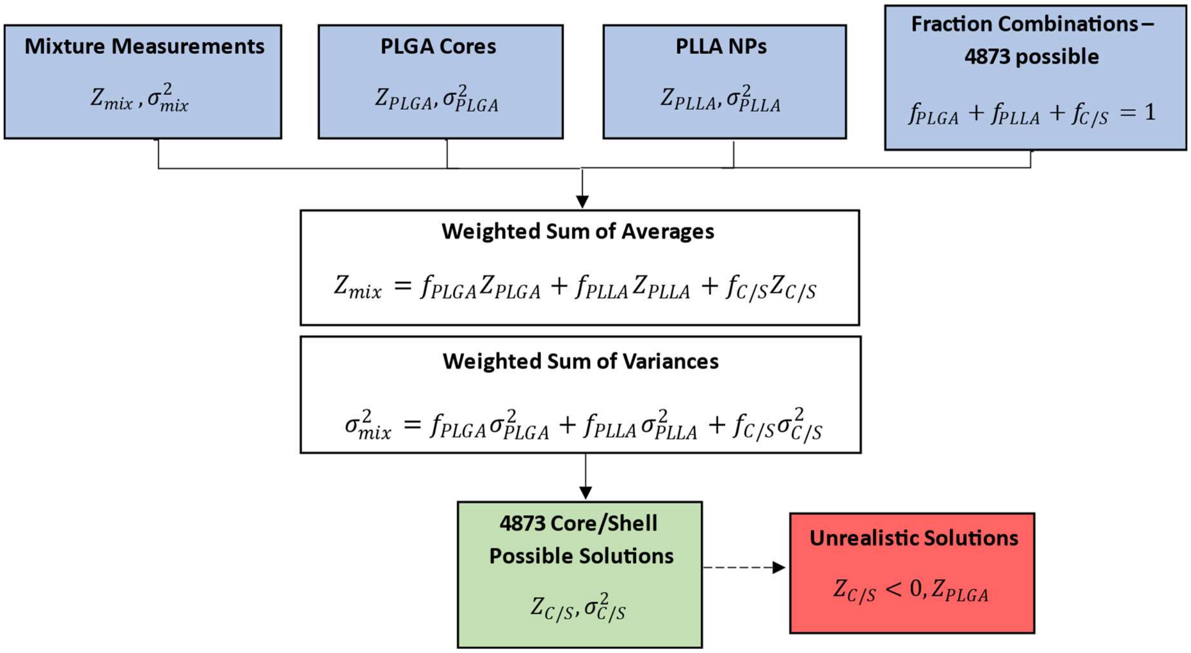

Figure 4.3.5: Brute Force Solution of All Possible Core/Shell Diameters and Variances

4.3.3 Fluorescent Dye Experiment Methodology

The predictions from the GMM method are decent estimations of the efficiencies and the resulting particle dimensions. It is important to remember that the estimations are just that; they are the most probable solutions based on the defined particles' size distribution means, variances, and synthesis inputs such as specific energy and polymer masses. Direct visualization of the polymer distribution would be highly beneficial in determining the true accuracy of the model predictions. A fluorescent dye tagging procedure was developed to attempt this visualization.

The technique uses two fluorescent dyes, Coumarin-6 (green) and Rhodamine B (red), to tag the individual polymers pre-synthesis. PLGA will be loaded with Coumarin 6, while Rhodamine B will be covalently conjugated to the PLLA chains using EDC/NHS chemistry. After using one of the core/shell methods with these tagged polymers, we will analyze the particle mixture under fluorescent microscopy. Core and shell nanoparticles will produce a yellow core surrounded by a red shell, while the pure PLGA and pure PLLA nanoparticles will just be green and red, respectively. A representation of this can be seen in Figure 4.3.6.

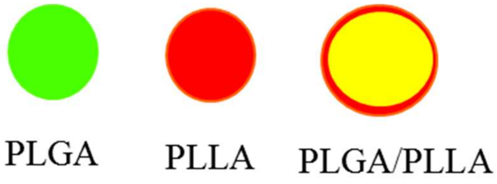

Figure 4.3.6: Fluorescent Dye Overlay – Core/Shell Polymer Distribution

Multiple images of the fluorescent nanoparticle slide will be taken to achieve a representative sample of the total particles. Then, these images are processed through a MATLAB image processing program, which finds and counts each particle. It measures the RGB values at the center of each found particle and sorts them into “green”, “red”, and “yellow” by RGB value boundaries. From these counts, each particle’s number fractions are calculated and saved for comparison to the model predictions. Any particles or false positives found that fall outside these category bounds will be discarded from the count.

There are limitations to this method. Firstly, the fluorescent microscope used for imaging has a magnification limit, restricting the practical resolution per pixel. The MATLAB imaging program can find particles of around 5 pixels in diameter at the minimum, corresponding to a diameter of around 380 nm. These particles are by design sub-300 nm, exceeding this resolution limit. The counting is therefore biased towards the more easily counted larger particles which exist due to the size distribution spread. There is a slight “corona” effect which makes particles appear larger due to the fluorescent light, which can make the smaller particles somewhat easier to count.

Additionally, the ability to find and count the particles is dependent on the image quality and the brightness of both dyes. Carboxylic acid groups are more limited on the PLLA polymer backbone than on PLGA so there will likely always be less Rhodamine B dye per polymer molecule and the PLGA/green will often out-fluoresce the PLLA/red. This bias can be somewhat corrected by lowering the exposure and light to the green filter during imaging, but some bias towards more of the green dye and the particles that contain green dye (pure PLGA and core/shell) will be difficult to avoid.

4.4 GMM Method Efficiency Predictions Trend Analysis

The GMM method successfully found the most probable solutions for 97 out of 101 total points using the emulsion-based method. The four missing points were unable to converge and resolve an answer. All four had very close predicted PLGA core and PLLA nanoparticle sizes, used very low volumes of PLLA/DCM (< 40 μL), and were dyed, which could have introduced too much error to solve. Likely, there could have been an error during the mixture measure, as the mixture diameters of all four were below that of the PLGA cores and PLLA nanoparticles, which is unrealistic. However, we have analyzed the solutions of the remaining points for optimizable parameters for efficiency and core/shell dimensions, if they exist.

Core and Shell Formation Efficiency

For the most probable solution, the solutions from the GMM method should match the known sizes of the PLGA cores, the predicted size of the PLLA nanoparticles from the power law, and mixture diameter should match if the solutions sizes and fractions are recombined. Below, in

Figure 4.4.1, we see excellent agreement between the experimental measurements and the GMM solutions, with correlation being >0.99 for both PLGA cores and pure PLLA particles, with two outliers.

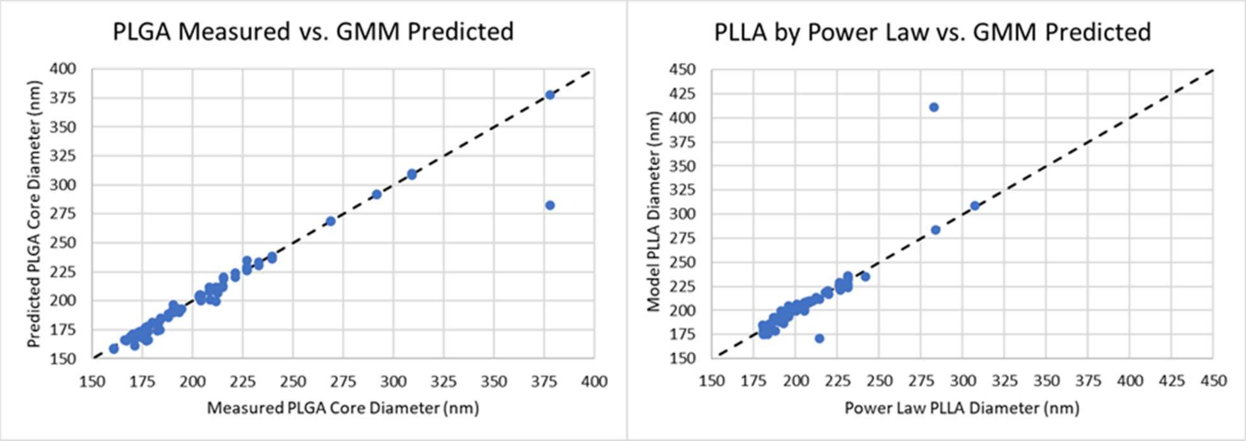

Figure 4.4.1: Measured/Power Law Predicted Diameter vs. GMM Solution Diameter for PLGA (left) and PLLA (right)

When we look at the GMM solutions for the mixture diameter vs the DLS measured mixture diameter (Figure 4.4.2), there is linear agreement, with slight underprediction of total mixture diameter at greater sizes. Still, the correlation is 0.902, sufficiently accurate to analyze the efficiency trends with respect to the various input parameters.

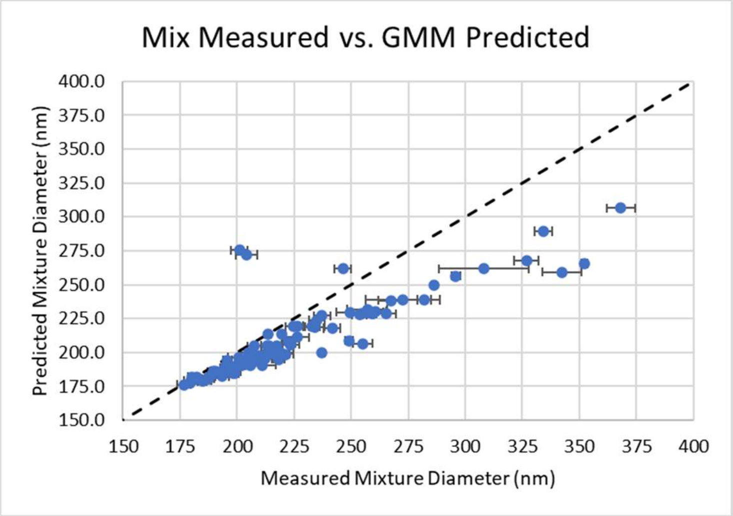

Figure 4.4.2: Measured Mixture Diameter vs. GMM Solution Prediction Diameter

The highest predicted core/shell efficiency found by the GMM method was 0.667, with an average of about 0.32 with a standard deviation of 0.10. This suggests that, in general, this process does not preferentially form core/shell nanoparticles within the tested parameter ranges over the other undesired populations, with our highest efficiency lying outside the standard deviation of all solutions.

Certain features did show tendency towards the higher efficiency range for core/shell formation, such as PLLA concentration and molar ratio. This matches literature, as others' emulsion-based methods have looked to take advantage of the immiscibility of PLGA and PLLA phases when both were dissolved in DCM at high concentration[70,108]. Therefore, we would expect the core/shell efficiency to increase as PLLA concentration increased, while the other two number fractions (efficiencies) decrease.

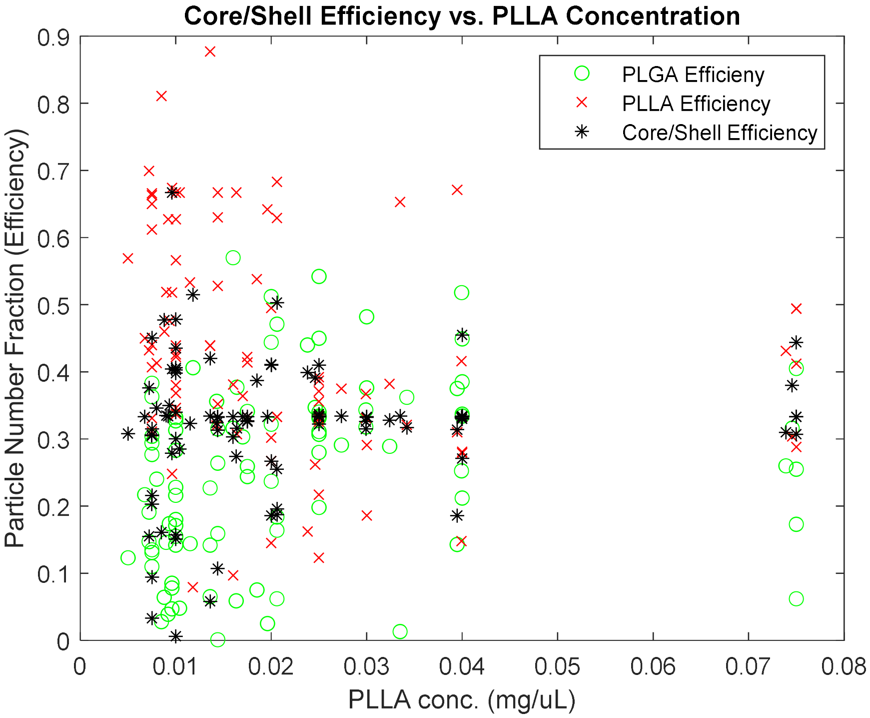

Figure 4.4.3: PLLA Concentration vs. Particle Efficiency from GMM

Figure 4.4.3 shows the relationship between the predicted particle efficiencies and the PLLA concentration. We do see slight trends corresponding to our hypothesized behavior. At low concentrations, there is large spread for all efficiencies, with a higher prevalence for the formation of pure PLLA particles over core/shell nanoparticles. The PLLA efficiencies reach as high as 90% for concentrations less than 0.02 and remain high (>60%) until 0.04 mg/μL. At the higher tested concentration (0.075), PLLA efficiency decreases to an average of 0.40, while core/shell efficiency increases to an average of about 0.40. This is a modest increase for core/shell efficiency; however, the smaller spread and overall higher average efficiency leads us to conclude that higher PLLA concentration had a slight positive effect on core/shell efficiency. PLGA efficiency also significantly decreases at this higher concentration, further suggesting that higher PLLA concentrations increase the likelihood of core/shell formation around PLGA cores. Future tests that test even higher PLLA concentrations would be beneficial to observe any continued efficiency change.

Similar to what was seen for PLGA core synthesis modeling, the PVA to PLLA molar ratio (total PVA moles and emulsion PVA moles) had an effect on the nanoparticle formation efficiencies. However, the general trend was a little surprising. Figure 4.4.4 shows the number fractions/efficiencies of each particle population versus the total molar ratio. The emulsion molar ratio shows the same trend.

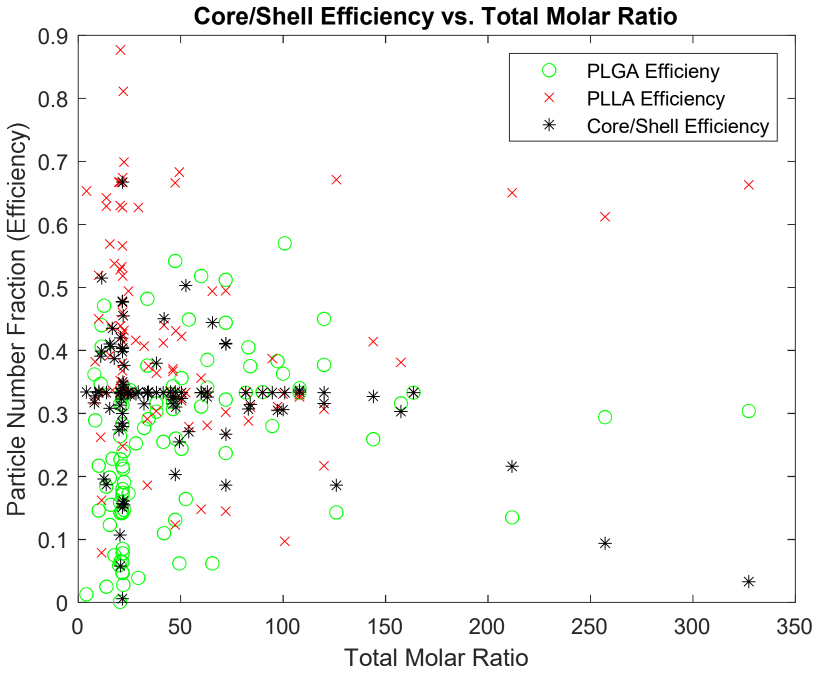

Figure 4.4.4: Total Molar Ratio vs. Particle Efficiency from GMM

At low total molar ratios (total moles PVA to moles PLLA in the process), we see a wide distribution of efficiencies for all particle types, with a decrease in PLGA and core/shell efficiency has molar ratio increases. PLLA efficiency remains consistently high (>60%). This suggests that higher PVA molecules per droplet of dissolved polymer (PLLA in this case) decrease the preference of the system to form core/shell nanoparticles. In contrast, for PLGA core synthesis higher PVA moles per mole of dissolved PLGA increased droplet stability and improved size control and monodispersity up to a certain range. For the core/shell emulsion method, an aqueous phase containing less PVA molecules seems to facilitate the formation of PLLA oil droplets around the PLGA cores. This makes sense, because as the PVA moles increase, the aqueous phase viscosity is higher and thus requires more energy to force the PLLA droplets past the dissolved PVA molecules. Additionally, more PVA molecules then can adsorb onto the surface of the PLGA cores, masking the cores and preventing core/shell formation. This masking hypothesis is supported because more efficient core/shell formation is seen closer to the

"Ouzo effect" regime that contains no surfactant for nanoprecipitation methods[112,119]. For emulsion methods some surfactant is necessary to stabilize the PLLA droplets, and so this will inherently decrease the efficiency of the method. As a result, the molar ratio trends suggests that the nanoprecipitation method will result in inherently higher efficiency, especially if turned to the "Ouzo effect" regime.

The final parameters we will discuss for core/shell formation efficiency are the specific energy and the specific energy ratio and their effects on the formation efficiencies. The plots for both can be seen in Figure 4.4.5.

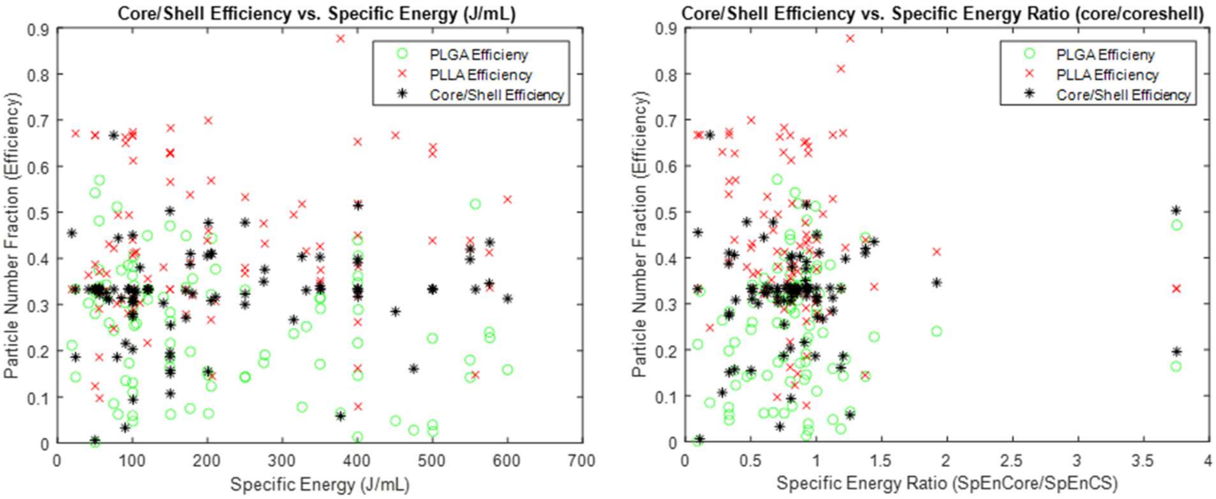

Figure 4.4.5: Particle Efficiencies vs. Specific Energy (left) and Specific Energy Ratio (right)

We would expect that as specific energy increased so would core/shell efficiency since the PLLA droplet would be decreasing in size as more energy is added to force the droplets. Ideally, this energy would also force more droplets around the PLGA cores. Instead, we only see a slight increase core/shell efficiency with a specific energy increase, with more variation seen below 200 J/mL. This trend was also seen for the PLGA synthesis size modeling, where the size and PDI variation greatly decrease past a specific energy of about 230 J/mL. It is unknown if this specific energy marks a thermodynamic threshold, above which the emulsion stabilizes, and this is unreported elsewhere in literature. Due to the power law relationship between size and specific energy for both PLGA and PLLA, we would also expect that as the specific energy used for the core/shell formation approaches the specific energy used to produce the core that the core/shell efficiency would increase. This hypothesis is based on the change in droplet size reducing so to only allow for a single core per droplet. This would be until the specific energy then exceeds the required amount to reduce PLLA droplet size below the PLGA core size, which would then reduce efficiency and promote pure PLLA nanoparticle formation. However, we do not observe this trend, as the efficiencies are generally spread for all specific energy ratios. It could be that the presence of surfactant and the PLLA concentration dominates the core/shell efficiency, as those trends were more easily seen. Since the maximum estimated core/shell efficiency was lower than expected (0.667) and no specific conditions (other than general trends) were discovered to optimize the efficiency, this unfortunately suggest that the emulsion-based method modeled here may be insufficiently efficient for the reliable production of polymeric PLGA/PLLA core/shell nanoparticles.

Shell Thickness Control

Despite the low efficiency, we would like to analyze whether shell thickness could be controlled at higher efficiencies. Using the scalable Multiple parameter previously defined, we can solve for the ratio of shell thickness to core radius to provide a relationship between the mass ratio and scalable shell formation on a adjustable core diameter.

$$M = \frac{m_{PLLA}}{m_{PLGA}} = \frac{\rho_{PLLA} V_{PLLA}^{shell}}{\rho_{PLGA} V^{core}} = \left(\frac{\rho_{PLLA}}{\rho_{PLGA}}\right) \frac{V^{C/S} - V^{core}}{V^{core}} = \rho_R \left(\frac{V^{C/S}}{V^{core}} - 1\right) \quad (21)$$

Solving the basic definition of Multiple, assuming ideal core/shell formation, allows to find the below non-linear expression. Of the three roots for the expression solution, one is real. The real root of the expression can be plotted against the density-scaled multiple to have the ideal relationship between shell-to-core ratio and multiple. The multiple here is divided by the ratio of the polymer densities (shell/core polymer), allowing us to customize the solutions in the future if different densities or polymers are used.

$$\frac{M}{3\rho_R} = \frac{1}{3}\left(\frac{X}{R_{core}}\right)^3 + \left(\frac{X}{R_{core}}\right)^2 + \left(\frac{X}{R_{core}}\right) \quad (22)$$

Each run was sorted into different bins for analysis. The bin names and ranges can be seen below in Table 4.4.1.

Table 4.4.1: Efficiency Bin Names and Corresponding Bins for Shell Control

Efficiency Ranges	**f_CS Values**
Low Efficiency	0 – 0.14
Mid-Low Efficiency	0.14 – 0.28
Mid-Hi Efficiency	0.28 – 0.42
High Efficiency	>= 0.42

Figure 4.4.6 shows the distribution of core/shell efficiency versus the density-scaled multiple. The lower efficiency runs (<0.28) expectantly formed much smaller shells per core radii than the ideal case (dashed line). The runs which had the higher efficiencies (>0.28) showed more runs closer to forming ideal shell thicknesses per core radii. Note: this does not mean that run is somehow ideal, since a small fraction of particles can form core/shell nanoparticles with ideal shell thickness per core radius. Therefore, without maximizing the efficiency, we cannot hope to have full control over the shell thickness. This is independent of control over the core dimensions, which we demonstrated in Chapter 3.

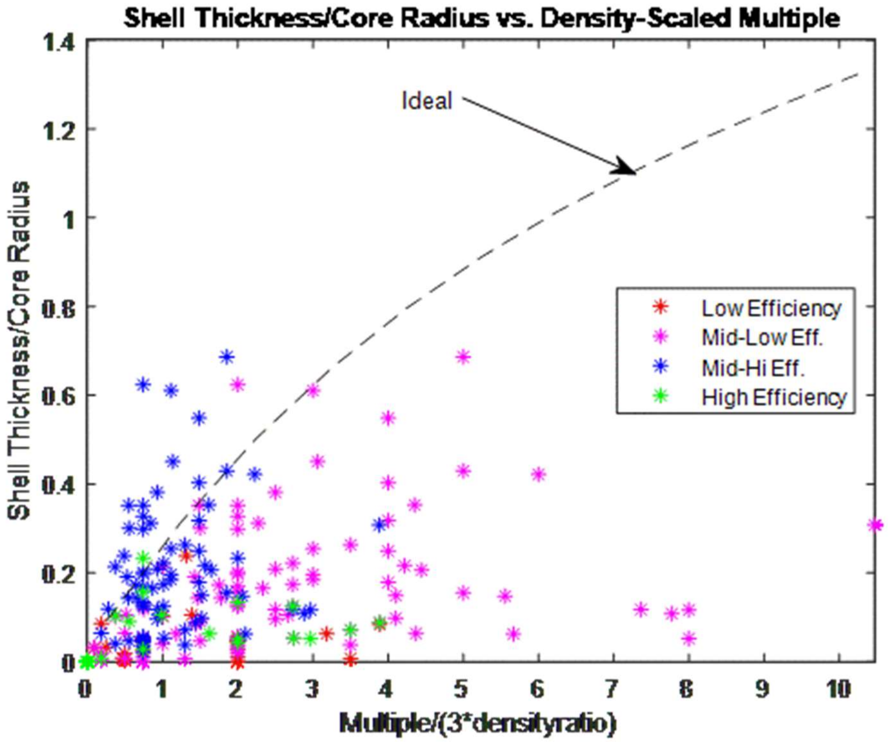

Figure 4.4.6: Multiple vs. Shell Thickness/Core Radius

4.5 Fluorescent Dye Tagging Results & Discussion

Direct visualization of polymer distribution was successfully performed on 10 emulsion-based core/shell runs. For each run, 15-25 images were used for counting. Table 4.5.1 shows the comparison of the GMM predicted particle number fractions versus the number fractions of the counted particles from the images.

Table 4.5.1: Fluorescent Image Tagging Experiment, Predicted – Measured via Counting

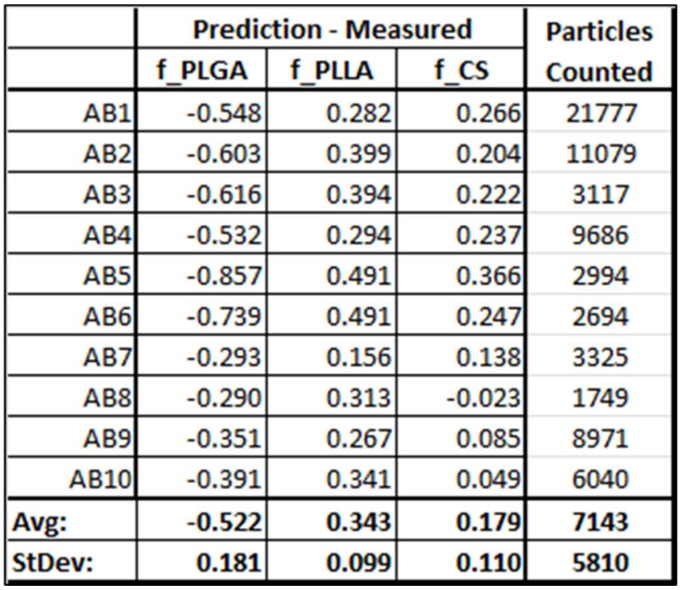

	Prediction - Measured			**Particles Counted**
	f_PLGA	**f_PLLA**	**f_CS**	
AB1	-0.548	0.282	0.266	21777
AB2	-0.603	0.399	0.204	11079
AB3	-0.616	0.394	0.222	3117
AB4	-0.532	0.294	0.237	9686
AB5	-0.857	0.491	0.366	2994
AB6	-0.739	0.491	0.247	2694
AB7	-0.293	0.156	0.138	3325
AB8	-0.290	0.313	-0.023	1749
AB9	-0.351	0.267	0.085	8971
AB10	-0.391	0.341	0.049	6040
Avg:	**-0.522**	**0.343**	**0.179**	**7143**
StDev:	**0.181**	**0.099**	**0.110**	**5810**

For the set of ten runs, the GMM model was more accurate in predicting the number fractions of the core/shell particles ($f_{C/S}$) of the counted particle populations and a poor predictor of the other two. The model tended to overpredict the core/shell NP efficiency by an average of about 0.179 ± 0.11, which is relatively close for the most important efficiency. The model severely underpredicted the fraction of PLGA nanoparticles, while overpredicting the PLLA nanoparticles. This could be due to the green bias discussed in the method section for this experiment. The limited presence of red dye compared to the high presence of green dye would biased the counting towards the pure PLGA particles and away from the pure PLLA particles. This in turn would result in an underestimating of the number of pure PLGA and overestimating of the pure PLLA, which is what we observe.

Looking at an example of one of the fluorescent images below in Figure 4.5.1, we can see just how prevalent and bright the PLGA nanoparticles are (green) along with the core/shell particles (yellow/red). The sizes are also difficult to accurately estimate due to the “corona” effect visible around many of the brighter particles.

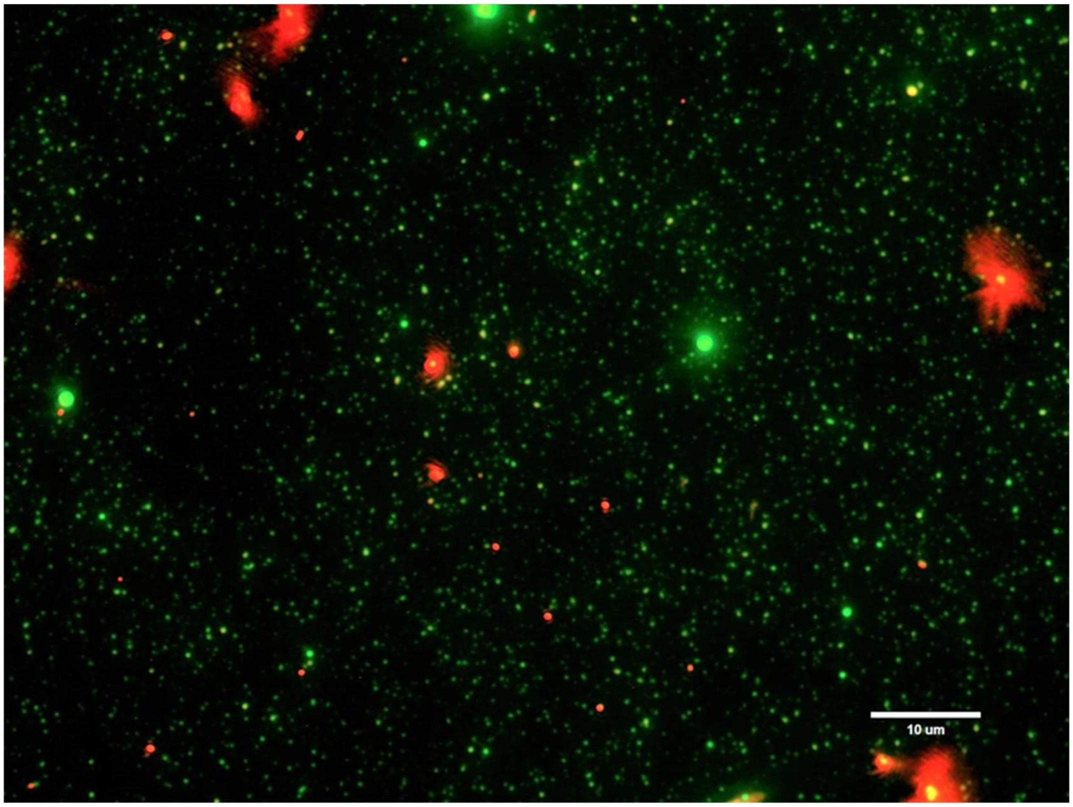

Figure 4.5.1: Example Fluorescent Image of Particle Distribution

When zooming into a cluster of particles in the middle of the example image (Figure 4.5.2), we can attempt to estimate the sizes of each type of particle and compare them to the prediction from the GMM method. The large core/shell particle in the middle has an estimated diameter of 1.62 μm, much larger than the GMM predictions. The reddish PLLA particle to the right of the core/shell is roughly 700 nm, while the small, faint green particles immediately surrounding the core/shell particle have an estimated diameter of 300-400 nm. From the GMM, the average diameters of the PLGA particles should be 220 ± 100 nm, which is in line with measurements. The average diameter of pure PLLA particles via GMM should be 205 ± 54 nm, much smaller than what is seen in this image. The smaller particles are approaching the resolution limitation of the optical microscope. We are unable to ascertain whether these measured diameters are truly measuring the particle diameter or just the radius of the fluorescent corona. Additionally, the dye brightness for particles any smaller than around 300 nm would be difficult to observe. DLS measurements and previous SEM images confirm the presence of nanoparticles of agreeing size ranges. It is to be concluded, then, that the fluorescent imaging technique developed here is unable to confirm or validate the GMM predications, nor can it generate predictions on its own. The resolution limitation, dye brightness bias, and image quality limit the qualitative data that can be gathered. However, we can visually confirm each of the hypothesized three particle populations, rejecting the assumptions of previous researchers that this type of method produces solely core/shell nanoparticles[69].

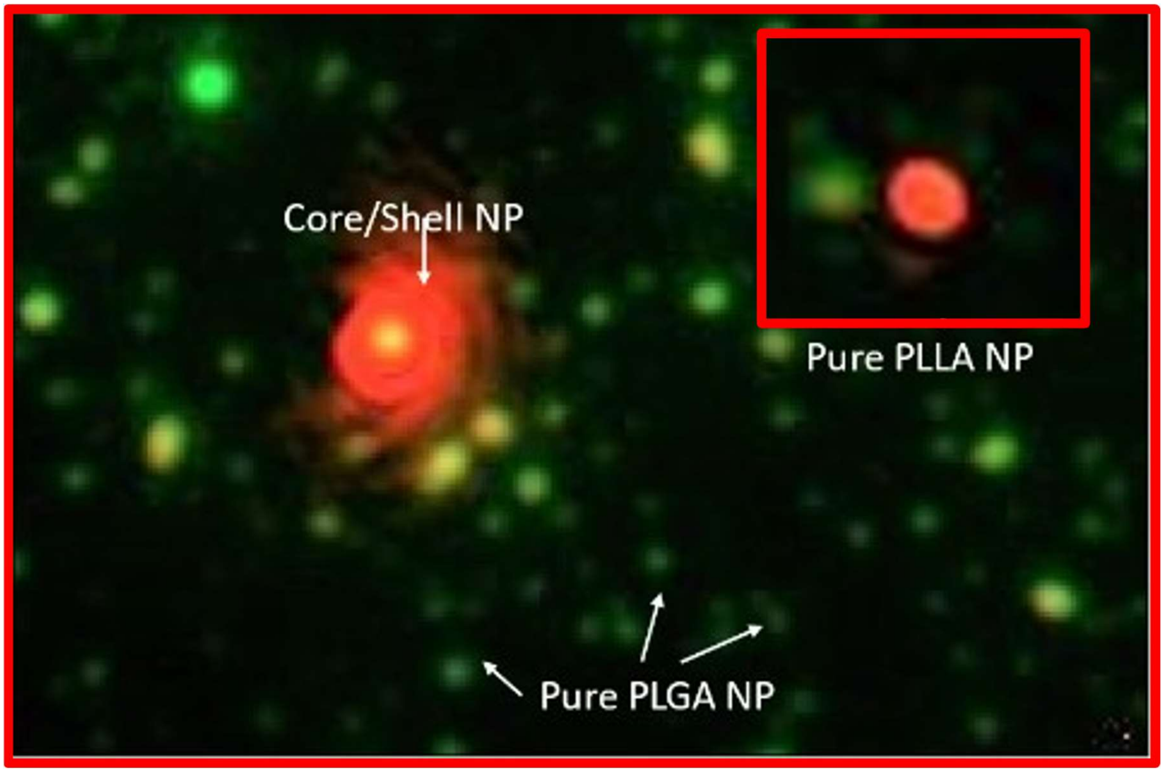

Figure 4.5.2: Optical Zoom of Core/Shell Nanoparticle Populations

4.6 Core and Shell Release Experiments

Based on the GMM prediction trend analysis and fluorescent imaging, we can speculate that the emulsion-based method for producing core and shell PLGA/PLLA nanoparticles is not as efficient in the ranges tested as we would desire for ideal controlled release of small, hydrophobic payloads such as chemotherapeutics. Despite the low efficiency, we will look to characterize the release from several core/shell nanoparticles to compare the release kinetics with bare nanoparticles and with the estimate shell thicknesses and shell-to-core ratios. In the following runs, we measured the total mass and percent release of hydrophobic coumarin-6 which was only loaded within the PLGA cores prior to the emulsion-based method. The PLLA was not dyed, and we calculated the release with the same general protocol as before. The PLGA cores contained a mean mass of 0.0049 mg C6 per 1 mg PLGA (0.49% loading capacity, with a loading efficiency of 98%).

Each release profile was fit to the release kinetic models as before. Table 4.6.1 shows a fit table for one such core/shell release profile. The models with the best GoF, expectantly due to the majority presence of PLLA, were the diffusion driven models (Korsmeyer-Peppas and Peppas-Sahlin). The exponent fit interpretation suggests non-Fickian transport, where chain relaxation and diffusion are roughly equal contributors. The erosion driven model (Hopfenberg) was a poor fit, indicating that the release was dominated by the PLLA and not the bare PLGA cores, especially in the first 60% of release. This is supported by the fact that the KP and PS models are only valid for the first 60% of release and fit the profiles extremely well over that time (for plots, see Appendix 3). Immediately after, the release profile shifted to a long and sustained release, with a total release time longer than pure PLLA of similar sizes. The release cannot be solely driven by either the PLGA because it is too long and diffusion driven. Nor can it be driven by only the pure PLLA, since no dye was loaded into these particles and the release kinetics do not match earlier characterization. This transition period from diffusion driven to a sustained release which is a poor fit to the diffusion model marks the transition from the PLLA shells release to that of the PLGA cores which had been previously coated. Prior to this point, the release is shared by both the PLLA shells and uncoated PLGA cores, and so is a mixture of diffusion and erosion driven, dependent on the number fractions of each type of particle.

Table 4.6.1: Release Kinetic Fit of Core/Shell Nanoparticles – P24

CoreShell-3 - P24 - 99.5 nm	**Cumulative Release Kinetic Model Fit Results:**					
Model	**Constants**			**R2**	**Adj R2**	**RMSE**
Korsmeyer-Peppas(n,k):	0.5398	0.0286		0.9958	0.9957	0.0115
Peppas-Sahlin(k1,k2,m):	0.0287	7.72E-10	0.5391	0.9958	0.9957	0.0115
Higuchi(n,k):	0.5	0.0254		0.725	0.725	0.1485
Hopfenberg(k0):	2.40E-22			0.4439	0.4354	0.2096
Weibull(a,b,T):	0.0194	6.81E-01	0	0.9958	0.9958	0.0184

The release profiles' change with respect to the estimated shell thickness and ratio also supports the formation of core/shell nanoparticles near the expected efficiencies and dimensions. Table 4.6.2 shows the samples and their dimensions estimated via GMM, while Figure 4.6.1 shows the release profiles relative to each other. There is a clear correlation between the expected shell thicknesses (and ratios) and the controlled release. The PLGA cores were all roughly the same size with PDIs ranging from 0.11 to 0.18, likely due to the presence of dye.

Table 4.6.2: Core and Shell Estimated Efficiency and Dimensions for Release

Sample	**Core Diameter (nm)**	**f_CS**	**Shell Thickness (nm)**	**X/Rcore**
P24	176.7	0.406	4.7	0.0535
P13	188.1	0.399	5.8	0.0624
P16	184	0.317	10	0.1080
P17	182.9	0.335	19.55	0.2163
P18	183.7	0.334	26.95	0.3078

P20	187.7	0.333	33.3	0.3529

The inset in Figure 4.6.1 shows a close up of the initial 60% release whether the diffusion driven models showed excellent fit. The stratification of release profile in the same general order as shell thickness is evident, and the duplicates showed excellent agreement. All runs were roughly equal core/shell efficiency (about 0.3-0.4), facilitating an easier comparison between the samples. The Korsmeyer-Peppas kinetic rate constant (k) decreased linearly with increasing shell-to-core ratio with a slope of about -0.102, while the exponent linearly increased with increasing shell-to-core ratio at a rate of 0.6253. This trend is encouraging, as it shows the potential of a higher efficiency process to achieve controlled sustained release of many days to weeks. From the analysis of the emulsion-based method, a different method such as a nanoprecipitation-based method will likely be required to achieve this higher efficiency for better controlled release of small hydrophobic payloads.

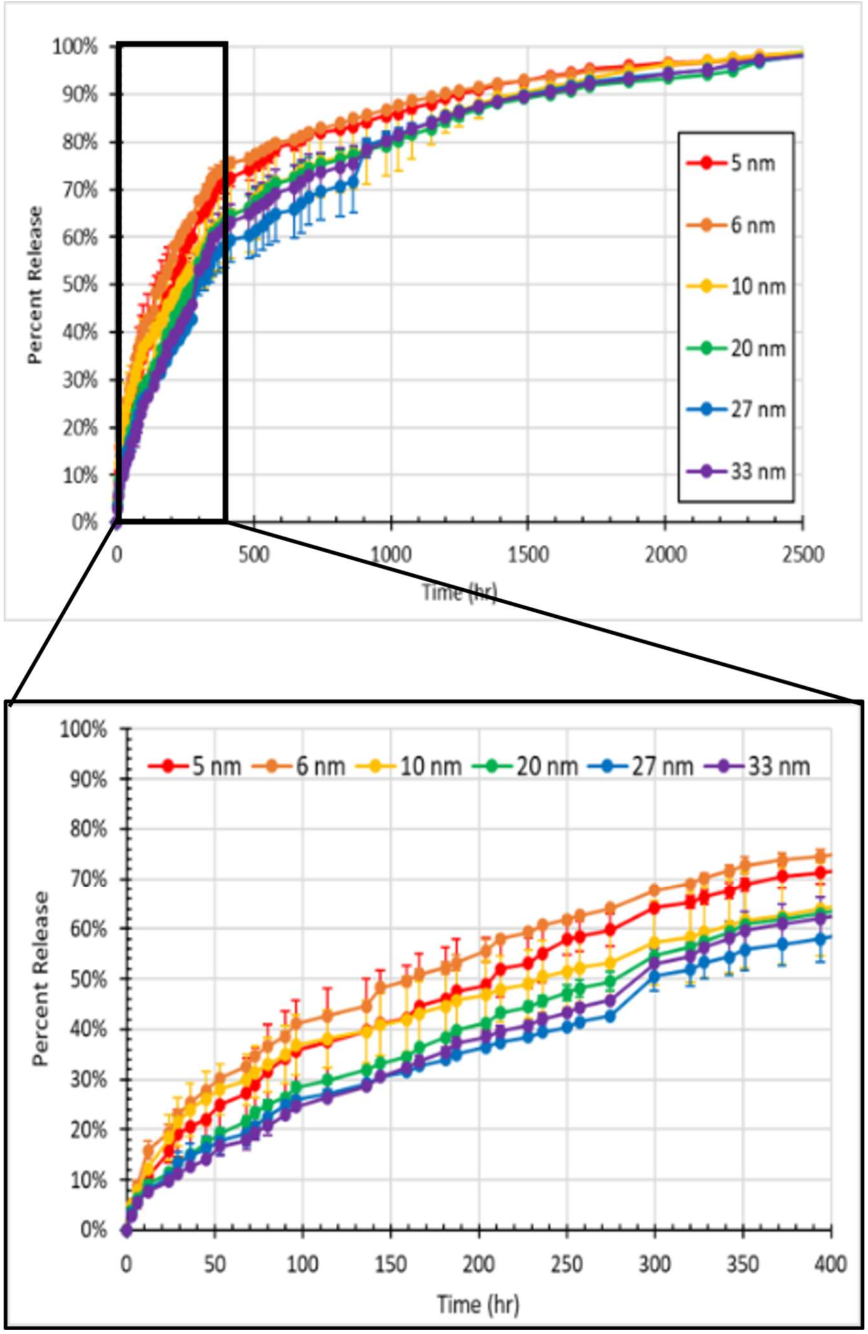

Figure 4.6.1: Core and Shell Nanoparticle Release Profiles, with increasing estimated Shell Thickness

4.7 Conclusion

Core and shell polymeric nanoparticles can offer more versatile controlled release than single polymeric cores for small, hydrophobic payloads. Altering the core and shell materials and dimensions allows improved control over release kinetics without sacrificing for larger, less optimum sizes or use of unapproved triggering molecules. Many different methods have been investigated for reliably producing this core and shell structure including emulsion-based methods and nanoprecipitation microfluidic methods. Each has its advantages and disadvantages. However, we sought to use our understanding and control over the emulsion method gained from PLGA core synthesis to optimize the formation of core and shell nanoparticles. Contrary to other's work on similar methods, we did not assume 100% efficiency of the method, instead we sought to understand how different synthesis parameters could potentially be used to control the efficiency. The goal of this chapter's work was to achieve high efficiency core/shell formation and independent control over the shell dimensions around the core.

Using a statistical modeling method called the Gaussian Mixture Model (GMM) as well as general mixture equations based on normal distributions, we estimated the most probable efficiencies of the three hypothesized particle types formed with this method. We were able to determine a few parameters which changed the predicted efficiency in different ways. The PLLA phase concentration was hypothesized to increase efficiency at higher concentrations, but it was unknown what concentration would be most beneficial. We tested concentrations up to 7.5% (w/v) and found that the efficiency did increase and become more consistently high. This is likely due to the reported immiscibility between PLGA and PLLA at higher polymer concentrations. In contrast, the total and emulsion molar ratios both showed lower efficiencies at higher PVA molar ratios. It is theorized in literature that this is due to a shielding effect that PVA could be having around the PLGA cores, preventing shell formations. Finally, we had predicted that the ratios of specific energies used to form both the cores and core/shells would have a great effect on the overall efficiency. We proposed there would be an optimum range less than 1 which would provide the highest efficiency, but the data did not show this trend. Instead, efficiency had some correlation to just the core/shell specific energy, and no correlation for the specific energy ratio. It is likely that other parameters such as the molar ratios are overcoming any specific energy effect. Overall, despite these trends, we were unable to achieve our goal of high efficiency core/shell formation within the tested parameter ranges, with the single highest predicted efficiency of 67%, with an average of only 32%. We compared these predictions with visually counted images of fluorescently tagged nanoparticles. Although we were able to confirm the three particle types being formed, the predictions and the counting did not match for all efficiencies.

We also measured the release of six core/shell particles which had similar sized cores, similar efficiencies, and increasing shell thickness. Encouragingly, even at unideal conditions, we saw varied release kinetics corresponding to the increasing shell thickness, as predicted for the core/shell design. Additionally, we saw evidence of the regions within the release time which were dominated by the shell release and then the core release due to the kinetic model fits and rate comparisons to pure polymer releases. This is encouraging, as it provides proof that these types of systems offer the highly versatile and sustained controlled release they promise. More work to increase efficiency is needed to fully unlock this promise. Potentially, an emulsion-based method could be used with nanoprecipitation. This could combine the advantages of both systems and offer better customizability of the core and shell than what currently exists. We believe the work presented in this chapter offers some guidance and knowledge to combine such a process.

Chapter 5: Alternate Applications: Polymeric Nanoparticle-Impregnated Chitosan Hydrogel for Multiple Regime Release

5.1 Introduction and Motivation

Controlled release from circulating polymeric nanoparticle formulations is a unique challenge, and such delivery systems can address a variety of disease states and conditions. However, some medical applications require different release performances, which are inappropriate for nanoparticles alone. Complex wounds are one such application. Depending on the healing progression, wounds can be categorized as acute or chronic. Chronic wounds typically stall within one healing stage and are treated differently than acute wounds. Acute wounds include traumatic and complex wounds from accidents, combat, or surgery and readily progress through the four stages of healing: hemostasis, inflammation, proliferation, and remodeling[120]. Recent global combat has led to a rise in acute, traumatic, and complex injuries. While modern equipment and medical treatment have improved the survivability of these wounds, casualties remain a concern[121,122]. Most combat casualties are caused by improvised explosive devices (IEDs) or gunshot wounds affecting various body parts with different severity levels and coverage requirements.[123] Regardless of severity, treatment must address four complications that roughly correspond to the stages of healing, occurring at different times: hemorrhage, infection, pain management, and tissue regeneration[120,124]. Typical wound dressings address the hemorrhage and may protect against infection with proper and immediate application. An ideal wound dressing would address all four complications: being sterile, biocompatible, oxygen-permeable, and retaining a moist environment to encourage angiogenesis, epidermal migration, and tissue regeneration[125]. Currently, no commercial or military wound dressings are hemostatic, antimicrobial, pain relieving, and promote healing[126]. We hypothesize that a single system addressing all complications can significantly improve wound treatment. It can do this with simultaneous, controlled delivery of standard administered drugs to give continuous and successive treatment for all stages of wound healing. This work investigates different formulations of a common wound dressing polymer, chitosan. We tested different drying and crosslinking effects on the swelling and release kinetics so that they can be tuned for different pain and antimicrobial/antifungal drugs. We also introduced PLGA nanoparticles into the chitosan hydrogel formulations, which offer a more sustained release of pain management, infection prophylaxis, and tissue growth factors. These are initial investigations, with dyes used as model payloads in place of the drugs but demonstrate the proof-of-concept for this combined, multimodal controlled release system. An example of this type of release timing regime they would address is seen in Figure 5.1.1.

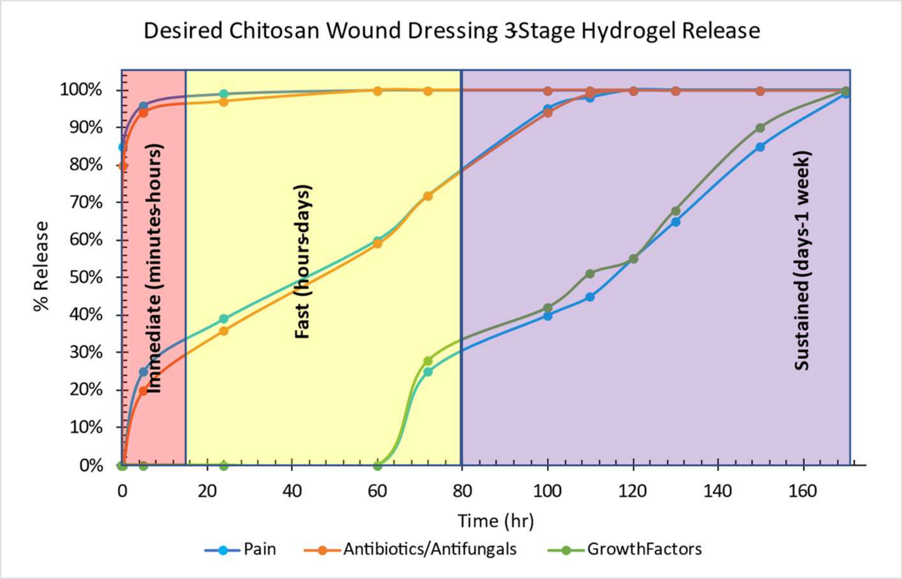

Figure 5.1.1: Proposed Multimodal Release Regime for Chitosan Hydrogel Wound Dressing

5.2 Chitosan Hydrogel Material and Methods

Chitosan (99% deacetylation, Low MW: 120 kDA) was purchased from Sigma Aldrich (St. Louis, MO) while High Molecular Weight (MW: 200 kDA) was purchased from Acros Organics

(Morris Plains, NJ). Acetic acid (glacial) was purchased from Macron Fine Chemicals (Allentown, PA). Glutaraldehyde (25% concentration) was purchased from Sigma Aldrich (St. Louis, MO). Tween80 was purchased from Amresco (Dallas, TX). A Labconco FreeZone 4.5 was used for all lyophilization, with access provided by Dr. Ed Davis and Dr. Virginia Davis, Auburn University.

5.2.1 Formation and Crosslinking

Chitosan was dissolved in 2% (v/v) acetic acid under vigorous stirring at 50°C until homogenous. Small drops of 0.1% Tween80 were added to prevent clumps. If large clumps persisted, the solution was filtered before crosslinking. Glutaraldehyde (GTA, 1%) was added to the stirring mixture at a desired volume to give a mass ratio of GTA:Chit. The recorded crosslink density is the mass ratio times 1000. Glutaraldehyde acts as a chemical crosslinker, reacting with the primary amine on the chitosan backbones to covalently bond two polymer backbones (see Figure 5.2.1). The glutaraldehyde and chitosan were allowed to react for 15 minutes before pouring into molds that contained 0.1 M NaOH to neutralize the solution. If necessary, more dilute NaOH was added to the mold to complete the neutralization. The crosslinking reaction causes a noticeable color change, from yellowish white for uncrosslinked to dark orangish-brown as the crosslink density increases. This color change is the formation of chitosan-Schiff-bases (CSBs) from aldehydes' reactions to the chitosan backbones' primary amines. CSBs have many positive effects on chitosan systems' properties used for biomedical applications. CSB-forming crosslinking has been shown to increase the mechanical strength of chitosan hydrogels[127] and introduces self-healing mechanisms when hydrated.[128,129] While chitosan has shown to be inherently hemostatic due to its charged functional groups, the addition of CSBs has shown to add antibacterial and antifungal activity[128,129], with Omer et al.[130] showing that CSB formation inhibited E. coli (Gram-negative) and Staphylococcus aureus (Gram-positive) growth. They also demonstrated that CSBs encourage anti-diabetic enzymatic activity and inhibited cancer proliferation in limited tests, and they showed effective encapsulation of different cells and drugs to promote tissue regeneration[130,131]. However, developing bacterial resistance to CSBs has been observed.[132] Therefore, the proposed addition of controlled multi-release of other antibiotics and antifungals is likely necessary as more bacterial and fungal strains develop resistance.

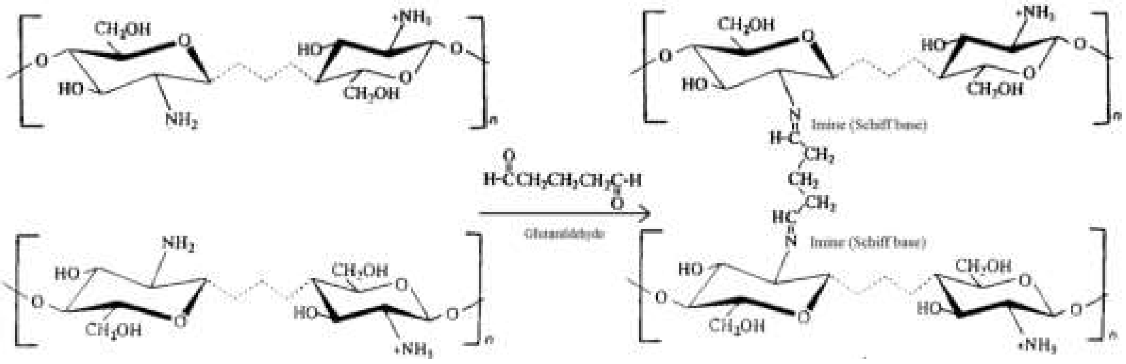

Figure 5.2.1: Glutaraldehyde Chitosan Crosslinking Mechanism with Schiff Base Formation[131]

5.2.2 Drying Method

Once poured into the molds and neutralized, we used two drying methods to produce different dried hydrogel formulations. For the air-drying method, the molds are placed in the fume hood, and the acidic fluid is allowed to evaporate over at least two days before being neutralized. The samples can be placed in a 40-50°C oven to accelerate the drying without negative effects. This method forms thin plastic-like sheets. The uncrosslinked samples are more transparent, flexible, and a slight brownish yellow, but as the crosslink density increases the color darkens and becomes semi-opaque due to CSB formation. The samples become more rigid as well. For the freeze-drying method, after pouring into the molds the samples are immediately placed in the -80°C cryofreezer and left overnight to ensure complete freezing. The frozen samples are then placed in a lyophilizer under vacuum and left to dry fully for at least 24-48 hours.

5.3 Endpoint and Kinetic Swelling Behavior

Multiple release regimes will require fine control of release kinetics; these are controlled by the hydrogel swelling characteristics which are controlled by the polymer chain network structure and crosslinking. The general method for quantifying the swelling is the percent change in mass.

$$\%\,Change\ Mass = \frac{Wet\ Mass - Dry\ Mass}{Dry\ Mass} * 100\% \qquad (23)$$

It is also desirable for hydrated wound dressings to expand into the wound site to increase contact and pressure on the wound for hemorrhage control, protection, and hydration. This quality will be quantified by the percent change in surface area (in the x-y direction) and the percent change in volume, which measures the vertical change. Endpoint and kinetic swelling characterization are typical tests to quantify swelling. Endpoint swelling measures the max swelling and is measured by placing the hydrogel or dressing samples in a plastic Petri dish and hydrating with 25 mL of DI water for 30+ minutes. The samples are then taken out and weighed and measured. Kinetic swelling measures the rate of change in mass over time; the samples' masses are measured at set time points to understand how quickly swelling occurs. It is often difficult to accurately measure surface area and volume during kinetic studies, so only the percent change in mass is recorded in this work.

5.3.1 Commercial Wound Dressing Swelling

Before analyzing how chitosan molecular weight, drying method, or crosslinking density affects swelling and release, it is necessary to compare typical swelling characteristics of commercially available gauze products. These materials were provided by a collaborator, David Crumbley (MSN, RN, CWCN), as products commonly used in hospitals. Mepilex is a silicone foam absorbent dressing with variations that have an adhesive border ("Brder") or silver nanoparticles for antibacterial effects ("Ag"). The base Mepilex has the highest swelling of the three variations, peaking at a +1200% change in mass. Melgisorb, an alginate-cellulose absorbent dressing, had the most significant swelling of all products tested, surprisingly exceeding the Xtrasorb polymer-silicone foam swelling behavior. Only QuikClot Gauze, a cloth gauze impregnated with a hemostatic inorganic mineral, showed any other significant swelling. DuoDerm showed no real change, while MediHoney degraded over time. The main takeaway is that while most commercial products tested showed decent swelling (>300% change in mass), only Xtrasorb showed any significant dimension change, nearly tripling its height. Again, this type of swelling helps hemorrhage control and improves contact, so not seeing this for most products was surprising.

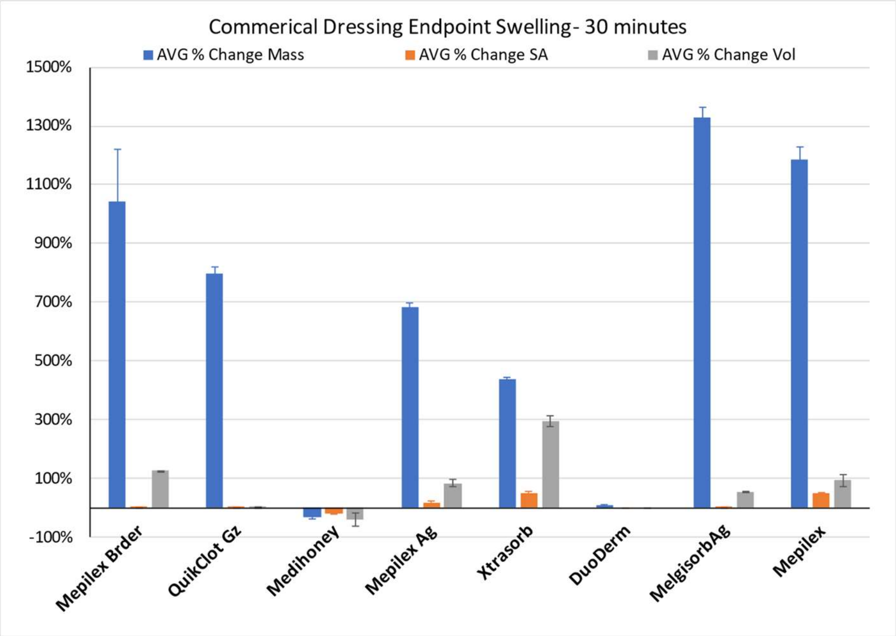

Figure 5.3.1: Endpoint Swelling Behavior of Commercial Wound Dressings

5.3.2 Endpoint Swelling Chitosan Hydrogel Formulations

For simplicity, we use a three-letter code to designate formulations for all following experiments and plots. Low molecular weight (120 kDa) will begin with an "L" and high molecular weight

(200 kDa) will begin with an “H”. Next, if the sample is uncrosslinked, there will be a “U” or a “C” for crosslinked. Finally, the drying method will be the last letter, with “F” for freeze-dried and “A” for air-dried. For the crosslink density studies, the number following the code is the crosslink density, which is the mass ratio of glutaraldehyde to chitosan times 1000. The mass change was measured using a scale, with the dry mass recorded before hydration. After the hydration duration, the samples were transferred to a dry tray and lightly shaken to remove no absorbed water, before being weighed in another dry tray. The change in surface area was measured by hand with a ruler, measuring the change in the x and y direction (horizontal, parallel to the benchtop). The thickness (height, z-direction) was also measured to change in volume.

The first endpoint swelling experiment results for the air-dried formulations in Figure 5.3.2 compare the difference between molecular weights and uncrosslinked vs. crosslinked. Increasing molecular weight for uncrosslinked air-dried samples significantly decreased the swelling, especially the mass change. Between the crosslinked samples, molecular weight had little effect, except that the lower molecular weight had a more significant vertical change, in the z-direction measured by the thickness change. This height change is likely due to the longer polymer chain length and greater entanglement for the higher molecular weight chitosan. This leads to reduced free movement upon hydration and thus less swelling. Similarly, this is why crosslinked samples had less swelling than uncrosslinked samples, with the crosslinker limiting polymer chain relaxation and movement.

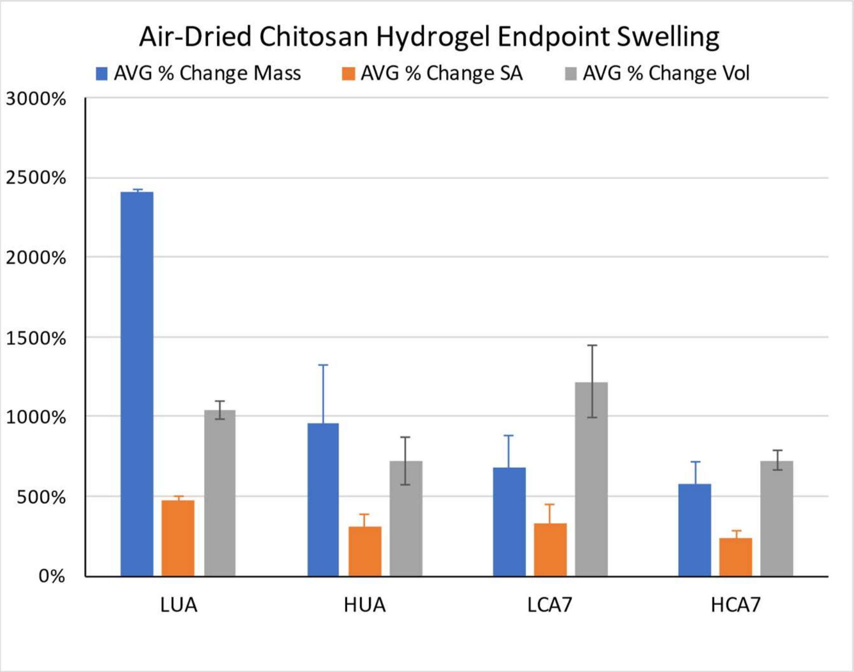

Figure 5.3.2: Effect of MW and Crosslinked on Air-Dried CSHG Swelling

Interestingly, the maximum swelling seen for the air-dried samples exceeded the commercial products' swelling capability over a similar time. When comparing the air-dried samples to the freeze-dried formulations (Figure 5.3.3), the freeze-dried samples all showed an order of magnitude greater mass change for swelling, with the low and high molecular weight uncrosslinked freeze-dried samples showed nearly +12500% increase each. There was a slight decrease in percent mass change for the crosslinked freeze-dried formulations and a more considerable drop for the change in surface area and volume after crosslinking for both air and freeze-dried. This again demonstrates that the crosslinked chains create a matrix that can encapsulate a large amount of water but sufficiently limit the physical size from changing significantly compared to the uncrosslinked formulations. This suggests that the crosslinked formulations are more desirable for the proposed multilayer scheme because it introduces mechanical stability and improves swelling over commercial products, while also introducing CSBs to introduce additional antibacterial and antifungal properties to the wound dressing. However, there is less vertical change with the crosslinked samples tested here, and ideally, the crosslink density could be optimized to allow some vertical swelling for wound pressure.

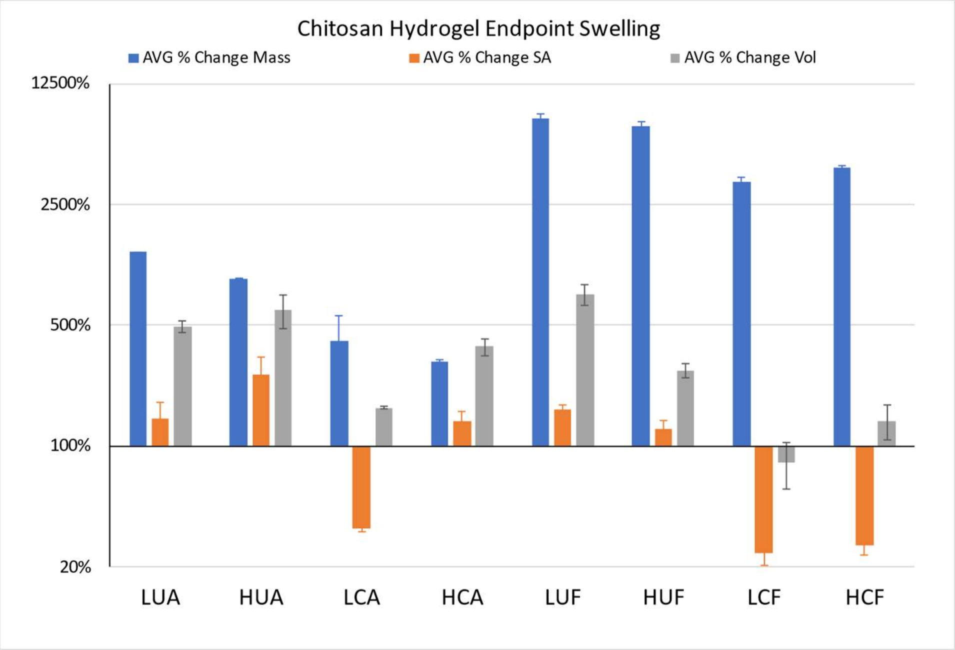

Figure 5.3.3: Effect of Drying, MW, Crosslinking on CSHG Swelling Behavior (note: log y-axis)

5.3.3 Kinetic Swelling

The endpoint swelling tests showed that freeze drying significantly increases the max swelling of the CSHG, but understanding the kinetics of that swelling will allow better control over the release dependent on the swelling. We first looked at the kinetic swelling of the air-dried samples, comparing the uncrosslinked and the crosslinked formulations (Figure 5.3.4).

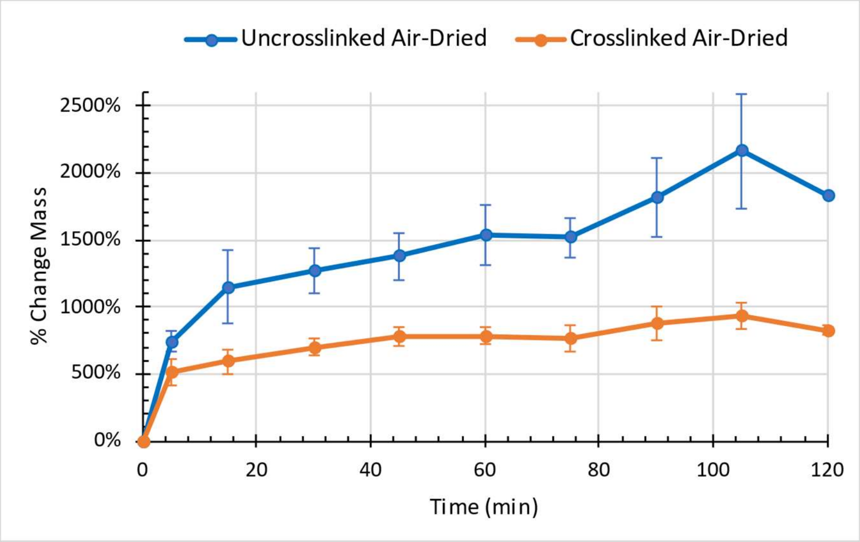

Figure 5.3.4: Kinetic Swelling Behavior of Uncrosslinked vs. Crosslinked Air-Dried CSHG

Crosslinking significantly reduced the time until the air-dried hydrogel reached an equilibrium swelling state, remaining stable after about 45 minutes. The uncrosslinked samples had higher maximum swelling but continued to increase for the two hours tested, varying much more than the crosslinked. This is likely due to the increasing instability of the polymer matrix in the uncrosslinked hydrogels. As the polymer chains move apart, any heterogeneity or degradation will destabilize the bulk structure and cause variations in the total mass. Similar behavior was seen with OU et al.[133], where the uncrosslinked chitosan hydrogels did not reach equilibrium during the test hour. Introducing crosslinking caused the hydrogels to stabilize within an hour and increasing the crosslink density (1.50 to 0.75 in their definition) decreased the total swelling. Interestingly, the total swelling they saw for their samples (50-100%) was much less than for our samples (500-1500%). This could be due to some unreported differences in processing or preparing the hydrogel samples, but the exact reasons is unclear. What is evident is that the swelling kinetics of the crosslinked air-dried samples match what is desired for the immediate release regimes proposed for the multilayer hydrogel system. The majority of release occurs as the swelling rate changes due to increasing diffusion gradient change and opening of the pore network. The uncrosslinked air-dried samples should then show a burst release within the first 5 minutes of hydration, ideal for rapidly delivering pain management and antimicrobials upon wound dressing application.

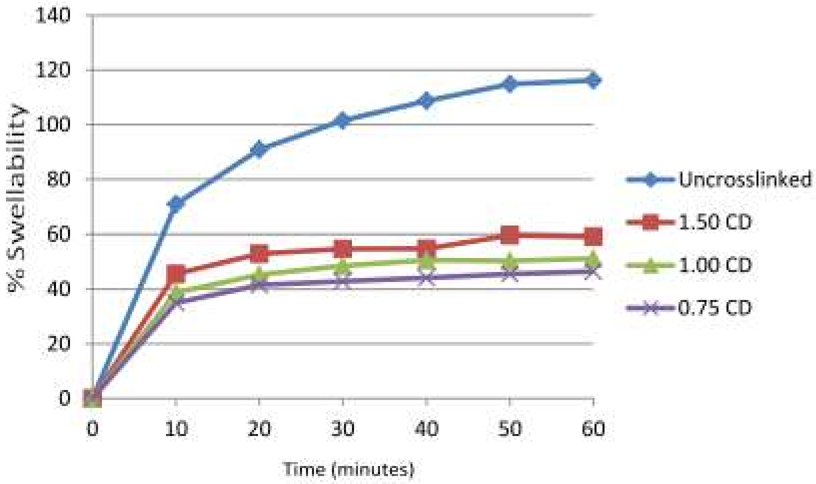

Figure 5.3.5: Kinetic Swelling Behavior of Uncrosslinked vs. Crosslinked Air-Dried CSHG from OU et al.[133]

Literature and other experiments showed that different crosslink densities for the air-dried samples did not significantly affect the swelling kinetics. Future experiments may be needed to optimize for mechanical strength vs. flexibility, but this is outside this work.

Figure 5.3.6 shows the kinetic swelling characteristics for low molecular weight freeze-dried formulations, increasing crosslink density from uncrosslinked to 14.

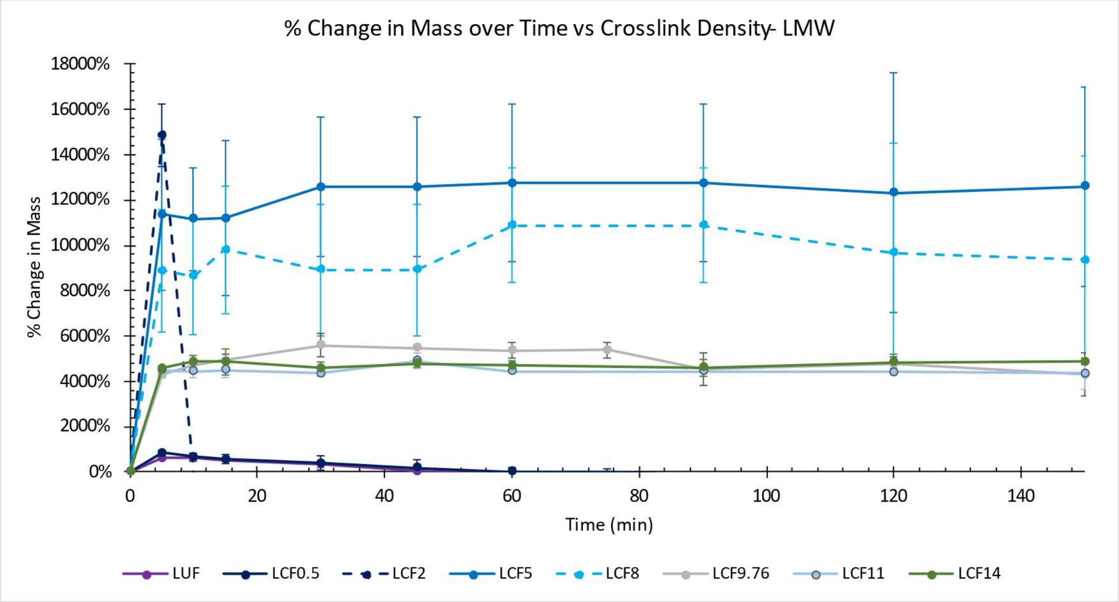

Figure 5.3.6: Percent Mass Change for Low MW CSHG vs. Crosslink Density

Crosslink density demonstrated a significant effect and trend of the kinetic swelling behavior for LxF samples. The uncrosslinked and 0.5 crosslinked density swelled to about 1500% before rapidly degrading at nearly the same rate. After increasing the crosslink density to 2, the kinetic swelling increased by nearly 16000%, the highest for any sample so far. Despite the high swelling, the crosslinking did not improve mechanical stability. In 15 minutes, the sample had broken apart and could not be measured. From CD 5 on, however, the kinetic swelling reached stable equilibrium, with the maximum swelling decreasing as CD increased. CD 11 and 14 showed nearly identical kinetic swelling behavior, likely due to a crosslinking concentration limit.

A similar trend was seen for the high molecular weight freeze-dried formulations, seen in Figure 5.3.7. The uncrosslinked sample again quickly degraded over an hour, but the HCF0.5 did not degrade as quickly, instead swelling to a nearly 30000% increase in mass, the highest seen for any experiment. It is clear from these two tests that a very low crosslink density maximizes the swelling capability of freeze-dried samples but is not enough for mechanical stability, as these formulations degrade within 15 minutes.

Increasing the CD to 1.4 improved the stability while slightly decreasing the swelling, but further increasing it to 2 resulted in worse mechanical stability and swelling. This shift may represent some critical transition region, where crosslink density is sufficient to increase swelling but not extensive throughout the polymer chain network to prevent degradation. Both experiments suggest the minimum CD needed for a stable freeze-dried hydrogel would be close to 5. For crosslink densities five and greater, swelling reached equilibrium and was dependent again on the CD, as was seen for the low molecular weight.

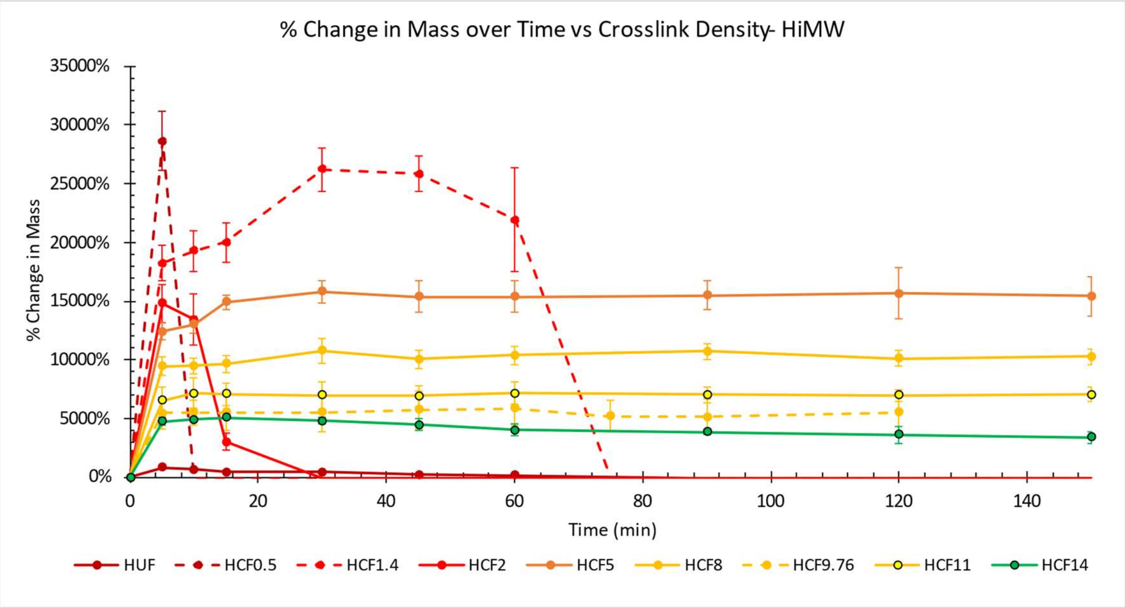

Figure 5.3.7: Percent Mass Change for High MW CSHG vs. Crosslink Density

To better see the crosslink density-dependent trends and the comparison between the molecular weights, we plotted the maximum % swelling versus the CS in Figure 5.3.8. There was no difference seen for the uncrosslinked samples. The polymer chain length would not affect the swelling and polymer movement with no crosslinker. At low CDs, some freedom of movement for the polymer chains results in maximum swelling, with greater swelling occurring for the longer polymer chains due to larger gaps between bound crosslinkers. These formulations are not stable when hydrated for more than 15 minutes. From CD 2 to 5, swelling is constant and similar for both MWs, possibly demarcating the stable CD transition range. At CDs greater than 5, both MWs showed a similar linear decrease for swelling characteristics until CD of 9, where crosslink saturation looks to have been reached for both MWs. This suggests that the most effective CD range for changing release while maintaining stability would be CDs greater than 5 and less than 11, since little change is seen at greater CDs than 11.

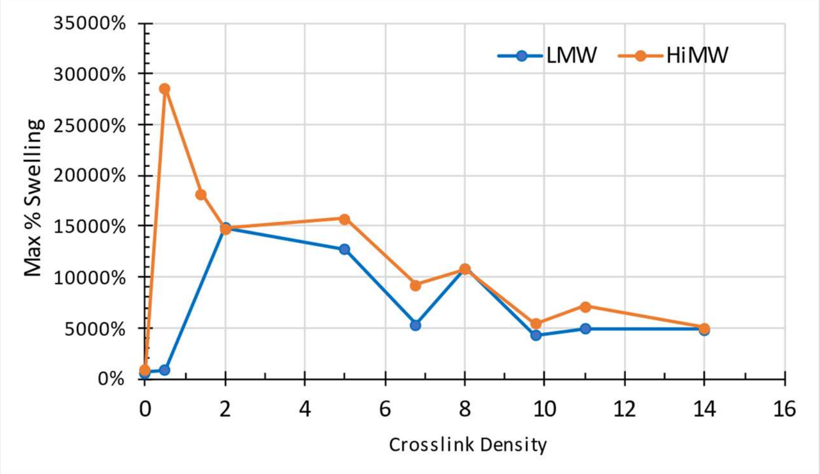

Figure 5.3.8: Max Percent Mass Change, MW vs. Crosslink Density

5.4 Release Studies

In the proposed multilayer chitosan hydrogel scheme, the different layers themselves will handle the release of the free drug loaded within. Swelling characteristics contribute to both the hydrogel's mechanical stability as well as the release kinetics. Free fluorescent dye (carboxyfluorescein, CF) was used as a model for these drugs to measure the release kinetics more easily. The effect of MW, drying method, and crosslinking density could then be evaluated and compared to the trends seen for the swelling so that formulations appropriate to achieve the desired loading, release, and mechanical stability could be determined.

5.4.1 Free Dye Release

CF Dye was loaded into the hydrogel formulations via swelling. CF was dissolved in ethanol at 5 mg/mL concentration, and 25 mL of this dye solution was placed in a clean dish. Each sample was placed in the ethanol dye solution and left to swell for 5 minutes before being removed and placed in a 40°C oven for 2 days to fully re-dry the samples. The dried samples surfaces were lightly wiped with a wipe dampened with small volume of ethanol to remove any unabsorbed dye on the surface. For the release studies, each dried sample was weighed and measured, then placed in 25 mL of 1X PBS (pH 7.45) in a plate stirrer-incubator kept at 37°C. PBS was chosen to maintain neutral pH to prevent the degradation seen for the swelling experiments previously. At each time point, 1 mL of bulk fluid PBS was removed and replaced with fresh 1X PBS. Three samples of 100 μL were then measured via UV-Vis Spectrophotometer and quantified by a pre-measured standard to determine concentration and mass.

Table 5.4.1: Loading and Release of Free Dye for CSHG Formulations

Sample	**mg Dye loaded/cm^2**	**mg Dye release/cm^2**	**Dye released/loaded**
LCA	1.49	0.028	0.017
HUA	0.40	0.043	0.157
HCA	0.92	0.024	0.025
LUF	6.03	1.14	0.188
LCF	9.32	0.88	0.094
HUF	9.07	4.85	0.523
HCF	8.18	0.96	0.117

The expected burst release from air-dried samples can be seen in Figure 5.4.1, which matches the kinetic swelling seen for both formulations in Figure 5.3.4. There was no visible difference between different molecular weights or crosslinking. The brief expansion seen is likely due to the compressed and tangled structure of the thin hydrogel. The polymer chains tangle during the evaporation process, leading to miniscule gaps within the dried thin hydrogel. Upon exposure to fluid, the polymer chain movement is limited due to this tangling. This is true even for uncrosslinked formulations. Crosslinking only limits the potential translational distance. This explains the higher endpoint and kinetic swelling for uncrosslinked versus crosslinked, as well as the limited loading of free dye compared to the freeze-dried samples. Table 5.4.1 shows that the air-dried samples had significantly lower loaded dye mass and released only about a small fraction of that mass, with the remaining dye being trapped inside. The freeze-dried samples had orders of magnitude higher mass loaded and released. A higher fraction of the loaded was also released, with the maximum seen was around 50%. The low loading efficiency and dye retention of the air-dried samples are not ideal for eventual drug loading and release. For example, if similar loading and release was achieved for lidocaine, for a typical topical dose (3 mg/kg) to an average male (90 kg), an air-dried layer would need to cover a surface area of 6750 cm^2, which is too large to be practical. More experiments are needed to improve loading to deliver an effective dose.

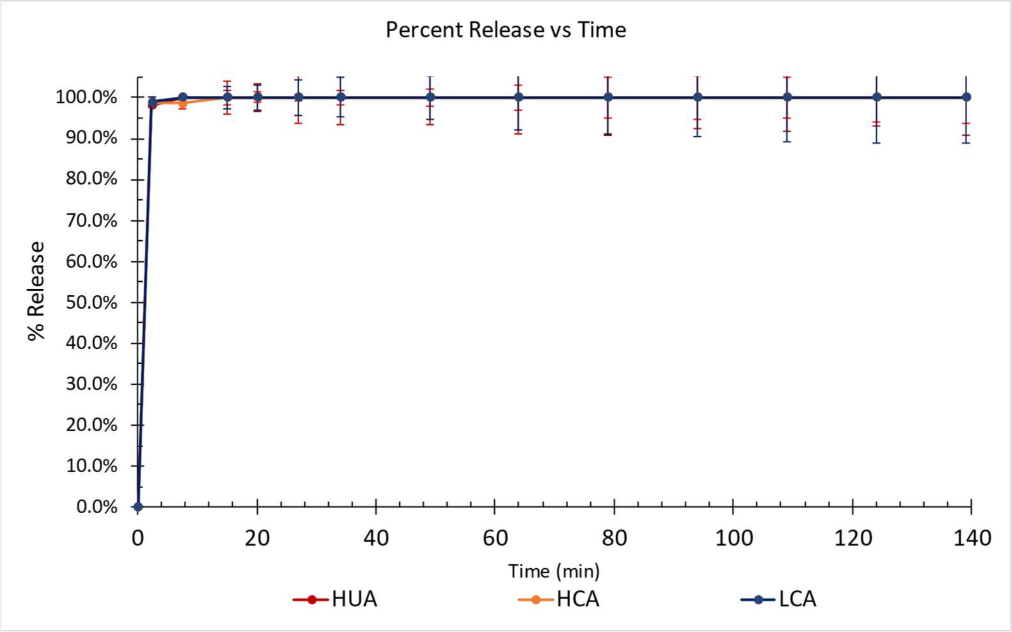

Figure 5.4.1: Free Dye % Release Air-Dried CSHG, with Crosslinking and MW

Figure 5.4.2 compares the dye release from the freeze-dried formulations. In contrast to the air-dried samples, the release was much more sustained. The uncrosslinked formulations displayed a much slower release rate, driven by higher swelling (+7000%) than the crosslinked formulations (+3600%). Contrastingly, within uncrosslinked/crosslinked pairs the formulation that had the highest maximum swelling showed the faster release rate when evaluating the effect of molecular weight (HCF and LUF), although the swelling differences are small. This demonstrates that the crosslinking density is the primary factor for controlling release, followed by, and that the polymer chain length has a secondary effect.

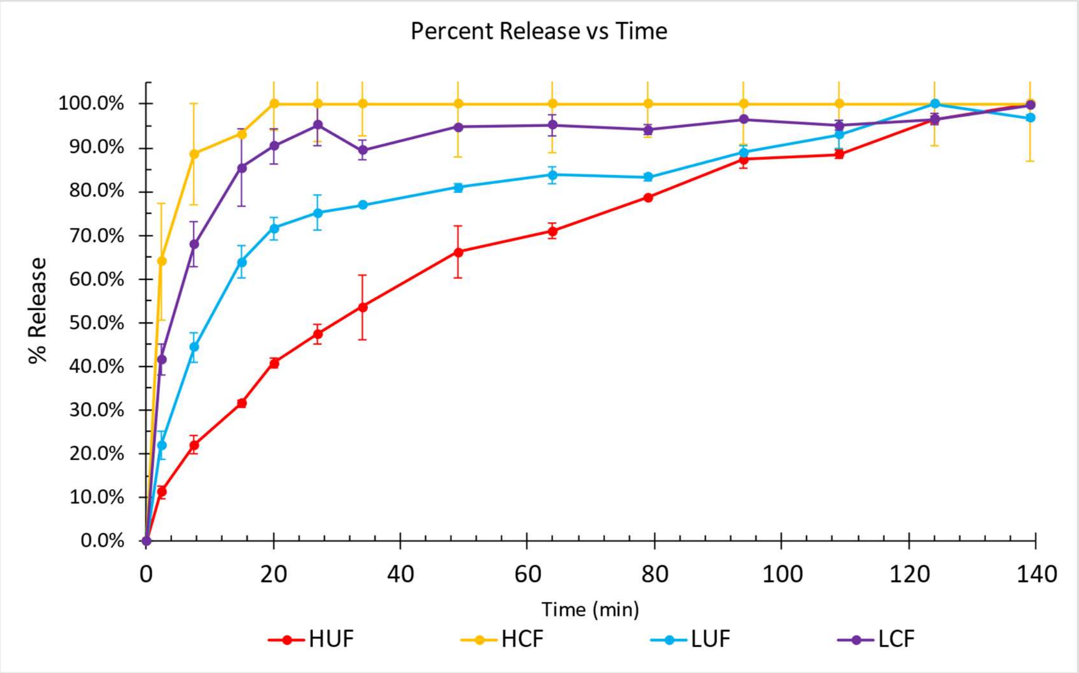

Figure 5.4.2: Free Dye % Release Freeze-Dried CSHG, with Crosslinking and MW

The different crosslink densities' releases for the low molecular weight freeze-dried formulations can be seen in Figure 5.4.3. The high molecular weight formulations' release is not shown but is similar. The same trend to what was seen for the kinetic swelling study was measured for the release. The uncrosslinked release showed sustained release, but increasing the CD to 2 resulted in fast, near-burst release before a second phase after 20-30 minutes of more sustained slow release. Increasing the crosslink density then slowed the release until a CD of 11, where there was no significant difference with any further increase of CD. The high molecular weight uncrosslinked formulation was also slower than the CD 2, decreasing as well to CD 5, which then showed no difference as CD increased to 14. Both of these match the kinetic swelling experiments, and other's studies on glutaraldehyde-crosslinked freeze-dried hydrogels saw the exact same trend (Figure 5.4.4). Mirzaei et al.[134] hypothesized what we also did: that for the uncrosslinked formulations the polymer chains can move more freely and so this introduces more surface area and volume. This expansion results in a higher barrier for dye diffusion and release, resulting in a slower release rate. Crosslinking prevents this expansion until it reaches a saturation point. Based on the molecular structure of chitosan and known crosslinking mechanism, the theoretical maximum crosslinking density is 65. However, the swelling and release behavior in our experiments stops changing at roughly 15% of the theoretical maximum. This could represent a practical maximum, where the crosslinking forces a porous morphology which shields the reactive amines or does not allow them to link to other chains. Regardless, the sustained release and sufficient loading (Table 5.4.1) show that the freeze-dried formulations have potential for achieving the multi-regime release proposed in the introduction.

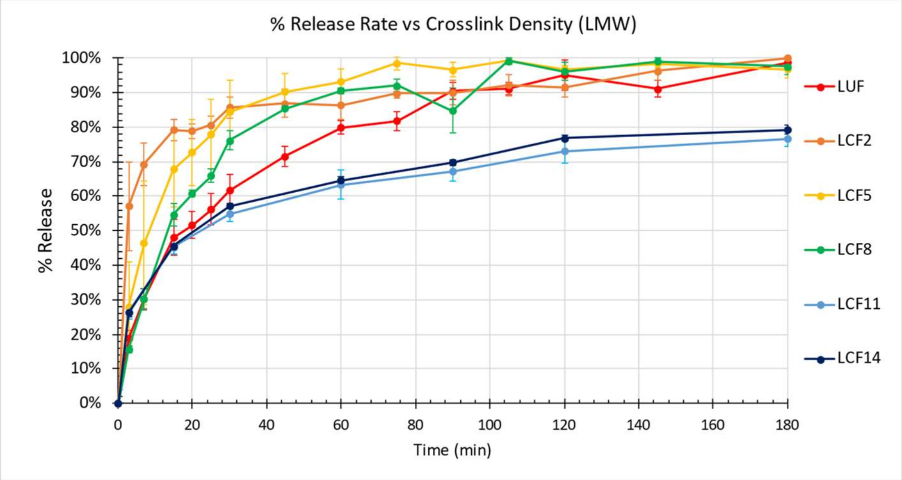

Figure 5.4.3: Free Dye % Release of Low MW CSHG vs. Crosslink Density

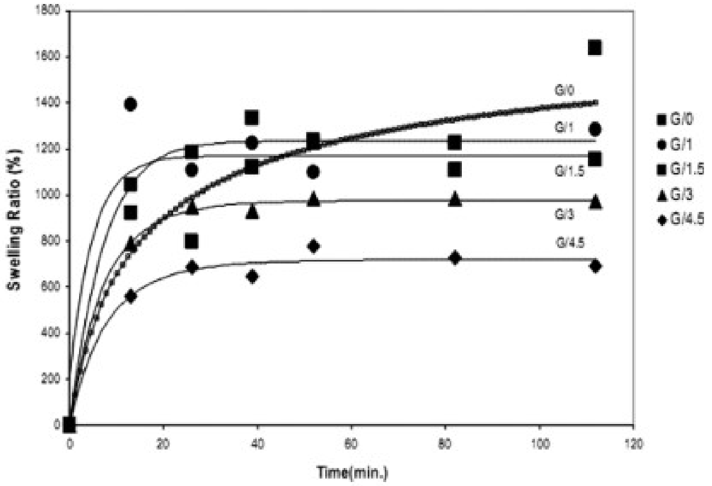

Figure 5.4.4: Kinetic Swelling of Freeze-Dried Chitosan Hydrogels with increasing CD, Mirzaei et al.[134]

5.4.2 Nanoparticle Release Studies

For the proposed multi-regime release wound dressing, the hydrogel swelling properties control the release kinetics for the immediate and fast delivery timings. The sustained release requires the use of PLGA nanoparticles, as they can release for the days to weeks required. Fluorescently-dyed PLGA nanoparticles (200 nm) were loaded into the hydrogels prior to loading and crosslinking by adding a NP dispersion directly into a room temperature chitosan solution and allowing it to stir for 15 minutes at 600 RPM to fully disperse the particles throughout the chitosan. The hydrogels were then formed as previously described. The same release protocol for PLGA cores and core/shell particles was used.

Figure 5.4.5 shows the NP release from the air-dried formulations of increasing crosslink density. Compared to non-encapsulated PLGA nanoparticles of similar size (black), the chitosan-impregnated release showed an initial burst release before slowing to a sustained release for many hours past that of bare PLGA NPs. The release rate appears to be dependent on the crosslink density. As the crosslink density increases, the release rate decreases, except for CA14, which had high variability between triplicate samples. This suggests that the chitosan hydrogel effectively bound to the PLGA nanoparticles a little after hydration, possibly after 24-48 hours when the rate slowed from the initial burst release. The acidic conditions within the newly hydrated interior would accelerate the particles' degradation somewhat, which could explain why initially we see a burst. Electrostatic interactions could then be capturing the PLGA nanoparticles to the hydrogel polymer chains, since PLGA is negatively charged and chitosan is positive. This binding then immobilized and shielded parts of the PLGA NPs surface, causing the release rate to decrease.

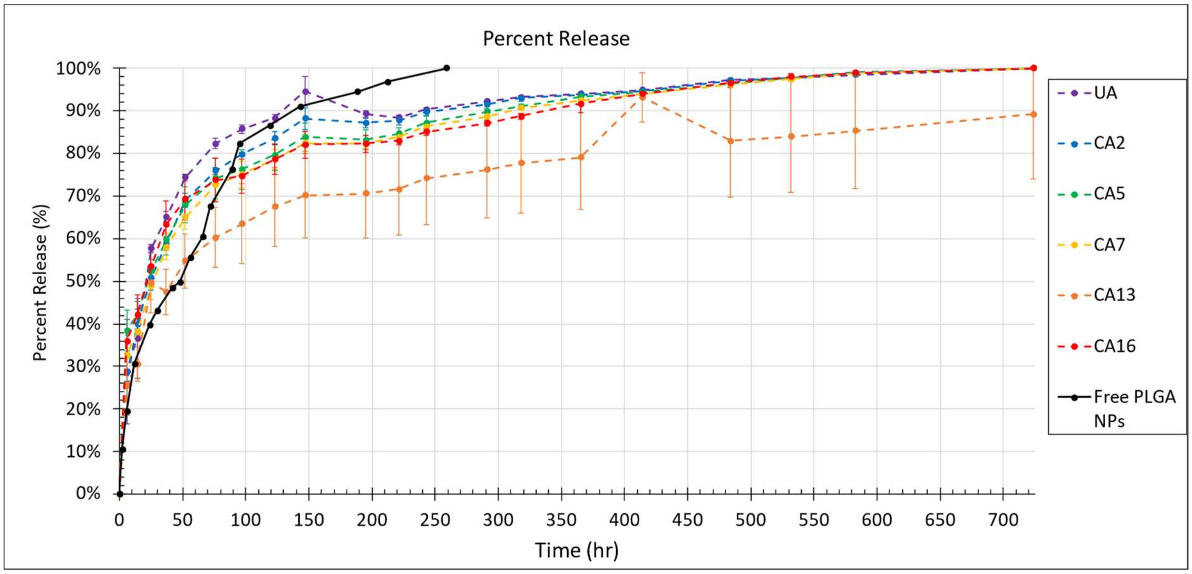

Figure 5.4.5: Percent Release from NPs loaded in Air-Dried CSHG vs. Crosslink Density

If our hypothesis is accurate, then the greater pore volume and porosity of the freeze-dried samples as well as the greater swelling should reduce the potential for nanoparticle trapping. This would lead to faster degradation from acidic interior. We see in Figure 5.4.6. results that follow very closely to this. All formulations showed a burst release compared to the free PLGA NP release (black). Uncrosslinked and CF2 and CF5 completely released all their payload within 50 hours of hydration. We saw in the swelling experiments that these formulations showed the highest maximum swelling. Thus, the expanded volume likely sufficiently prevented NP trapping, more so than when CD was increased. At high CDs, swelling is limited, and with a decreased in pore volume comes an increased likelihood of PLGA NP trapping. We hypothesize that this is what causes a distinct change in release rate for CF7 and above, where at 48 hours the rate changes and becomes nearly linear. This sustained release then lasts for many hours after the control of PLGA nanoparticles, like what was seen for the air-dried samples. This leads us to believe that our hypothesis is supported by these results, and that chitosan hydrogel properties can have a significant effect on loaded PLGA nanoparticles' release.

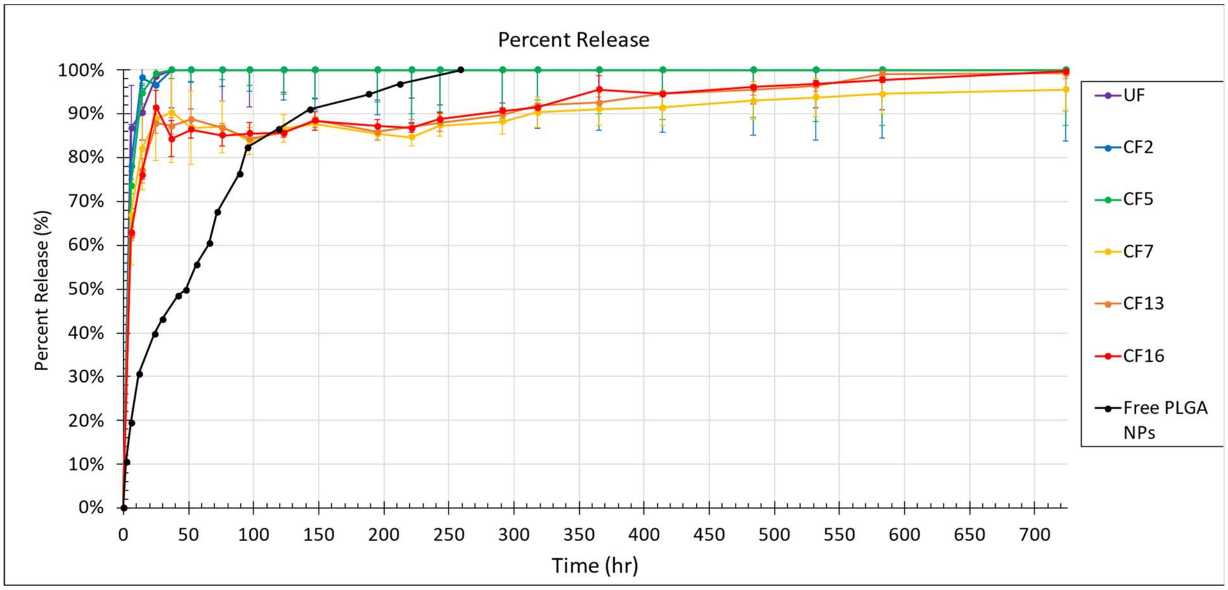

Figure 5.4.6: Percent Release from NPs loaded in Freeze-Dried CSHG vs. Crosslink Density

An interesting trend for PLGA nanoparticle loading can be found in Figure 5.4.7. All PLGA nanoparticles had roughly the same mass of C6 dye loaded in them and were roughly the same average size, and so the total mass released can give us some understanding of how effectively they could release the dye. Looking at the plot, it is evident that total mass release is highly dependent on the crosslink density and the drying method. For both drying methods, the total mass released increased as crosslink density increased.

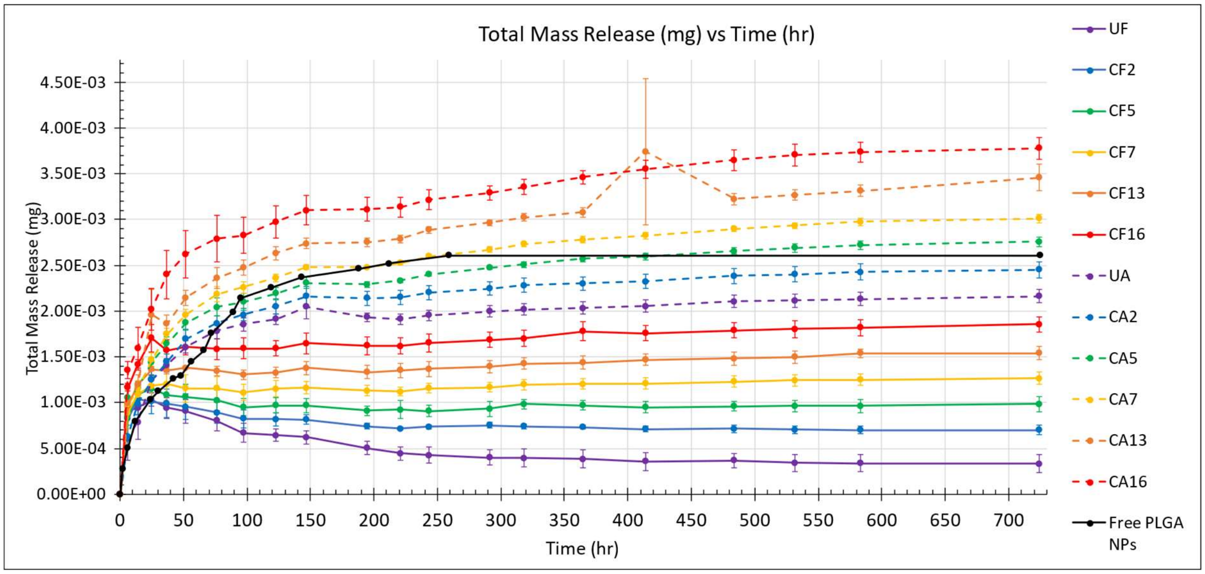

Figure 5.4.7: Total Mass Release (mg) from NPs loaded in Air-Dried and Freeze-Dried CSHG vs. Crosslink Density

The air-dried samples all released a greater amount of dye than any of the freeze-dried samples. The reason for this trend is unclear. We hypothesize that the glutaraldehyde crosslinker or the chitosan hydrogel polymer itself has a greater interaction with the dye and PLGA nanoparticles than predicted. The PLGA nanoparticles have a negative surface charge, which would be attracted to the positively charged chitosan functional groups. The glutaraldehyde crosslinker reacts with these chitosan functional groups, which removes the positive amine groups and replaces them with a Chitosan-Schiff Base, which is neutral or negative depending on the protonation state. Therefore, a higher crosslink density would result in less electrostatic interaction with the PLGA nanoparticles. This matches well with the trend we see within the air-dried and freeze-dried formulations. Additionally, the swellability could provide a rationale for a greater release seen for the air-dried formulations versus the freeze-dried formulation. Greater swelling would increase the pore volume and specific surface area available for PLGA-Chitosan interactions, which would lead to more PLGA nanoparticle “shielding” and less release with the higher swelling formulations. The freeze-dried formulations all had much higher swelling than the air-dried, and indeed we do see that all freeze-dried samples had lower release than the air-dried.

We saw that the uncrosslinked and low CD samples degraded quickly during the kinetic swelling experiments, but not during any of the release experiments. DI water was used as the hydration medium for the swelling experiment, while PBS buffer was used for all release experiments. This means that the pH likely changed to more acidic during the kinetic swelling, which destabilized the hydrogels which were not sufficiently crosslinked. The buffer solution maintained a neutral pH, and so all hydrogels remained stable, and allowed the uncrosslinked and low CD hydrogels to reach greater swelling than in water. The swelling then, we hypothesize, is the likely answer to the difference in total dye released.

5.5 Morphology and Porosity Investigations

The swelling and release experiments displayed many trends which we hypothesized were due to the polymer chain network structure and morphology. The following sections are our characterization of this structure and morphology and the effect of crosslink density using Scanning Electron Microscopy and BET Analysis. The SEM was a ThermoFisher Phenom Desktop made available by Dr. Symone Alexander. BET was performed on Micromeritics TriStar II, operated by Daniel Meadows and made available by Dr. Virginia Davis. BET samples were degassed at 180°C for 24 hours prior to BET, where BJH used to calculate specific surface area, pore distribution, and pore volume.

5.5.1 SEM

Chitosan hydrogels of increasing crosslink densities were visualized under low magnification SEM. The air-dried formulations (not shown here) all showed the same smooth, flat morphology, demonstrating compressed non porous sheet that is described in literature[135,136]. Only on the cut edges could any detail of the compressed sheet structure, and so examination was limited. The freeze-dried samples, in contrast, showed highly porous and varying morphology and structure. Figure 5.5.1 shows the folded sheet-like morphology of the uncrosslinked formulations. This structure was also reported by others, such as Zheng et al.[137]. These uncrosslinked sheets allow fluid penetration and can move past each other easily to expand, leading to the high swelling seen in earlier experiments.

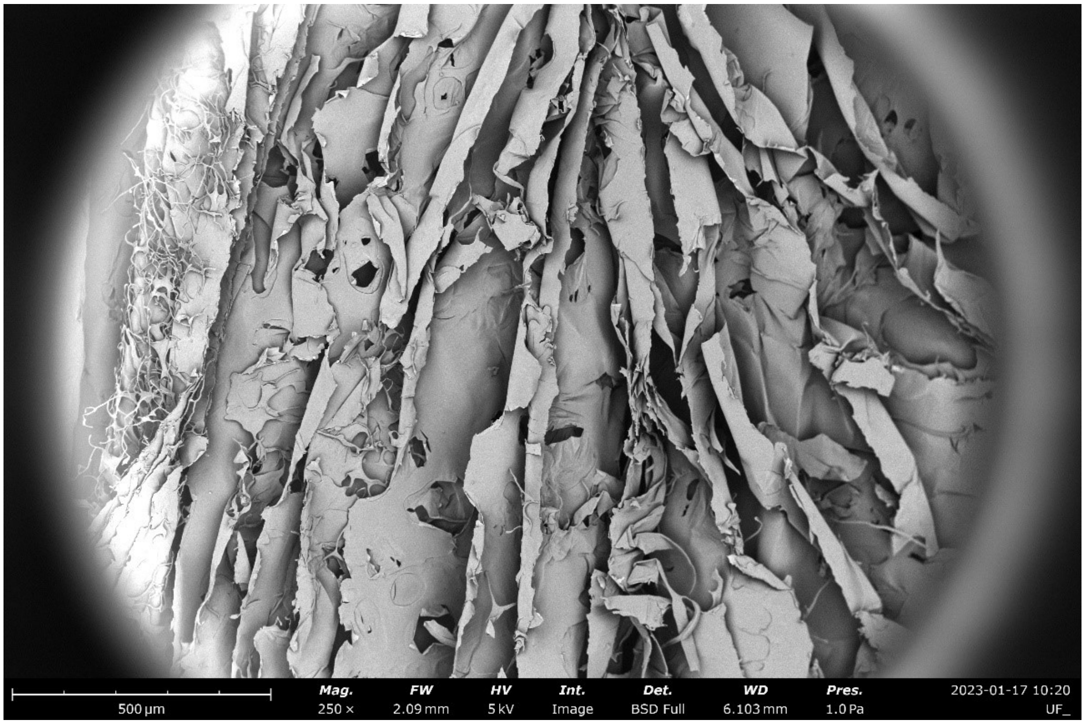

Figure 5.5.1: SEM Image of Uncrosslinked Freeze-Dried CSHG Sheet Morphology

As crosslink density was increased, the sheet-like morphology was replaced by a more stringy and highly folded morphology. Figure 5.5.2 shows the morphology for CF2, which showed high swelling but low stability in kinetic swelling tests. You can see on the upper left side of the image that the crosslinking has introduced regions where polymer chains have formed an interconnected network. These crosslinked chains allow for more mechanical stability upon hydration, preventing or at least slowing full separation of the sheet regions. The prevalence of the crosslinked regions increase as the crosslink density increases, until at high CDs, such as at CF14 in Figure 5.5.3, the majority of the structure is this highly porous and interconnected structure. These images confirm that the crosslink structure is responsible for the swelling behavior and thus responsible for the free dye and nanoparticle release performance to be used for the multilayer wound dressing.

Figure 5.5.2: SEM Image of CSHG, CF2 Partially Crosslinked Morphology

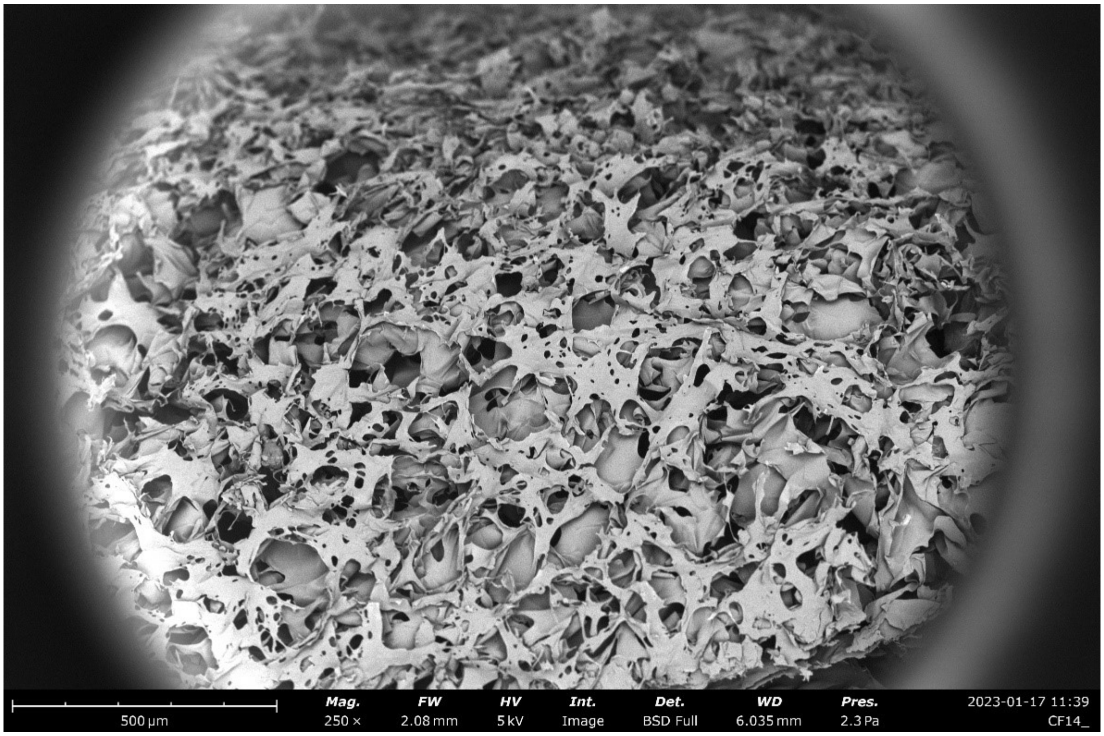

Figure 5.5.3: SEM Image of CSHG, CF14 Fully Crosslinked Morphology

5.5.2 BET

SEM morphology visualization was a qualitative analysis, as reliably measuring the pore size or porosity was difficult with software and sample preparation complexity. Instead, an initial BET analysis was performed on a range of crosslinked freeze-dried samples. BET (Brunaeur-Emmet-Teller) uses Langmuir monolayer atomic adsorption of nitrogen to measure the surface area and pore size of highly porous networks, while the Barrett-Joyner-Halenda (BJH) method uses the Kelvin equation to calculate pore size distribution[138]. Often, density functional theory (DFT), which uses Monte Carlo molecular simulations on adsorption isotherms to calculate pore size distribution, is used in conjunction with BJH to validate results. For this experiment, we used BET with BJH and DFT to quantify the specific surface area (SSA), the pore width, the pore volume, and pore size distribution to better understand the relationship between crosslink density and pore structure.

The nitrogen physisorption isotherms can categorized in six categories depending on the pore size and type[138]. The freeze-dried samples isotherms were near linear, with slight curves at the high relative pressures, which indicate Type II macroporous structure. Figure 5.5.4 shows the calculated SSA (in m2/g) with respect to the crosslink densities. There is a peak SSA at CD of 8, at which you would expect the highest swelling with great mechanical stability. We previously hypothesized that this peak would lie at a CD of around 5, from the swelling stability transition region that was seen during the kinetic swelling experiments. This was based on that a CD of 5 was the lowest tested crosslink density that remained stable during kinetic swelling and had the highest maximum swelling. It is possible that additional crosslinker past CD 5 continues to strengthen the pore structure to CD 8, after which more crosslinker starts to constrict the hydrogel and reduces the surface area.

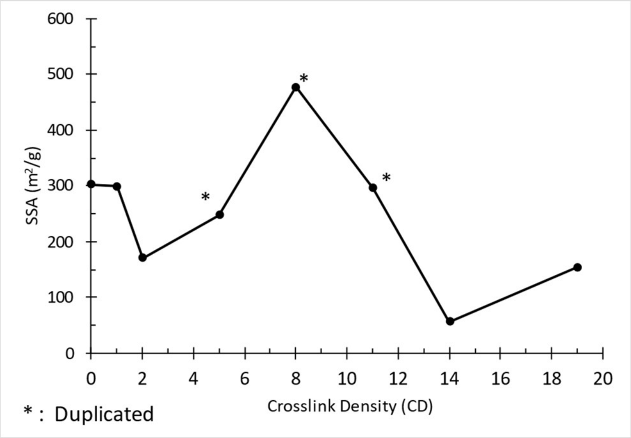

Figure 5.5.4: Specific Surface Area (m^2/g) vs. CD, Freeze-Dried CSHG

Pore volume showed the same trend as SSA, with a peak at CD 8. The pore width relationship with crosslinking density displays an interesting trend with CD, seen in Figure 5.5.5. Pore width increased until CD 5 before remaining constant until CD11. CD11 was the point during the free dye release experiments at which any higher crosslinking resulted in the same release kinetics. The pore width peak at CD5 matches what was the expected peak during the kinetic swelling experiments but carries on through CD 8 and 11. This could suggest that the pore width is what controls the swelling behavior. This could be related to the SSA and pore volume, but it is unclear why the pore width suddenly drops at CD11. It could be more duplications are needed, as only duplications were run on CD 5-11 samples. DFT also calculated pore size/volume distribution, with mesoporosity and macropores evident. These results support the SEM visualization results.

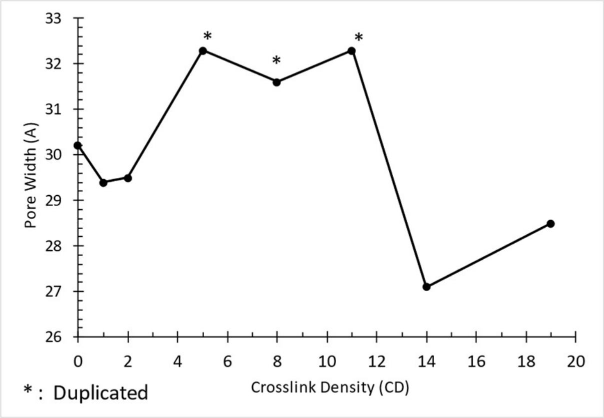

Figure 5.5.5: Pore Width (A) vs. CD, Freeze-Dried CSHG

5.6 Conclusion

Though far from complete, we performed initial investigations on chitosan hydrogels formulations for multimodal consecutive release as part of a multilayer wound dressing. Characterizing the swelling behavior demonstrated how properties such as MW, crosslinking, and drying method affected the formulation mechanical stability and swelling. In general, higher MW, CDs greater than 2, and freeze-dried formulations had the desirable combination of high swelling and stability over the hours tested. Characterizing the formulations' release. two formulations were determined suitable for achieving the "immediate" (seconds to minutes) and "fast" (minutes to hours) release timing. LMW freeze-dried formulations of CD 5 to CD 11 showed controlled, sustained release over three hours, matching the desired release profile for the "fast" timing regime. All air-dried samples had a burst release, and so a high molecular weight slightly crosslinked formulation likely wound ensure mechanical stability. However, loading and release efficiency remains a concern for air-dried samples, and more experiments are needed to determine if the air-dried crosslinked formulations are too rigid for a practical wound dressing. Finally, nanoparticles loaded within CSHG formulations all showed the ability to achieve "sustained" (hours to days) release. However, nanoparticles loaded within the freeze-dried samples displayed a "shielding" effect, dependent on the crosslink density and degree of swelling. These results were hypothesized to be a result of the pore structure and morphology, and this was supported by SEM and BET analysis. This shielding effect will need to be taken into account, as it decreases the release efficiency of the drug loaded within the PLGA nanoparticles compared to the non-encapsulated PLGA. In summary, in Figure 5.6.1, we propose a three-layer CSHG, with layers made of formulations which showed release kinetics appropriate to achieve the desired target drugs releases in Figure 5.1.1.

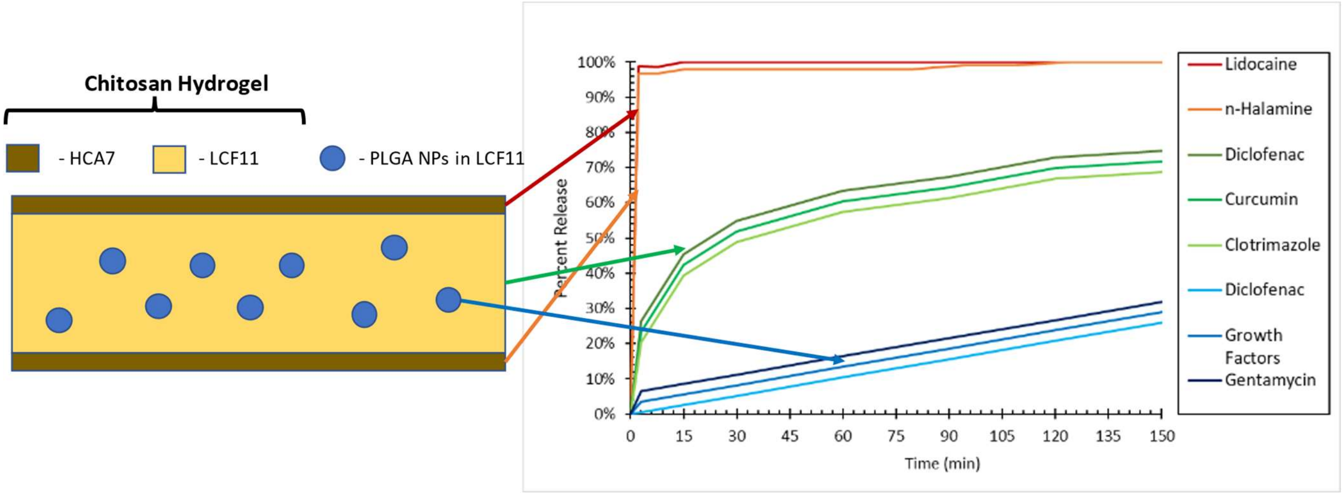

Figure 5.6.1: Updated Multi-layer Chitosan Hydrogel Wound Dressing for Multi-Regime Release

Chapter 6: Summary, Significance, and Future Directions

Controlling a drug's bioavailability and pharmacokinetics is a particular problem for small molecular weight, hydrophobic drugs, as it reduces their efficacy, increases often severe side effects and limits their potential for positive treatment. In fact, most drugs' bioavailability and pharmacokinetics are poor due to their small molecular weight and hydrophobicity. Many chemotherapeutics are also difficult to deliver at safe doses due to their narrow therapeutic effective windows, where they can have therapeutic effect without causing toxic side effects. Different systems which can release these drugs into circulation at controlled rates have been developed counter these complications. One such system that has shown promise for this type of controlled release are PLGA polymeric nanoparticles. These systems' release and degradation kinetics are well understood, and they are proven safe within the body. However, there are size, material, and manufacturing limitations which have prevented these highly promising and versatile systems from reaching clinical use. One such modification to these systems is coating the PLGA core with a thin polymer shell (such as PLLA) which degrades at a slower rate, lengthening the time it can offer sustained release without greatly increasing the size. Additionally, these core and shell polymeric nanoparticles have other advantages, as they prevent premature burst release often seen with cores and offer a multimodal release structure with individually controlled components. Therefore, it is the goal of this work to develop improved models and methods for controlling PLGA cores and PLGA/PLLA core and shell nanoparticles independently, thereby allowing for improved sustained controlled release of small, hydrophobic payloads.

We used several different aspects of chemical engineering to address this goal: transport and thermodynamic phenomena when analyzing the release behavior and emulsion synthesis method of these nanoparticles, statistical modeling and probability algorithms for measuring and modeling the effect of synthesis parameters on PLGA core and core/shell properties, as well as process design for theoretical scale-up production modeling, as well material science and characterization for characterizing the polymeric nanoparticles and hydrogel systems which are an additional application of these formulations.

Chapters 1 and 2 introduce and provide background on the concepts and challenges this dissertation addresses, as well as provide literature background on some alternative applications of these techniques and systems.

Chapter 3 focuses on developing a model for the reliable production of PLGA cores. This is to establish a baseline method for producing a consistent formulation on which we will attempt to form shells at variable thicknesses later. We first captured all controllable synthesis parameters as well as the key output features which have been shown to determine release behavior: size and size distribution (PDI). We used two rounds of data gathering and machine learning to learn about significant features and which algorithms and models led to the best predictions. The machine learning model Random Forest gave the best fit of the ML algorithms; however the best overall fit was a power law model dependent on a feature which came out of this modeling: specific energy. Specific energy is a scalable feature we had hypothesized would be contributor to the final size and PDI, but from the machine learning results it had higher importance than expected (>95% of variance explained for size, >90% for PDI). To further improve this power law model, we used the determined second most important features, the PVA to PLGA molar ratios. By binning the data and analyzing how the model goodness of fit and monodispersity changed, we were able to determine that there were optimum ranges of around 13-25 for total molar ratio and 5-9 for emulsion molar ratio. We also characterized the release kinetics and mechanisms of PLGA cores and found that they were degradation driven while PLLA nanoparticles were diffusion driven, agreeing with other literature reports. Finally, we performed theoretical calculations to translate this batch model for size and PDI control to a continuous process to attempt to address the scale-up limitation of these particles. The future directions of this work can be built on the knowledge gained in this chapter. The specific energy power law relationship is purely experimental and is valid only for this specific system modeled in this work. It would be useful to develop a thermodynamically-based model, which takes into account viscosities, densities, and material properties to predict droplet size. This could then be applied to a wide range of systems. Even with the chosen materials with this system, more characterization and experiments could be done to further optimize and understand it. The effect of PVA molecular weight on the emulsion and droplet size, as well optimal washing and collection could improve mass yield for smaller sizes or change the effect seen for molar ratios. NMR, FTIR, and SEM could be used to quantify PVA adsorption, as well as quantification assays. Additionally, more experiments are needed to test the theoretical continuous process and the accuracy of the size control model. The release studies used model dye to measure release kinetics, however more experiments using drugs, with different sizes and properties, may change release kinetics. Also, since PLGA NPs will need to be surface characterized with PEG or another coating to neutralize surface charge, this coating's effect on release compared to bare particles will be valuable for clinical translation.

Having achieved good size and PDI control over the PLGA cores and characterizing their release, in Chapter 4 we presented work to add PLLA shells around these cores at thicknesses dependent on various synthesis conditions. We proposed an emulsion-based method due to the similarity to the core synthesis method and the hope we could control it using similar parameters.

We hypothesized this adapted method would produce populations of three types of particles: pure PLGA cores, pure PLLA particles, and core/shell particles. The ratios of these particles represent the efficiency of the method, which we want to maximize to allow the fine control over the shell we desire. We confirmed via fluorescent imaging the formation of these three types. However, using estimated efficiencies found via a statistical distribution method, the Gaussian Mixture Model, we were unable to determine synthesis parameters which would allow us to maximize the efficiency or control the shell thickness. Despite this negative outcome, we did see favorable controlled release properties, with varied release kinetics correlating to the estimated shell thicknesses. We suggest that for future work building on this chapter, that instead of an emulsion-based method to form the core and shell, one is just used to form the core. These cores could then be used in a nanoprecipitation-based method, which has been very promising in literature for producing uniform core/shells at high efficiency in a continuous microfluidic process. If necessary, the GMM algorithm can be improved, with additional optimization and modeling to capture the realistic solution could be achieved. Additionally, a new theoretical release model should be developed to more accurately describe and predict the release from a core/shell nanoparticle. Current models generally assume a single core, and either degradation or diffusion dominated release. However, from our initial release experiments, there isn't a model which could capture a change in release from one to the other, depending on the core and shell materials as well as the dimensions of both.

Finally, in Chapter 5 we present work on an alternative controlled release application of polymeric nanoparticles. We proposed a polymer chitosan hydrogel system, made of different formulations and layers, which could provide multimodal release of multiple drugs as a wound dressing for complex wounds. Polymeric nanoparticles could offer a more sustained release which it was suspected that the hydrogels could not achieve. We analyzed the swelling characteristics of different formulations, focusing on the effect that drying method, crosslink density, and molecular weight had on kinetics and stability. We found that our formulations showed greater swelling than commercial wound dressings, and generally reach equilibrium within 5-15 minutes of hydration, which is ideal for rapid treatment of complex wounds. The freeze-dried formulations showed greater swelling than the air-dried, and crosslinked decreased the overall swelling capability but improved stability after a crosslink density of around 5 (mg GlA/g chitosan). Further increasing the CD to 11 decreased the maximum swelling capability, but CD past 11 did not show any effect. These results were hypothesized to due to the hydrogel pore width, structure, and morphology. Addition crosslinkers would stabilize and force the hydrogel structure to form wide pores (CD <5), but adding additional crosslinker would start to constrict those pores ($5 < CD < 11$) until the link sites were saturated ($CD > 11$). These trends were confirmed with SEM and BET analysis, which showed changing pore structure from lamellar in crosslinked formulations to more interconnected networks, with a specific surface area peak at around CD 5-8 and a leveling off of pore width after CD 11. We also investigated if we could achieve the proposed multimodal release timing with different formulation. All air-dried formulations show immediate (< 5 minutes) burst release which is ideal for immediate pain and antibiotic delivery, but suffered from poor loading and release efficiency, which will need to be addressed in future studies. Freeze-dried formulations showed controlled, sustained release at CD greater than 2 to 5, with decreasing rate with increasing CD up to a CD of 11, similar to the swelling experimental results. These formulations would be able to delivery multiple drugs within minutes to hours of hydration for the second stage of release. We also impregnated these hydrogel formulations with PLGA nanoparticles to test its effect on the release. The PLGA nanoparticles showed sustained release over many days, which could improve wound sterility and healing if growth factors, antibiotics, and pain medications were loaded within those particles. However, there was a “shielding” effect seen, correlating with increasing CD, where the nanoparticles seemed to electrostatically attract to the chitosan chains, which varied the release efficiency. More work is need to determine the exact layering process and whether actual drugs, not model dye, would have a different interaction with the chitosan. Much more work is needed to determine exact hydration and hydrogel properties post-drying, as this will have an effect on release and swelling. It is still unknown whether the PLGA nanoparticles diffuse out of the hydrogels, despite attempted experiments. It would be valuable to measure the true fate of these particles, as in some conditions it could be advantageous for the NPs to diffuse out and deposit into wounds. Additionally, a formation process which is more easily scaled up should be developed.

In conclusion, we believe the work presented in this dissertation significantly contributes to the current knowledge of controlled release systems and offers some solutions and ways forward for delivering small, hydrophobic payloads within the body. The majority of the stated future work looks to address some limitations of scale-up or to introduce more versatility for performance of these polymeric systems. Some represent blind spots in base scientific understanding, which would be valuable to illuminate. The work presented here represents many hours and years of dedicated effort and drive, and we hope that we have helped the field of nanomedicine and drug delivery improve treatments to future patients.

Chapter 7: References

(1) Price, G.; Patel, D. A. Drug Bioavailability. In *StatPearls [Internet]*; StatPearls Publishing, 2021.

(2) Alqahtani, M. S.; Kazi, M.; Alsenaidy, M. A.; Ahmad, M. Z. Advances in Oral Drug Delivery . *Frontiers in Pharmacology* . 2021.

(3) Currie, G. M. Pharmacology, Part 2: Introduction to Pharmacokinetics. *J. Nucl. Med. Technol.* **2018**, *46* (3), 221–230. https://doi.org/10.2967/jnmt.117.199638.

(4) Paul, A. Drug Absorption and Bioavailability. In *Introduction to Basics of Pharmacology and Toxicology*; Raj, G. M., Raveendran, R., Eds.; Springer Singapore: Singapore, 2019; pp 81–88. https://doi.org/10.1007/978-981-32-9779-1_5.

(5) Li, Y.; Meng, Q.; Yang, M.; Liu, D.; Hou, X.; Tang, L.; Wang, X.; Lyu, Y.; Chen, X.; Liu, K.; et al. Current Trends in Drug Metabolism and Pharmacokinetics. *Acta Pharm. Sin. B* **2019**, *9* (6), 1113–1144. https://doi.org/10.1016/j.apsb.2019.10.001.

(6) Currie, G. M. Pharmacology, Part 1: Introduction to Pharmacology and Pharmacodynamics. *J. Nucl. Med. Technol.* **2018**, *46* (2), 81–86. https://doi.org/10.2967/jnmt.117.199588.

(7) Zou, H.; Banerjee, P.; Leung, S. S. Y.; Yan, X. Application of Pharmacokinetic-Pharmacodynamic Modeling in Drug Delivery: Development and Challenges . *Frontiers in Pharmacology* . 2020.

(8) Kang, J. S.; Lee, M. H. Overview of Therapeutic Drug Monitoring. *Korean J. Intern. Med.* **2009**, *24* (1), 1–10. https://doi.org/10.3904/kjim.2009.24.1.1.

(9) Lee, J. H.; Yeo, Y. Controlled Drug Release from Pharmaceutical Nanocarriers. *Chem. Eng. Sci.* **2015**, *125*, 75–84. https://doi.org/10.1016/j.ces.2014.08.046.

(10) Uhrich, K. E.; Cannizzaro, S. M.; Langer, R. S.; Shakesheff, K. M. Polymeric Systems for Controlled Drug Release. *Chem. Rev.* **1999**, *99* (11), 3181–3198. https://doi.org/10.1021/cr940351u.

(11) Fitzgerald, M. Principles of Pharmacokinetics. *J. Am. Acad. Nurse Pract.* **2007**, *6* (12), 581–583. https://doi.org/10.1111/j.1745-7599.1994.tb00913.x.

(12) Siegel, R. A.; Rathbone, M. J. Overview of Controlled Release Mechanisms. In *Fundamentals and Applications of Controlled Release Drug Delivery. Advances in Delivery Science and Technology*; Siepmann, J., Siegel, R. A., Rathbone, M. J., Eds.; Springer US: Boston, MA, 2012; pp 19–43. https://doi.org/10.1007/978-1-4614-0881-9_2.

(13) Vargason, A. M.; Anselmo, A. C.; Mitragotri, S. The Evolution of Commercial Drug Delivery Technologies. *Nat. Biomed. Eng.* **2021**, *5* (9), 951–967. https://doi.org/10.1038/s41551-021-00698-w.

(14) Chiang, C. L.; Cheng, M. H.; Lin, C. H. From Nanoparticles to Cancer Nanomedicine: Old Problems with New Solutions. *Nanomaterials* **2021**, *11* (7), 1–19. https://doi.org/10.3390/nano11071727.

(15) Osorno, L. L.; Brandley, A. N.; Maldonado, D. E.; Yiantsos, A.; Mosley, R. J.; Byrne, M. E. Review of Contemporary Self-Assembled Systems for the Controlled Delivery of Therapeutics in Medicine. *Nanomaterials* **2021**, *11* (2), 1–28. https://doi.org/10.3390/nano11020278.

(16) Carasco, C. F.; Fletcher, P.; Maconochie, I. Review of Commonly Used Age-Based Weight Estimates for Paediatric Drug Dosing in Relation to the Pharmacokinetic Properties of Resuscitation Drugs. *Br. J. Clin. Pharmacol.* **2016**, *81* (5), 849–856. https://doi.org/10.1111/bcp.12876.

(17) Harashima, H.; Abbasi, S.; Sato, Y.; Kajimoto, K. New Design Strategies for Controlling the Rate of Hydrophobic Drug Release from Nanoemulsions in Blood Circulation. *Mol. Pharm.* **2020**, *17* (10), 3773–3782. https://doi.org/10.1021/acs.molpharmaceut.0c00542.

(18) US Food and Drug Administration Center for Drug Evaluation and Research. New Drugs at FDA: CDER's New Molecular Entities and New Therapeutic Biological Products https://www.fda.gov/drugs/development-approval-process-drugs/new-drugs-fda-cders-new-molecular-entities-and-new-therapeutic-biological-products.

(19) Ngo, H. X.; Garneau-Tsodikova, S. What Are the Drugs of the Future? *Medchemcomm* **2018**, *9* (5), 757–758. https://doi.org/10.1039/c8md90019a.

(20) Chhikara, B. S.; Parang, K. Global Cancer Statistics 2022: The Trends Projection Analysis. *Chem. Biol. Lett. Chem. Biol. Lett* **2022**, *2023* (1), 451.

(21) Siegel, R. L.; Miller, K. D.; Fuchs, H. E.; Jemal, A. Cancer Statistics, 2022. *CA. Cancer J. Clin.* **2022**, *72* (1), 7–33. https://doi.org/10.3322/caac.21708.

(22) Kakde, D.; Jain, D.; Shrivastava, V.; Kakde, R.; Patil, A. T. Cancer Therapeutics-Opportunities, Challenges and Advances in Drug Delivery. *J. Appl. Pharm. Sci.* **2011**, *1* (9), 1–10.

(23) Kamaly, N.; Yameen, B.; Wu, J.; Farokhzasd, O. C. Degradable Controlled-Release

Polymers and Polymeric Nanoparticles: Mechanisms of Controlling Drug Release. *Chem. Rev.* **2017**, *116* (4), 2602–2663. https://doi.org/10.1021/acs.chemrev.5b00346.Degradable.

(24) Zhong, L.; Li, Y.; Xiong, L.; Wang, W.; Wu, M.; Yuan, T.; Yang, W.; Tian, C.; Miao, Z.; Wang, T.; et al. Small Molecules in Targeted Cancer Therapy: Advances, Challenges, and Future Perspectives. *Signal Transduct. Target. Ther.* **2021**, *6* (1). https://doi.org/10.1038/s41392-021-00572-w.

(25) Krischke, M.; Hempel, G.; Völler, S.; André, N.; D'Incalci, M.; Bisogno, G.; Köpcke, W.; Borowski, M.; Herold, R.; Boddy, A. V.; et al. Pharmacokinetic and Pharmacodynamic Study of Doxorubicin in Children with Cancer: Results of a "European Pediatric Oncology Off-Patents Medicines Consortium" Trial. *Cancer Chemother. Pharmacol.* **2016**, *78* (6), 1175–1184. https://doi.org/10.1007/s00280-016-3174-8.

(26) Shafei, A.; El-Bakly, W.; Sobhy, A.; Wagdy, O.; Reda, A.; Aboelenin, O.; Marzouk, A.; El Habak, K.; Mostafa, R.; Ali, M. A.; et al. A Review on the Efficacy and Toxicity of Different Doxorubicin Nanoparticles for Targeted Therapy in Metastatic Breast Cancer. *Biomed. Pharmacother.* **2017**, *95* (September), 1209–1218. https://doi.org/10.1016/j.biopha.2017.09.059.

(27) Edwards, S. J.; Barton, S.; Thurgar, E.; Trevor, N. Topotecan, Pegylated Liposomal Doxorubicin Hydrochloride, Paclitaxel, Trabectedin and Gemcitabine for Advanced Recurrent or Refractory Ovarian Cancer: A Systematic Review and Economic Evaluation. *Health Technol. Assess.* **2015**, *19* (7), 1–480. https://doi.org/10.3310/hta19070.

(28) Chen, Y.; Wan, Y.; Wang, Y.; Zhang, H.; Jiao, Z. Anticancer Efficacy Enhancement and Attenuation of Side Effects of Doxorubicin with Titanium Dioxide Nanoparticles. *Int. J.*

Nanomedicine **2011**, *6*, 2321–2326. https://doi.org/10.2147/IJN.S25460.

(29) Xu, C.; Wang, P.; Zhang, J.; Tian, H.; Park, K.; Chen, X. Pulmonary Codelivery of Doxorubicin and SiRNA by PH-Sensitive Nanoparticles for Therapy of Metastatic Lung Cancer. *Small* **2015**, *11* (34), 4321–4333. https://doi.org/10.1002/smll.201501034.

(30) Escherich, G.; Zimmerman, M.; Janka-Schaub, G. Doxorubicin or Daunorubicin Given Upfront in a Therapeutic Window Are Equally Effective in Children With Newly Diagnosed Acute Lymphoblastic Leukemia. A Randomized Comparison in Trial CoALL 07-03. *Pediatr. Blood Cancer* **2013**, *60* (1), 254–257. https://doi.org/10.1002/pbc.24273.

(31) Gabizon, A.; Shmeeda, H.; Barenholz, Y. Pharmacokinetics of Pegylated Liposomal Doxorubicin: Review of Animal and Human Studies. *Clin. Pharmacokinet.* **2003**, *42* (5), 419–436. https://doi.org/10.2165/00003088-200342050-00002.

(32) Thorn, C. F.; Oshiro, C.; Marsh, S.; Hernandez-Boussard, T.; McLeod, H.; Klein, T. E.; Altman, R. B. Doxorubicin Pathways: Pharmacodynamics and Adverse Effects. *Pharmacogenet. Genomics* **2011**, *21* (7), 440–446. https://doi.org/10.1097/FPC.0b013e32833ffb56.

(33) Ventola, C. L. Progress in Nanomedicine: Approved and Investigational Nanodrugs. *P T* **2017**, *42* (12), 742–755.

(34) Barenholz, Y. Doxil® - The First FDA-Approved Nano-Drug: Lessons Learned. *J. Control. Release* **2012**, *160* (2), 117–134. https://doi.org/10.1016/j.jconrel.2012.03.020.

(35) Huang, X.; Brazel, C. S. On the Importance and Mechanisms of Burst Release in Matrix-Controlled Drug Delivery Systems. *J. Control. Release* **2001**, *73* (2–3), 121–136.

https://doi.org/10.1016/S0168-3659(01)00248-6.

(36) Brazel, C. S.; Huang, X. The Cost of Optimal Drug Delivery: Reducing and Preventing the Burst Effect in Matrix Systems. *ACS Symp. Ser.* **2004**, *879*, 267–282. https://doi.org/10.1021/bk-2004-0879.ch019.

(37) Dorta, M. J.; Santoveña, A.; Llabrés, M.; Fariña, J. B. Potential Applications of PLGA Film-Implants in Modulating in Vitro Drugs Release. *Int. J. Pharm.* **2002**, *248* (1–2), 149–156. https://doi.org/10.1016/S0378-5173(02)00431-3.

(38) Budhian, A.; Siegel, S. J.; Winey, K. I. Controlling the in Vitro Release Profiles for a System of Haloperidol-Loaded PLGA Nanoparticles. *Int. J. Pharm.* **2008**, *346* (1–2), 151–159. https://doi.org/10.1016/j.ijpharm.2007.06.011.

(39) Yao, S.; Liu, H.; Yu, S.; Li, Y.; Wang, X.; Wang, L. Drug-Nanoencapsulated PLGA Microspheres Prepared by Emulsion Electrospray with Controlled Release Behavior. *Regen. Biomater.* **2016**, *3* (5), 309–317. https://doi.org/10.1093/rb/rbw033.

(40) Makadia, H. K.; Siegel, S. J. Poly Lactic-Co-Glycolic Acid (PLGA) as Biodegradable Controlled Drug Delivery Carrier. *Polymers (Basel).* **2011**, *3* (3), 1377–1397. https://doi.org/10.3390/polym3031377.

(41) Dash Suvakanta, P. N. .; Lilakanta, N.; Chowdhury, P. Kinetic Modeling on Drug Release From Controlled Drug Delivery Systems. *Acta Pol. Pharm. ñ Drug Res.* **2010**, *67* (3), 217–223. https://doi.org/10.2307/3237001.

(42) Freire, M. C. L. C.; Alexandrino, F.; Marcelino, H. R.; Picciani, P. H. de S.; e Silva, K. G. de H.; Genre, J.; de Oliveira, A. G.; do Egito, E. S. T. Understanding Drug Release Data

through Thermodynamic Analysis. *Materials (Basel).* **2017**, *10* (6), 1–18. https://doi.org/10.3390/ma10060651.

(43) Baggi, R. B.; Kilaru, N. B. Calculation of Predominant Drug Release Mechanism Using Peppas-Sahlin Model, Part-I (Substitution Method): A Linear Regression Approach. *Asian J. Pharm. Technol.* **2016**, *6* (4), 223. https://doi.org/10.5958/2231-5713.2016.00033.7.

(44) Costa, P.; Lobo, J. M. S. Modeling and Comparison of Dissolution Profiles. *Eur. J. Pharm. Sci.* **2001**, *13* (5), 123–135.

(45) Katzhendler, I.; Hoffman, A.; Goldberger, A.; Friedman, M. Modeling of Drug Release from Erodible Tablets. *J. Pharm. Sci.* **1997**, *86* (1), 110–115. https://doi.org/10.1021/js9600538.

(46) Hadjitheodorou, A.; Kalosakas, G. Analytical and Numerical Study of Diffusion-Controlled Drug Release from Composite Spherical Matrices. *Mater. Sci. Eng. C* **2014**, *42*, 681–690. https://doi.org/10.1016/j.msec.2014.06.009.

(47) Ignacio, M.; Chubynsky, M. V; Slater, G. W. Interpreting the Weibull Fitting Parameters for Diffusion-Controlled Release Data. *Phys. A Stat. Mech. its Appl.* **2017**, *486* (C), 486–496.

(48) Bhattacharjee, S. DLS and Zeta Potential - What They Are and What They Are Not? *J. Control. Release* **2016**, *235*, 337–351. https://doi.org/10.1016/j.jconrel.2016.06.017.

(49) Crucho, C. I. C.; Barros, M. T. Polymeric Nanoparticles: A Study on the Preparation Variables and Characterization Methods. *Mater. Sci. Eng. C* **2017**, *80*, 771–784. https://doi.org/10.1016/j.msec.2017.06.004.

(50) Malvern Ltd. Malvern Zetasizer SZ User Manual. *Malvern Zetasizer SZ User Man.* **2013**, 1–250.

(51) Modena, M. M.; Rühle, B.; Burg, T. P.; Wuttke, S. Nanoparticle Characterization: What to Measure? *Adv. Mater.* **2019**, *31* (32), 1–26. https://doi.org/10.1002/adma.201901556.

(52) nanoScience Instruments. Scanning Electron Microscopy https://www.nanoscience.com/techniques/scanning-electron-microscopy/#.

(53) Abdellatif, A. A. H.; Alsowinea, A. F. Approved and Marketed Nanoparticles for Disease Targeting and Applications in COVID-19. *Nanotechnol. Rev.* **2021**, *10* (1), 1941–1977. https://doi.org/10.1515/ntrev-2021-0115.

(54) Operti, M. C.; Bernhardt, A.; Grimm, S.; Engel, A.; Figdor, C. G.; Tagit, O. PLGA-Based Nanomedicines Manufacturing: Technologies Overview and Challenges in Industrial Scale-Up. *Int. J. Pharm.* **2021**, *605* (April), 120807. https://doi.org/10.1016/j.ijpharm.2021.120807.

(55) Stavis, S. M.; Fagan, J. A.; Stopa, M.; Liddle, J. A. Nanoparticle Manufacturing-Heterogeneity through Processes to Products. *ACS Appl. Nano Mater.* **2018**, *1* (9), 4358–4385. https://doi.org/10.1021/acsanm.8b01239.

(56) Todaro, B.; Santi, M. Characterization and Functionalization Approaches for the Study of Polymeric Nanoparticles: The State of the Art in Italian Research. *Micro*. 2023, pp 9–21. https://doi.org/10.3390/micro3010002.

(57) Mohammad, A. K.; Reineke, J. J. Quantitative Detection of PLGA Nanoparticle Degradation in Tissues Following Intravenous Administration. *Mol. Pharm. A. K.,*

Reineke, J. J. (2013). Quant. Detect. PLGA nanoparticle Degrad. tissues Follow. Intraven. Adm. Mol. Pharm. 10(6), 2183–2189. https//doi.org/10.1021/mp300559v **2013**, *10* (6), 2183–2189. https://doi.org/10.1021/mp300559v.

(58) Mitchell, M. J.; Billingsley, M. M.; Haley, R. M.; Wechsler, M. E.; Peppas, N. A.; Langer, R. Engineering Precision Nanoparticles for Drug Delivery. *Nat. Rev. Drug Discov.* **2021**, *20* (2), 101–124. https://doi.org/10.1038/s41573-020-0090-8.

(59) Elsabahy, M.; Wooley, K. L. Design of Polymeric Nanoparticles for Biomedical Delivery Applications. *Chem. Soc. Rev.* **2012**, *41* (7), 2707–2717. https://doi.org/10.1039/c2cs15327k.

(60) Doane, T. L.; Burda, C. The Unique Role of Nanoparticles in Nanomedicine: Imaging, Drug Delivery and Therapy. *Chem. Soc. Rev.* **2012**, *41* (7), 2885–2911. https://doi.org/10.1039/c2cs15260f.

(61) Song, X.; Zhao, Y.; Hou, S.; Xu, F.; Zhao, R.; He, J.; Cai, Z.; Li, Y.; Chen, Q. Dual Agents Loaded PLGA Nanoparticles: Systematic Study of Particle Size and Drug Entrapment Efficiency. *Eur. J. Pharm. Biopharm.* **2008**, *69* (2), 445–453. https://doi.org/https://doi.org/10.1016/j.ejpb.2008.01.013.

(62) Dawes, G. J. S.; Fratila-Apachitei, L. E.; Mulia, K.; Apachitei, I.; Witkamp, G. J.; Duszczyk, J. Size Effect of PLGA Spheres on Drug Loading Efficiency and Release Profiles. *J. Mater. Sci. Mater. Med.* **2009**, *20* (5), 1089–1094. https://doi.org/10.1007/s10856-008-3666-0.

(63) Fredenberg, S.; Wahlgren, M.; Reslow, M.; Axelsson, A. The Mechanisms of Drug

Release in Poly(Lactic-Co-Glycolic Acid)-Based Drug Delivery Systems - A Review. *Int. J. Pharm.* **2011**, *415* (1–2), 34–52. https://doi.org/10.1016/j.ijpharm.2011.05.049.

(64) Lee, B. K.; Yun, Y.; Park, K. PLA Micro- and Nano-Particles. *Adv. Drug Deliv. Rev.* **2016**, *107* (24), 176–191. https://doi.org/10.1016/j.addr.2016.05.020.

(65) Nie, H.; Dong, Z.; Arifin, D. Y.; Hu, Y.; Wang, C. H. Core/Shell Microspheres via Coaxial Electrohydrodynamic Atomization for Sequential and Parallel Release of Drugs. *J. Biomed. Mater. Res. - Part A* **2010**, *95* (3 A), 709–716. https://doi.org/10.1002/jbm.a.32867.

(66) Zhu, D.; Wu, S.; Hu, C.; Chen, Z.; Wang, H.; Fan, F.; Qin, Y.; Wang, C.; Sun, H.; Leng, X.; et al. Folate-Targeted Polymersomes Loaded with Both Paclitaxel and Doxorubicin for the Combination Chemotherapy of Hepatocellular Carcinoma. *Acta Biomater.* **2017**, *58*, 399–412. https://doi.org/10.1016/j.actbio.2017.06.017.

(67) Chen, J.; Cui, Y.; Xu, X.; Wang, L. Q. Direct and Effective Preparation of Core-Shell PCL/PEG Nanoparticles Based on Shell Insertion Strategy by Using Coaxial Electrospray. *Colloids Surfaces A Physicochem. Eng. Asp.* **2018**, *547* (38), 1–7. https://doi.org/10.1016/j.colsurfa.2018.03.010.

(68) Liu, R.; Priestley, R. D. Rational Design and Fabrication of Core–Shell Nanoparticles through a One-Step/Pot Strategy. *J. Mater. Chem. A* **2016**, *4* (18), 6680–6692. https://doi.org/10.1039/C5TA09607C.

(69) Cardoso, M. M.; Peca, I. N.; Lopes, T.; Gardner, R.; Bicho, A. Double-Walled Poly-(D,l-Lactide-Co-Glycolide) (Plga) and Poly(l-Lactide) (Plla) Nanoparticles for the Sustained

Release of Doxorubicin. *Polymers (Basel).* **2021**, *13* (19). https://doi.org/10.3390/polym13193230.

(70) Xiao, C. Da; Shen, X. C.; Tao, L. Modified Emulsion Solvent Evaporation Method for Fabricating Core-Shell Microspheres. *Int. J. Pharm.* **2013**, *452* (1–2), 227–232. https://doi.org/10.1016/j.ijpharm.2013.05.020.

(71) Dutta, D.; Fauer, C.; Hickey, K. Tunable Delayed Controlled Release Profile from Layered Polymeric Microparticles. *J. Mater. Chem. B* **2017**, *5* (23), 4487–4498. https://doi.org/10.1039/C7TB00138J.

(72) Yeh, H. W.; Chen, D. R. In Vitro Release Profiles of PLGA Core-Shell Composite Particles Loaded with Theophylline and Budesonide. *Int. J. Pharm.* **2017**, *528* (1–2), 637–645. https://doi.org/10.1016/j.ijpharm.2017.06.032.

(73) Xia, Y.; Ribeiro, P. F.; Pack, D. W. Controlled Protein Release from Monodisperse Biodegradable Double-Wall Microspheres of Controllable Shell Thickness. *J. Control. Release* **2013**, *172*, 707–714. https://doi.org/10.1561/2200000016.

(74) Gupta, P.; Vermani, K.; Garg, S. Hydrogels: From Controlled Release to PH-Responsive Drug Delivery. *Drug Discov. Today* **2002**, *7* (10), 569–579. https://doi.org/https://doi.org/10.1016/S1359-6446(02)02255-9.

(75) Ahmed, E. M. Hydrogel: Preparation, Characterization, and Applications: A Review. *J. Adv. Res.* **2015**, *6* (2), 105–121. https://doi.org/https://doi.org/10.1016/j.jare.2013.07.006.

(76) Bhattarai, N.; Gunn, J.; Zhang, M. Chitosan-Based Hydrogels for Controlled, Localized Drug Delivery. *Adv. Drug Deliv. Rev.* **2010**, *62* (1), 83–99.

https://doi.org/https://doi.org/10.1016/j.addr.2009.07.019.

(77) Welz, M. M.; Ofner, C. M. Examination of Self-Crosslinked Gelatin as a Hydrogel for Controlled Release. *J. Pharm. Sci.* **1992**, *81* (1), 85–90. https://doi.org/https://doi.org/10.1002/jps.2600810117.

(78) Chen, J.; Park, K. Synthesis and Characterization of Superporous Hydrogel Composites. *J. Control. Release* **2000**, *65* (1), 73–82. https://doi.org/https://doi.org/10.1016/S0168-3659(99)00238-2.

(79) Treesuppharat, W.; Rojanapanthu, P.; Siangsanoh, C.; Manuspiya, H.; Ummartyotin, S. Synthesis and Characterization of Bacterial Cellulose and Gelatin-Based Hydrogel Composites for Drug-Delivery Systems. *Biotechnol. Reports* **2017**, *15*, 84–91. https://doi.org/https://doi.org/10.1016/j.btre.2017.07.002.

(80) Pal, K.; Banthia, A. K.; Majumdar, D. K. Polymeric Hydrogels: Characterization and Biomedical Applications. *Des. Monomers Polym.* **2009**, *12* (3), 197–220. https://doi.org/10.1163/156855509X436030.

(81) Agnihotri, S. A.; Mallikarjuna, N. N.; Aminabhavi, T. M. Recent Advances on Chitosan-Based Micro- and Nanoparticles in Drug Delivery. *J. Control. Release* **2004**, *100* (1), 5–28. https://doi.org/10.1016/j.jconrel.2004.08.010.

(82) Ghasemiyeh, P.; Mohammadi-Samani, S. Hydrogels as Drug Delivery Systems; Pros and Cons. *Trends Pharm. Sci.* **2019**, *5* (1), 7–24. https://doi.org/10.30476/tips.2019.81604.1002.

(83) Anitha, A.; Deepagan, V. G.; Divya Rani, V. V.; Menon, D.; Nair, S. V.; Jayakumar, R.

Preparation, Characterization, in Vitro Drug Release and Biological Studies of Curcumin Loaded Dextran Sulphate-Chitosan Nanoparticles. *Carbohydr. Polym.* **2011**, *84* (3), 1158–1164. https://doi.org/10.1016/j.carbpol.2011.01.005.

(84) Peers, S.; Montembault, A.; Ladavière, C. Chitosan Hydrogels for Sustained Drug Delivery. *J. Control. Release* **2020**, *326*, 150–163. https://doi.org/https://doi.org/10.1016/j.jconrel.2020.06.012.

(85) Xu, J.; Strandman, S.; Zhu, J. X. X.; Barralet, J.; Cerruti, M. Genipin-Crosslinked Catechol-Chitosan Mucoadhesive Hydrogels for Buccal Drug Delivery. *Biomaterials* **2015**, *37*, 395–404. https://doi.org/https://doi.org/10.1016/j.biomaterials.2014.10.024.

(86) Ren, Y.; Zhao, X.; Liang, X.; Ma, P. X.; Guo, B. Injectable Hydrogel Based on Quaternized Chitosan, Gelatin and Dopamine as Localized Drug Delivery System to Treat Parkinson's Disease. *Int. J. Biol. Macromol.* **2017**, *105*, 1079–1087. https://doi.org/https://doi.org/10.1016/j.ijbiomac.2017.07.130.

(87) Chang, G.; Chen, Y.; Li, Y.; Li, S.; Huang, F.; Shen, Y.; Xie, A. Self-Healable Hydrogel on Tumor Cell as Drug Delivery System for Localized and Effective Therapy. *Carbohydr. Polym.* **2015**, *122*, 336–342. https://doi.org/https://doi.org/10.1016/j.carbpol.2014.12.077.

(88) Zhang, W.; Jin, X.; Li, H.; Zhang, R.-R.; Wu, C.-W. Injectable and Body Temperature Sensitive Hydrogels Based on Chitosan and Hyaluronic Acid for PH Sensitive Drug Release. *Carbohydr. Polym.* **2018**, *186*, 82–90. https://doi.org/10.1016/j.carbpol.2018.01.008.

(89) Mohammed, M. A.; Syeda, J. T. M.; Wasan, K. M.; Wasan, E. K. An Overview of

Chitosan Nanoparticles and Its Application in Non-Parenteral Drug Delivery. *Pharmaceutics* **2017**, *9* (4), 53. https://doi.org/10.3390/pharmaceutics9040053.

(90) Osswald, C. R.; Kang-Mieler, J. J. Controlled and Extended Release of a Model Protein from a Microsphere-Hydrogel Drug Delivery System. *Ann. Biomed. Eng.* **2015**, *43* (11), 2609–2617. https://doi.org/10.1007/s10439-015-1314-7.

(91) Hernández-Giottonini, K. Y.; Rodríguez-Córdova, R. J.; Gutiérrez-Valenzuela, C. A.; Peñuñuri-Miranda, O.; Zavala-Rivera, P.; Guerrero-Germán, P.; Lucero-Acuña, A. PLGA Nanoparticle Preparations by Emulsification and Nanoprecipitation Techniques: Effects of Formulation Parameters. *RSC Adv.* **2020**, *10* (8), 4218–4231. https://doi.org/10.1039/c9ra10857b.

(92) Halayqa, M.; Domańska, U. PLGA Biodegradable Nanoparticles Containing Perphenazine or Chlorpromazine Hydrochloride: Effect of Formulation and Release. *Int. J. Mol. Sci.* **2014**, *15* (12), 23909–23923. https://doi.org/10.3390/ijms151223909.

(93) Iqbal, M.; Valour, J.-P.; Fessi, H.; Elaissari, A. Preparation of Biodegradable PCL Particles via Double Emulsion Evaporation Method Using Ultrasound Technique. *Colloid Polym. Sci.* **2015**, *293* (3), 861–873. https://doi.org/10.1007/s00396-014-3464-9.

(94) Zambaux, M. F.; Bonneaux, F.; Gref, R.; Maincent, P.; Dellacherie, E.; Alonso, M. J.; Labrude, P.; Vigneron, C. Influence of Experimental Parameters on the Characteristics of Poly(Lactic Acid) Nanoparticles Prepared by a Double Emulsion Method. *J. Control. Release* **1998**, *50* (1–3), 31–40. https://doi.org/10.1016/S0168-3659(97)00106-5.

(95) Shekar, M. C.; Chary, B. B.; Srinivas, S.; Kumar, B. R.; Mahendrakar, M. D.; Varma, M.

V. K. Effect of Ultrasonication on Stability of Oil in Water Emulsions. *Int. J. Drug Deliv.* **2011**, *3* (1), 133–140. https://doi.org/10.5138/ijdd.2010.0975.0215.03063.

(96) Haque, S.; Boyd, B. J.; McIntosh, M. P.; Pouton, C. W.; Kaminskas, L. M.; Whittaker, M. Suggested Procedures for the Reproducible Synthesis of Poly(d,l-Lactideco-Glycolide) Nanoparticles Using the Emulsification Solvent Diffusion Platform. *Curr. Nanosci.* **2018**, *14* (5), 448–453. https://doi.org/10.2174/1573413714666180313130235.

(97) Rao, J. P.; Geckeler, K. E. Polymer Nanoparticles: Preparation Techniques and Size-Control Parameters. *Prog. Polym. Sci.* **2011**, *36* (7), 887–913. https://doi.org/10.1016/j.progpolymsci.2011.01.001.

(98) Konwar, R.; Ahmed, A. B. Nanoparticle: An Overview of Preparation, Characterization and Application. *Int. Res. J. Pharm.* **2013**, *4* (4), 47–57. https://doi.org/10.7897/2230-8407.04408.

(99) Iqbal, M.; Zafar, N.; Fessi, H.; Elaissari, A. Double Emulsion Solvent Evaporation Techniques Used for Drug Encapsulation. *Int. J. Pharm.* **2015**, *496* (2), 173–190. https://doi.org/10.1016/j.ijpharm.2015.10.057.

(100) Geißler, D.; Gollwitzer, C.; Sikora, A.; Minelli, C.; Krumrey, M.; Resch-Genger, U. Effect of Fluorescent Staining on Size Measurements of Polymeric Nanoparticles Using DLS and SAXS. *Anal. Methods* **2015**, *7* (23), 9785–9790. https://doi.org/10.1039/c5ay02005k.

(101) Breiman, L. Random Forests. *Mach. Learn.* **2001**, *45* (1), 5–32.

(102) Schiller, S.; Hanefeld, A.; Schneider, M.; Lehr, C. M. Focused Ultrasound as a Scalable

and Contact-Free Method to Manufacture Protein-Loaded PLGA Nanoparticles. *Pharm. Res.* **2015**, *32* (9), 2995–3006. https://doi.org/10.1007/s11095-015-1681-7.

(103) O'Sullivan, J.; Murray, B.; Flynn, C.; Norton, I. Comparison of Batch and Continuous Ultrasonic Emulsification Processes. *J. Food Eng.* **2015**, *167*, 114–121. https://doi.org/10.1016/j.jfoodeng.2015.05.001.

(104) Fonte, P.; Soares, S.; Sousa, F.; Costa, A.; Seabra, V.; Reis, S.; Sarmento, B. Stability Study Perspective of the Effect of Freeze-Drying Using Cryoprotectants on the Structure of Insulin Loaded into PLGA Nanoparticles. *Biomacromolecules* **2014**, *15* (10), 3753–3765. https://doi.org/10.1021/bm5010383.

(105) Abdelwahed, W.; Degobert, G.; Stainmesse, S.; Fessi, H. Freeze-Drying of Nanoparticles: Formulation, Process and Storage Considerations. *Adv. Drug Deliv. Rev.* **2006**, *58* (15), 1688–1713. https://doi.org/10.1016/j.addr.2006.09.017.

(106) Nicolas, J.; Mura, S.; Brambilla, D.; MacKiewicz, N.; Couvreur, P. Design, Functionalization Strategies and Biomedical Applications of Targeted Biodegradable/Biocompatible Polymer-Based Nanocarriers for Drug Delivery. *Chem. Soc. Rev.* **2013**, *42* (3), 1147–1235. https://doi.org/10.1039/c2cs35265f.

(107) Ramli, R. A.; Laftah, W. A.; Hashim, S. Core-Shell Polymers: A Review. *RSC Adv.* **2013**, *3* (36), 15543–15565. https://doi.org/10.1039/c3ra41296b.

(108) Lee, T. H.; Wang, J.; Wang, C. H. Double-Walled Microspheres for the Sustained Release of a Highly Water Soluble Drug: Characterization and Irradiation Studies. *J. Control. Release* **2002**, *83* (3), 437–452. https://doi.org/10.1016/S0168-3659(02)00235-3.

(109) Bilati, U.; Allémann, E.; Doelker, E. Development of a Nanoprecipitation Method Intended for the Entrapment of Hydrophilic Drugs into Nanoparticles. *Eur. J. Pharm. Sci.* **2005**, *24* (1), 67–75. https://doi.org/https://doi.org/10.1016/j.ejps.2004.09.011.

(110) Chiesa, E.; Dorati, R.; Modena, T.; Conti, B.; Genta, I. Multivariate Analysis for the Optimization of Microfluidics-Assisted Nanoprecipitation Method Intended for the Loading of Small Hydrophilic Drugs into PLGA Nanoparticles. *Int. J. Pharm.* **2018**, *536* (1), 165–177. https://doi.org/https://doi.org/10.1016/j.ijpharm.2017.11.044.

(111) Yan, X.; Bernard, J.; Ganachaud, F. Nanoprecipitation as a Simple and Straightforward Process to Create Complex Polymeric Colloidal Morphologies. *Adv. Colloid Interface Sci.* **2021**, *294*, 102474. https://doi.org/https://doi.org/10.1016/j.cis.2021.102474.

(112) Chen, T.; Peng, Y.; Qiu, M.; Yi, C.; Xu, Z. Recent Advances in Mixing-Induced Nanoprecipitation: From Creating Complex Nanostructures to Emerging Applications beyond Biomedicine. *Nanoscale* **2023**, 3594–3609. https://doi.org/10.1039/d3nr00280b.

(113) Liu, D.; Zhang, H.; Cito, S.; Fan, J.; Mäkilä, E.; Salonen, J.; Hirvonen, J.; Sikanen, T. M.; Weitz, D. A.; Santos, H. A. Core/Shell Nanocomposites Produced by Superfast Sequential Microfluidic Nanoprecipitation. *Nano Lett.* **2017**, *17* (2), 606–614. https://doi.org/10.1021/acs.nanolett.6b03251.

(114) Lerch, F.; Ultsch, A.; Lötsch, J. Distribution Optimization: An Evolutionary Algorithm to Separate Gaussian Mixtures. *Sci. Rep.* **2020**, *10* (1), 1–10. https://doi.org/10.1038/s41598-020-57432-w.

(115) Sun, Q.; Zheng, J. Clone Granular Soils with Mixed Particle Morphological

Characteristics by Integrating Spherical Harmonics with Gaussian Mixture Model, Expectation–Maximization, and Dirichlet Process. *Acta Geotech.* **2020**, *15* (10), 2779–2796. https://doi.org/10.1007/s11440-020-00963-3.

(116) Crawford, A. The Use of Gaussian Mixture Models with Atmospheric Lagrangian Particle Dispersion Models for Density Estimation and Feature Identification. *Atmosphere*. 2020. https://doi.org/10.3390/atmos11121369.

(117) Carrasco, O. C. Gaussian Mixture Models Explained: From intuition to implementation https://towardsdatascience.com/gaussian-mixture-models-explained-6986aaf5a95 (accessed Mar 1, 2023).

(118) Roeder, K.; Wasserman, L. Practical Bayesian Density Estimation Using Mixtures of Normals. *J. Am. Stat. Assoc.* **1997**, *92* (439), 894–902. https://doi.org/10.2307/2965553.

(119) Lepeltier, E.; Bourgaux, C.; Couvreur, P. Nanoprecipitation and the "Ouzo Effect": Application to Drug Delivery Devices. *Adv. Drug Deliv. Rev.* **2014**, *71*, 86–97. https://doi.org/https://doi.org/10.1016/j.addr.2013.12.009.

(120) Frykberg, R. G.; Banks, J. Challenges in the Treatment of Chronic Wounds. *Adv. Wound Care* **2015**, *4* (9), 560–582. https://doi.org/10.1089/wound.2015.0635.

(121) Howard, J. T.; Kotwal, R. S.; Stern, C. A.; Janak, J. C.; Mazuchowski, E. L.; Butler, F. K.; Stockinger, Z. T.; Holcomb, B. R.; Bono, R. C.; Smith, D. J. Use of Combat Casualty Care Data to Assess the US Military Trauma System during the Afghanistan and Iraq Conflicts, 2001-2017. *JAMA Surg.* **2019**, *154* (7), 600–608. https://doi.org/10.1001/jamasurg.2019.0151.

(122) Cannon, J. W.; Holena, D. N.; Geng, Z.; Stewart, I. J.; Huang, Y.; Yang, W.; Mayhew, E. R.; Nessen, S. C.; Gross, K. R.; Schwab, C. W. Comprehensive Analysis of Combat Casualty Outcomes in US Service Members from the Beginning of World War II to the End of Operation Enduring Freedom. *J. Trauma Acute Care Surg.* **2020**, *89* (2S).

(123) Popivanov, G.; Mutafchiyski, V. M.; Belokonski, E. I.; Parashkevov, A. B.; Koutin, G. L. A Modern Combat Trauma. *J. R. Army Med. Corps* **2014**, *160* (1), 52–55. https://doi.org/10.1136/jramc-2013-000132.

(124) Demidova-Rice, T. N.; Hamblin, M. R.; Herman, I. M. Acute and Impaired Wound Healing: Pathophysiology and Current Methods for Drug Delivery, Part 1: Normal and Chronic Wounds: Biology, Causes, and Approaches to Care. *Adv. Skin Wound Care* **2012**, *25* (7), 304–314. https://doi.org/10.1097/01.ASW.0000416006.55218.d0.

(125) Dhivya, S.; Padma, V. V.; Santhini, E. Wound Dressings - A Review. *Biomed.* **2015**, *5* (4), 24–28. https://doi.org/10.7603/s40681-015-0022-9.

(126) Rajendran, N. K.; Kumar, S. S. D.; Houreld, N. N.; Abrahamse, H. A Review on Nanoparticle Based Treatment for Wound Healing. *J. Drug Deliv. Sci. Technol.* **2018**, *44* (January), 421–430. https://doi.org/10.1016/j.jddst.2018.01.009.

(127) Pinto, R. V; Gomes, P. S.; Fernandes, M. H.; Costa, M. E. V; Almeida, M. M. Glutaraldehyde-Crosslinking Chitosan Scaffolds Reinforced with Calcium Phosphate Spray-Dried Granules for Bone Tissue Applications. *Mater. Sci. Eng. C* **2020**, *109*, 110557. https://doi.org/https://doi.org/10.1016/j.msec.2019.110557.

(128) Antony, R.; Arun, T.; Manickam, S. T. D. A Review on Applications of Chitosan-Based

Schiff Bases. *Int. J. Biol. Macromol.* **2019**, *129*, 615–633. https://doi.org/10.1016/j.ijbiomac.2019.02.047.

(129) Wang, X.; Song, R.; Johnson, M.; A, S.; He, Z.; Milne, C.; Wang, X.; Lara-Sáez, I.; Xu, Q.; Wang, W. An Injectable Chitosan-Based Self-Healable Hydrogel System as an Antibacterial Wound Dressing. *Mater. (Basel, Switzerland)* **2021**, *14* (20). https://doi.org/10.3390/ma14205956.

(130) Omer, A. M.; Eltaweil, A. S.; El-Fakharany, E. M.; Abd El-Monaem, E. M.; Ismail, M. M. F.; Mohy-Eldin, M. S.; Ayoup, M. S. Novel Cytocompatible Chitosan Schiff Base Derivative as a Potent Antibacterial, Antidiabetic, and Anticancer Agent. *Arab. J. Sci. Eng.* **2023**. https://doi.org/10.1007/s13369-022-07588-6.

(131) Rojas Pirela, M.; Rojas, V.; Pérez Pérez, E.; Lárez Velásquez, C. Cell Encapsulation Using Chitosan: Chemical Aspects and Applications. *Av. en Quim.* **2021**, *16* (3), 89–103.

(132) Hassan, M. A.; Omer, A. M.; Abbas, E.; Baset, W. M. A.; Tamer, T. M. Preparation, Physicochemical Characterization and Antimicrobial Activities of Novel Two Phenolic Chitosan Schiff Base Derivatives. *Sci. Rep.* **2018**, *8* (1), 11416. https://doi.org/10.1038/s41598-018-29650-w.

(133) OU, A.; BO, I. Chitosan Hydrogels and Their Glutaraldehyde-Crosslinked Counterparts as Potential Drug Release and Tissue Engineering Systems - Synthesis, Characterization, Swelling Kinetics and Mechanism. *J. Phys. Chem. Biophys.* **2017**, *07* (03). https://doi.org/10.4172/2161-0398.1000256.

(134) Mirzaei B., E.; Ramazani, A.; Shafiee, M.; Danaei, M. Studies on Glutaraldehyde

Crosslinked Chitosan Hydrogel Properties for Drug Delivery Systems. *Int. J. Polym. Mater. Polym. Biomater.* **2013**, *62* (11), 605–611. https://doi.org/10.1080/00914037.2013.769165.

(135) Patel, V. R.; Amiji, M. M. Preparation and Characterization of Freeze-Dried Chitosan-Poly(Ethylene Oxide) Hydrogels for Site-Specific Antibiotic Delivery in the Stomach. *Pharm. Res.* **1996**, *13* (4), 588–593. https://doi.org/10.1023/a:1016054306763.

(136) Kurian, M.; Stevens, R.; McGrath, K. M. Towards the Development of Artificial Bone Grafts: Combining Synthetic Biomineralisation with 3D Printing. *J. Funct. Biomater.* **2019**, *10* (1). https://doi.org/10.3390/jfb10010012.

(137) Zheng, Y.; Pan, N.; Liu, Y.; Ren, X. Novel Porous Chitosan/N-Halamine Structure with Efficient Antibacterial and Hemostatic Properties. *Carbohydr. Polym.* **2021**, *253*, 117205. https://doi.org/10.1016/j.carbpol.2020.117205.

(138) Bardestani, R.; Patience, G. S.; Kaliaguine, S. Experimental Methods in Chemical Engineering: Specific Surface Area and Pore Size Distribution Measurements—BET, BJH, and DFT. *Can. J. Chem. Eng.* **2019**, *97* (11), 2781–2791. https://doi.org/https://doi.org/10.1002/cjce.23632.

Appendix

Appendix 1: MATLAB Code

Molar Ratio Analysis

```
clc,clear all, close all
% Set up the Import Options and import the data
opts = spreadsheetImportOptions("NumVariables", 33);

% Specify sheet and range
opts.Sheet = "MasterList";
opts.DataRange = "A3:AG430";

% Specify column names and types
opts.VariableNames = ["RunOrder", "Sample", "PLGACONC", "PLGA_DCMVol", "PLGAMass",
"PLGAMoles", "PVACONC", "PVAFlaskVol", "PVAEmulsVol", "PVAWashVol", "TotPVAVol",
"TotEmulsVol", "PVAFlaskMoles", "PVAEmulsMoles", "PVAWashMoles", "TotalPVAMoles",
"TotPVAMoles_molesPLGA", "EmulsPVAMoles_molesPLGA", "Amp", "Time", "ActEnergy",
"SonicPower", "SpecEnergy", "TotMolarEnergy", "EmulsMolarEnergy", "TotRatioEnergy",
"EmulRatioEnergy", "AvgHD", "StDevHD", "AvgPDI", "StDevPDI", "Dyed", "DyeConc"];
opts.VariableTypes = ["double", "string", "double", "double", "double", "double",
"double", "double", "double", "double", "double", "double", "double", "double",
"double", "double", "double", "double", "double", "double", "double", "double",
"double", "double", "double", "double", "double", "double", "double", "double",
"double", "categorical", "double"];

% Specify variable properties
opts = setvaropts(opts, "Sample", "WhitespaceRule", "preserve");
opts = setvaropts(opts, ["Sample", "Dyed"], "EmptyFieldRule", "auto");

% Import the data
AllPLGArunsnew = readtable("C:\Users\bkh0003\Documents\Experiments\PLGA
NPs\PLGA_size_modeling\AllPLGAruns_new.xlsx", opts, "UseExcel", false);


% Clear temporary variables
clear opts

SpEn=AllPLGArunsnew.SpecEnergy;
TotMolEn=AllPLGArunsnew.TotMolarEnergy;
EmulsMolEn=AllPLGArunsnew.EmulsMolarEnergy;
TotRatEn=AllPLGArunsnew.TotRatioEnergy;
EmulsRatEn=AllPLGArunsnew.EmulRatioEnergy;
TotMolRatio=AllPLGArunsnew.TotPVAMoles_molesPLGA;
EmulsMolRatio=AllPLGArunsnew.EmulsPVAMoles_molesPLGA;
AvgHD=AllPLGArunsnew.AvgHD;
AvgPDI=AllPLGArunsnew.AvgPDI;
IsDyed=AllPLGArunsnew.Dyed;
Amp=AllPLGArunsnew.Amp;
Power=AllPLGArunsnew.SonicPower;
PVAconc=AllPLGArunsnew.PVACONC;
```

```
dyedSpEn=SpEn(IsDyed=="Y");
dyedTotMolEn=TotMolEn(IsDyed=="Y");
dyedEmulsMolEn=EmulsMolEn(IsDyed=="Y");
dyedTotRatEn=TotRatEn(IsDyed=="Y");
dyedEmulRatEn=EmulsRatEn(IsDyed=="Y");
dyedTotMolRatio=TotMolRatio(IsDyed=="Y");
dyedEmulsMolRatio=EmulsMolRatio(IsDyed=="Y");
dyedHD=AvgHD(IsDyed=="Y");
dyedPDI=AvgPDI(IsDyed=="Y");
dyedAmp=Amp(IsDyed=="Y");
dyedPower=Power(IsDyed=="Y");


nondyedSpEn=SpEn(IsDyed=="N");
nondyedTotMolEn=TotMolEn(IsDyed=="N");
nondyedEmulsMolEn=EmulsMolEn(IsDyed=="N");
nondyedTotRatEn=TotRatEn(IsDyed=="N");
nondyedEmulRatEn=EmulsRatEn(IsDyed=="N");
nondyedTotMolRatio=TotMolRatio(IsDyed=="N");
nondyedEmulsMolRatio=EmulsMolRatio(IsDyed=="N");
nondyedHD=AvgHD(IsDyed=="N");
nondyedPDI=AvgPDI(IsDyed=="N");
nondyedAmp=Amp(IsDyed=="N");
nondyedPower=Power(IsDyed=="N");

HighPVAAmp=Amp(PVAconc>7 & PVAconc<9);
HighPVAPower=Power(PVAconc>7 & PVAconc<9);


logTotMolRatio=log(TotMolRatio);
logEmulsMolRatio=log(EmulsMolRatio);

lognondyedTotMolRatio=log(nondyedTotMolRatio);
lognondyedEmulsMolRatio=log(nondyedEmulsMolRatio);

% Define Edges of bins for equal number of points in each bin
nbins=7;
numpointbin_HD=floor(length(logTotMolRatio)./nbins);
numpointbin_PDI=floor(length(lognondyedTotMolRatio)./nbins);

logTotMol_SpEnHD=[logTotMolRatio,SpEn,AvgHD];
logEmulsMol_SpEnHD=[logEmulsMolRatio,SpEn,AvgHD];
logndTotMol_SpEnPDI=[lognondyedTotMolRatio,nondyedSpEn,nondyedPDI];
logndEmulsMol_SpEnPDI=[lognondyedEmulsMolRatio,nondyedSpEn,nondyedPDI];


logTotMol_SpEnHD=sortrows(logTotMol_SpEnHD,1);
logEmulsMol_SpEnHD=sortrows(logEmulsMol_SpEnHD,1);
logndTotMol_SpEnPDI=sortrows(logndTotMol_SpEnPDI,1);
logndEmulsMol_SpEnPDI=sortrows(logndEmulsMol_SpEnPDI,1);

for i=1:(nbins-1)
        Edges_HDTotMR(i+1)=logTotMol_SpEnHD(i.*numpointbin_HD);
        Edges_HDTotMR(nbins+1)=max(logTotMol_SpEnHD(:,1));
        Edges_HDTotMR(1)=0;
```

```
end
for i=1:(nbins-1)
        Edges_HDEmulsMR(i+1)=logEmulsMol_SpEnHD(i.*numpointbin_HD);
        Edges_HDEmulsMR(nbins+1)=max(logEmulsMol_SpEnHD(:,1));
        Edges_HDEmulsMR(1)=-1;
end
for i=1:(nbins-1)
        Edges_PDITotMR(i+1)=logndTotMol_SpEnPDI(i.*numpointbin_PDI);
        Edges_PDITotMR(nbins+1)=max(logndTotMol_SpEnPDI(:,1));
        Edges_PDITotMR(1)=0;
end
for i=1:(nbins-1)
        Edges_PDIEmulsMR(i+1)=logndEmulsMol_SpEnPDI(i.*numpointbin_PDI);
        Edges_PDIEmulsMR(nbins+1)=max(logndEmulsMol_SpEnPDI(:,1));
        Edges_PDIEmulsMR(1)=-1;
end


%% Total Molar Ratio Goodness of Fit Effect Analysis
% make sure to clear variables not found in first section (run first
% section again)
clc, close all
edges_HD=Edges_HDTotMR;
[Y_all,E_all]=discretize(logTotMolRatio,edges_HD);

for i=1:length(Y_all)
    HDgroup(i,1)=SpEn(i);
    HDgroup(i,Y_all(i)+1)=AvgHD(i);
end

edges_PDI=Edges_PDITotMR;
[Y_nondye,E_nondye]=discretize(lognondyedTotMolRatio,edges_PDI);
for j=1:length(Y_nondye)
    PDIgroup_nondye(j,1)=SpEn(j);
    PDIgroup_nondye(j,Y_nondye(j)+1)=nondyedPDI(j);
end

for r1=1:length(Y_all)
    for c1=1:length(edges_HD)
        if HDgroup(r1,c1)==0
            HDgroup(r1,c1)="";
        end
    end
end
for r2=1:length(Y_nondye)
    for c2=1:length(edges_PDI)
        if PDIgroup_nondye(r2,c2)==0
            PDIgroup_nondye(r2,c2)="";
        end
    end
end

numpoints_HDbins=length(HDgroup)-sum(isnan(HDgroup(:,2:end)));
numpoints_PDIbins=length(PDIgroup_nondye)-sum(isnan(PDIgroup_nondye(:,2:end)));
```

```
for k=1:nbins
    try
    [HDfit_bin,HDgof_bin]=createPowerFit_HD(HDgroup(:,1),HDgroup(:,k+1));
    HDBin_R2(k)=HDgof_bin.adjrsquare;
    close all
    catch
    HDBin_R2(k)="NaN";
    close all
    end
end

for k=1:nbins
    try

[PDIfit_bin,PDIgof_bin]=createPowerFit_PDI(PDIgroup_nondye(:,1),PDIgroup_nondye(:,k+1
));
    PDIBin_R2(k)=PDIgof_bin.adjrsquare;
    close all
    catch
    PDIBin_R2(k)="NaN";
    close all
    end
end

%
x_all=E_all(2:end);
x_nondye=E_nondye(2:end);

%
figure
plot((edges_HD(2:end)),HDBin_R2,'-*g')
title('Goodness of Fit - Adj R2 vs Tot. Molar Ratio')
xlabel('Ln(Total Molar Ratio)')
ylabel('Goodness of Fit (GOF) Adj. R2')
ylim([0 1])
hold on
plot((edges_PDI(2:end)),PDIBin_R2,'-*r')
legend('HD (nm)','PDI','Location','southeast')
hold off

numpoints_HDbins
numpoints_PDIbins

%% Emulsion Molar Ratio Goodness of Fit Effect Analysis
% make sure to clear variables not found in first section (run first
% section again)
clc

edges_HD=Edges_HDEmulsMR;
[Y_all,E_all]=discretize(logEmulsMolRatio,edges_HD);

for i=1:length(Y_all)
    HDgroup(i,1)=SpEn(i);
    HDgroup(i,Y_all(i)+1)=AvgHD(i);
end
```

```
edges_PDI=Edges_PDIEmulsMR;
[Y_nondye,E_nondye]=discretize(lognondyedEmulsMolRatio,edges_PDI);
for j=1:length(Y_nondye)
    PDIgroup_nondye(j,1)=SpEn(j);
    PDIgroup_nondye(j,Y_nondye(j)+1)=nondyedPDI(j);
end

for r1=1:length(Y_all)
    for c1=1:length(edges_HD)
        if HDgroup(r1,c1)==0
            HDgroup(r1,c1)="";
        end
    end
end
for r2=1:length(Y_nondye)
    for c2=1:length(edges_PDI)
        if PDIgroup_nondye(r2,c2)==0
            PDIgroup_nondye(r2,c2)="";
        end
    end
end

numpoints_HDbins=length(HDgroup)-sum(isnan(HDgroup(:,2:end)));
numpoints_PDIbins=length(PDIgroup_nondye)-sum(isnan(PDIgroup_nondye(:,2:end)));

for k=1:nbins
    try
    [HDfit_bin,HDgof_bin]=createPowerFit_HD(HDgroup(:,1),HDgroup(:,k+1));
    HDBin_R2(k)=HDgof_bin.adjrsquare;
    close all
    catch
    HDBin_R2(k)="NaN";
    close all
    end
end

for k=1:nbins
    try

[PDIfit_bin,PDIgof_bin]=createPowerFit_PDI(PDIgroup_nondye(:,1),PDIgroup_nondye(:,k+1
));
    PDIBin_R2(k)=PDIgof_bin.adjrsquare;
    close all
    catch
    PDIBin_R2(k)="NaN";
    close all
    end
end

%
x_all=E_all(2:end);
x_nondye=E_nondye(2:end);

%
```

```
figure
plot((edges_HD(2:end)),HDBin_R2,'-*g')
title('Goodness of Fit - Adj R2 vs Emuls. Molar Ratio')
xlabel('Ln(Emuls Molar Ratio)')
ylabel('Goodness of Fit (GOF) Adj. R2')

hold on
plot((edges_PDI(2:end)),PDIBin_R2,'-*r')
legend('HD (nm)','PDI','Location','southeast')
numpoints_HDbins
numpoints_PDIbins


%% Find Fraction of PDI In each Molar Ratio that are "Monodisperse"
% Run first section before running this so as to clear any dual used
% variables
clc, close all
edgesTot_PDI=Edges_PDITotMR;
[YTot_nondye,ETot_nondye]=discretize(lognondyedTotMolRatio,edgesTot_PDI);
for j=1:length(YTot_nondye)
    PDIgroupTot_nondye(j,1)=SpEn(j);
    PDIgroupTot_nondye(j,YTot_nondye(j)+1)=nondyedPDI(j);
end

edgesEmuls_PDI=Edges_PDIEmulsMR;
[YEmuls_nondye,EEmuls_nondye]=discretize(lognondyedEmulsMolRatio,edgesEmuls_PDI);
for j=1:length(YEmuls_nondye)
    PDIgroupEmuls_nondye(j,1)=SpEn(j);
    PDIgroupEmuls_nondye(j,YEmuls_nondye(j)+1)=nondyedPDI(j);
end

for r1=1:length(YTot_nondye)
    for c1=1:length(edgesTot_PDI)
        if PDIgroupTot_nondye(r1,c1)>0 && PDIgroupTot_nondye(r1,c1)<=0.1
            MondispersePDI_Tot(r1,c1)=1;
        else
            MondispersePDI_Tot(r1,c1)=0;
        end
    end
end
for r2=1:length(YEmuls_nondye)
    for c2=1:length(edgesEmuls_PDI)
        if PDIgroupEmuls_nondye(r2,c2)>0 && PDIgroupEmuls_nondye(r2,c2)<=0.1
            MondispersePDI_Emuls(r2,c2)=1;
        else
            MondispersePDI_Emuls(r2,c2)=0;
        end
    end
end



for r1=1:length(YTot_nondye)
    for c1=1:length(edgesTot_PDI)
        if PDIgroupTot_nondye(r1,c1)==0
```

```
            PDIgroupTot_nondye(r1,c1)="";
        end
    end
end
for r2=1:length(YEmuls_nondye)
    for c2=1:length(edgesEmuls_PDI)
        if PDIgroupEmuls_nondye(r2,c2)==0
            PDIgroupEmuls_nondye(r2,c2)="";
        end
    end
end


numpoints_TotPDIbins=length(PDIgroupTot_nondye)-
sum(isnan(PDIgroupTot_nondye(:,2:end)));
numpoints_EmulsPDIbins=length(PDIgroupEmuls_nondye)-
sum(isnan(PDIgroupEmuls_nondye(:,2:end)));

fits_Total=sum(MondispersePDI_Tot);
fits_Emuls=sum(MondispersePDI_Emuls);

PercentMonodisperse_TotRatio=fits_Total(2:end)./numpoints_TotPDIbins;
PercentMonodisperse_EmulsRatio=fits_Emuls(2:end)./numpoints_EmulsPDIbins;

tiledlayout(2,1)
nexttile
plot((edgesTot_PDI(2:end)),PercentMonodisperse_TotRatio,'-*k')
xlabel('Ln(Total Molar Ratio)')
ylabel('Percent Monodisperse')
title('% Monodispersity vs Total Molar Ratio')
xlim([2 5.5])
ylim([0 1])

nexttile
plot((edgesEmuls_PDI(2:end)),PercentMonodisperse_EmulsRatio,'-*b')
xlabel('Ln(Emulsion Molar Ratio)')
ylabel('Percent Monodisperse')
title('% Monodispersity vs Emulsion Molar Ratio')

ylim([0 1])
```

Batch-to-Continuous Sonication Scale-Up

```
SonicationFreq=20000;       %   Hz
AmpPctSetting=[0:5:100];   % amplitude % setting range


% Batch Probe Sonication Specification
batchprobeDiam=0.16;        % cm
batchprobeAmp=320*(1E-4);   % cm
batchprobeHeight=4.8;       % cm
```

```
batchprobeSA=batchprobeDiam.*pi()*batchprobeHeight+2*pi()*((batchprobeDiam/2).^2);
% cm2
batchprobeTipAmp=(AmpPctSetting./100).*batchprobeAmp;   % cm
batchVibDistRate=(4.*batchprobeTipAmp).*SonicationFreq; % cm/s
coefs1=polyfit(AmpPctSetting,batchVibDistRate,1);
batchprobeVibDis_slope=coefs1(1);

% FlowCell Sonication
contprobeDiam=2.54;     % cm
contprobeAmp=35*(1E-4);  % cm
contprobeHeight=43.18;  % cm
contprobeSA=contprobeDiam.*pi()*contprobeHeight+2*pi()*((contprobeDiam/2).^2);
% cm2
contprobeTipAmp=(AmpPctSetting./100).*contprobeAmp;   % cm
contVibDistRate=(4.*contprobeTipAmp).*SonicationFreq; % cm/s
coefs2=polyfit(AmpPctSetting,contVibDistRate,1);
contprobeVibDis_slope=coefs2(1);

% FloCell Volume Specification
FlowCellVol=400;        % cm3
FlowMaxVolRate=333.33;   % cm3/s


% Batch Probe Sonication Data
% Set up the Import Options and import the data
opts = spreadsheetImportOptions("NumVariables", 29);

% Specify sheet and range
opts.Sheet = "EnergyRuns";
opts.DataRange = "A3:AC366";

% Specify column names and types
opts.VariableNames = ["PLGACONC", "PLGA_DCMVol", "PLGAMass", "PLGAMoles", "PVACONC",
"PVAFlaskVol", "PVAEmulsVol", "PVAWashVol", "TotPVAVol", "TotEmulsVol",
"PVAFlaskMoles", "PVAEmulsMoles", "PVAWashMoles", "TotalPVAMoles",
"TotPVAMoles_molesPLGA", "EmulsPVAMoles_molesPLGA", "Amp", "Time", "ActEnergy",
"SonicPower", "SpecEnergy", "TotMolarEnergy", "EmulsMolarEnergy", "TotRatioEnergy",
"EmulRatioEnergy", "AvgHD", "StDevHD", "AvgPDI", "StDevPDI"];
opts.VariableTypes = ["double", "double", "double", "double", "double", "double",
"double", "double", "double", "double", "double", "double", "double", "double",
"double", "double", "double", "double", "double", "double", "double", "double",
"double", "double", "double", "double", "double", "double", "double"];

% Import the data
BatchToContinuous =
readtable("G:\Dissertation_backupfiles\DataFiles_for_Dissertation\PLGA_size_modeling_
backup\BatchToContinuousCalcs.xlsx", opts, "UseExcel", false);


% Clear temporary variables
clear opts
batchEmulsAmp=BatchToContinuous.Amp;    % percent
batchEmulsTime=BatchToContinuous.Time;   % time (s)
batchEmulsPower=BatchToContinuous.SonicPower;  % power (W)
batchEmulsSpEn=BatchToContinuous.SpecEnergy;   % J/emulsion volume
```

```
batchEmulsVol=BatchToContinuous.TotEmulsVol;    % emulsion volume (mL)



% Probe Vibrational Distance Calculations
batchEmulsVibRate=batchprobeVibDis_slope.*batchEmulsAmp;    % cm/s
batchEmulsTotVibDist=batchEmulsVibRate.*batchEmulsTime;     % cm
batchVibDist_EmulsVol=batchEmulsTotVibDist./batchEmulsVol;  % cm/cm3
batchVibDistRate_EmulsVol=batchVibDist_EmulsVol./batchEmulsTime;    %cm/s/(cm3)

batchprobe_Lc=batchEmulsVol./batchprobeSA;          % cm3/cm2 = cm
batchVibDis_Lc=batchEmulsTotVibDist.*batchprobe_Lc;  %cm*cm = cm2
lnSpEn=log(batchEmulsSpEn);


%CREATEFIT(LNSPEN,BATCHVIBDIS_LC)
%  Create a fit.
%
%  Data for 'ExponentialFit' fit:
%      X Input: lnSpEn
%      Y Output: batchVibDis_Lc
%  Output:
%      fitresult : a fit object representing the fit.
%      gof : structure with goodness-of fit info.
%
%  See also FIT, CFIT, SFIT.

%  Auto-generated by MATLAB on 14-Feb-2023 11:58:50


% Fit: 'ExponentialFit'.
[xData, yData] = prepareCurveData( lnSpEn, batchVibDis_Lc );

% Set up fittype and options.
ft = fittype( 'exp1' );
opts = fitoptions( 'Method', 'NonlinearLeastSquares' );
opts.Display = 'Off';
opts.Robust = 'Bisquare';
opts.StartPoint = [1.28846584410963e-06 1.01379260254063];

% Fit model to data.
[fitresult, gof] = fit( xData, yData, ft, opts );

FlowCell_Lc=FlowCellVol./contprobeSA;       % cm3/cm2 = cm


% Power Law for Specific Energy vs Size and PDI
DesiredSize=[175 200 225 250 275 300];  % nm

FlowAmplitude=[20 30 40 50 60 70 80 90 100];      % power setting of flowcell probe

for i=1:length(FlowAmplitude)
    for j=1:length(DesiredSize)

    ReqSpEn=exp((log((DesiredSize(j)-78.42)./403.2))./-0.2265);
```

```
    lnReqSpEn=log(ReqSpEn);
    ReqVibDist_Lc=(fitresult.a).*exp(fitresult.b.*lnReqSpEn);
    ReqFlow_VibDistTot=ReqVibDist_Lc./FlowCell_Lc;      % cm
    FlowVibRate=FlowAmplitude(i).*contprobeVibDis_slope;   % cm/s at power setting
    ReqFlow_VibTime=ReqFlow_VibDistTot./FlowVibRate;    % required residence times
(sec) to achieve total vibrational distance over flowcell probe
    ReqFlow_VolFlowRate(i,j)=(FlowCellVol./ReqFlow_VibTime)*60; % mL/min
    end
end

plot(FlowAmplitude,ReqFlow_VolFlowRate(:,1),'-
r',FlowAmplitude,ReqFlow_VolFlowRate(:,2),'-
g',FlowAmplitude,ReqFlow_VolFlowRate(:,3),'-
b',FlowAmplitude,ReqFlow_VolFlowRate(:,4),'-
c',FlowAmplitude,ReqFlow_VolFlowRate(:,5),'-
m',FlowAmplitude,ReqFlow_VolFlowRate(:,6),'-k');
xlim([20 100])
ylim([0 350])
yticks([0:25:350])

grid on
xlabel('Amplitude Power Setting (%)')
ylabel('Volumetric Flowrate (mL/min)')
legend('D=175 nm','D=200 nm','D=225 nm','D=250 nm','D=275 nm','D=300
nm','Location','northwest');
```

Release Fitting

```
%% Import Release Data
clc,clear all


density_PLLA=1.15E-18;  % mg/nm3
density_PLGA=1.28E-18;  %  mg/nm3

%Constants: used for calculations
MW_Dye=350.46/1000;      % mg/umol

% Pure PLGA
clc

% Set up the Import Options and import the data
opts = spreadsheetImportOptions("NumVariables", 25);

% Specify sheet and range
opts.Sheet = "PurePLGA";
opts.DataRange = "A2:Y19";

% Specify column names and types
```

```
opts.VariableNames = ["Timehr", "F12", "Y1", "StdevY1", "F13", "Y2", "StdevY2",
"F14", "Y3", "StdevY3", "F15", "Y4", "StdevY4", "F16", "Y5", "StdevY5", "F17", "Y6",
"StdevY6", "F18", "Y7", "StdevY7", "F19", "Y8", "StdevY8"];
opts.VariableTypes = ["double", "double", "double", "double", "double", "double",
"double", "double", "double", "double", "double", "double", "double", "double",
"double", "double", "double", "double", "double", "double", "double", "double",
"double", "double", "double"];

% Import the data
tbl =
readtable("E:\Dissertation_backupfiles\DataFiles_for_Dissertation\NPRelease\UpdatedRe
leaseFitData.xlsx", opts, "UseExcel", false);

% Convert to output type
Timehr = tbl.Timehr;
F12 = tbl.F12;
Y1 = tbl.Y1;
StdevY1 = tbl.StdevY1;
F13 = tbl.F13;
Y2 = tbl.Y2;
StdevY2 = tbl.StdevY2;
F14 = tbl.F14;
Y3 = tbl.Y3;
StdevY3 = tbl.StdevY3;
F15 = tbl.F15;
Y4 = tbl.Y4;
StdevY4 = tbl.StdevY4;
F16 = tbl.F16;
Y5 = tbl.Y5;
StdevY5 = tbl.StdevY5;
F17 = tbl.F17;
Y6 = tbl.Y6;
StdevY6 = tbl.StdevY6;
F18 = tbl.F18;
Y7 = tbl.Y7;
StdevY7 = tbl.StdevY7;
F19 = tbl.F19;
Y8 = tbl.Y8;
StdevY8 = tbl.StdevY8;


% Clear temporary variables
clear opts tbl

% Data prep for fits
t=Timehr;
SampleName=['F12';'F13';'F14';'F15';'F16';'F17';'F18';'F19'];
Mt_Minf=[Y1,Y2,Y3,Y4,Y5,Y6,Y7,Y8];
D=[F12(1),F13(1),F14(1),F15(1),F16(1),F17(1),F18(1),F19(1)];
R=D./2;                         % radii of NPs
Dye=[F12(2),F13(2),F14(2),F15(2),F16(2),F17(2),F18(2),F19(2)];
Co=Dye.*density_PLGA;           % mg dye/nm3 NP


clc
```

```
Mvalidrange=Mt_Minf <= 0.6;
t60=Mvalidrange.*t;
Mt_Minf60=Mvalidrange.*Mt_Minf;

for r=2:length(t)
    for c=1:length(D)
        if t60(r,c) == 0
            t60(r,c)="";
            Mt_Minf60(r,c)="";
        end
    end
end


%% Pure PLLA1
clc,clear all
density_PLLA=1.15E-18;  % mg/nm3
density_PLGA=1.28E-18;  %  mg/nm3

%Constants: used for calculations
MW_Dye=350.46/1000;      % mg/umol
% Set up the Import Options and import the data
opts = spreadsheetImportOptions("NumVariables", 16);

% Specify sheet and range
opts.Sheet = "PurePLLA1";
opts.DataRange = "A2:P44";

% Specify column names and types
opts.VariableNames = ["Timehr", "PLLA21", "Y1", "StdevY1", "PLLA22", "Y2", "StdevY2",
"PLLA23", "Y3", "StdevY3", "PLLA24", "Y4", "StdevY4", "PLLA25", "Y5", "StdevY5"];
opts.VariableTypes = ["double", "double", "double", "double", "double", "double",
"double", "double", "double", "double", "double", "double", "double", "double",
"double", "double"];

% Import the data
tbl =
readtable("E:\Dissertation_backupfiles\DataFiles_for_Dissertation\NPRelease\UpdatedRe
leaseFitData.xlsx", opts, "UseExcel", false);

% Convert to output type
Timehr = tbl.Timehr;
PLLA21 = tbl.PLLA21;
Y1 = tbl.Y1;
StdevY1 = tbl.StdevY1;
PLLA22 = tbl.PLLA22;
Y2 = tbl.Y2;
StdevY2 = tbl.StdevY2;
PLLA23 = tbl.PLLA23;
Y3 = tbl.Y3;
StdevY3 = tbl.StdevY3;
PLLA24 = tbl.PLLA24;
Y4 = tbl.Y4;
StdevY4 = tbl.StdevY4;
PLLA25 = tbl.PLLA25;
```

```
Y5 = tbl.Y5;
StdevY5 = tbl.StdevY5;

% Clear temporary variables
clear opts tbl

t=Timehr;
SampleName=['PLLA21';'PLLA22';'PLLA23';'PLLA24';'PLLA25'];
Mt_Minf=[Y1,Y2,Y3,Y4,Y5];
D=[PLLA21(1),PLLA22(1),PLLA23(1),PLLA24(1),PLLA25(1)];
R=D./2;                         % radii of NPs
Dye=[PLLA21(2),PLLA22(2),PLLA23(2),PLLA24(2),PLLA25(2)];
Co=Dye.*density_PLLA;           % mg dye/nm3 NP

clc
Mvalidrange=Mt_Minf <= 0.6;
t60=Mvalidrange.*t;
Mt_Minf60=Mvalidrange.*Mt_Minf;

for r=2:length(t)
    for c=1:length(D)
        if t60(r,c) == 0
            t60(r,c)="";
            Mt_Minf60(r,c)="";
        end
    end
end


%% Pure PLLA2
clc,clear all
density_PLLA=1.15E-18;  % mg/nm3
density_PLGA=1.28E-18;  %  mg/nm3

%Constants: used for calculations
MW_Dye=350.46/1000;      % mg/umol
% Set up the Import Options and import the data
opts = spreadsheetImportOptions("NumVariables", 13);

% Specify sheet and range
opts.Sheet = "PurePLLA2";
opts.DataRange = "A2:M58";

% Specify column names and types
opts.VariableNames = ["Timehr", "PPLLA6", "Y1", "StdevY1", "PPLLA7", "Y2", "StdevY2",
"PPLLA9", "Y3", "StdevY3", "PPLLA10", "Y4", "StdevY4"];
opts.VariableTypes = ["double", "double", "double", "double", "double", "double",
"double", "double", "double", "double", "double", "double", "double"];

% Import the data
tbl =
readtable("E:\Dissertation_backupfiles\DataFiles_for_Dissertation\NPRelease\UpdatedRe
leaseFitData.xlsx", opts, "UseExcel", false);

% Convert to output type
```

```
Timehr = tbl.Timehr;
PPLLA6 = tbl.PPLLA6;
Y1 = tbl.Y1;
StdevY1 = tbl.StdevY1;
PPLLA7 = tbl.PPLLA7;
Y2 = tbl.Y2;
StdevY2 = tbl.StdevY2;
PPLLA9 = tbl.PPLLA9;
Y3 = tbl.Y3;
StdevY3 = tbl.StdevY3;
PPLLA10 = tbl.PPLLA10;
Y4 = tbl.Y4;
StdevY4 = tbl.StdevY4;

% Clear temporary variables
clear opts tbl
t=Timehr;
SampleName=['PPLLA7';'PPLLA8';'PPLLA9';'PLLA10'];
Mt_Minf=[Y1,Y2,Y3,Y4];
D=[PPLLA6(1),PPLLA7(1),PPLLA9(1),PPLLA10(1)];
R=D./2;                         % radii of NPs
Dye=[PPLLA6(2),PPLLA7(2),PPLLA9(2),PPLLA10(2)];
Co=Dye.*density_PLLA;           % mg dye/nm3 NP

clc
Mvalidrange=Mt_Minf <= 0.6;
t60=Mvalidrange.*t;
Mt_Minf60=Mvalidrange.*Mt_Minf;

for r=2:length(t)
    for c=1:length(D)
        if t60(r,c) == 0
            t60(r,c)="";
            Mt_Minf60(r,c)="";
        end
    end
end
%% Chiosan-Shell
density_PLLA=1.15E-18;  % mg/nm3
density_PLGA=1.28E-18;  %  mg/nm3

%Constants: used for calculations
MW_Dye=350.46/1000;      % mg/umol
% Set up the Import Options and import the data
opts = spreadsheetImportOptions("NumVariables", 22);

% Specify sheet and range
opts.Sheet = "Chit_Shell";
opts.DataRange = "A2:V28";

% Specify column names and types
opts.VariableNames = ["Timehr", "CHIT1", "Y1", "StdevY1", "CHIT2", "Y2", "StdevY2",
"CHIT3", "Y3", "StdevY3", "CHIT4", "Y4", "StdevY4", "CHIT5", "Y5", "StdevY5",
"CHIT6", "Y6", "StdevY6", "CHIT7", "Y7", "StdevY7"];
```

```
opts.VariableTypes = ["double", "double", "double", "double", "double", "double",
"double", "double", "double", "double", "double", "double", "double", "double",
"double", "double", "double", "double", "string", "double", "double", "string"];

% Specify variable properties
opts = setvaropts(opts, ["StdevY6", "StdevY7"], "WhitespaceRule", "preserve");
opts = setvaropts(opts, ["StdevY6", "StdevY7"], "EmptyFieldRule", "auto");

% Import the data
tbl =
readtable("E:\Dissertation_backupfiles\DataFiles_for_Dissertation\NPRelease\UpdatedRe
leaseFitData.xlsx", opts, "UseExcel", false);

% Convert to output type
Timehr = tbl.Timehr;
CHIT1 = tbl.CHIT1;
Y1 = tbl.Y1;
StdevY1 = tbl.StdevY1;
CHIT2 = tbl.CHIT2;
Y2 = tbl.Y2;
StdevY2 = tbl.StdevY2;
CHIT3 = tbl.CHIT3;
Y3 = tbl.Y3;
StdevY3 = tbl.StdevY3;
CHIT4 = tbl.CHIT4;
Y4 = tbl.Y4;
StdevY4 = tbl.StdevY4;
CHIT5 = tbl.CHIT5;
Y5 = tbl.Y5;
StdevY5 = tbl.StdevY5;
CHIT6 = tbl.CHIT6;
Y6 = tbl.Y6;
StdevY6 = tbl.StdevY6;
CHIT7 = tbl.CHIT7;
Y7 = tbl.Y7;
StdevY7 = tbl.StdevY7;

% Clear temporary variables
clear opts tbl


t=Timehr;
SampleName=['CHIT1';'CHIT2';'CHIT3';'CHIT4';'CHIT5';'CHIT6';'CHIT7'];
Mt_Minf=[Y1,Y2,Y3,Y4,Y5,Y6,Y7];
D=[CHIT1(1),CHIT2(1),CHIT3(1),CHIT4(1),CHIT5(1),CHIT6(1),CHIT7(1)];
R=D./2;                         % radii of NPs
Dye=[CHIT1(2),CHIT2(2),CHIT3(2),CHIT4(2),CHIT5(2),CHIT6(2),CHIT7(2)];
Co=Dye.*density_PLGA;           % mg dye/nm3 NP

clc
Mvalidrange=Mt_Minf <= 0.6;
t60=Mvalidrange.*t;
Mt_Minf60=Mvalidrange.*Mt_Minf;

for r=2:length(t)
```

```
    for c=1:length(D)
        if t60(r,c) == 0
            t60(r,c)="";
            Mt_Minf60(r,c)="";
        end
    end
end
%% HiMWPLLA & PCL
density_PLLA=1.15E-18;  % mg/nm3
density_PLGA=1.28E-18;  %  mg/nm3

%Constants: used for calculations
MW_Dye=350.46/1000;      % mg/umol
% Set up the Import Options and import the data
opts = spreadsheetImportOptions("NumVariables", 13);

% Specify sheet and range
opts.Sheet = "HIPLLA_PCL";
opts.DataRange = "A2:M67";

% Specify column names and types
opts.VariableNames = ["Timehr", "HiMWPLLA1", "Y1", "StdevY1", "HiMWPLLA2", "Y2",
"StdevY2", "PCL1", "Y3", "StdevY3", "PCL2", "Y4", "StdevY4"];
opts.VariableTypes = ["double", "double", "double", "double", "double", "double",
"double", "double", "double", "double", "double", "double", "double"];

% Import the data
tbl =
readtable("E:\Dissertation_backupfiles\DataFiles_for_Dissertation\NPRelease\UpdatedRe
leaseFitData.xlsx", opts, "UseExcel", false);

% Convert to output type
Timehr = tbl.Timehr;
HiMWPLLA1 = tbl.HiMWPLLA1;
Y1 = tbl.Y1;
StdevY1 = tbl.StdevY1;
HiMWPLLA2 = tbl.HiMWPLLA2;
Y2 = tbl.Y2;
StdevY2 = tbl.StdevY2;
PCL1 = tbl.PCL1;
Y3 = tbl.Y3;
StdevY3 = tbl.StdevY3;
PCL2 = tbl.PCL2;
Y4 = tbl.Y4;
StdevY4 = tbl.StdevY4;

% Clear temporary variables
clear opts tbl

t=Timehr;
SampleName=['HIPLLA1';'HIPLLA2';'PCLNPS1';'PCLNPS2'];
Mt_Minf=[Y1,Y2,Y3,Y4];
D=[HiMWPLLA1(1),HiMWPLLA2(1),PCL1(1),PCL2(1)];
R=D./2;                            % radii of NPs
Dye=[HiMWPLLA1(2),HiMWPLLA2(2),PCL1(2),PCL2(2)];
```

```
Co=Dye.*density_PLGA;           % mg dye/nm3 NP

clc
Mvalidrange=Mt_Minf <= 0.6;
t60=Mvalidrange.*t;
Mt_Minf60=Mvalidrange.*Mt_Minf;

for r=2:length(t)
    for c=1:length(D)
        if t60(r,c) == 0
            t60(r,c)="";
            Mt_Minf60(r,c)="";
        end
    end
end
%% Core/Shell PLGA/PLLA NPs
clc, clear all
density_PLLA=1.15E-18;  % mg/nm3
density_PLGA=1.28E-18;  %  mg/nm3

%Constants: used for calculations
MW_Dye=350.46/1000;      % mg/umol
% Set up the Import Options and import the data
opts = spreadsheetImportOptions("NumVariables", 19);

% Specify sheet and range
opts.Sheet = "CoreShell";
opts.DataRange = "A2:S69";

% Specify column names and types
opts.VariableNames = ["Timehr", "P13", "Y1", "StdevY1", "P16", "Y2", "StdevY2",
"P24", "Y3", "StdevY3", "P17", "Y4", "StdevY4", "P18", "Y5", "StdevY5", "P20", "Y6",
"StdevY6"];
opts.VariableTypes = ["double", "double", "double", "double", "double", "double",
"double", "double", "double", "double", "double", "double", "double", "double",
"double", "double", "double", "double", "double"];

% Import the data
tbl =
readtable("E:\Dissertation_backupfiles\DataFiles_for_Dissertation\NPRelease\UpdatedRe
leaseFitData.xlsx", opts, "UseExcel", false);

% Convert to output type
Timehr = tbl.Timehr;
P13 = tbl.P13;
Y1 = tbl.Y1;
StdevY1 = tbl.StdevY1;
P16 = tbl.P16;
Y2 = tbl.Y2;
StdevY2 = tbl.StdevY2;
P24 = tbl.P24;
Y3 = tbl.Y3;
StdevY3 = tbl.StdevY3;
P17 = tbl.P17;
Y4 = tbl.Y4;
```

```
StdevY4 = tbl.StdevY4;
P18 = tbl.P18;
Y5 = tbl.Y5;
StdevY5 = tbl.StdevY5;
P20 = tbl.P20;
Y6 = tbl.Y6;
StdevY6 = tbl.StdevY6;

% Clear temporary variables
clear opts tbl
t=Timehr;
SampleName=['P13';'P16';'P24';'P17';'P18';'P20'];
Mt_Minf=[Y1,Y2,Y3,Y4,Y5,Y6];
D=[P13(1),P16(1),P24(1),P17(1),P18(1),P20(1)];
R=D./2;                         % radii of NPs
Dye=[P13(2),P16(2),P24(2),P17(2),P18(2),P20(2)];
Co=Dye.*density_PLGA;           % mg dye/nm3 NP

clc
Mvalidrange=Mt_Minf <= 0.6;
t60=Mvalidrange.*t;
Mt_Minf60=Mvalidrange.*Mt_Minf;

for r=2:length(t)
    for c=1:length(D)
        if t60(r,c) == 0
            t60(r,c)="";
            Mt_Minf60(r,c)="";
        end
    end
end

%% Release Model Fits

% Korsmeyer-Peppas
%only accounts for 60% of release
% Mt/Minf=k*(t^n)
clc,close all

for i=1:length(D)
    [KPfit,KPgof]=KorsmeyerPeppasFit(t60(:,i),Mt_Minf60(:,i));

    kKP(i)=KPfit.kKP;
    nKP(i)=KPfit.nKP;
    R2_KP(i)=KPgof.rsquare;
    AdjR2_KP(i)=KPgof.adjrsquare;
    RMSE_KP(i)=KPgof.rmse;
    close all
end

% Peppas-Sahlin
for i=1:length(D)
    [PSfit,PSgof]=PeppasSahlinFit(t60(:,i),Mt_Minf60(:,i));

    k1PS(i)=PSfit.k1PS;
```

```
    k2PS(i)=PSfit.k2PS;
    mPS(i)=PSfit.mPS;
    R2_PS(i)=PSgof.rsquare;
    AdjR2_PS(i)=PSgof.adjrsquare;
    RMSE_PS(i)=PSgof.rmse;
    close all
end

%
% Hopfenberg
%Mt/Minf=1-(1-k0*t/CLr)^n
clc
for i=1:length(D)

    A_Hpf=Co(i).*R(i);    %hopfenberg constant (Co*r)
    x_Hpf=t(1:end);
    x_Hpf=x_Hpf';
    y_Hpf=Mt_Minf(1:end,i);
    y_Hpf=y_Hpf';

    X_Hpf=1-nthroot((1-y_Hpf),3);
    k_Hpf=(A_Hpf*X_Hpf)/x_Hpf;
    k_HopfFit(i)=k_Hpf;


    f_Hpf=1-((1-((k_Hpf.*x_Hpf)./(A_Hpf))).^3);

    J_Hpf=sum((f_Hpf-y_Hpf).^2);
    S_Hpf=sum((y_Hpf-mean(y_Hpf)).^2);
    R2_Hpf(i)=1-(J_Hpf/S_Hpf);
    AdjR2_Hpf(i)=1-((length(y_Hpf)-1)/(length(y_Hpf)-2))*(J_Hpf/S_Hpf);
    RMSE_Hpf(i)=sqrt(J_Hpf./length(y_Hpf));
end

% Higuchi
% Mt/Minf = kH(t^0.5)
for i=1:length(D)
    [Higfit,Higgof]=HiguchiFit(t,Mt_Minf(:,i));
    nHig=0.5;
    kHig(i)=Higfit.kHig;
    R2_Hig(i)=Higgof.rsquare;
    AdjR2_Hig(i)=Higgof.adjrsquare;
    RMSE_Hig(i)=Higgof.rmse;
    close all
end

% Weibull
% Mt/Minf=[1-exp((t-T)^b/a))
for i=1:length(D)
    [WBfit,WBgof]=WeibullFit(t,Mt_Minf(:,i));

    a_WB(i)=WBfit.aWB;
    b_WB(i)=WBfit.b;
    T_WB=0;
    R2_WB(i)=WBgof.rsquare;
```

```
    AdjR2_WB(i)=WBgof.adjrsquare;
    RMSE_WB(i)=WBgof.rmse;
    close all
end
%%
close all
scatter(2.*R,k_HopfFit./Co)



%% Table of all results once have been run
clc
% Print Results and Plot
    %For copy and paste
    SampleName=cellstr(SampleName);
    PolymerName='CoreShell';

for i=1:length(D)
    fprintf('%s-%.0f - %s - %.1f nm \tCumulative Release Kinetic Model Fit 
Results:\n',PolymerName,i,SampleName{i},R(i))
    fprintf('Model\tConstants\t\t\tR2\tAdj R2\tRMSE\n');
    fprintf('Korsmeyer-
Peppas(n,k):\t%4.4f\t%4.4f\t\t%4.4f\t%4.4f\t%4.4f\n',nKP(i),kKP(i),R2_KP(i),AdjR2_KP(
i),RMSE_KP(i));
    fprintf('Peppas-
Sahlin(k1,k2,m):\t%4.4f\t%4.4e\t%4.4f\t%4.4f\t%4.4f\t%4.4f\n',k1PS(i),k2PS(i),mPS(i),
R2_PS(i),AdjR2_PS(i),RMSE_PS(i));

fprintf('Higuchi(n,k):\t%4.4f\t%4.4f\t\t%4.4f\t%4.4f\t%4.4f\n',nHig,kHig(i),R2_Hig(i)
,AdjR2_Hig(i),RMSE_Hig(i));

fprintf('Hopfenberg(k0):\t%4.4e\t\t\t%4.4f\t%4.4f\t%4.4f\n',k_HopfFit(i),R2_Hpf(i),Ad
jR2_Hpf(i),RMSE_Hpf(i));

fprintf('Weibull(a,b,T):\t%4.4f\t%4.4e\t%4.4f\t%4.4f\t%4.4f\t%4.4f\n\n',a_WB(i),b_WB(
i),T_WB,R2_WB(i),AdjR2_WB(i),RMSE_WB(i));
end

%% Plots
close all

for i=1:length(D)
    for j=1:length(t)
        fitKP(j,i)=kKP(i).*(t(j).^nKP(i));
        fitPS(j,i)=k1PS(i).*(t(j).^mPS(i))+k2PS(i).*(t(j).^(2.*mPS(i)));
        fitHopf(j,i)=1-((1-((k_HopfFit(i).*t(j))./(Co(i).*R(i)))).^3);
    end
    figure(i)
    plot(t,Mt_Minf(:,i),'*b',t,fitKP(:,i),'-k',t,fitPS(:,i),'-b',t,fitHopf(:,i),'-
r');
    xlabel('Time (hr)')
    ylabel('Percent Release')
    legend('Release Data','Korsmeyer-Peppas','Peppas-
Sahlin','Hopfenberg','Location','southeast')
    title(sprintf('%s-%.0f    Radius = %.1f nm',PolymerName,i,R(i)));
```

```
    xlim([0 max(t)])
    ylim([0 1])
end
```

Gaussian Mixture Model Distribution Solution

```
clc, clear all, close all

% Import C/S Data Spreadsheet

%Set up the Import Options and import the data
opts = spreadsheetImportOptions("NumVariables", 53);

% Specify sheet and range
opts.Sheet = "Sheet1";
opts.DataRange = "A3:BA103";

% Specify column names and types
opts.VariableNames = ["RunIndex", "CoreRunName", "SpEnCore", "AvgCoreHD",
"AvgCorePDI", "CSRunName", "Vol_1NP", "Mass1NP", "PLGAMass", "NumPLGANPS", "SA_np",
"TotSANPs", "PLLAmass", "Multiple", "PLLAmol", "VolDCM", "PLLA_Conc", "FlaskPVAvol",
"EmulsPVAvol", "WashPVAvol", "TotEmulsVol", "PVAConc", "VolRatio", "FlaskPVAmol",
"EmulsPVAmol", "WashPVAmol", "TotPVAMol", "TotMolRatio", "EmulMolRatio", "Amp",
"Energy", "Time", "Power", "SpEn", "SpEnRatio", "CSHD", "CSHDDev", "CSPDI", "CSPDI1",
"f1_mu", "f1_std", "f2_mu", "f2_std", "f3_mu", "f3_std", "TotEff_mu", "TotEff_std",
"X_R1_mu", "X_R1_std", "Z3_mu", "Z3_std", "ShellThick_mu", "ShellThick_std"];
opts.VariableTypes = ["double", "string", "double", "double", "double", "string",
"double", "double", "double", "double", "double", "double", "double", "double",
"double", "double", "double", "double", "double", "double", "double", "double",
"double", "double", "double", "double", "double", "double", "double", "double",
"double", "double", "double", "double", "double", "double", "double", "double",
"double", "string", "string", "string", "string", "string", "string", "string",
"string", "string", "string", "string", "string", "string", "string"];

% Specify variable properties
opts = setvaropts(opts, ["CoreRunName", "CSRunName", "f1_mu", "f1_std", "f2_mu",
"f2_std", "f3_mu", "f3_std", "TotEff_mu", "TotEff_std", "X_R1_mu", "X_R1_std",
"Z3_mu", "Z3_std", "ShellThick_mu", "ShellThick_std"], "WhitespaceRule", "preserve");
opts = setvaropts(opts, ["CoreRunName", "CSRunName", "f1_mu", "f1_std", "f2_mu",
"f2_std", "f3_mu", "f3_std", "TotEff_mu", "TotEff_std", "X_R1_mu", "X_R1_std",
"Z3_mu", "Z3_std", "ShellThick_mu", "ShellThick_std"], "EmptyFieldRule", "auto");

% Import the data
PLLACSMethod1SolMethod3 =
readtable("E:\Dissertation_backupfiles\DataFiles_for_Dissertation\CoreShellModeling\P
LLA_CS_Method1_SolMethod3.xlsx", opts, "UseExcel", false);

% Clear temporary variables
clear opts



% Specificy known mu's and sigma's for PLGA and Zmix from the spreadsheet
PLGAcore_mu=round(PLLACSMethod1SolMethod3.AvgCoreHD,0);
```

```
PLGAcore_PDI=PLLACSMethod1SolMethod3.AvgCorePDI;
Mix_mu= round(PLLACSMethod1SolMethod3.CSHD,0);
Mix_mu_std=PLLACSMethod1SolMethod3.CSHDDev;
Mix_PDI=PLLACSMethod1SolMethod3.CSPDI;
Mix_PDI_std=PLLACSMethod1SolMethod3.CSPDI1;
SpEnCS=round(PLLACSMethod1SolMethod3.SpEn,0);


% Import and fit PLLA size and PDI data vs. Specific Energy to calculate
% the mu's and sigma's for PLLA NPs based on the specific energy used
% Set up the Import Options and import the data
opts = spreadsheetImportOptions("NumVariables", 28);

% Specify sheet and range
opts.Sheet = "Sheet1";
opts.DataRange = "A3:AB35";

% Specify column names and types
opts.VariableNames = ["Run", "Name", "C6MassIn", "C6MassmgNP", "MassPLLA",
"PLLA_conc", "DCMVol", "MolesPLLA", "PVA", "PVAFlaskVol", "PVAEmulsVol",
"PVAWashVol", "TotalPVAVol", "TotEmulVol", "PVAFlaskMole", "PVAEmulsMole",
"PVAWashMole", "TotalMolesPVA", "molesEmulsPVAmolesPLLA", "molePVAmolePLLA",
"Energy", "SpecificEnergyJmL", "Amp", "Time", "HD", "StDevHD", "PDI", "StDevPDI"];
opts.VariableTypes = ["double", "string", "double", "double", "double", "double",
"double", "double", "double", "double", "double", "double", "double", "double",
"double", "double", "double", "double", "double", "double", "double", "double",
"double", "double", "double", "double", "double", "double"];

% Specify variable properties
opts = setvaropts(opts, "Name", "WhitespaceRule", "preserve");
opts = setvaropts(opts, "Name", "EmptyFieldRule", "auto");

% Import the data
PLLAsizeModelingnew =
readtable("E:\Dissertation_backupfiles\DataFiles_for_Dissertation\CoreShellModeling\P
LLA_sizeModelingnew.xlsx", opts, "UseExcel", false);

% Clear temporary variables
clear opts

PLLA_En=PLLAsizeModelingnew.SpecificEnergyJmL;
PLLAnp_HD=PLLAsizeModelingnew.HD;
PLLAnp_PDI=PLLAsizeModelingnew.PDI;

% Fit: 'mu'.
[xData, yData] = prepareCurveData( PLLA_En, PLLAnp_HD );

% Set up fittype and options.
ft = fittype( 'power2' );
excludedPoints = excludedata( xData, yData, 'Indices', [12 18] );
opts = fitoptions( 'Method', 'NonlinearLeastSquares' );
opts.Display = 'Off';
opts.Lower = [-Inf -Inf 0];
opts.MaxFunEvals = 10000;
opts.MaxIter = 10000;
```

```
opts.Robust = 'Bisquare';
opts.StartPoint = [12720.3214027574 -0.8217093807582 -90.6799628828523];
opts.Exclude = excludedPoints;

% Fit model to data.
[fitresult_PLLAmu, gof_PLLAmu] = fit( xData, yData, ft, opts );

% Fit: 'PDI'.
[xData, yData] = prepareCurveData( PLLA_En, PLLAnp_PDI );

% Set up fittype and options.
ft = fittype( 'power2' );
excludedPoints = excludedata( xData, yData, 'Indices', [12 18] );
opts = fitoptions( 'Method', 'NonlinearLeastSquares' );
opts.Display = 'Off';
opts.Lower = [-Inf -Inf 0];
opts.MaxFunEvals = 10000;
opts.MaxIter = 10000;
opts.Robust = 'Bisquare';
opts.StartPoint = [652.277137131291 -1.71331131389505 -0.262842504769239];
opts.Exclude = excludedPoints;

% Fit model to data.
[fitresult_PLLAPDI, gof_PLLAPDI] = fit( xData, yData, ft, opts );

PLLANP_mu=round((fitresult_PLLAmu.a).*(SpEnCS.^(fitresult_PLLAmu.b))+fitresult_PLLAmu
.c,0);
PLLANP_PDI=(fitresult_PLLAPDI.a).*(SpEnCS.^(fitresult_PLLAPDI.b))+fitresult_PLLAPDI.c
;

% Calculate the variance of the PLGA, PLLA, and the Zmix, using the known
% sigmas and Zaverages of each particle type

% PDI = (sigma/Z)^2
% sigma=sqrt(PDI)*Z
% Variance = sigma^2

PLGAcore_sigma=round(sqrt(PLGAcore_PDI).*PLGAcore_mu,0);
PLGAcore_variance=round(PLGAcore_sigma.^2,0);

PLLANP_sigma=round(sqrt(PLLANP_PDI).*PLLANP_mu,0);
PLLANP_variance=round(PLLANP_sigma.^2,0);

Mix_sigma=round(sqrt(Mix_PDI).*Mix_mu,0);
Mix_variance=round(Mix_sigma.^2,0);

% Find possible mu, variance, and sigma of C/S NP for each input (column)
% at each possible combination of number fractions (f1+f2+f3)=1,
% represented by f_combo
f1pos=0:0.01:1;        % number fraction PLGA NPs
f2pos=0:0.01:1;        % number fraction PLLA NPs
f3pos=0:0.01:1;         % number fraction C/S NPs
i=1;
for i1=1:length(f1pos)
    for i2=1:length(f2pos)
```

```
            for i3=1:length(f3pos)
                numfrac=f1pos(i1)+f2pos(i2)+f3pos(i3);
                if numfrac==1
                    f_combo(i,1)=f1pos(i1);
                    f_combo(i,2)=f2pos(i2);
                    f_combo(i,3)=f3pos(i3);
                    i=i+1;
                end
            end
        end
    end

    % For each combination of fractions (rows) and C/S data points (columns)
    % solves for core/shell NP diameters mu, sigma, and variances
    % If predicted diameters (mu) are less than PLGA core diameter (mu), then
    % discards these by setting terms to 0.

    % in matrices, first three columns are f1, f2 , and f3 combinations for
    % reference

    for c=1:length(PLGAcore_mu)
        for r=1:length(f_combo)
                f1=f_combo(r,1);
                f2=f_combo(r,2);
                f3=f_combo(r,3);
                mu_CS(r,1)=f1;
                mu_CS(r,2)=f2;
                mu_CS(r,3)=f3;
                var_CS(r,1)=f1;
                var_CS(r,2)=f2;
                var_CS(r,3)=f3;
                sigma_CS(r,1)=f1;
                sigma_CS(r,2)=f2;
                sigma_CS(r,3)=f3;
                if f3==0

                    mu_CS(r,c+3)=0;
                    var_CS(r,c+3)=0;
                    sigma_CS(r,c+3)=0;
                else
                    mu_CS(r,c+3)=round((Mix_mu(c)-f1.*PLGAcore_mu(c)-
    f2.*PLLANP_mu(c))./f3,0);
                    var_CS(r,c+3)=round((Mix_variance(c)-...
                        ((f1.^1).*PLGAcore_variance(c))-...
                        ((f2.^1).*PLLANP_variance(c)))./(f3.^1),0);
                        sCS=sqrt(var_CS(r,c+3));
                        if isreal(sCS)==0
                        sigma_CS(r,c+3)=0;
                        var_CS(r,c+3)=0;
                        else
                        sigma_CS(r,c+3)=sCS;
                        end
                    if mu_CS(r,c+3)<=(PLGAcore_mu(c))
                        mu_CS(r,c+3)="";
                        var_CS(r,c+3)="";
```

```
                    sigma_CS(r,c+3)="";
                else
                end
            end

    end
end


% Use Input Masses and Average Diameters to solve for Shell thicknesses,
% total numbers of each type of particle (n1, n2, n3)

mPLGA_in=PLLACSMethod1SolMethod3.PLGAMass;
mPLLA_in=PLLACSMethod1SolMethod3.PLLAmass;
Multiple_in=PLLACSMethod1SolMethod3.Multiple;
CoreDiameter=PLGAcore_mu;
CoreRadius=CoreDiameter./2;


%Constants
dPLGA=1.28E-18;        % Density of PLGA NP (mg/nm3)
dPLLA=1.15E-18;        % Density of PLLA NP (mg/nm3)
densityratio=dPLLA./dPLGA;
V_core=(4/3).*pi().*(CoreRadius.^3);        % core volume, nm3
m_core=V_core.*dPLGA;                       % core mass, mg
V2=(4/3).*pi().*((PLLANP_mu./2).^3);               % pure PLLA NP volume, nm3
m2=V2.*dPLLA;                               % pure PLLA NP mass, mg
ncores_in=mPLGA_in./(m_core);                % number of PLGA cores in
maxPLLANPS=mPLLA_in./m2;                    % max # of PLLA NPs
maxNPs=ncores_in+maxPLLANPS;                   % max # of NPs that could be made
mTot_in=mPLGA_in+mPLLA_in;

%%

for k=1:length(ncores_in)
for r=1:length(f_combo)
    try
        mu1=PLGAcore_mu(k);
        sigma1=PLGAcore_sigma(k);
        mu2=PLLANP_mu(k);
        sigma2=PLLANP_sigma(k);
        mu3=mu_CS(r,k+3);
        sigma3=sigma_CS(r,k+3);
        r1=mvnrnd(mu1,sigma1,1000);
        r2=mvnrnd(mu2,sigma2,1000);
        r3=mvnrnd(mu3,sigma3,1000);
        X=[r1;r2;r3];
        gm1=fitgmdist(X,3);
        mingm1_place=find(gm1.mu==min(gm1.mu));
        maxgm1_place=find(gm1.mu==max(gm1.mu));
        placegm1=mingm1_place+maxgm1_place;
        switch placegm1
            case 3
                midgm1_place=3;
            case 4
```

```
                midgm1_place=2;
            case 5
                midgm1_place=1;
        end
        gm1_sol(r,1)=round(gm1.mu(mingm1_place),1);
        gm1_sol(r,2)=round(gm1.mu(midgm1_place),1);
        gm1_sol(r,3)=round(gm1.mu(maxgm1_place),1);
        gm1_sol(r,4)=round(gm1.ComponentProportion(mingm1_place),3);
        gm1_sol(r,5)=round(gm1.ComponentProportion(midgm1_place),3);
        gm1_sol(r,6)=round(gm1.ComponentProportion(maxgm1_place),3);
        gm1_sol(r,7)=round(gm1.Sigma(:,:,mingm1_place),1);
        gm1_sol(r,8)=round(gm1.Sigma(:,:,midgm1_place),1);
        gm1_sol(r,9)=round(gm1.Sigma(:,:,maxgm1_place),1);

        muMix=Mix_mu(k);
        sigmaMix=Mix_sigma(k);
        rMix=mvnrnd(muMix,sigmaMix,1000);
        Xmix=[rMix];
        gmMix=fitgmdist(Xmix,3);
        mingmMix_place=find(gmMix.mu==min(gmMix.mu));
        maxgmMix_place=find(gmMix.mu==max(gmMix.mu));
        placegmMix=mingmMix_place+maxgmMix_place;
        switch placegmMix
            case 3
                midgmMix_place=3;
            case 4
                midgmMix_place=2;
            case 5
                mingmMix_place=1;
        end
        gmMix_sol(r,1)=round(gmMix.mu(mingmMix_place),1);
        gmMix_sol(r,2)=round(gmMix.mu(midgmMix_place),1);
        gmMix_sol(r,3)=round(gmMix.mu(maxgmMix_place),1);
        gmMix_sol(r,4)=round(gmMix.ComponentProportion(mingmMix_place),3);
        gmMix_sol(r,5)=round(gmMix.ComponentProportion(midgmMix_place),3);
        gmMix_sol(r,6)=round(gmMix.ComponentProportion(maxgmMix_place),3);
        gmMix_sol(r,7)=round(gmMix.Sigma(:,:,mingmMix_place),1);
        gmMix_sol(r,8)=round(gmMix.Sigma(:,:,midgmMix_place),1);
        gmMix_sol(r,9)=round(gmMix.Sigma(:,:,maxgmMix_place),1);
    catch
        gm1_sol(r,1)="";
        gm1_sol(r,2)="";
        gm1_sol(r,3)="";
        gm1_sol(r,4)="";
        gm1_sol(r,5)="";
        gm1_sol(r,6)="";
        gm1_sol(r,7)="";
        gm1_sol(r,8)="";
        gm1_sol(r,9)="";
        gmMix_sol(r,1)="";
        gmMix_sol(r,2)="";
        gmMix_sol(r,3)="";
        gmMix_sol(r,4)="";
        gmMix_sol(r,5)="";
        gmMix_sol(r,6)="";
```

```
        gmMix_sol(r,7)="";
        gmMix_sol(r,8)="";
        gmMix_sol(r,9)="";
    end
end
try
gmComb=gm1_sol-gmMix_sol;
sumgmComb=sum(gmComb(:,1:3),2);
minindex=find(sumgmComb==min(sumgmComb));
if length(minindex)>1
    sol_col(k,1)=mean(gm1_sol(minindex,1));
    sol_col(k,2)=mean(gm1_sol(minindex,2));
    sol_col(k,3)=mean(gm1_sol(minindex,3));
    sol_col(k,4)=mean(gm1_sol(minindex,4));
    sol_col(k,5)=mean(gm1_sol(minindex,5));
    sol_col(k,6)=mean(gm1_sol(minindex,6));
    sol_col(k,7)=mean(gm1_sol(minindex,7));
    sol_col(k,8)=mean(gm1_sol(minindex,8));
    sol_col(k,9)=mean(gm1_sol(minindex,9));
else
    sol_col(k,1)=(gm1_sol(minindex,1));
    sol_col(k,2)=(gm1_sol(minindex,2));
    sol_col(k,3)=(gm1_sol(minindex,3));
    sol_col(k,4)=(gm1_sol(minindex,4));
    sol_col(k,5)=(gm1_sol(minindex,5));
    sol_col(k,6)=(gm1_sol(minindex,6));
    sol_col(k,7)=(gm1_sol(minindex,7));
    sol_col(k,8)=(gm1_sol(minindex,8));
    sol_col(k,9)=(gm1_sol(minindex,9));
end
catch
end
fprintf('Now finished with point %d...\n',k)
end




%%
clc
gmComb=gm1_sol-gmMix_sol;
sumgmComb=sum(gmComb(:,1:3),2);
minindex=find(sumgmComb==min(sumgmComb));
gm1_sol(minindex,:)


%%

k=95;
for r=1:length(f_combo)
    try
        mu1=PLGAcore_mu(k);
        sigma1=PLGAcore_sigma(k);
        mu2=PLLANP_mu(k);
        sigma2=PLLANP_sigma(k);
```

```
    mu3=mu_CS(r,k+3);
    sigma3=sigma_CS(r,k+3);
    r1=mvnrnd(mu1,sigma1,1000);
    r2=mvnrnd(mu2,sigma2,1000);
    r3=mvnrnd(mu3,sigma3,1000);
    X=[r1;r2;r3];
    gm1=fitgmdist(X,3);
    mingm1_place=find(gm1.mu==min(gm1.mu));
    maxgm1_place=find(gm1.mu==max(gm1.mu));
    placegm1=mingm1_place+maxgm1_place;
    switch placegm1
        case 3
            midgm1_place=3;
        case 4
            midgm1_place=2;
        case 5
            midgm1_place=1;
    end
    gm1_sol(r,1)=round(gm1.mu(mingm1_place),1);
    gm1_sol(r,2)=round(gm1.mu(midgm1_place),1);
    gm1_sol(r,3)=round(gm1.mu(maxgm1_place),1);
    gm1_sol(r,4)=round(gm1.ComponentProportion(mingm1_place),2);
    gm1_sol(r,5)=round(gm1.ComponentProportion(midgm1_place),2);
    gm1_sol(r,6)=round(gm1.ComponentProportion(maxgm1_place),2);
    gm1_sol(r,7)=round(gm1.Sigma(:,:,mingm1_place),1);
    gm1_sol(r,8)=round(gm1.Sigma(:,:,midgm1_place),1);
    gm1_sol(r,9)=round(gm1.Sigma(:,:,maxgm1_place),1);

    muMix=Mix_mu(k);
    sigmaMix=Mix_sigma(k);
    rMix=mvnrnd(muMix,sigmaMix,2000);
    Xmix=[rMix];
    gmMix=fitgmdist(Xmix,3);
    mingmMix_place=find(gmMix.mu==min(gmMix.mu));
    maxgmMix_place=find(gmMix.mu==max(gmMix.mu));
    placegmMix=mingmMix_place+maxgmMix_place;
    switch placegmMix
        case 3
            midgmMix_place=3;
        case 4
            midgmMix_place=2;
        case 5
            mingmMix_place=1;
    end
    gmMix_sol(r,1)=round(gmMix.mu(mingmMix_place),1);
    gmMix_sol(r,2)=round(gmMix.mu(midgmMix_place),1);
    gmMix_sol(r,3)=round(gmMix.mu(maxgmMix_place),1);
    gmMix_sol(r,4)=round(gmMix.ComponentProportion(mingmMix_place),2);
    gmMix_sol(r,5)=round(gmMix.ComponentProportion(midgmMix_place),2);
    gmMix_sol(r,6)=round(gmMix.ComponentProportion(maxgmMix_place),2);
    gmMix_sol(r,7)=round(gmMix.Sigma(:,:,mingmMix_place),1);
    gmMix_sol(r,8)=round(gmMix.Sigma(:,:,midgmMix_place),1);
    gmMix_sol(r,9)=round(gmMix.Sigma(:,:,maxgmMix_place),1);
catch
    gm1_sol(r,1)="";
```

```
        gm1_sol(r,2)="";
        gm1_sol(r,3)="";
        gm1_sol(r,4)="";
        gm1_sol(r,5)="";
        gm1_sol(r,6)="";
        gm1_sol(r,7)="";
        gm1_sol(r,8)="";
        gm1_sol(r,9)="";
        gmMix_sol(r,1)="";
        gmMix_sol(r,2)="";
        gmMix_sol(r,3)="";
        gmMix_sol(r,4)="";
        gmMix_sol(r,5)="";
        gmMix_sol(r,6)="";
        gmMix_sol(r,7)="";
        gmMix_sol(r,8)="";
        gmMix_sol(r,9)="";
    end
end
gm1_sol=str2double(gm1_sol(:,:));

gmComb=gm1_sol-gmMix_sol;
sumgmComb=sum(gmComb(:,1:3),2);
minindex=find(sumgmComb==min(sumgmComb));
if length(minindex)>1
    sol_col(1,1)=mean(gm1_sol(minindex,1));
    sol_col(1,2)=mean(gm1_sol(minindex,2));
    sol_col(1,3)=mean(gm1_sol(minindex,3));
    sol_col(1,4)=mean(gm1_sol(minindex,4));
    sol_col(1,5)=mean(gm1_sol(minindex,5));
    sol_col(1,6)=mean(gm1_sol(minindex,6));
    sol_col(1,7)=mean(gm1_sol(minindex,7));
    sol_col(1,8)=mean(gm1_sol(minindex,8));
    sol_col(1,9)=mean(gm1_sol(minindex,9));
else
    sol_col(1,1)=(gm1_sol(minindex,1));
    sol_col(1,2)=(gm1_sol(minindex,2));
    sol_col(1,3)=(gm1_sol(minindex,3));
    sol_col(1,4)=(gm1_sol(minindex,4));
    sol_col(1,5)=(gm1_sol(minindex,5));
    sol_col(1,6)=(gm1_sol(minindex,6));
    sol_col(1,7)=(gm1_sol(minindex,7));
    sol_col(1,8)=(gm1_sol(minindex,8));
    sol_col(1,9)=(gm1_sol(minindex,9));
end
sol_col(1,:)

%%
sizerange=0:1:500;
PLGAnorm=normpdf(sizerange,PLGAcore_mu(78),PLGAcore_sigma(78));
PLLAnorm=normpdf(sizerange,PLLANP_mu(78),PLLANP_sigma(78));
Mixnorm=normpdf(sizerange,Mix_mu(78),Mix_sigma(78));

CSnorm=normpdf(sizerange,239.4,118);
```

```
plot(sizerange,0.5.*PLGAnorm,'-g',sizerange,0.5.*PLLAnorm,'-r',sizerange,Mixnorm,'-
b',sizerange,0.*CSnorm,'--k')
title('Size Distribution Curves')
legend('PLGA NPs','PLLA NPs','Meas. Mixture','Proposed Core/Shell')
annotation('textarrow',[0.785 0.68],[0.5 0.25],'String','Possible Solution?')

%%
filename='DistCurveworkspaceSaved.mat';
save(filename)

%% load workspace again

load(filename)
```

Fluorescent Image Nanoparticle Counting

```
%% Program to process images and count number of red, green, yellow particles in them

clc, clear all,close all
warning('off','all')
warning
%First set which folder you want to analyze, and sample name
samplename='Z81';
path=cd;


% Break check before renaming files to make sure correct sample name and
% folder name is given
check=1;
while(check>0)
    startingFolder=path;
    folder2read=uigetdir(startingFolder);
    filePattern=fullfile(folder2read,'*.jpg');
    files=dir(filePattern);
for k=1:length(files)
    fullFolderName=fullfile(folder2read,files(k).name);
    fprintf('Now processing file %s...\n',fullFolderName);
end
promptMessage=sprintf('Folder: %s \nAll images changed to sample name: %s\nCheck that
is correct and press Continue or Cancel to abort',...
    folder2read,samplename);
button=questdlg(promptMessage,'Continue','Continue','Cancel','Continue');
if strcmpi(button,'Cancel')
    break
end
try
%First will rename all images so that can do batch processing
% Do NOT have replicate images in folder so that same particles are counted
% multiple times.
d=dir(fullfile(folder2read,'*.jpg')); % reads all jpg images in folder
fileNames={d.name};                   % pulls names of images
    for iFile=1:numel(d)
        newName=fullfile(folder2read,sprintf('%s_%02d.jpg',samplename,iFile));
        movefile(fullfile(folder2read,fileNames{iFile}),newName);
```

```
    end
catch

end

    clc
    n=numel(d);

cd(folder2read)
for numImage=1:n
% filename, can read .jpg or .tif but JPEG seems to work better
    rgbFilename=sprintf('%s_%02d.jpg',samplename,numImage);
    rgb=imread(rgbFilename);


% Changing radius constraints and sensitivity can reduce false positives
    rmin=5;        % minimum pixel radius of circle (5 is minimum for function)
    rmax=50;       % maximum pixel radius of circle
    Sens=0.92;     % sensitivity of metric (how perfect a circle)
    try [cb, rb, mb] = imfindcircles(rgb,[rmin rmax],'ObjectPolarity',...
            'bright', 'Sensitivity',Sens);
% [cd, rd, md] = imfindcircles(rgb,[rmin rmax],'ObjectPolarity','dark', ...
%     'Sensitivity',Sens);

%Remove any circles found due to scale bar at 100x magnification
%coordinates of edges of scale bars and numbers
        leftsidescale=[1049.3,854.8772];
        rightsidescale=[1173.6,855.5498];
        numberscale1=[1100.3,872.779];
        numberscale2=[1121.6,874.2996];
        radiusscale=8;

    for scalei=1:length(cb)
            difleftx=abs(cb(scalei,1)-leftsidescale(1));
            diflefty=abs(cb(scalei,2)-leftsidescale(2));
            difrightx=abs(cb(scalei,1)-rightsidescale(1));
            difrighty=abs(cb(scalei,2)-rightsidescale(2));
            difnum1x=abs(cb(scalei,1)-numberscale1(1));
            difnum1y=abs(cb(scalei,2)-numberscale1(2));
            difnum2x=abs(cb(scalei,1)-numberscale2(1));
            difnum2y=abs(cb(scalei,2)-numberscale2(2));
        if difleftx<radiusscale && diflefty<radiusscale || ...
            difrightx<radiusscale && difrighty<radiusscale || ...
            difnum1x<radiusscale && difnum1y<radiusscale ||...
            difnum2x<radiusscale && difnum2y<radiusscale
                cb(scalei,:)=0;
        end
    end

    numbercirclesfound=length(cb);       % determines number of cirlce found
    pixelRGB=impixel(rgb,cb(:,1),cb(:,2));          % finds RGB value of center of
each circle found and populates n x 3 matrix
% NPcount=zeros(numbercirclesfound,length(numImage));    % creates empty matrix for
counting particles in for loop
```

```
        for index=1:numbercirclesfound
        % Determines if particle is red, green, or yellow (at center)
        redvalue=pixelRGB(index,1);
        greenvalue=pixelRGB(index,2);
        bluevalue=pixelRGB(index,3);
        r2g=redvalue./greenvalue;
        g2r=greenvalue./redvalue;
        r2b=redvalue./bluevalue;
        g2b=greenvalue./bluevalue;

    % Based on looking at rgb scale and subjective point at where
    % transition is
            if r2g>=2
                NPcount(index,numImage)=2; % red particles are labeled 2
            elseif g2r>=1.30
                NPcount(index,numImage)=1; % green particles are labeled 1
            elseif r2g<2 && g2r<1.30
                NPcount(index,numImage)=3; % yellow particles are labeled 3
            elseif redvalue<75 && greenvalue<75 && bluevalue<75
                NPcount(index,numImage)=6; % if black then false positive and labeled
0
            else
                NPcount(index,numImage)=5; % if other color, then label 5 to analyze
later
            end
        end

% Takes count of every type of particle counted
% Column Order: (1) Green (2) Red (3) Yellow (4) Black (5) Other
    CountNPs(numImage,1)=sum(NPcount(:,numImage)==1);
    CountNPs(numImage,2)=sum(NPcount(:,numImage)==2);
    CountNPs(numImage,3)=sum(NPcount(:,numImage)==3);
    CountNPs(numImage,4)=sum(NPcount(:,numImage)==6);
    CountNPs(numImage,5)=sum(NPcount(:,numImage)==5);
    CountNPs(numImage,6)=sum(CountNPs(numImage,:));

    catch
% If no circles found, will catch error and popular image's count with 0's
% and moves onto the next image
% Column Order: (1) Green (2) Red (3) Yellow (4) Black (5) Other
        CountNPs(numImage,1)=0;
        CountNPs(numImage,2)=0;
        CountNPs(numImage,3)=0;
        CountNPs(numImage,4)=0;
        CountNPs(numImage,5)=0;
        CountNPs(numImage,6)=0;
        continue
    end

    fprintf('Processing image: %s_%02d.jpg\n',samplename,numImage);
end


% Once finished with all images, Writes NP count and calculation to excel file
folder=folder2read;
```

```
if ~exist(folder,'dir')
    mkdir(folder);
end
baseFileName=sprintf('%scount.xlsx',samplename);
fullFileName=fullfile(folder,baseFileName);

GreenNPs=sum(CountNPs(:,1));
RedNPs=sum(CountNPs(:,2));
YellowNPs=sum(CountNPs(:,3));
FalseNPs=sum(CountNPs(:,4));
OtherNPs=sum(CountNPs(:,5));
TotalValidNPs=GreenNPs+RedNPs+YellowNPs;
TotalFound=TotalValidNPs+FalseNPs+OtherNPs;
f1meas=GreenNPs./TotalValidNPs;
f2meas=RedNPs./TotalValidNPs;
f3meas=YellowNPs./TotalValidNPs;
SumNPs=[GreenNPs,RedNPs,YellowNPs,FalseNPs,OtherNPs,TotalFound];

ArrayNPs=[CountNPs;SumNPs];
fNPs=zeros(n+1,1);
fNPs(1,1)=f1meas;
fNPs(2,1)=f2meas;
fNPs(3,1)=f3meas;
ArrayNPs=[ArrayNPs,fNPs];

dnew=dir(fullfile(folder2read,'*.jpg')); % reads all jpg images in folder
ImageNames={dnew.name,'Sum'}; % Last one must be "Sum"
Tnps=array2table(ArrayNPs,'VariableNames',{'Green','Red','Yellow','False
+','Other','Circles/Image','f_meas'});
Tnps.Properties.RowNames=ImageNames;
Summary=summary(Tnps);

recycle on %send old excel file to recycle bin
delete(fullFileName); %Delete old excel file in folder
writetable(Tnps,fullFileName,'WriteRowNames',true)


fprintf('Finished.\n');
% End for break check, must be at very end of all code
check=0;
end
```

Appendix 2: Protocols

Polymeric Nanoparticle Synthesis: Emulsion Solvent Evaporation Method

Preparation of Variables:

Total number of runs: ________ * usually each desired size is unique run

To determine mass of particles after freeze drying, weigh empty collection tube prior to use

Tube Mass (w/ lid): __________mg

Organic Phase: PLGA Polymer dissolved in organic solvent (dichloromethane, DCM)

PLGA Conc. (mg/uL): _________ **mass PLGA/run**: __________mg **Vol DCM/run**: _________uL

*Note: PLGA% = PLGA conc. (mg/uL) x 100%, typical ranges: Conc: 1-5%, Mass: 5 mg, Vol: 500uL

* If loading hydrophobic drug/dye, dissolve directly with PLGA in DCM

* if drug/dye is hydrophilic, use double emulsion evaporation method (see end)

Water Phase: DI Water with Poly vinyl alcohol (PVA) surfactant dissolved

PVA Conc. (g/mL *100):______ **PVA Flask Vol** (mL):_________ mL **PVA EmulsionVol** (mL):_________ mL

*Note: Typical ranges: PVA conc: 2-3%, PVA Flask Vol: 3-6 mL, PVA Emulsion Vol: 3-4 mL

Total Emulsion Vol (mL) = **Vol DCM/run** (mL) + **PVA Emulsion Vol** (mL) =__________mL

Energy: **Total Energy** from sonicator (Joules) divided by **Total Emulsion Vol**: = Specific Energy (J/mL)

Particle Diameter (nm) = 403.2*(Specific Energy^ -0.2265)+ 78.42 R2: 0.9347 RMSE: 26.71

1. Weigh out total PLGA needed for all runs, add required total volume DCM, let dissolve with light vortexing for 5-10 minutes until no polymer crystals are visible.
2. Place a round bottom flask on plate stirrer, with crosshead magnetic stirrer. Add Flask Volume PVA to this flask, and begin stirring at 500 rpm.
3. In a 15 mL conical tube, add Emulsion Volume PVA, then once PLGA is fully dissolved, add volume of PLGA/DCM per run to each emulsion tube. DCM phase will be immiscible and separate at the bottom of the tube under the PVA phase.
4. Prepare ice or water bath that will cover total volume in emulsion tube.
5. Set sonicator amplitude (%) and increase set time above required sonication time.
6. Lift sonicator probe tip and insert into PVA/DCM liquid, around a third of the way from the top of the combined liquids. Be careful to not touch the probe tip to the tube sides or the bottom at any time.

7. Turn on sonicator by pressing START, and then move probe tip up and down throughout the entire liquid for initial emulsion is evenly distributed. Do this until about 100 J or 30 seconds if time allows. For shorter sonication times/energies, make sure emulsion is fully milky white throughout for better particle size distribution.
8. Press PAUSE at 100 J/30 second time, and re-position sonicator so that the emulsion tube is in the ice bath and will not move or shift. Once set, press RESUME on the sonicator.
9. Sonicate the emulsion for required **total energy** (J) required. If amplitudes >=60 are being used, pause around every 100 J/30 seconds to keep temperature controlled for at least 1 minute before pressing RESUME.
10. At the desired total energy (J), press pause, and record the time and actual energy (J) attained.
11. Transfer the emulsion from the emulsion tube to the PVA in the round bottom flask under stirring using a pipette.
12. Let emulsion stir at room temperature for at least 2 hours and until the milk white color as cleared somewhat.
13. After evaporation time, transfer liquid in the flask to a pre-weighed conical tube (it can be same one used as emulsion tube). Dilute with DI water.
14. For multiple simultaneous runs, weigh each tube and add DI Water to balance all tubes' masses, before placing in centrifuge.
15. Centrifuge at high speed (17,000 xg) for at least 30 minutes, until pellet is collected near the bottom of each tube.
16. Carefully pour out liquid into sink, and add DI water to each tube. Sonicate each pellet separately at low amplitude (30%) for about 1 minute until the pellet is broken up and redispersed into the water.
17. If the tubes are still balanced, place all back into the centrifuge and centrifuge again for 30 minutes at high speed (17000 xg).
18. Dispose of the water in each tube, and refill with fresh DI Water. Redisperse each pellet with same parameters as in step 16. Particles are ready for DLS sizing. *Note: if higher PVA conc is used, more than one wash step might be necessary. Repeat steps 16-18 for each wash

Double Emulsion:

For hydrophilic payloads:

1) Dissolved hydrophilic payload in DI water/buffer to be used at known concentration. This is **water phase 2**.
2) Add volume of **water phase 2** to desired volume of PLGA/DCM. * The volume of **water phase 2** must be less than the volume of DCM/PLGA.
3) Sonicate this mixture for desired energy and time, until a water-in-oil emulsion is formed. Recommend using low amplitude (20-40%)
4) Add this primary emulsion to emulsion PVA and follow steps 3-18 the same.

Core/Shell Synthesis Method 1: Modified Emulsion Solvent Evaporation

This method looks to take advantage of the hydrophobicity similarity of the pre-formed PLGA core and the PLLA/DCM phase that we want to form around each core. Basically, we are using sonication to force a hydrophobic PLGA nanoparticle into a hydrophobic liquid droplet in which PLLA is dissolved and trying to optimize synthesis parameters to only form core/shell particles. On the figure below, the left image is an idealized case, where every PLGA nanoparticle we add forms one core/shell particle, with no polymer waste. Realistically, depending on what conditions we use, three types of particles are made: 1) PLGA nanoparticles (with no shell), 2) PLLA nanoparticles (no core), and 3) core/shell nanoparticles (right image in figure). After synthesis, we will use DLS measurements, fluorescent microscopy, and model calculations to estimate the core/shell formation efficiency, or how close to the idealized case we are (with 1 being ideal).

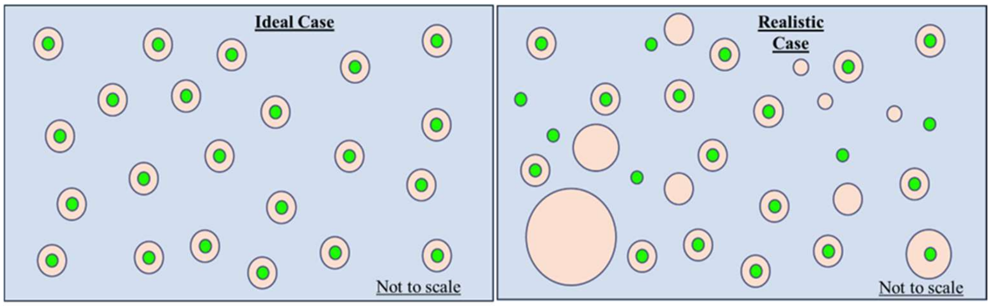

Preparation: We must know the size and the total mass of PLGA nanoparticles being used for each run to later estimate the core/shell formation efficiency. The PLGA NPs PDI also should be known, and as low (monodisperse) as possible.

PLGA NP Diameter (±StDev): __________nm PLGA Mass:_________mg/run PLGA NP PDI:___________.

We must then specify how much PLLA to use, quantified by the Multiple = mass PLLA/mass PLGA, and the concentration and volume of DCM to use to dissolve the PLLA. Note: a higher concentration (>0.05 g/mL) is preferred, but more optimization is needed, and may not be possible to accurately use a higher concentration.

Organic Phase: PLLA Polymer dissolved in organic solvent (dichloromethane, DCM)

Multiple:_________→PLLA Mass:_________mg/run PLLA Conc: mg/uL→DCM vol:________uL/run

Water Phase: DI Water with Polyvinyl alcohol (PVA) surfactant dissolved.

PVA Conc. (g/mL *100):______ **PVA Flask Vol** (mL):_________ mL **PVA EmulsionVol** (mL):_________ mL

Total Emulsion Vol (mL) = **Vol DCM/run** (mL) + **PVA Emulsion Vol** (mL) =__________mL

Energy: **Total Energy** from sonicator (Joules) divided by **Total Emulsion Vol**: = Specific Energy (J/mL)

*Core/shell Specific Energy should be less than the Specific energy used to form the PLGA NPs. This is an imprecise measurement and needs further refinement. Typically, multiply specific energy used to produce PLGA NPs by 0.8-0.95 to get desired specific energy for Core/shell formation.

1. Prepare ice or water bath that will cover total volume in emulsion tube.
2. Place a round bottom flask on plate stirrer, with crosshead magnetic stirrer. Add Flask Volume PVA to this flask, and begin stirring at 500 rpm.
3. Weigh out PLGA NPs for each run into a 15 mL tube which will be the emulsion tube. Use desired Multiple to calculate required PLLA needed per run and weigh out corresponding PLLA polymer for each run in their own Eppendorf microfuge 1.5 mL tube.
4. Add required DCM volume for desired PLLA concentration to each PLLA tube, and vortex until fully dissolved.
5. To the 15 mL emulsion tube that has the PLGA NPs in them, add the PVA Emulsion volume. At amplitude 20-40%, sonicate PVA/NP mixture until NPs are fully dispersed, at least 1 minute.
6. Once PLLA is fully dissolved in DCM, add required PLLA/DCM volume to each 15 mL emulsion tube. PLLA/DCM will be immiscible with the PVA and settle at the bottom.
7. Set sonicator amplitude (%) and increase set time above required sonication time.
8. Lift sonicator probe tip and insert into PVA/DCM liquid, around a third of the way from the top of the combined liquids. Be careful to not touch the probe tip to the tube sides or the bottom at any time.
9. Turn on sonicator by pressing START, and then move probe tip up and down throughout the entire liquid for initial emulsion is evenly distributed. Do this until about 100 J or 30 seconds if time allows. For shorter sonication times/energies, make sure emulsion is fully milky white throughout for better particle size distribution.
10. Press PAUSE at 100 J/30 second time, and re-position sonicator so that the emulsion tube is in the ice bath and will not move or shift. Once set, press RESUME on the sonicator.
11. Sonicate the emulsion for required **total energy** (J) required. If amplitudes >=60 are being used, pause around every 100 J/30 seconds to keep temperature controlled for at least 1 minute before pressing RESUME.
12. At the desired total energy (J), press pause, and record the time and actual energy (J) attained.
13. Transfer the emulsion from the emulsion tube to the PVA in the round bottom flask under stirring using a pipette.
14. Let emulsion stir at room temperature for at least 2 hours and until the milk white color as cleared somewhat.
15. After evaporation time, transfer liquid in the flask to a pre-weighed conical tube (it can be same one used as emulsion tube). Dilute with DI water and.
16. For multiple simultaneous runs, weigh each tube and add DI Water to balance all tubes' masses, before placing in centrifuge.
17. Centrifuge at high speed (17,000 xg) for at least 30 minutes, until a pellet is collected near the bottom of each tube.
18. Carefully pour out liquid into sink and add DI water to each tube. Sonicate each pellet separately at low amplitude (30%) for about 1 minute until the pellet is broken up and redispersed into the water.
19. If the tubes are still balanced, place all back into the centrifuge and centrifuge again for 30 minutes at high speed (17000 xg).

20. Dispose of the water in each tube, and refill with fresh DI Water. Redisperse each pellet with same parameters as in step 16. Particles are ready for DLS sizing. *Note: if higher PVA conc is used, more than one wash step might be necessary. Repeat steps 16-18 for each wash.

One-pot Variation: if not using pre-formed PLGA NPs, you can do it all in one step, forming an oil-oil-water emulsion.

1. Dissolve PLGA polymer and PLLA polymer in separate Eppendorf microfuge tubes in DCM. Use higher concentrations (>0.05g/mL) since at higher concentrations organic phases are immiscible. **The volume of PLGA/DCM for each run should be less than the volume of PLLA/DCM for proper emulsion.**
2. Combine PLGA/DCM and PLLA/DCM in a single Eppendorf microfuge tube. Sonicate at desired amplitude and time until a desired total energy.
   1st Emulsion Volume: PLGA/DCM volume + PLLA/DCM volume
   First Emulsion (O/O) Emulsion Specific Energy:_______J/mL (total energy/1st emulsion volume)
3. Add this primary emulsion to PVA Emulsion volume in 15 mL tube. Follow steps 1-20.

Core/Shell Synthesis Method 2: Solvent/Non-Solvent Method

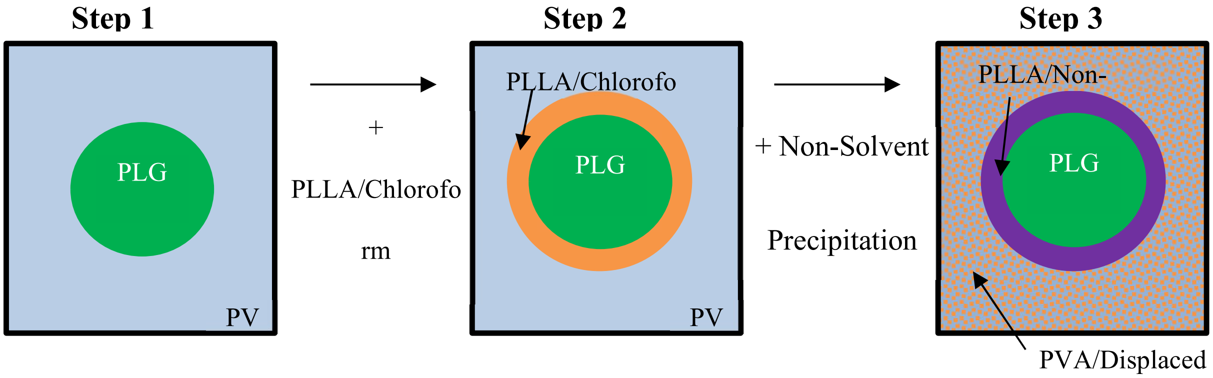

This method looks to take advantage of differences in solubilities and the hydrophobicity of PLGA/PLLA/DCM/Chloroform to encourage core/shell nanoparticle formation. The PLGA cores are formed via sonication using the normal emulsion method. Then, PLLA dissolved in chloroform, which is miscible with the PLGA/DCM but not the PVA, is added with sonication to the first emulsion. This system is unstable, so then a “non-solvent” is added (methanol or hexane), which is miscible with DCM, chloroform, and PVA. However, PLLA is insoluble in methanol (and hexane), and so when the concentration of this non-solvent exceeds that of chloroform, it flash precipitates the PLLA which is around a still-liquid PLGA/DCM core. The chloroform is displaced out of the shell. This method locks the dimensions of the core/shell particles, and the whole system is stirred for several hours to allow the DCM, chloroform, and the hexane/methanol to evaporate.

Organic Phases: PLGA Polymer dissolved in Dichloromethane (DCM), PLLA dissolved in Chloroform

PLGA Conc. (mg/uL): _________ **mass PLGA/run**: _________mg **Vol DCM/run**: ________uL

Multiple (mass PLGA/mass PLLA):__________.

PLLA Conc. (mg/uL): _________ **mass PLLA/run**: _________mg **Vol Ch/run**: ______uL

Water Phase: DI Water with Polyvinyl alcohol (PVA) surfactant dissolved

PVA Conc. (g/mL *100):______ **PVA Flask Vol** (mL):_________ mL **PVA EmulsionVol** (mL):_________ mL

Non-Solvent:

Non-solvent Volume:_________mL **Time Added:__________minute**

1st Total Emulsion Vol (mL) = **Vol DCM/run** (mL) + **PVA Emulsion Vol** (mL) = mL

2nd Total Emulsion Vol (mL) = **Vol Ch/run** (mL) + **Vol DCM/run** (mL) + **PVA Emulsion Vol** (mL) =__________mL

Energy: **1st Total Energy** from sonicator (Joules) divided by 1st **Total Emulsion Vol**: = 1st Specific Energy (J/mL)

2nd Total Energy from sonicator (Joules) divided by 2nd **Total Emulsion Vol**: = 2nd Specific Energy (J/mL)

1. Weigh out total PLGA needed for all runs, add required total volume DCM, let dissolve with light vortexing for 5-10 minutes until no polymer crystals are visible.
2. Weigh out total PLLA needed for all runs, add required total volume chloroform, let dissolve with vortexing for 15-20 minutes until no polymer is visible.
3. Prepare ice or water bath that will cover total volume in emulsion tube.
4. Place a round bottom flask on plate stirrer, with crosshead magnetic stirrer. Add Flask Volume PVA to this flask, and begin stirring at 500 rpm.
5. In a 15 mL conical tube, add Emulsion Volume PVA, then once PLGA is fully dissolved, add volume of PLGA/DCM per run to each emulsion tube. DCM phase will be immiscible and separate at the bottom of the tube under the PVA phase.
6. Set sonicator amplitude (%) and increase set time above required sonication time.
7. Lift sonicator probe tip and insert into PVA/DCM liquid, around a third of the way from the top of the combined liquids. Be careful to not touch the probe tip to the tube sides or the bottom at any time.
8. Turn on sonicator by pressing START, and then move probe tip up and down throughout the entire liquid for initial emulsion is evenly distributed. Do this until about 100 J or 30 seconds if time allows. For shorter sonication times/energies, make sure emulsion is fully milky white throughout for better particle size distribution.

9. Press PAUSE at 100 J/30 second time, and re-position sonicator so that the emulsion tube is in the ice bath and will not move or shift. Once set, press RESUME on the sonicator.
10. Sonicate the emulsion for required 1st **total energy** (J) required. If amplitudes >=60 are being used, pause around every 100 J/30 seconds to keep temperature controlled for at least 1 minute before pressing RESUME.
11. At the desired 1st total energy (J), press pause, and record the time and actual energy (J) attained.
12. Add PLLA/Chloroform volume/run. Set amplitude and adjust time to 2nd emulsion desired settings.
13. Sonicate in same way as PLGA/DCM steps, until 2nd total energy (J) is achieved. Record time and actual energy.
14. Transfer the emulsion from the emulsion tube to the PVA in the round bottom flask under stirring using a pipette.
15. At desired time (variable), add volume of non-solvent, with volume sufficient to displace chloroform. Record time and volume of addition.
16. Let emulsion stir at room temperature for at least 8 hours and until the milk white color is cleared.
17. After evaporation time, transfer liquid in the flask to a pre-weighed conical tube (it can be same one used as emulsion tube). Dilute with DI water and place in balanced centrifuge.
18. For multiple simultaneous runs, weigh each tube and add DI Water to balance all tubes' masses, before placing in centrifuge.
19. Centrifuge at high speed (17,000 xg) for at least 30 minutes, until pellet is collected near the bottom of each tube.
20. Carefully pour out liquid into sink, and add DI water to each tube. Sonicate each pellet separately at low amplitude (30%) for about 1 minute until the pellet is broken up and redispersed into the water.
21. If the tubes are still balanced, place all back into the centrifuge and centrifuge again for 30 minutes at high speed (17000 xg).
22. Dispose of the water in each tube, and refill with fresh DI Water. Redisperse each pellet with same parameters as in step 16. Particles are ready for DLS sizing. *Note: if higher PVA conc is used, more than one wash step might be necessary. Repeat steps 17-22 for each wash.

Appendix 3: Supplemental Data

Power Regression Fits and Residuals for Size for Full Data Set

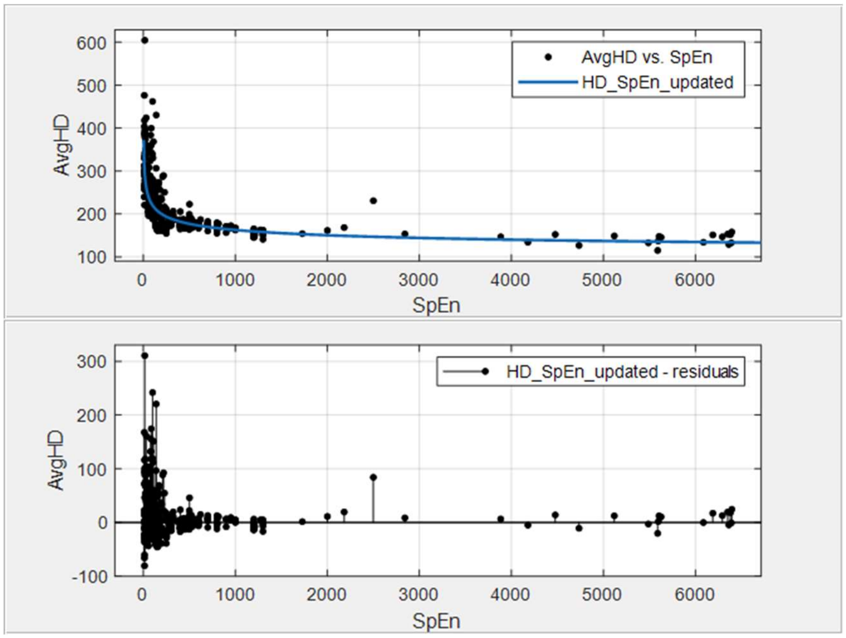

Power Regression Fits and Residuals for PDI for Full Data Set

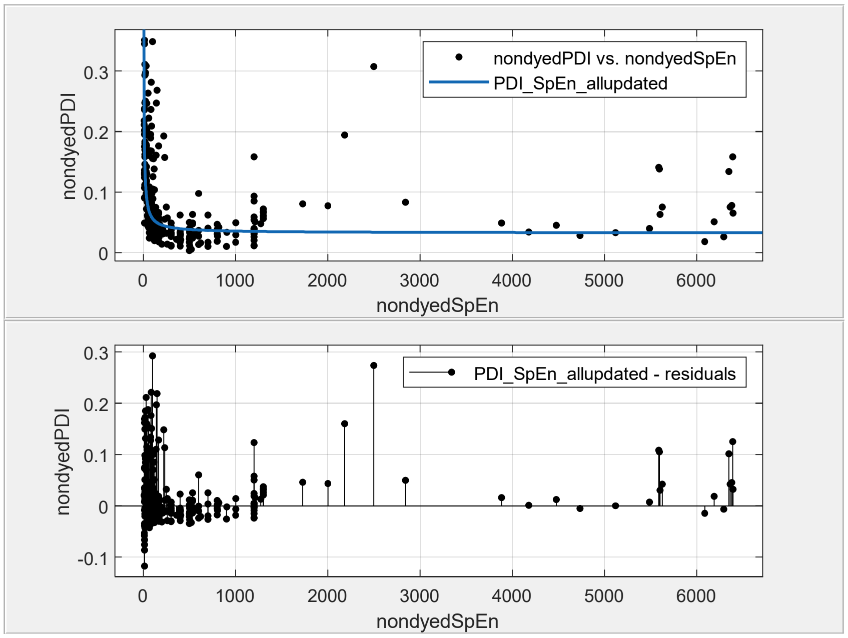

Power vs. Amplitude (%), with Fit and Residuals

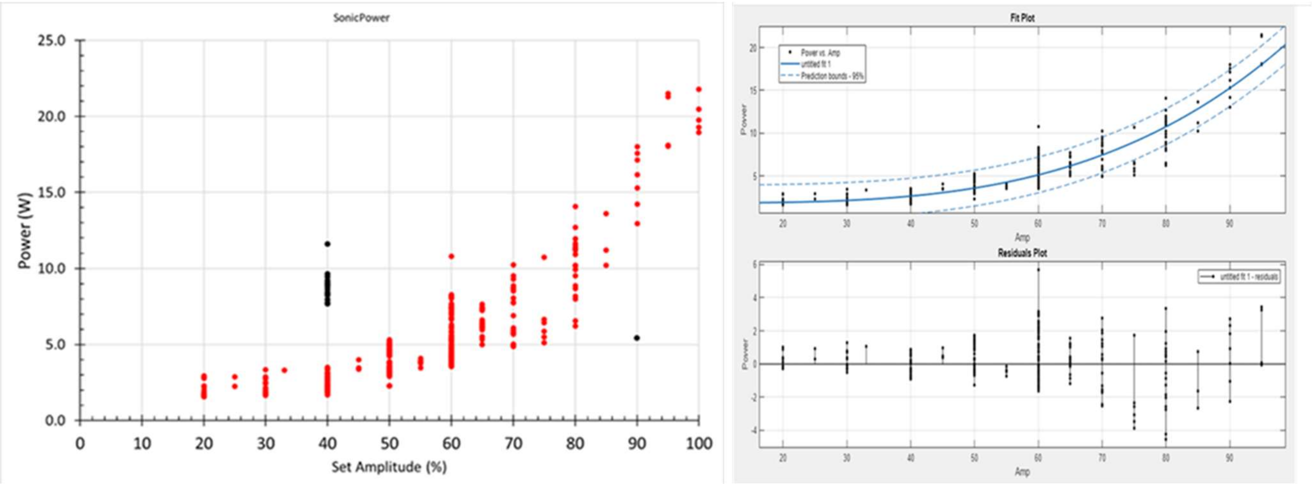

Core and Shell Release Profile Fits (KP, PS, and Hopf)

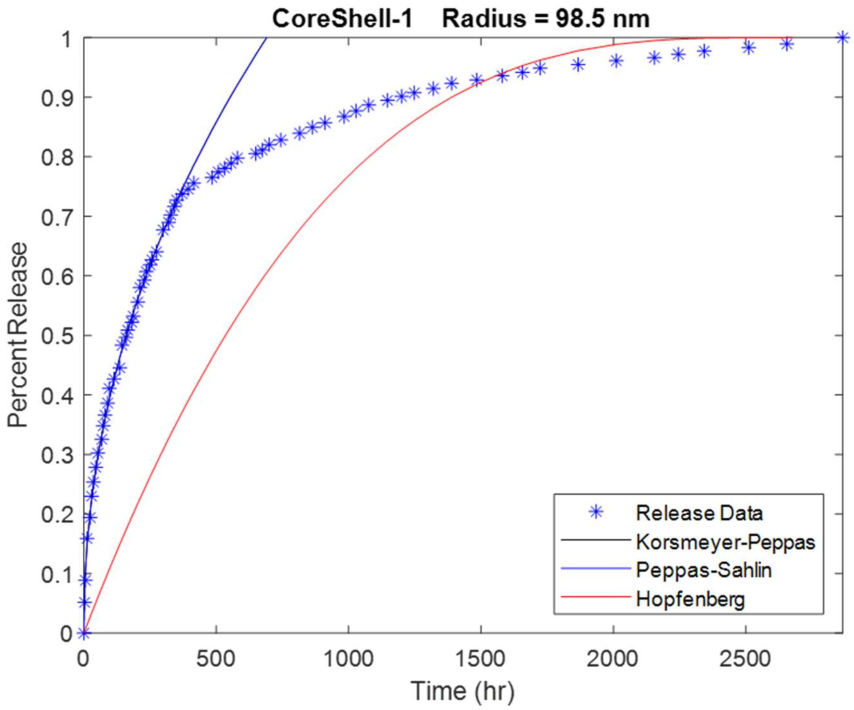

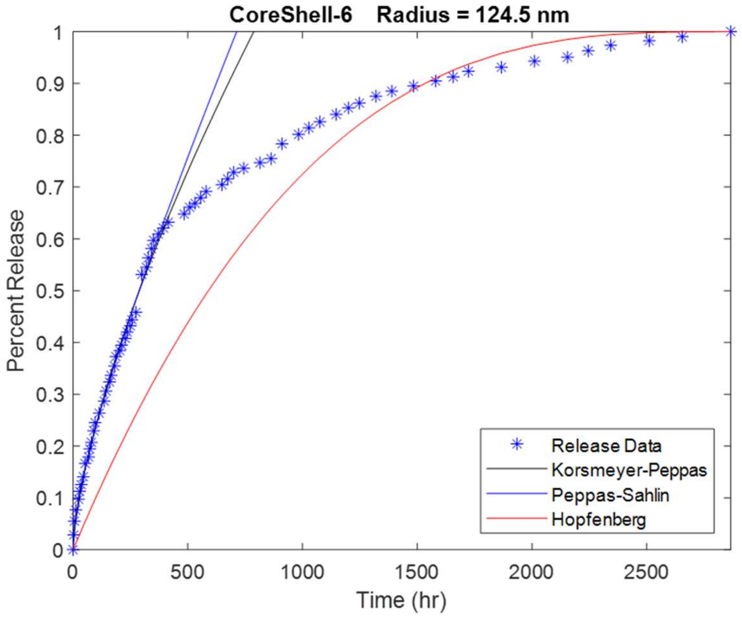

Chitosan Hydrogel and Commercial Dressing Properties Table for Endpoint Swelling

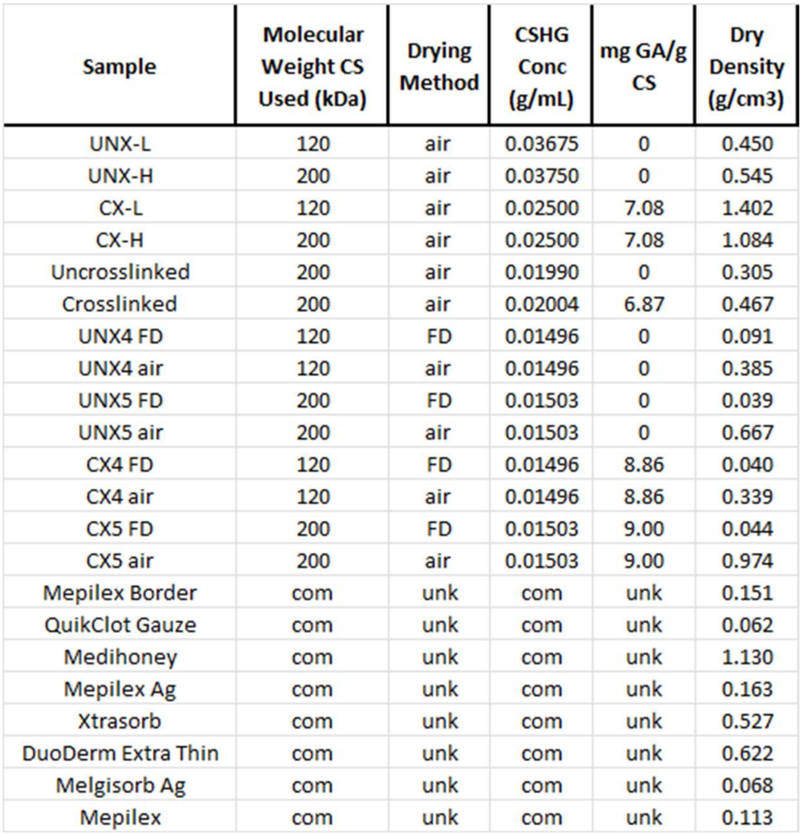

Sample	Molecular Weight CS Used (kDa)	Drying Method	CSHG Conc (g/mL)	mg GA/g CS	Dry Density (g/cm3)
UNX-L	120	air	0.03675	0	0.450
UNX-H	200	air	0.03750	0	0.545
CX-L	120	air	0.02500	7.08	1.402
CX-H	200	air	0.02500	7.08	1.084
Uncrosslinked	200	air	0.01990	0	0.305
Crosslinked	200	air	0.02004	6.87	0.467
UNX4 FD	120	FD	0.01496	0	0.091
UNX4 air	120	air	0.01496	0	0.385
UNX5 FD	200	FD	0.01503	0	0.039
UNX5 air	200	air	0.01503	0	0.667
CX4 FD	120	FD	0.01496	8.86	0.040
CX4 air	120	air	0.01496	8.86	0.339
CX5 FD	200	FD	0.01503	9.00	0.044
CX5 air	200	air	0.01503	9.00	0.974
Mepilex Border	com	unk	com	unk	0.151
QuikClot Gauze	com	unk	com	unk	0.062
Medihoney	com	unk	com	unk	1.130
Mepilex Ag	com	unk	com	unk	0.163
Xtrasorb	com	unk	com	unk	0.527
DuoDerm Extra Thin	com	unk	com	unk	0.622
Melgisorb Ag	com	unk	com	unk	0.068
Mepilex	com	unk	com	unk	0.113

Chitosan Hydrogel and Commercial Dressing Swelling Performance

Sample	Time (min)	AVG % Change Mass	StDev Change Mass	AVG % Change SA	StDev Change SA	AVG % Change Vol	StDev Change Vol	AVG % Change Den	StDev Change Den
UNX-L	60	2411%	13%	469%	27%	1038%	54%	121%	9%
UNX-H	60	961%	368%	311%	75%	722%	150%	25%	22%
CX-L	60	677%	200%	328%	117%	1220%	230%	-37%	26%
CX-H	60	573%	145%	239%	42%	726%	64%	-17%	24%
Uncrosslinked	60	2116%	971%	370%	222%	840%	445%	137%	48%
Crosslinked	60	1148%	259%	132%	93%	365%	187%	187%	48%
UNX4 FD	30	7917%	464%	162%	12%	754%	104%	847%	60%
UNX4 air	30	1322%	1%	143%	34%	491%	37%	141%	15%
UNX5 FD	30	7107%	357%	124%	16%	274%	26%	1842%	232%
UNX5 air	30	931%	8%	258%	68%	615%	136%	50%	30%
CX4 FD	30	3376%	222%	24%	3%	80%	24%	1848%	132%
CX4 air	30	404%	163%	33%	1%	166%	3%	90%	63%
CX5 FD	30	4076%	80%	26%	3%	139%	32%	1681%	270%
CX5 air	30	307%	5%	138%	21%	376%	43%	-14%	9%
Mepilex Border	30	1044%	176%	2%	2%	126%	1%	406%	80%
QuikClot Gauze	30	796%	25%	3%	0%	3%	0%	774%	22%
Medihoney	30	-32%	7%	-19%	2%	-39%	22%	32%	59%
Mepilex Ag	30	683%	12%	18%	5%	84%	13%	326%	24%
Xtrasorb	30	438%	8%	48%	7%	295%	19%	36%	4%
DuoDerm Extra Thin	30	8%	3%	0%	0%	0%	0%	8%	3%
Melgisorb Ag	30	1327%	38%	3%	1%	55%	1%	820%	16%
Mepilex	30	1186%	43%	49%	4%	93%	20%	569%	45%